Remote Laser-Based Spectroscopy of Nuclear Materials Enabled by Femtosecond Laser Filamentation

by

Patrick J. Skrodzki

A dissertation submitted in partial fulfillment
of the requirements for the degree of
Doctor of Philosophy
(Nuclear Engineering and Radiological Sciences)
in The University of Michigan
2021

Doctoral Committee:

Professor Igor Jovanovic, Chair
Doctor Sivanandan Harilal, Pacific Northwest National Laboratory
Professor Karl Krushelnick
Assistant Professor Louise Willingale

Patrick J. Skrodzki
pskrodzk@umich.edu
ORCID ID: 0000-0002-3324-9641

ACKNOWLEDGEMENTS

I would like to thank my advisor, Professor Igor Jovanovic, for the mentorship and guidance which have helped shape my knowledge, for the motivation which is reflected in my own passion for research, and for the opportunities provided for me to prosper as a scientist. I also thank Doctor Sivanandan Harilal, who offered me my first opportunity for research sparking my enthusiasm for science, and who has since been a mentor and role model for my career. I extend my gratitude also to the other members of my committee, Professor Karl Krushelnick and Assistant Professor Louise Willingale, whose insights have enhanced my research and its broader impacts. I thank Doctor Miloš Burger, whose direct guidance and friendship have sculpted my development not only as a scientist but also as a person. I thank John Nees for providing the mentorship and resourcefulness for working as a laser scientist. I thank Doctor Mark Phillips for the guidance to grow as a spectroscopist as well as the career and personal mentorship. And I thank Assistant Professor Prasoon Diwakar for the early research career and undergraduate mentorship.

I thank Doctor Jeremy Yeak for his contributions to various experiments in this work as well as insightful discussions and career guidance. I thank Assistant Professor Kyle Hartig for contributions to the uranium spectroscopy and filament ablation experiments as well as useful discussions and research direction. I thank Lauren Ibon, Xuan Xiao, and Jinpu Lin for their contributions to various uranium spectroscopy and filament ablation experiments presented here as well as their friendship. I thank Doctor Brian Brumfield for his contributions to various experiments in this work as

well as early career guidance. I thank Doctor Nicole LaHaye for her contributions to the uranium spectroscopy experiments presented in this work. I thank also Doctor Elizabeth Kautz for her contributions to the uranium spectroscopy experiments. I thank Professors Frederic Poineau, David Hatchett, and Ken Czerwinski at the University of Nevada Las Vegas, and their group members, Samundeeswari Mariappan Balasekaran and Cassara Higgins for their contributions to the uranyl fluoride laser-induced fluorescence spectroscopy experiments.

I thank also the funding sources which made this research possible. My research was supported by the National Science Foundation Graduate Research Fellowship Program (DGE 1256260). The work presented in this dissertation was partially supported by the Consortium for Verification Technology (DE-NA0002534) and Consortium for Monitoring, Verification, and Technology (DE-NE000863) sponsored by the Department of Energy National Nuclear Security Administration as well as the Air Force Office of Scientific Research (AFOSR) FA9550-16-1-0121 and the Department of Defense, Defense Threat Reduction Agency (HDTRA1-20-2-0002).

Lastly, I would like to thank my family: especially my fiancée Rachel, my brother David, and my parents Halina and Jerzy, for their unconditional love, support, encouragement, and motivation throughout this journey. Rachel has endured and fueled my passion for science and research, and I cannot imagine how I could have succeeded without her. David has been my source of relief and encouragement, at the times when I most needed each. And my parents provided guidance and framed the ethic and determination to persevere through my work.

TABLE OF CONTENTS

LIST OF FIGURES

Figure

LIST OF TABLES

Table

LIST OF APPENDICES

Appendix

LIST OF ABBREVIATIONS

BBO β-$Ba(BO_2)_2$

CCD charge-coupled devices

CMOS complementary metal-oxide-semiconductor

CPA chirped-pulse amplification

CW continuous wave

FIBS filament-induced breakdown spectroscopy

FL focal length

FOV field-of-view

FROG frequency-resolved optical gating

fs femtosecond

FWHM full-width at half-maximum

GDD group delay dispersion

GVD group velocity dispersion

HEU highly-enriched uranium

IB inverse bremsstrahlung

LA laser ablation

LAMIS laser ablation molecular isotopic spectrometry

LAS laser absorption spectroscopy

LEU low-enriched uranium

LIBS laser-induced breakdown spectroscopy

LIDAR light detection and ranging

LIF laser-induced fluorescence

LPP laser-produced plasma

LTE local thermal equilibrium

MCP micro-channel plate

MPI multi-photon ionization

ns nanosecond

OES optical emission spectroscopy

OTOFS optical time-of-flight spectroscopy

ps picosecond

PMT photomultiplier tubes

ROC Receiver operating characteristic

SHG second harmonic generation

SPM self-phase modulation

TIR total internal reflection

U uranium

ABSTRACT

Laser-based optical spectroscopy is an emerging technology which fulfills the criteria for safe, efficient, and economical measurement of various materials, including those relevant to nuclear energy and nuclear security. The primary spectroscopy techniques discussed in this work include laser-induced breakdown spectroscopy (LIBS), laser-induced fluorescence (LIF) spectroscopy, and laser ablation-laser absorption spectroscopy (LA-LAS). All-in-one advantages of these methods include capabilities for *in-situ*, rapid, and remote measurements, fieldable/portable systems, and sensitivity to various forms of the target: any state of matter, solid, liquid, gas; and any form or abundance of the target constituents – radioactive, nonradioactive, elemental, ionic, molecular, and even isotopic. This work demonstrates the use of laser-based optical spectroscopy for detection and classification of various materials, in particular uranium and its compounds. Optical emission spectroscopy is used to identify a characteristic visible-range signature from heavier gas-phase uranium oxide species in a laser-produced plasma (LPP), for the first time. This signature, as well as improved understanding of the evolution of uranium oxides in LPPs, have implications for *in-situ* distinction of uranium isotopes using LIBS and LA-LAS, relevant to nuclear security and safety.

Further, this work investigates the propagation of intense laser pulses in nonlinear media, such as air, which results in filamentation. Filamentation presents a promising mode for extended delivery of the laser excitation source. This nonlinear propagation regime can augment analytical spectroscopy methods to enable remote sensing at distances that could potentially extend to several hundreds of meters or

even kilometers. The transient structures associated with filamentation in gases have been demonstrated in previous work to be useful for waveguiding optical signals also. Filament-driven guiding may be applied not only to the delivery of the excitation source but also to collection of distant optical signals. Fundamental aspects of filamentation are experimentally studied, including the onset of multi-filamentation for high-peak-power lasers and multi-filament interactions during target ablation. Filamentation is combined with analytical spectroscopy techniques including LIBS and LIF to demonstrate standoff excitation and detection of nuclear materials relevant to nuclear security and safety (namely, uranium and its compounds like uranyl fluoride, vital to uranium enrichment processes). Finally, this work demonstrates that the lasting thermal structures left in the gas following dissipation of the filament plasma can be used to improve analytical performance of the LIBS technique. The refractive index change of gas traversed by the filament is used as an anti-guide to suppress time-varying optical signals, such as unwanted backgrounds from an LPP. Furthermore, two filament waveguide structures are concatenated to improve collection of the spectroscopic emission from an LPP, enabling prospects for scalability of such waveguides to greater distances using a series of laser pulses.

CHAPTER 1

Laser-Based Sensing of Nuclear Materials

1.1 Introduction

Since the commercialization of nuclear power in the 1960s, its popularity has grown to comprise approximately 20% of the total electricity generation in the United States [6] and between 13–16% of the world's total electricity production [5]. Development of safer nuclear reactor technologies, prospects of cleaner energy generation, and the volatility of prices for competing fuels used for electricity generation, like oil and natural gas prices, drive continued interest in nuclear power [175]. The foundation for nuclear power generation is the nuclear fuel cycle (Fig. 1.1); a majority of existing and developing reactor designs are based on uranium (U) as the primary fuel constituent. The standard nuclear fuel cycle begins with mining and processing natural uranium to form yellowcake (U_3O_8), which is followed by conversion to gaseous uranium hexafluoride (UF_6) and enrichment to fuel-grade concentrations of the fissile isotope U-235. Next, the fuel is fabricated to fit the structural and compositional requirements of the designated reactor type. In the final stages of the cycle, the spent fuel is either stored or, in some states, reprocessed and recycled [175]. Advancements in nuclear technologies pertaining to nuclear power generation and the nuclear fuel cycle, not to mention more nefarious or military uses of nuclear technology [136, 193], motivate concurrent advancements in detection and measurement methods which can be im-

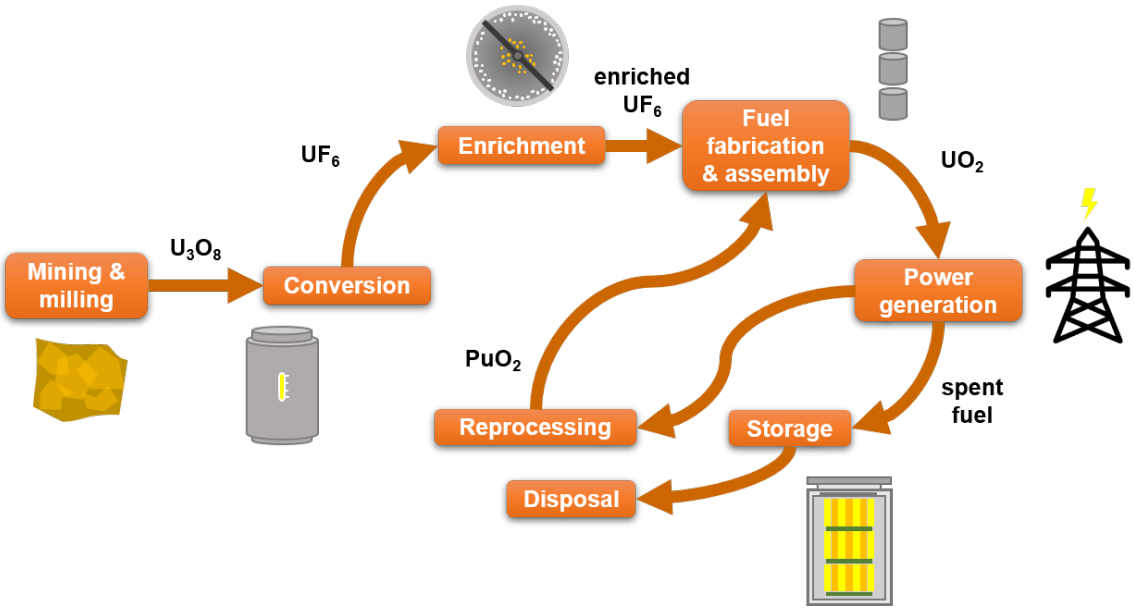

Figure 1.1: The standard nuclear fuel cycle begins with mining and processing natural U to form yellowcake (U_3O_8). Yellowcake is converted to uranium hexafluoride (UF_6) for enrichment. Following enrichment, the fuel is fabricated to fit the structural and compositional requirements of the designated reactor type. Spent fuel is either disposed or reprocessed in some countries.

plemented for safe, efficient, and economical categorization of materials used in the nuclear fuel cycle. These technical means are critical to nuclear security, safeguards, and nonproliferation.

Laser-based optical spectroscopy is an emerging technology which fulfills the criteria for safe, efficient, and economical measurement of various materials, including those relevant to nuclear energy and nuclear security. Laser-based optical spectroscopy, as referred to in this dissertation, encompasses the general laser-based excitation (followed by emission) or probing (*e.g.*, absorption) of optical-range electronic transitions. Some relevant techniques involve pulsed laser ablation (LA) and/or breakdown of a target to form a laser-produced plasma (LPP) such as laser-induced breakdown spectroscopy (LIBS), commonly also referred to in a more general sense as LA-optical emission spectroscopy (OES), and LA-laser absorption spectroscopy (LAS). Other techniques, such as laser-induced fluorescence (LIF), involve

direct probing of electronic transitions with or without breakdown. In general, one or more laser sources is used to actively interrogate a target, and either passive or active forms of spectroscopy provide information about the identity and abundance of the target's constituents. These methods complement existing, more mature detection techniques like those which passively or actively interrogate radioactive materials, looking for ionization radiation signatures from nuclear decay processes as opposed to electronic transitions [136]. Briefly, all-in-one advantages of such methods include capabilities for *in-situ*, rapid, and remote measurements, fieldable/portable systems, and sensitivity to various forms of the target: any state of matter, solid, liquid, gas; and any form or abundance of the target constituents – radioactive, nonradioactive, elemental, ionic, molecular, and even isotopic. This dissertation describes recent work demonstrating the use of laser-based optical spectroscopy for detection and classification of various materials, in particular uranium and its compounds, relevant to nuclear security and safety.

The propagation of intense laser pulses in nonlinear media, such as air, results in filamentation. Filamentation presents a promising mode for extended delivery of the laser excitation source, which can be combined with the aforementioned analytical techniques to enable remote sensing at distances that could potentially extend to several hundreds of meters or even kilometers [20]. A major focus of this dissertation is the application of filamentation to remote sensing. This includes overcoming the challenge of collection of distant optical signals, with the particular application of uranium detection. The microscopic polarizability response of molecules in the propagation medium to the strong electric field of the intense laser pulse results, macroscopically, in an intensity-dependent refractive index change, yielding self-focusing of the laser beam. Subsequently, ionization of the propagation medium induces a free-electron distribution which results in de-focusing of the laser beam. A dynamic balance between self-focusing, plasma de-focusing, and diffraction facilitates a mode of extended

propagation referred to as filamentation. The filament sustains a high intensity sufficient for excitation or ablation/breakdown over distances which significantly exceed the Rayleigh length [20]. Filamentation has been combined with existing laser-based analytical spectroscopy methods, for example LIBS [often referred to as filament-induced breakdown spectroscopy (FIBS)] and light detection and ranging (LIDAR), pushing the range of detection of such methods to scales on order of tens and even hundreds of meters [148, 196]. High-peak-power laser pulses, those greatly exceeding the threshold power for self-focusing, exhibit formation of several intense filament cores nucleated by noise or instabilities in the intensity profile of the beam; this multiple filamentation regime is especially relevant for applications which require greater initial laser energies for long-range propagation. The transient structures associated with filamentation in gases have also been demonstrated to be useful for guiding of optical beams [117, 137, 143, 197] and microwaves [34]. Such guiding techniques may be applied not only to the delivery of the excitation source but also to collection of distant optical signals. Here, recent work is presented which studies the fundamental aspects of filamentation including the onset of multi-filamentation for high-peak-power lasers and multi-filament interactions during target ablation, demonstrates filament excitation and optical spectroscopy of nuclear materials relevant to nuclear security and safety (namely, uranium and its compounds), and investigates prospects for improving collection of distant optical signals using filament guiding.

1.2 Laser-based optical spectroscopy

Various forms of optical spectroscopy are used throughout this dissertation not only for detection and measurements with nuclear-relevant materials but also to study the physics and identify the conditions in both LPPs and plasmas formed in air during laser filamentation. Benefits of laser-based analytical spectroscopy for detection include rapid measurement times, sensitivity to all states of matter as well as both ra-

dioactive and nonradioactive species, sensitivity to atoms, ions, compounds, and even isotopes, detection range, and simplicity of the excitation and detection schemes. Additionally, optical spectroscopy is used to identify the conditions, for example temperatures, number densities, and equilibrium status, in relevant plasma environments. The forms of spectroscopy discussed in this dissertation can be classified into two categories: emission and absorption.

Both optical emission and absorption of light by an atom provide characteristic signatures corresponding to transitions between discrete electron energy states E_i; the frequency ν or wavelength λ of the emitted or absorbed photon is given by the difference between two levels:

$$E_2 - E_1 = h\nu = \frac{hc}{\lambda}, \tag{1.1}$$

where h is Planck's constant, and c is the speed of light. Spectroscopy of the emitted or absorbed photons, therefore, is used to identify parent species, because electronic state configurations are unique for different elements, compounds, and even isotopes. Moreover, the magnitude of the emission or absorption is proportional to the (local) number density of the parent species, and spectroscopy may therefore be used to determine concentrations and ratios of species in various targets. Section 2.1 discusses in further detail the relationship between the magnitude of emission or absorption and the parent species' number density in LPPs, as well as spectroscopy-based plasma diagnostics.

The most prevalent form of optical spectroscopy discussed in this dissertation is OES. Specifically, OES can be used not only detect nuclear-relevant materials using analytical techniques such as LIBS but also to reveal the complex physics of LPPs, including the air plasma channels formed during filamentation. As such, the majority of the experiments and results from OES presented here involve the formation of a

plasma following excitation with a pulsed laser. Briefly, the light-matter interaction mechanisms which result in plasma formation vary largely with laser parameters such as the pulse duration and wavelength, and the form and properties of the target. For example, LA of solids may precede a direct sublimation phase transition in the case of ultrashort [∼femtosecond (fs)]-pulses or melting and evaporation stages in the case of longer pulses [∼nanosecond (ns)]. OES of LPPs observes electronic de-excitation transitions from excited species; absorption, on the other hand, for example LAS, involves probing unexcited species in such plasmas, usually with a tunable, narrow-line or broad-spectrum laser source. Absorption spectroscopy is a powerful tool which provides complementary information to emission spectroscopy and offering in some cases improved sensitivity with the tradeoff of a more complex pump-probe scheme more suited to a laboratory setting. In either case, spectroscopy in the optical regime simply involves mapping emission or absorption spectral domain signatures to the space domain using a diffractive element such as a prism or grating.

LIF is another form of emission spectroscopy, in which a laser is used to directly excite fluorescence of an analyte. A variation of LIF may be used in combination with LA to resonantly excite and enhance the emission from LPPs [183]. Here, LIF is used to directly excite and then observe molecular signatures from uranyl fluoride (UO_2F_2). LIF for detection of uranyl fluoride proves advantageous when compared to LA-OES or LAS because LA and breakdown results in dissociation of larger molecules like uranyl fluoride into their atomic and ionic constituents. Uranyl fluoride forms via hydrolysis of uranium hexafluoride, a compound used in gaseous uranium enrichment methods. Consequently, the presence of uranyl fluoride as an aerosol or particulate is an indicator of nearby enrichment activities, because leaking uranium hexafluoride readily and rapidly reacts with water vapor in the atmosphere. Additionally, higher detector spectral resolution is required to observe narrow atomic or ionic line emissions, and complicated stoichiometric analysis is necessary to infer the

presence and concentration of molecular species before LA [211]. On the other hand, the broad fluorescence spectrum of uranyl compounds has been extensively studied following continuous wave (CW) or short-pulsed laser excitation. The broad molecular spectrum lessens the requirement for a high-resolution spectroscopic system, while also enabling direct observation of the molecular species, whose presence may be an indicator of enrichment activities.

1.3 Remote laser-based sensing enabled by filamentation

A major advantage of direct detection methods based on optical spectroscopy for nuclear materials like uranium, is the range of the laser interrogation source as well as optical signals in air, which contrasts with the ionization radiation signatures from nuclear decay of radioactive materials. For example, the range of α-radiation with energies in the range of those from natural decay of uranium is on the order of just a few centimeters [132]. The range of low-energy β-radiation, such as that from decay of tritium, in air is approximately 30 cm [26]. Laser beams and optical signals, on the other hand, can propagate through air over extended distances if their wavelength is within the atmospheric transmission windows.

Filamentation of high-peak-power laser pulses in gas media, such as air, is particularly attractive for extended delivery of an intense excitation source. Although several works demonstrate long-range sensing on order of several tens of meters using techniques such as LIBS with short-pulse (ns) excitation [39, 200], there remain physical challenges which limit the delivery of intensities sufficient for excitation and especially ablation/breakdown. Major limiting factors include diffraction and air turbulence [140]. Laser filamentation establishes a dynamic balance with diffraction via nonlinear propagation, allowing the pulse to sustain a high intensity over distances which greatly exceed the Rayleigh length [20]. The Rayleigh length is the distance along the propagation axis over which the area of the beam doubles from the

beam waist position. In the linear propagation regime, this length, defines the range through which a focused beam can maintain high intensity. The diffraction-limited scale length for a general beam shape is given by:

$$z_R = \frac{2w_0^2 n_0}{1.22\lambda}, \tag{1.2}$$

where n_0 is the refractive index, and the Rayleigh range for a Gaussian beam is defined as $z_R = \frac{\pi w_0^2}{\lambda}$. The Rayleigh length for a Gaussian beam with beam waist (w_0) 1 mm and wavelength (λ) of 633 nm is z_R ~5 m; whereas filamentation has been shown to extend the propagation distances, generating laser peak intensities on order of 10^{13} W.cm^{-2} to several hundreds of meters and even kilometers [59, 194]. The work presented herein explores the fundamental physics which lead to filamentation, how filamentation can be combined with analytical spectroscopic methods like LIBS or LIF for remote sensing applications, and considerations for collection of distant optical signals.

1.4 Dissertation structure

The contributions in this dissertation are motivated by the broader goal to further the capabilities of laser-based optical spectroscopy methods for direct detection and analytical measurements of nuclear materials, like uranium and its compounds. However, the dissertation may be divided into two relevant focus-areas: (1) optical spectroscopy of uranium following short-pulsed LA of uranium metal, and (2) remote sensing enabled by filamentation. The following two chapters, Chapters 2–3, concentrate on general principles and considerations for the various forms of optical spectroscopy herein discussed, with Chapter 3 describing recent experimental investigation of uranium-containing LPPs conducted in collaboration and at facilities at Pacific Northwest National Laboratory; whereas, subsequent chapters, Chapters 4–9,

focus on developing fundamental understanding of the filamentation phenomenon and its applications pertinent to nuclear security, safeguards, and nonproliferation. The experiments presented in this dissertation regarding filamentation were conducted at the University of Michigan in facilities of the Gérard Morou Center for Ultrafast Optical Science. Chapters 2 and 4 provide background and the fundamental physics and deliberations relevant to optical spectroscopy and filamentation as a means for remote sensing, respectively. All remaining chapters, except Chapter 10 that provides a conclusion and outlook, present results from recent experimental campaigns. Some chapters that feature individual campaigns, for example, the work which investigated filament-LIF spectroscopy of uranyl fluoride (Chapter 7), present the relevant context in their respective introductory sections. This dissertation compiles some previously published results from:

[24] M. Burger, L. A. Finney, L. Garrett, S. S. Harilal, K. C. Hartig, J. Nees, P. J. Skrodzki, X. Xiao, and I. Jovanovic. Laser ablation spectrometry for studies of uranium plasmas, reactor monitoring, and spent fuel safety. *Spectrochimica Acta Part B: Atomic Spectroscopy*, 179:106095, 2021.

[26] M. Burger, P. J. Skrodzki, L. A. Finney, J. Hermann, J. Nees, and I. Jovanovic. Isotopic analysis of deuterated water via single- and double-pulse laser-induced breakdown spectroscopy, *Physics of Plasmas*, 25(8):083115, 2018.

[27] M. Burger, P. J. Skrodzki, L. A. Finney, J. Nees, and I. Jovanovic. Remote detection of uranium using self-focusing intense femtosecond laser pulses. *Remote Sensing*, 12(8):1281, 2020.

[28] M. Burger, P. J. Skrodzki, I. Jovanovic, M. C. Phillips, and S. S. Harilal. Laser-produced uranium plasma characterization and Stark broadening measurements. *Physics of Plasmas*, 26(9):093103, 2019.

[29] M. Burger, P. J. Skrodzki, J. Lin, J. Nees, K. Krushelnick, and I. Jovanovic. Intense laser filament-solid interactions from near-ultraviolet to mid-infrared. *Optics Express*, 26(13):16456–16465, 2018.

[30] M. Burger, P. J. Skrodzki, J. Nees, and I. Jovanovic. Electrical conductance of near-infrared femtosecond air filmanets in the multi-filament regime. *Optics Letters*, 43(55), 5520–5523, 2018.

[71] L. A. Finney, P. J. Skrodzki, M. Burger, J. Nees, S. S. Harilal, and I. Jovanovic. Single-shot, multi-signature remote detection of uranium by filament-induced breakdown spectroscopy. *Optics Letters*, 44(11):2783–2786, 2019.

[72] L. A. Finney, P. J. Skrodzki, M. Burger, X. Xiao, J. Nees, and I. Jovanovic. Optical emission from ultrafast laser filament-produced air plasmas in the multiple filament regime. *Optics Express*, 26(22):29110–29122, 2018.

[99] S. S. Harilal, E. J. Kautz, B. E. Bernacki, M. C. Phillips, P. J. Skrodzki, M. Burger, and I. Jovanovic. Physical conditions for UO formation in laser-produced uranium plumes. *Physical Chemistry Chemical Physics*, 21(29):16161–16169, 2019.

[125] E. J. Kautz, P. J. Skrodzki, M. Burger, B. E. Bernacki, I. Jovanovic, and S. S. Harilal. Time-resolved imaging of atoms and molecules in laser-produced uranium plasmas. *Journal of Analytical Atomic Spectrometry*, 34(11):2236–2243, 2019.

[216] P. J. Skrodzki, M. Burger, L. A. Finney, F. Poineau, S. M. Balasekaran, J. Nees, K. Czerwinski, and I. Jovanovic. Ultrafast laser filament-induced fluorescence spectroscopy of uranyl fluoride. *Scientific Reports*, 8(1):11629, 2018.

[218] P. J. Skrodzki, M. Burger, and I. Jovanovic. Transition of femtosecond-filament-solid interactions from single to multiple filament regime. *Scientific Reports*,

7:12740, 2017.

[219] P. J. Skrodzki, M. Burger, I. Jovanovic, M. C. Phillips, B. E. Brumfield, and S. S. Harilal. Tracking of oxide formation in laser-produced uranium plasmas. *Optics Letters*, 43(20):5118–5121, 2018.

[220] P. J. Skrodzki, M. Burger, I. Jovanovic, M. C. Phillips, J. Yeak, B. E. Brumfield, and S. S. Harilal. Plume dynamics and gas-phase molecular formation in transient laser-produced uranium plasmas. *Physics of Plasmas*, 26(8):083508, 2019.

[222] P. J. Skrodzki, N. P. Shah, N. Taylor, K. C. Hartig, N. L. LaHaye, B. E. Brumfield, I. Jovanovic, M. C. Phillips, and S. S. Harilal. Significance of ambient conditions in uranium absorption and emission features of laser ablation plasmas. *Spectrochimica Acta Part B: Atomic Spectroscopy*, 125:112–119, 2016.

CHAPTER 2

Introduction to Laser Ablation and Breakdown, Optical Spectroscopy, Plasma Diagnostics, and Spectroscopy of Uranium-Containing Plasmas

Several laser-based analytical spectroscopic techniques described in this dissertation, including LIBS, LA-LAS, and LA-LIF, involve ablation and/or breakdown of a target which may be comprised of various states of matter (solid, liquid, gas). Pulsed LA is a complex field of study and a subject of ongoing comprehensive theoretical and experimental investigation. Here, the influential parameters and mechanisms associated with short- and ultrashort-pulsed LA of solids are introduced. Besides the pulse duration, parameters which dictate the physical mechanisms associated with LA and/or breakdown include laser wavelength, fluence, various material properties (absorption length, thermal properties, and phase transition thresholds), and ambient conditions (pressure, temperature, and nature of surrounding gas). This chapter discusses the physics associated with ultrashort-(fs) and short-pulsed LA and breakdown in the context of the various forms of optical spectroscopy. Further, the critical considerations for design and implementation of an optical spectroscopy experiment, with or without ablation/breakdown of a target (in the case of LIF) are introduced.

2.1 Fundamentals of laser ablation, breakdown, and relevant optical spectroscopy techniques

2.1.1 Pulsed laser ablation and breakdown

LA can be principally categorized by the ablation laser pulse duration because of the discrepant timescales between fast [$\mathcal{O}$(fs–picosecond (ps))] seed ionization and heat transfer with plasma formation [$\mathcal{O}$(ps–ns)]. The relevant pulse durations discussed herein are termed *ultrashort*, encompassing fs–ps pulse durations, and *short*, involving ns pulses. For ultrashort pulses, thermal conduction can be neglected, and LA involves a direct solid-vapor transition. In contrast, short-pulse LA involves laser heating of the target: first, to the melting and then, to the vaporization temperatures. Therefore, heat conduction in the target is the dominant energy dissipation mechanism. Within this dissertation, the short- and ultrashort-LA regimes are distinguished because primarily ns-LA and fs- (or filament) ablation are discussed. Further, the discussion is focused to ablation of metals and semiconductors; more detailed discussion of ablation of other forms of solids including ceramics and dielectrics may be found in Ref. [161].

In metals and semiconductors, free electrons absorb laser energy and electron-electron collisions cause thermalization on fs timescales. Subsequently, electron-phonon interactions occur over timescales on the order of several ps. These interactions are described by the two-temperature diffusion model that includes the electron and lattice temperatures, T_e and T, respectively [161, 204]:

$$C_e\frac{\partial T_e}{\partial t} = \frac{\partial}{\partial z}\left(k_e\frac{\partial T_e}{\partial z}\right) - \Gamma_{e-p}(T_e - T) + 1 - R)\alpha I(t)\exp\left(-\alpha z\right) \tag{2.1}$$

and

$$C\frac{\partial T_e}{\partial t} = \Gamma_{e-p}(T_e - T), \tag{2.2}$$

where C_e and C represent the specific heat capacities of electrons and the lattice, respectively; Γ_{e-p} is the electron-phonon coupling constant; R is material reflectivity; and $I(t)$ is the laser intensity. The two-temperature model defines three important timescales: the electron cooling time, $\tau_e = C_e/\Gamma_{e-p}$; the lattice heating time, $\tau_p = C/\Gamma_{e-p}$; and the laser pulse duration, τ_L.

Ultrashort-pulsed LA involves the condition in which the laser pulse duration is shorter than the electron cooling time ($\tau_L \ll \tau_e$) and electron-lattice coupling can be neglected, leading to a simple solution of Eq. (2.1), also neglecting the electron heat conduction term [37, 161]:

$$C_e'\frac{\partial T_e^2}{\partial t} = 2I_a\alpha\exp\left(-\alpha z\right), \tag{2.3}$$

yielding the solution:

$$T_e = \sqrt{T_0^2 + \frac{2I_a\alpha}{C_e'}\exp\left(-\alpha z\right)}, \tag{2.4}$$

where $I_a = (1-R)I_0$ represents the absorbed laser intensity (assuming a constant intensity throughout the pulse duration), and T_0 represents the initial temperature. After the interaction with the laser pulse, electrons rapidly transfer energy to the lattice. The extremely short timescales of ultrashort LA trigger a direct solid-vapor transition, resulting in the formation and expansion of a plasma. Both ablation and the formation and expansion of the vapor and plasma occurs on much longer timescales than the duration of the laser pulse. During ablation, heat conduction can be considered negligible. Further, direct interactions between the laser and lattice can

also be ignored. After ablation, the laser does not interact with the vapor/plasma, because the duration of the ultrashort, femtosecond, pulse is several orders of magnitude shorter than the picosecond-timescales for vapor/plasma formation. Instead, field ionization mechanisms such as multi-photon ionization (MPI) and tunneling ionization compete to provide seed electrons for forming the ultrashort LPP, and collisional processes like electron impact ionization [98] dominate the increasing degree of ionization in such plasmas.

The MPI mechanism dominates for lower incident electric field strengths, with ionization rate $W = \sigma_K I^K$, where σ_K is the K-photon ionization cross section, I is the laser intensity, and K is the number of photons which overcome the ionization potential $Kh\nu > U$ (h is the Planck constant; ν is the laser frequency; and U is the ionization potential). In tunneling ionization, the combined electronic Coulomb and incident field potential dips below the bound energy level, allowing the electron to tunnel out of its bound state. Tunneling ionization becomes prevalent for greater field strengths; and the degree of ionization mechanism can be determined by the Keldysh parameter γ, which compares the ionization potential U to the electric field strength E [114, 190, 265]:

$$\gamma = \frac{\omega\sqrt{2m_e U}}{eE}. \tag{2.5}$$

Here, ω is the angular frequency of the laser and m_e and e are the electron mass and charge, respectively. MPI dominates in the range $\gamma \gg 1$, and tunneling ionization prevails in the range $\gamma \ll 1$. Figure 2.1 maps the Keldysh parameter for a relevant range of laser intensities and wavelengths for ultrashort-pulsed ionization of air. The ionization potential used in the calculation is that for the oxygen molecule (O_2) and equals 12 eV [201]. These results are specifically useful for understanding seed ionization during ultrashort laser filamentation, but the concept is applicable to ultrashort

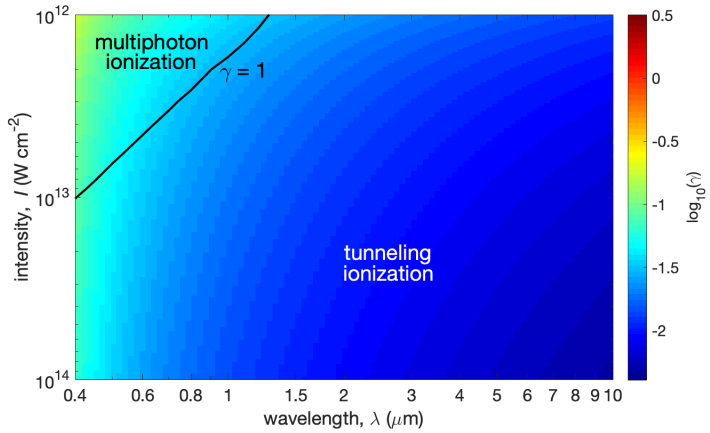

Figure 2.1: The Keldysh parameter is evaluated for a relevant range of laser intensities and wavelengths for ionization of air with an ionization potential from O_2 of 12 eV. These results are specifically useful for understanding seed ionization during ultrashort laser filamentation, but the concept is applicable to ultrashort laser ablation of metals.

laser ablation of metals. Notably, tunneling ionization is prevalent for longer laser wavelengths in the range of laser intensities between 10^{12} and 10^{14} W.cm^{-2}.

On the other hand, short-pulsed LA (ns) involves additional light-phonon and light-plasma interactions on longer timescales within the pulse duration. Short-pulse durations exceed the lattice heating time ($\tau_L >> \tau_p$), and under this condition the electron and lattice temperatures are equal, reducing Eq. (2.1) and (2.2) to the heat equation [37, 161]:

$$C\frac{\partial T}{\partial t} = \frac{\partial}{\partial z}\left(k\frac{\partial T}{\partial z}\right) + I_a\alpha\exp\left(-\alpha z\right). \tag{2.6}$$

Short-pulse laser irradiation of a solid first causes heating of the target surface resulting in melting followed by vaporization. Plasma formation, expansion, and interaction with the laser follows the vaporization stage of short-pulse LA for fluences greater than approximately 2 J cm^{-2} [161]. Greater laser fluence yields vapor temperatures sufficiently high for seed ionization of ablated species, which in turn triggers a cascade of ionization because the vapor becomes opaque to the laser leading to plasma

formation. The opacity of a plasma (or metal in some frameworks) is derived from the plasma frequency ω_p, given by

$$\omega_p = \sqrt{\frac{N_e e^2}{\varepsilon_0 m_e}}, \tag{2.7}$$

which is considered as the resonant frequency of a group of free electrons in a plasma with density N_e, where ε_0 is the permittivity of free space. A simplified dispersion relation $\omega^2 = \omega_p^2 + c^2k^2$ yields the frequency-dependent refractive index n of the plasma:

$$n = \frac{ck}{\omega} = \sqrt{1 - \frac{\omega_p^2}{\omega^2}}. \tag{2.8}$$

Equation (2.8) further yields the critical density, which describes the condition for plasma opacity to light. The plasma is transparent for the range of laser frequencies greater than the plasma frequency and reflective for laser frequencies smaller than the plasma frequency. The critical density N_c is, therefore, defined for the case where $\omega_p = \omega$:

$$N_c = \frac{\varepsilon_0 m_e \omega^2}{e^2}. \tag{2.9}$$

Notably, in plasmas formed via LA, the laser interacts with a density gradient such that the laser may be partially absorbed via mechanisms such as inverse bremsstrahlung (IB) and photoionization [161].

The following section (Sec. 2.1.2) discusses in more detail the morphology of such plasmas; here, possible laser-plasma interaction mechanisms are explored. The dominant light absorption mechanisms in LPPs include IB and photoionization. During IB absorption, electrons gain energy from laser photons during collisions with neutral and ionic species in the plasma. The IB absorption coefficient α_{IB} for electron-ion

interactions is given by [161]

$$\alpha_{IB} = \sigma_{IB} N_e = \frac{4}{3}\sqrt{\frac{2\pi}{3k_B T_e m_e^3}}\frac{Z^2 e^6}{hc\nu^3}\left(1 - \exp\left(-\frac{h\nu}{k_B T_e}\right)\right) N_i N_e, \tag{2.10}$$

where σ_{IB} is the IB cross-section; N_i and N_e are the ion and electron number densities, respectively; Z is the ion charge; k_B is the Boltzmann constant; and c is the speed of light. The electron-neutral IB interaction is particularly important during the early stages of plasma formation providing the seed electrons and ions for further IB interactions in addition to those from photoionization and electron impact ionization. From Eq. (2.10), IB is more efficient for longer laser wavelengths. For shorter wavelengths, photoionization becomes the dominant light absorption mechanism. The photoionization absorption coefficient α_{PI} is approximated by [161]

$$\alpha_{PI}(\mathrm{cm}^{-1}) = \sigma_{PI} N_n \approx \sum_n 2.9 \times 10^{-17} \frac{\varepsilon_n^{5/2}}{(h\nu)^3} N_n, \tag{2.11}$$

where σ_{PI} is the photoionization cross section; $(h\nu)$ is the photon energy (eV); and ε_n (eV) and N_n (cm^{-3}) are the ionization energy and number density of the excited state n, respectively. The energy levels considered in the summation include those which satisfy the condition $h\nu > \varepsilon_n$ [161]. Both IB and photoionization, as well as collisional ionization mechanisms such as electron impact, contribute to the formation of the LPP during short-pulse ablation. Ultimately, the different ablation timescales and mechanisms between ultrashort- and short-pulse LA result in largely different initial conditions in each LPP. These initial conditions as well as the evolution of LPPs are discussed further in Sec. 2.1.2.

2.1.2 Evolution of laser-produced plasmas

The evolution of LPPs involves collisional processes which lead to recombination, deceleration, and ultimately plasma dissipation. This section concentrates on LA in

an ambient gas where the interaction of the plume species with ambient species as well as the formation and expansion of a shockwave are also considered. Although mechanical interactions are dominant throughout the evolution of the plasma, electric and radiative interactions are still of interest during early stages in plume expansion. At early times, there typically exists a notable segregation between fast-moving, negatively-charged electrons and slower, positively-charged ion species. This segregation drives plume expansion in the early stages and is referred to as *Coulomb explosion*. In general, important electron processes in the LPP can be classified into radiative and collisional categories [111, 161]. Radiative processes include photoionization and the reverse process of direct recombination of free electrons resulting from the interaction with a photon. Collisional processes include various types of electron impact mechanisms which result in either (de)-excitation or ionization/three-body recombination [111].

At later times, collisions between particles in the plume lead to increased lateral motion of the plume, whereas, in free space and without collisions, the plume would expand in the perpendicular direction with respect to the target surface characterized by a free expansion model in which plume size exhibits a linear time dependence [95, 96]. Further, recombination between atomic and ionic species in the plume with electrons represents an important loss mechanism that competes with ionization. Radiative recombination processes similarly contribute to a decreasing degree of ionization. Recombination time scales for three-body (3B) and radiative (rad) processes are approximated in the following empirical relations [192]:

$$\tau_{3\mathrm{B}} \approx 1.1 \times 10^{26} \frac{T_e^{9/2}}{Z^3 N_e^2}, \tag{2.12}$$

and

$$\tau_{\text{rad}} \approx 3.7 \times 10^{12} \frac{T_e^{3/4}}{Z^2 N_e}, \tag{2.13}$$

where T_e is given units of in eV, and N_e is given in cm^{-3}. However, collisions between particles in the ablation plume and in the ambient are considered as the predominant deceleration mechanism for overall plume expansion. Plume dissipation occurs when the ablated species reaches diffusion equilibrium with the ambient. In lower pressure environments, for typical short- or ultrashort-pulsed LA, this dissipation occurs on microsecond time scales at distances on the order of a few centimeters. At higher pressures, significant plume confinement is observed, increasing the rate of collisional interactions and expediting plasma dissipation [161].

Overall, there is a complex interplay of various interactions during plasma expansion, including electronic and chemical recombination, and collisional interactions between plasma species and ambient species. In general, the rate of plasma expansion, as measured by the plasma size L, lies somewhere between a model based on drag $L = A - B\exp(-Ct)$ [95, 96] and the spherical blast (or Sedov) model $L = At^{2/5}$ [207, 261], where A, B, and C are general shape parameters. For a general range of pressures near atmospheric conditions (∼0.1–1 atm), a strong, discontinuity pressure wave, referred to as the shock or shockwave, forms alongside the plume and confines its expansion. The blast model for a general geometry describes shockwave expansion for the relevant dimension L as a function of time t:

$$L(t) = \left(\frac{E_d}{C_\gamma \rho_0}\right)^{1/(2+\xi)} t^{2/(2+\xi)}, \tag{2.14}$$

where E_d is the blast detonation energy; C_γ is a parameter which depends on the adiabatic constant ratio γ; ρ_0 is the initial ambient gas density; and ξ is a geometry parameter ($\xi = 1$ represents a plane wave, $\xi = 2$ cylindrical wave, and $\xi = 3$ spherical

wave). For LA of solids, the shockwave is assumed to expand with a semi-spherical geometry; whereas, a cylindrical geometry is a reasonable assumption for a filament plasma. In reality, more complex interactions exist, for example between the shockwave and the target, which may compromise the assumptions of a simple geometry. Nevertheless, the expansion of the shockwave is an important consideration when discussing overall plume expansion, as the shock can both shield and mediate collisional interactions between plume species and the ambient. For example, the collapse of the shock nearer to its interface with the target surface during the late stages in ablation of solids may allow penetration of reactive ambient species and promote chemical interactions in the plasma regions nearer the target. The high temperature and degree of ionization in the plasma make it an ideal site for not only exothermic but also endothermic inelastic processes such as chemical reactions. Chemistry in the plume is another contributing mechanism to plasma dissipation and may consist of reactions between species solely from the target and/or between target and ambient species. In the next section (Sec. 2.1.3), radiative electronic transitions and the use of various optical diagnostic techniques for measurements with LPPs are discussed.

2.1.3 Plasma spectroscopy and relevant diagnostics

It is useful to measure or ascertain certain properties of LPPs including the number densities and temperatures of various species, its refractive index which dictates, macroscopically, the interaction of light with the plasma, and the equilibrium state. In this section, the physical origins of various forms of emission from LPPs, and how these types of emission can be used alongside other diagnostic methods to measure important plasma properties or to determine target constituents using various analytical spectroscopic methods are discussed. Figure 2.2 shows a diagram of the different types and sources of emission with approximate timescales in a ns-LPP, beginning with continuum at the earliest times when the plasma is hottest from which line

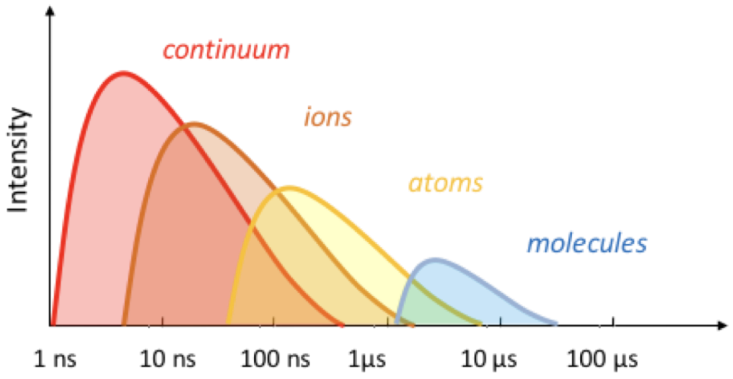

Figure 2.2: Continuum emission dominates the early timescales of the evolution of laser-produced plasmas originating from black-body emission, bremsstrahlung, and recombination. As the plasma cools, spectroscopic lines from ionic and neutral species appear on the intermediate timescales. Molecular recombination begins at a later timescale.

emission from ionic and neutral species appear. Molecular recombination and emission from compounds follows at later timescales, when the temperature among other plasma conditions are favorable.

At the earliest times in the evolution of typical LPPs, emission resembles a continuum. This continuum is comprised of emission from radiative hot-body transitions, bremsstrahlung, and recombination interactions. Black-body (BB) emission results from the high temperatures at the earliest times in the LPP and is described by Planck's law for a body which emits and absorbs a range of frequencies in an equilibrium state [112]:

$$\frac{dP_{\mathrm{BB}}}{d\Omega} = \frac{2h\nu^3}{c^2} \frac{1}{\exp\left(\frac{h\nu}{k_B T}\right) - 1}, \tag{2.15}$$

where $\frac{dP_{\mathrm{BB}}}{d\Omega}$ is the emitting power per unit solid angle and T is the temperature of the body (plasma). Bremsstrahlung emission occurs from deceleration of fast-moving charged particles. Recombination emission results from three-body electron-ion collisional processes which occur at higher rates at early times due to the particle speeds and densities. In ultrashort-pulse LPPs, the continuum is usually short-lived

(on order of several tens to hundreds of ns) relative to that from their short-pulsed counterparts (on order of several hundreds of ns to several µs for a ns-LPP) because of lower initial temperatures and ionization fractions [111].

At later stages in the plasma evolution, as the plasma cools, line emission from electronic transitions of plasma constituents appear. During these stages, the LPP departs from the complete thermal equilibrium state which is characterized by Eq. (2.15) and enters a less complete local thermal equilibrium (LTE), where plasma species adopt state populations N_i given by the Boltzmann distribution $N_i \propto \exp(-E_i/T)$. Here, E_i is the upper energy level of state i, but the radiation is not necessarily thermal. In this form of equilibrium, emission rates are no longer equal to absorption, but there may be some degree of absorption depending on the local state populations. Introducing the probabilities for spontaneous decay may be used to determine the emitted line intensity I_{ul} for a particular transition between lower state l and upper state u for species i under the LTE assumption [111]:

$$I_{ul}\lambda_{ul} = \frac{N_i}{U(T)} A_{ul} g_u \exp\left(-\frac{E_u}{k_B T}\right). \tag{2.16}$$

This yields a relation which can be useful for directly determining plasma temperature by comparing the state populations (or line intensities) of like species under the LTE assumption:

$$\frac{I_b}{I_a} = \frac{N_b A_b g_b \lambda_a}{N_a A_a g_a \lambda_b} \exp\left(-\frac{E_b - E_a}{k_B T}\right), \tag{2.17}$$

where λ_{ul} is the wavelength of the transition; $U(T)$ is the temperature-dependent partition function for the species; A_{ul} is the Einstein coefficient or rate of the spontaneous transition; and g_u and E_u are the upper state degeneracy and energy level, respectively. Equation (2.17) compares the populations of species a and b, while Eq. (2.16) gives the general relation useful also for analytical spectroscopic techniques such as

LIBS (or OES). These spectroscopic lines act as fingerprints for the emitting species and are used to identify plasma (and, consequently, target) constituents and infer their concentrations. Further, the Saha equation, which describes populations of consecutive ionization states i to $i+1$, is derived from the Boltzmann distribution and LTE assumption:

$$\frac{N_{i+1}}{N_i} N_e = \frac{g_{i+1}}{g_i} \left[\frac{2m_e^3}{h^3} \left(\frac{2\pi T}{m_e} \right)^{3/2} \right] \exp\left(\frac{U_i}{k_B T} \right), \tag{2.18}$$

where N_e is the free electron density, and U_i is the electron binding energy of state i. Hence methods comparing line ratios from like species are useful for determination of important plasma properties like the temperature and free electron density. However, it must be noted that such methods are viable only if the LTE condition is valid. A necessary, but insufficient, check for the validity of the LTE assumption is given by the McWhirter criterion [93, 157]:

$$N_e \gg 10^{19} \sqrt{T/e} \, (\Delta E/e)^3 \,, \tag{2.19}$$

where N_e is given in m^{-3}, and T/e and $\Delta E/e$ are the temperature and energy level difference in eV. Under certain circumstances, for example at very late stages in plasma evolution, LPPs may completely depart from LTE. Different species in the plasma exhibiting different temperatures may be one indicator of departure from LTE; in some circumstances, these different species may individually satisfy the LTE conditions, and are said to exhibit partial LTE (PLTE).

The spectroscopic line widths also carry information about useful plasma properties and may be used for diagnostics. Dominant line broadening mechanisms in the plasma for atomic and ionic emissions include pressure, Stark, and Doppler (temperature) broadening. Natural line broadening, derived from the Heisenberg uncertainty, $\Delta\lambda_{\mathrm{nat}} = 1/(2\pi c\tau)$, where τ is spontaneous emission lifetime of the excited state, is

typically orders of magnitude smaller than other broadening mechanisms in LPPs and usually considered negligible. Perturbations of the emitter wavefunction due to collisional interactions lead to pressure (also called van der Waals) broadening. Pressure broadening $\Delta\lambda_{p,\mathrm{hwhm}}$ and spectral line shift $\Delta\lambda_{p,0}$ may be determined by summing the contributions of different colliding species in the plasma [89, 90, 98]:

$$\Delta\lambda_{p,\mathrm{hwhm}} = \sum_i \sigma_i(T_{\mathrm{ref}}) P_i \left(\frac{T_{\mathrm{ref}}}{T}\right)^{n_i}, \tag{2.20}$$

$$\Delta\lambda_{p,0} = \sum_i \sigma_i(T_{\mathrm{ref}}) P_i \left(\frac{T_{\mathrm{ref}}}{T}\right)^{k_i}, \tag{2.21}$$

where $\sigma_i(T_{\mathrm{ref}})$ denotes the interaction cross-section at a reference temperature T_{ref} for perturber i; P_i is the partial pressure of the species; and n_i and k_i dictate the temperature dependence and are determined empirically. Stark broadening results from interactions of emitted photons with charged plasma species. The Stark width $\Delta\lambda_{\mathrm{S}}$ can be determined empirically as follows:

$$\Delta\lambda_{\mathrm{S}} = 2a\frac{N_e}{10^{17}} + 3.5A\left(\frac{N_e}{10^{17}}\right)^{1/4}\left(1 - \frac{3}{4N_D^{1/3}}\right)a\frac{N_e}{10^{17}}, \tag{2.22}$$

where a and A (typical units of nm or pm) are electron and ion width parameters, respectively; and N_D is the Debye number. These width parameters are typically defined for a given order of free electron density, and the 10^{17} convention is subject to change depending on how the width parameters are determined or reported. Typically, the free electron interactions far outweigh ion interactions, and the ion term can be neglected:

$$\Delta\lambda_{\mathrm{S}} \approx 2a\frac{N_e}{10^{17}}. \tag{2.23}$$

It it important to note that the width parameters vary weakly with temperature, and special care should be taken in order to determine the appropriate width for the working temperature range and convention. Natural, pressure, and Stark broadening of a spectral line exhibit a Lorentz shape $L(\lambda;\gamma) = \frac{\gamma}{\pi(\lambda^2+\gamma^2)}$, where 2γ is the full-width at half-maximum (FWHM). Doppler broadening exhibits a Gaussian line shape $G(\lambda;\sigma) = \frac{\exp(-\lambda^2/2\sigma^2)}{\sigma\sqrt{2\pi}}$, where the FWHM is $2\sigma\sqrt{2\ln 2}$, and the Doppler-shifted line width $\Delta\lambda_{\mathrm{D}}$ is expressed as:

$$\Delta\lambda_{\mathrm{D}} = \lambda_0\sqrt{\frac{8k_BT\ln 2}{m_ec^2}}, \tag{2.24}$$

where λ_0 is the line center. Hence, the overall observed line shape is best described by a Voigt profile [51, 239] which is a convolution of the Lorentz and Gaussian line shapes $V(\lambda;\gamma,\sigma) = \int_{-\infty}^{\infty} G(\lambda';\sigma)\cdot V(\lambda-\lambda';\gamma)d\lambda'$ from broadening mechanisms including natural, Stark, Doppler, and also instrumental broadening. Instrumental broadening results from the resolution limit of a measurement system, for example the slit function of a spectrometer observing emission or line width of a tunable probe laser for absorption measurements (Gaussian). Careful deconvolution of experimentally-observed line shapes, therefore, allows for determination of free electron densities and temperatures in the plasma using emission and absorption spectroscopic methods.

In the later stages of LPP evolution, on the timescale of tens to hundreds of microseconds, given appropriate conditions and species, molecular recombination becomes more prominent, resulting in the appearance of molecular bands in the emission spectrum. Figure 2.3 shows the energy level diagram based on the anharmonic oscillator model for a diatomic molecule. Fine vibrational and rotational level splitting from molecular motion results in closely spaced energy levels. Electronic (de-)excitation transitions result in band features comprised of fine rovibrational lines. For more complex molecular species (*e.g.*, more than two atoms or comprised of heavier, higher-Z

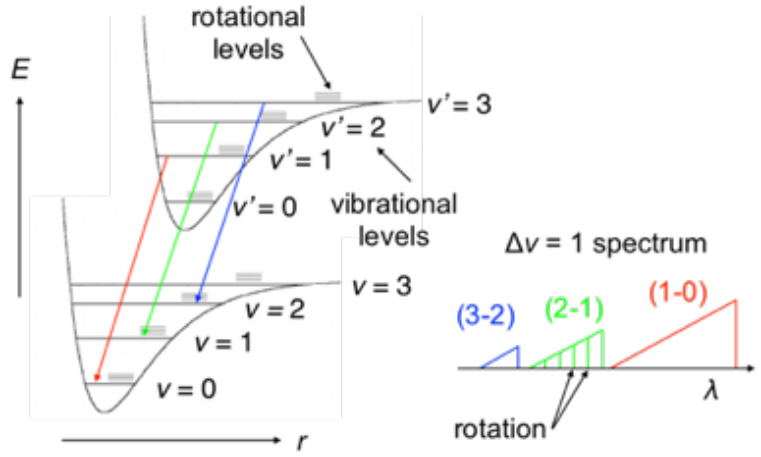

Figure 2.3: The anharmonic oscillator model for a diatomic molecule results in the given energy diagram with fine vibrational and rotational level splitting. Electronic (de-)excitation transitions result in the formation of band structures with identifiable signatures from closely-spaced rovibrational levels. v and v' represent specific vibrational levels, and the parenthetic notation defines the vibrational level transition.

constituents), these fine rovibrational transitions become increasingly difficult to resolve, and hence molecular emission is referred to as 'band-like' [111]. Section 2.2 introduces the significance of molecular emission features for discrimination of isotopes.

In addition to passive imaging or observing the emission from the LPP, active probing methods may be useful for determining plasma properties or observing associated phenomena such as shockwave evolution. LAS and LIF (for example, using tunable- or broad-spectrum laser sources) allows probing ground-state species or enhancing the emission of excited species, respectively. While the Einstein A_{ul} coefficient describes spontaneous emission, the B_{lu} coefficient describes the rate of absorption, and the B_{ul} coefficient describes stimulated emission. The principle of detailed balance defines the relationships between these coefficients [111]:

$$A_{ul} = \frac{8\pi h\nu_{ul}^3}{c^3} B_{ul}, \tag{2.25}$$

and

$$g_l B_{lu} = g_u B_{ul}. \tag{2.26}$$

where g represents the degeneracy of the corresponding state. Other probing techniques include those which can be used to measure changes of the refractive index from plasma phenomena. Two common techniques used for measurements of LPPs include interferometry and shadowgraphy. Interferometry is useful for directly probing small changes in the refractive index, while shadowgraphy is sensitive to the second-order spatial derivative of the index change, and is more useful for directly imaging phenomena with larger index changes such as shockwave expansion. Shadowgraphy, in particular, is used frequently throughout this dissertation. In Fig. 2.4, shadowgraphy is used to probe a slab with a perturbed index of length L. The index perturbation causes refraction of the incident probe rays separated by Δy at angles α and $\alpha + d\alpha$, respectively, over the distance to the detector screen L_{det} causing an offset Δy_{det}. The probe initially propagates along the z dimension, perpendicular to the slab and screen faces on the y dimension. The change in the observed intensity pattern $I_m - I_0$, where I_m is the measured intensity pattern, from the initial intensity pattern, I_0, is related to the change in separation of the incident rays and, consequently, the change in angle due to the refractive index perturbation in the slab:

$$\frac{I_m - I_0}{I_0} = \frac{\Delta y}{\Delta y_{\text{det}}} - 1 = -L_{\text{det}} \frac{d\alpha}{\Delta y_{\text{det}}} \approx -L_{\text{det}} \frac{d\alpha}{dy}, \tag{2.27}$$

where the change in angle can be related to the index change by Snell's law. Using the small-angle approximation yields:

$$\alpha = \frac{1}{n_0} \int_L \frac{dn}{dy} dz, \tag{2.28}$$

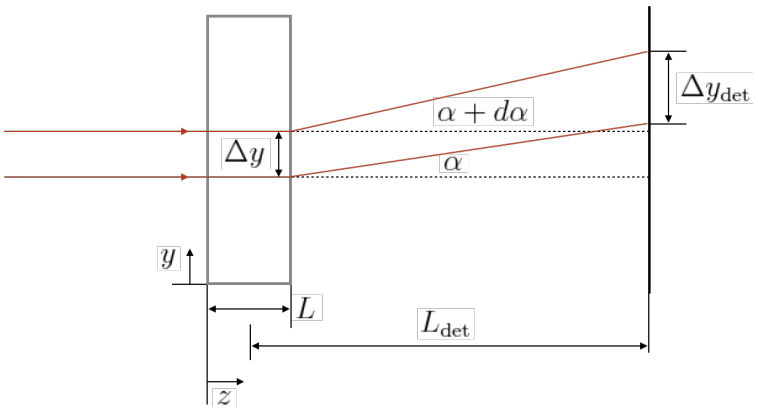

Figure 2.4: Shadowgraphy is used to probe a slab with a perturbed index of length L. The index perturbation causes refraction of the incident probe rays separated by Δy at angles α and $\alpha + d\alpha$, respectively, over the distance to the detector screen L_{det} causing an offset Δy_{det}. The probe initially propagates along the z dimension, perpendicular to the slab and screen faces on the y dimension.

where n represents the refractive index, and i denotes the initial condition. Equations (2.27) and (2.28) yield the observed change in the intensity pattern using the shadowgraphy technique, which is sensitive to the second-order derivative of the refractive index:

$$\frac{I_m - I_0}{I_0} = \frac{-L_{\text{det}}}{n_0} \int_L \frac{d^2 n}{dy^2} dz. \tag{2.29}$$

The refractive index change can be reconstructed numerically from Eq. (2.29) using methods like the finite difference technique [53].

2.1.4 Introduction to relevant analytical spectroscopic techniques

2.1.4.1 Basic experimental schemes for (LA-)OES, LAS, and LIF

The spectroscopic techniques featured in this dissertation can be categorized into emission and absorption. The emission-based analytical spectroscopy technique most frequently used in this dissertation is (LA-)OES (also referred to as LIBS or FIBS). Another technique, (LA-)LIF, relies on emission spectroscopy of resonantly-excited

transitions using a probe. An analytical absorption spectroscopy technique used in this dissertation is (LA-)LAS. The LA prefix denotes spectroscopy of LPPs, whereas these methods in practice may be useful for measurements with other analytes. For example, LIF following direct excitation of aqueous uranyl fluoride samples is advantageous for direct detection of the compound. Breakdown and the formation of an LPP typically involves dissociation of larger molecules to its atomic or ionic constituents, so complicated stoichiometric analysis may be required in order to infer the presence of a compound in the original sample.

Figure 2.5 illustrates the basic arrangement used for (a) LA-LAS and (b) LA-LAS, respectively. In both diagrams, a pulsed laser is used to initiate breakdown and the formation of a luminous plasma. LA-OES involves collection of the plasma emission, for example with a lens or equivalent optic (curved mirror, telescope). The emission is focused onto the slit of a Czerny-Turner spectrometer, within which a diffraction grating resolves the emission onto a detector screen. The design and considerations for a Czerny-Turner spectrometer as well as common detector types are discussed in detail in Sec. 2.1.4.2 and 2.1.4.3, respectively. An example emission spectrum showing spectral lines corresponding to ionic or atomic de-excitation transitions is shown in Fig. 2.5(a). Absorption spectroscopy instead observes the dips in the spectrum of a transmitted probe. Common examples of a probe include a tunable, narrowband laser or a broad-spectrum source as shown in the example in Fig. 2.5(b). Similarly, a Czerny-Turner spectrometer design may be used for absorption measurements with a broad-spectrum probe. LA-LIF involves observation of the enhanced emission from resonantly-excited transitions in the LPP. A more detailed review of LA-LIF may be found in [98]. Instrumental resolution is another major contributor to broadening of spectral lines. Several considerations for instrumental broadening in Czerny-Turner spectrometers are discussed in Sec. 2.1.4.2. In LAS measurements the absorption laser probe line width limits the resolution of the system.

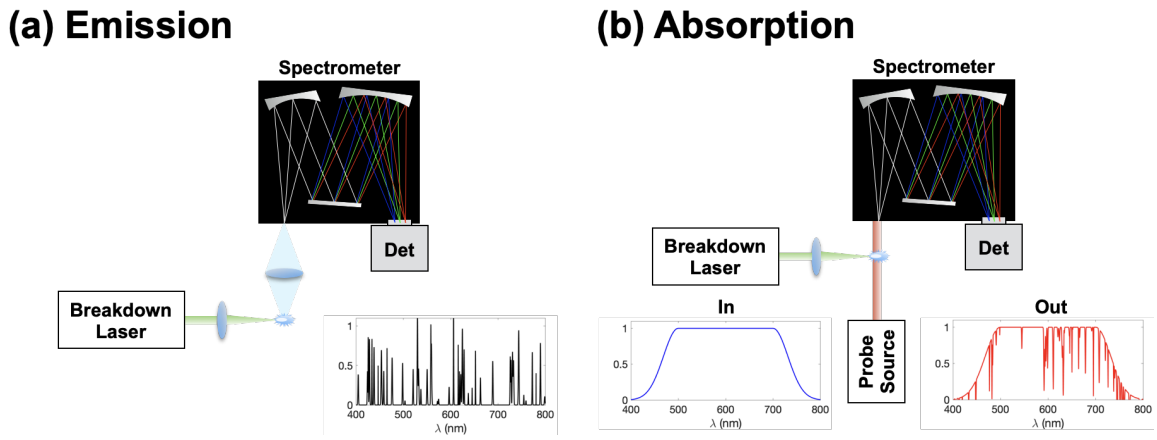

Figure 2.5: (a) Basic setup for emission spectroscopy of plasma from breakdown with a focused beam. Emission from the plasma is collected with a lens onto the slit of a Czerny-Turner spectrometer coupled to a detector (Det). An example emission spectrum is shown. (b) Basic setup for absorption spectroscopy using a broad-spectrum (In) probe source. The probe is transmitted through the plasma, and spectroscopy reveals dips in the initial spectrum from absorption transitions. An example transmitted absorption spectrum (Out) is shown.

In either LA-OES or LA-LAS, the observed spectral line or band intensities are related to the number densities of the species in the plasma. The number density may be determined from the emission using the Boltzmann distribution in Eq. (2.16) under the LTE or PLTE assumptions. Absorption signal, on the other hand, depends on the lower state population, and the observed transmission intensity is described by the Beer-Lambert law:

$$I = I_0 e^{-\sigma(\lambda) \int_L N_l(x) dx}, \tag{2.30}$$

where $\sigma(\lambda)$ is the wavelength-dependent absorption cross-section and $N_l(x)$ is the distribution of the lower state absorbing species integrated over the path length L. Consequently, both forms of spectroscopy may be useful for analytical purposes to derive the populations of various species in the LPP and infer concentrations or ratios in the original target.

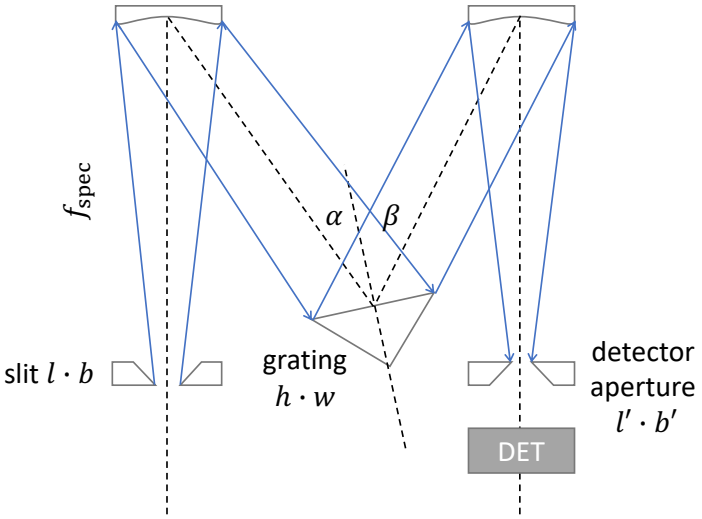

Figure 2.6: The input slit of height l and width b is imaged onto the exit (detector) slit of height l' and width b'. The f-number of the spectrometer f_{spec} is given by the ratio of the distance of the first concave mirror to the slit and the mirror size. The height and width of the diffraction grating are h and w, respectively. The incident and diffracted angles are α and β, respectively.

2.1.4.2 Czerny-Turner spectrometer design and considerations

The Czerny-Turner design is the most commonly used spectrometer type in this dissertation; a diagram showing the dimensions and relevant parameters is shown in Fig. 2.6. The input slit is imaged onto the exit slit (detector plane) using a pair of concave mirrors. The relationship between the incident angle α and the diffraction angle β is described by

$$nk\lambda = \sin\alpha + \sin\beta, \tag{2.31}$$

where n is the grating groove density; k is the diffraction order; and λ is the wavelength. The grating deviation angle is defined as $D_v = \alpha - \beta$. The resolving power R of the spectrometer is defined as the ability to distinguish separate, adjacent spectral lines by the Rayleigh criterion (maximum of one spectral line falls on the first

minimum of the other):

$$R = lnW = \frac{W}{\lambda}(\sin\alpha + \sin\beta). \tag{2.32}$$

The resolving power, consequently, depends on the active width and geometry of the grating as well as the wavelength. Additionally, the spectrometer bandpass (BP) affects both the instrumental resolution and geometric aberrations which may lead to losses in throughput:

$$\mathrm{BP} = \frac{\max(b, b')}{n f_{\mathrm{spec}} M}, \tag{2.33}$$

where f_{spec} is the f-number of the spectrometer defined by the ratio of the distance from the input slit to the first mirror (or mirror FL) and the mirror size; and M is the magnification of the imaging components in the spectrometer. From Eq. (2.33), the instrumental resolution is limited by the larger of the input or exit aperture, where the exit aperture may be defined by the size of the detector pixel. Important considerations for the efficiency of the spectrometer include the absolute throughput and signal-to-background degradation. Etendue (G) describes spreading losses to throughput and depends on the spectrometer bandpass:

$$G = \frac{lnk(hw)\mathrm{BP}}{f_{\mathrm{spec}}}. \tag{2.34}$$

Signal-to-background S/B degradation depends on both wavelength-dependent efficiency losses from the optical components and geometry:

$$S/B' = S/B\frac{\varepsilon(\lambda)}{C}\frac{T_g(\lambda)}{\cos\alpha}, \tag{2.35}$$

where $\varepsilon(\lambda)$ is the wavelength-dependent grating diffraction efficiency; C describes the overall quality of the optics (1 for a perfect system); and $T_g(\lambda)$ is the wavelength-dependent geometric transmission.

2.1.4.3 Common detector choices

The common types of detectors used in this dissertation rely on photoelectric conversion of optical signals and can be classified into three categories: single-pixel, pixel-array, and gated (or intensified) pixel-array detectors. Single-pixel detectors are coupled to the spectrometer in a monochromator arrangement, such that the detector observes a narrow range of wavelengths. Examples of single-pixel detectors used in this dissertation include photodiodes and photomultiplier tubes (PMT). Photodiodes are semiconductor devices operated in reverse-bias (photoconductive) mode and provide fast, time-sensitive response to incident optical signals. Silicon is a common semiconductor choice for observing optical transitions in the range of $\sim$200 nm and 1100 nm. PMTs similarly provide a time-sensitive response to incident optical signals. PMTs rely on photoelectric conversion followed by electron multiplication, which improves sensitivity to weaker signals. Time-sensitive measurements are especially useful for observing the transient phenomena and emission from LPPs.

Pixel-array detectors such as charge-coupled devices (CCD) and complementary metal-oxide-semiconductor (CMOS) devices can be used to observe a broad range of wavelengths when coupled to a Czerny-Turner spectrometer. A major drawback for such devices is the long shutter or exposure times relative to the timescales of LPP evolution. However, these devices can be connected to an image intensifier which consists of a photocathode, a micro-channel plate (MCP), and a phosphor screen. Photoelectrons generated by the photocathode are accelerated towards the MCP by an applied voltage, and the electrons are multiplied in the MCP. The electrons are accelerated towards the phosphor plate which converts them back to photons.

Finally, the photons are detected by the CCD or CMOS device. The applied bias which accelerates photoelectrons provides an electronic shutter enabling fast time-gating. The intensified CCD (ICCD) devices additionally provide better sensitivity than regular CCD or CMOS cameras alongside capability for fast time-gating; ICCD devices are frequently used in this dissertation for spectroscopy and imaging. Each photosensitive device has a wavelength-dependent response function. The quantum efficiency $\mathrm{QE}(\nu) = N_{\mathrm{pe}}/N_{\nu}$ describes the conversion ratio of incident photons N_{ν} to photoelectrons N_{pe}.

2.2 Spectroscopy of laser ablation plasmas containing uranium

This dissertation focuses on spectroscopy for direct measurements of uranium and its compounds in LPPs. Uranium is central to both civilian and military applications of nuclear technology and is found throughout the nuclear fuel cycle. Natural uranium is comprised of fissionable/fertile (99.28% U-238) and fissile (0.72% U-235) isotopes but may be enriched to varied isotope fractions for use in different types of nuclear reactors or in nuclear explosive devices. Two grades of enrichment pertinent to various applications of nuclear technology and the fuel cycle include low-enriched uranium (LEU) (3–20% U-235); and highly-enriched uranium (HEU) (>20% U-235) [24]. LEU is used as fuel in various types of nuclear reactors, while HEU is often referred to as weapons-grade if enriched beyond 90% in U-235 and is used in nuclear detonation devices [85]. Optical spectroscopy of uranium in LPPs can help identify uranium isotopes and classify enrichment grades for use in safeguards, security, and nonproliferation [202].

Another application of laser spectroscopy for measurements with uranium-containing LPPs is to better understand the processes that occur in nuclear explosions [86]. The

high temperatures and densities in the nuclear detonation plasma form a complex environment in which uranium, fission products, and structural materials may react with background species. For example, uranium readily reacts with oxygen in air to form oxides, contributing to the formation of debris which is relevant to post-detonation nuclear forensics [65]. The uranium-containing LPP can be used as a laboratory-scale surrogate for such detonations, simulating the conditions and components of the blast (*e.g.* shocks) which promote chemical reactions in plasma.

Both optical emission and absorption techniques following LA have been used for measurements of uranium-containing targets [12, 32, 39, 40, 58, 62, 98, 101, 105, 155, 164, 183–185, 202, 213, 214, 224, 230, 246, 248, 253]. LIBS is particularly attractive for its simple setup and straightforward implementation, as well as the capability to provide portable, rapid, *in-situ* measurements requiring minimal sample preparation, which bodes well for field applications. Moreover, OES can distinguish among various uranium species: atoms and ions [222], isotopes [224], and molecules [104, 155]. Absorption and LIF techniques have similarly been used for measurements of uranium-LPPs to probe or enhance emission from unexcited species, respectively [101, 164, 184, 230, 246]. These methods are typically considered more sensitive, or, in the case of LIF, improve the sensitivity of the emission-based technique [183], and can be used similarly to distinguish atoms, ions, isotopes, and molecules. Further, both emission and absorption spectroscopy methods can be used to evaluate the conditions in the uranium-LPP which mimic those found in nuclear detonations.

The primary challenge for both emission and absorption arises from the complexity of the uranium spectrum. The high-Z actinide alone yields a congested spectrum comprised of over 10^5 fine lines from electronic transitions of the atomic and single-ionized species [98]. An example emission spectrum in the visible region is shown in Fig. 2.7. The spectrum is recorded from a uranium-LPP formed in a low-

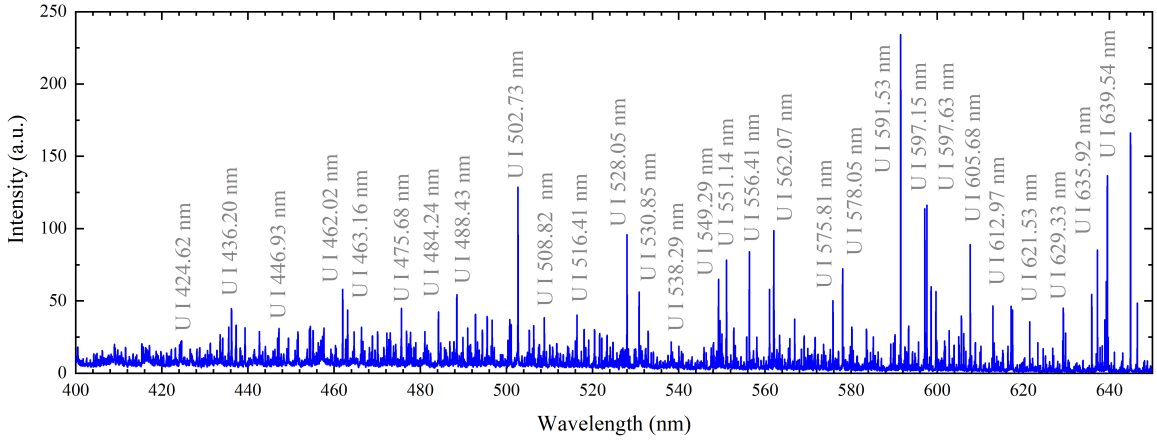

Figure 2.7: The example visible emission spectrum is recorded from a U-LPP formed in a low-pressure (10 mTorr) background of nitrogen gas to inhibit chemical reactions in the plasma. A 10-ns, 50-mJ, Nd:YAG (1064 nm) laser pulse was used to ablate a depleted U metal target. The spectrum was recorded using an ICCD coupled to a 0.5-m Czerny-Turner spectrometer with 2400 l/mm groove density with a gate delay (after the ablation laser pulse) and width of 1 µs and 2 µs, respectively. Prominent atomic U (U I) emission lines are labeled [24].

pressure (10 mTorr) background of pure nitrogen gas to inhibit reactions and emission from molecular species. A 10-ns, 50-mJ, Nd:YAG (1064 nm) laser pulse was used to ablate a depleted uranium metal target. The collection apparatus consisted of an ICCD coupled to a 0.5-m Czerny-Turner spectrometer with 2400 l/mm groove density, and the recording parameters include a gate delay (after the ablation laser pulse) and width of 1 µs and 2 µs, respectively. The uranium spectrum may be further congested as a result of matrix effects as well as by complex uranium molecular band features comprised of fine and hyperfine ro-vibrational lines. The complexity and density of the uranium spectrum necessitates the use of high-resolution spectroscopic instruments, especially for measurements of uranium-isotope line shifts.

Distinguishing uranium-isotopes is vital for applications in the nuclear fuel cycle, safeguards, and security. For example, classification of various uranium material grades is required for assessing the nuclear proliferation threats. Atomic (or ionic) line shifts observed via emission or absorption methods can be used to distinguish among isotopes. Mass (denoted by the subscript M) and field (subscript F) differences

contribute to the shift in frequency of an electronic transition i between two isotopes of mass A and A':

$$\Delta\nu_i^{AA'} = \Delta\nu_{i,\mathrm{M}}^{AA'} + \Delta\nu_{i,\mathrm{F}}^{AA'}. \tag{2.36}$$

The mass contribution is further separated into a normal mass shift from the introduction of the reduced mass $\mu = \frac{mm'}{m+m'}$ in the kinetic energy and a specific mass shift from the influence of electron motion correlations on the nuclear recoil energy. For the U-238 and U-235 isotope pair, the normal mass shift is typically eight orders of magnitude smaller than the frequency of the transition, corresponding to a 0.018-pm shift for a transition at 600 nm. The specific mass shift is typically even smaller. Field shifts, on the other hand, span a larger range caused by the variations in electron configurations. The total isotopic shifts between U-238 and U-235 for the 549 uranium atomic (U I) transitions in the visible wavelengths between 285 and 882 nm span -27 to 49 pm with an average shift of 7.5 pm. The shifts for the 823 single-ionized (U II) transitions span -74 to 84 pm with an average shift of 7.0 pm [98]. Further differences in hyperfine structure of uranium-isotopes may contribute to observed differences in the emission and absorption transitions between U-238 and U-235. Hyperfine splitting of atomic levels is caused by the interactions of electric field near the nucleus with nuclear dipole moments. Further details about hyperfine splitting in uranium can be found elsewhere [183]; however, the most pronounced effect from hyperfine splitting between U-238 and U-235 is that U-235 generally exhibits broadened features with lower amplitudes in comparison to those of U-238 [98].

Earlier works in which various emission [222] and absorption [222, 230] methods were used to study uranium-LPPs revealed significant quenching of uranium atomic signals in oxygen-containing backgrounds, such as air, in contrast to chemically inert fill-gases, such as nitrogen or argon. Rapidly diminishing atomic signals in the

presence of oxygen posed another challenge using LIBS among other techniques for in-field, *in-situ* discrimination of uranium isotopes, adding to challenges which necessitate high-resolution instrumentation [133]. However, the observation of the U monoxide emission band at 593.55 nm provided a solution to distinguishing uranium-isotopes from uranium-LPPs formed in oxygen-containing environments using laser ablation molecular isotopic spectrometry (LAMIS) [105, 155] with a reduced instrumental resolution requirement. For a diatomic molecule, isotope splitting is dominated by the effects of the reduced mass μ on the spacing between rovibrational levels and can be orders of magnitude greater than splitting for atomic or ionic transitions. For example, within the anharmonic oscillator framework, the ratio of reduced masses $\rho = \sqrt{\frac{\mu}{\mu*}}$ between the isotopologues, μ and $\mu*$, dictates the difference in rovibronic energies ε and $\varepsilon*$, respectively [98]:

$$\begin{aligned}\varepsilon - \varepsilon* = (1-\rho)&\left[\omega'_e\left(v'+\frac{1}{2}\right) - \omega''_e\left(v''+\frac{1}{2}\right)\right] \\ &- (1-\rho^2)\left[\omega'_e\chi'_e\left(v'+\frac{1}{2}\right)^2 - \omega''_e\chi''_e\left(v''+\frac{1}{2}\right)^2\right] \\ &+ (1-\rho^2)\left[B'_eJ'\left(J'+1\right) - B''_eJ''\left(J''+1\right)\right] \\ &- (1-\rho^3)\left[\alpha'_e\left(v'+\frac{1}{2}\right)J'(J'+1) + \alpha''_e\left(v''+\frac{1}{2}\right)J''(J''+1)\right] \\ &- (1-\rho^4)\left[D'J'^2\left(J'+1\right)^2 - D''J''^2\left(J''+1\right)^2\right], \quad (2.37)\end{aligned}$$

where v and J represent the vibrational and rotational quantum numbers, respectively. The first two terms in Eq. (2.37) describe shifts in the vibrational band head, and the last three terms describe shifts in rotational levels. The differences in isotope splitting between atomic and molecular transitions become less significant for heavier species; however, the isotope shift between ^{238}UO and ^{235}UO of $\sim$40 pm is still notably larger than the average atomic shift of 7.5 pm [98]. Consequently, the molecular signatures from uranium oxides are promising for applications which require

uranium-isotope discrimination. Also, it may actually be advantageous to perform uranium-LA experiments in air where uranium species from the target are likely to react with oxygen from the environment.

LA of uranium in oxygen-containing environments, such as air, yields other uranium oxide bands in the visible region of the spectrum which, until recently, were largely unidentified in the literature but may be useful for uranium-isotope discrimination. In recent years, the UO 593.55 nm band has been studied more extensively in the literature [105, 248], and several additional monoxide features have been identified [98]. However, current literature lacks sufficient information about the visible features from heavier, polyatomic uranium oxide species. The lack of mature understanding regarding the formation and evolution of uranium oxides in LPPs and the potential to use the uranium oxide bands for isotope discrimination motivates the experimental investigation presented in the Chapter 3.

CHAPTER 3

Experimental Investigation of Uranium Oxide Formation and Evolution in Nanosecond-Laser-Produced Plasmas

Uranium is a cornerstone element for both civilian and military applications of nuclear technology, as discussed in Sec. 2.2. Laser-based spectroscopy, for example LIBS and LA-LAS, has several desirable characteristics for measurements of uranium-containing compounds. Briefly, those methods are speed, *in situ* operation, ability to distinguish uranium from other elements, ability to detect uranium compounds and its isotopes, applicability to various forms of the target (solid, liquid, gas), and ability to complement the established detection and measurement methods which observe the emission of radioactive decay products. In this chapter, a comprehensive experimental investigation of uranium-containing LPPs formed from short-pulsed LA is presented. In a broader context, further research is necessary to foster the capabilities of optical spectroscopy techniques towards mature and reliable nuclear material sensing.

In Sec. 3.2, the validity of equilibrium assumptions in the uranium-LPP is assessed in order to ascertain thermodynamic properties, which benefits improved understanding of the physical processes such as chemical reactions in uranium-LPPs. One challenge is the complexity of the uranium spectrum, which makes the choice of

emission lines for quantitative analysis difficult. Further, the limited information in existing literature pertaining to the spectroscopic coefficients of uranium transitions, such as the ones for Stark widths and shifts, is addressed. This section includes edited portions of Ref. [28].

In following sections, OES and derivative techniques like optical time-of-flight spectroscopy (OTOFS) are used to track the evolution of uranium and its oxides in the ns-LPP. Mature understanding of the uranium-oxygen chemistry in LPPs, which is relevant for analytical spectroscopy applications as well as simulating the physics which occur in nuclear detonations on a laboratory scale, is still lacking. Here, novel results which offer direct insight into the molecular dynamics in uranium plasmas are presented; and the observation of emission features attributed to heavier gas-phase uranium oxides, previously not seen in such LPPs, is reported. This chapter includes edited portions from Refs. [99, 125, 219, 220].

3.1 Experiment

The experimental setup utilized in the experiments presented in this chapter is depicted in Fig. 3.1. A Nd:YAG (1064 nm, 6 ns, 75 mJ) laser focused to a spot diameter ($1/e^2$) of $\sim$1 mm using a lens with 15-cm FL is used to ablate a uranium metal target (natural isotopic concentration, 1.0×1.0×0.1 cm^3). The laser fluence is estimated to be approximately 10 J cm^{-2} on the target surface. The target was housed in a containment vessel with quartz windows, which was evacuated to a pressure of 5 mTorr and purged with pure nitrogen (99.999%) gas between successive experiments. The target was translated periodically to prevent target drilling; approximately 20 laser cleaning shots were applied at each new target position in order to remove the oxidation layer present on the sample surface for each new sample position.

For direct imaging of the morphology of the plasma and its constituents us-

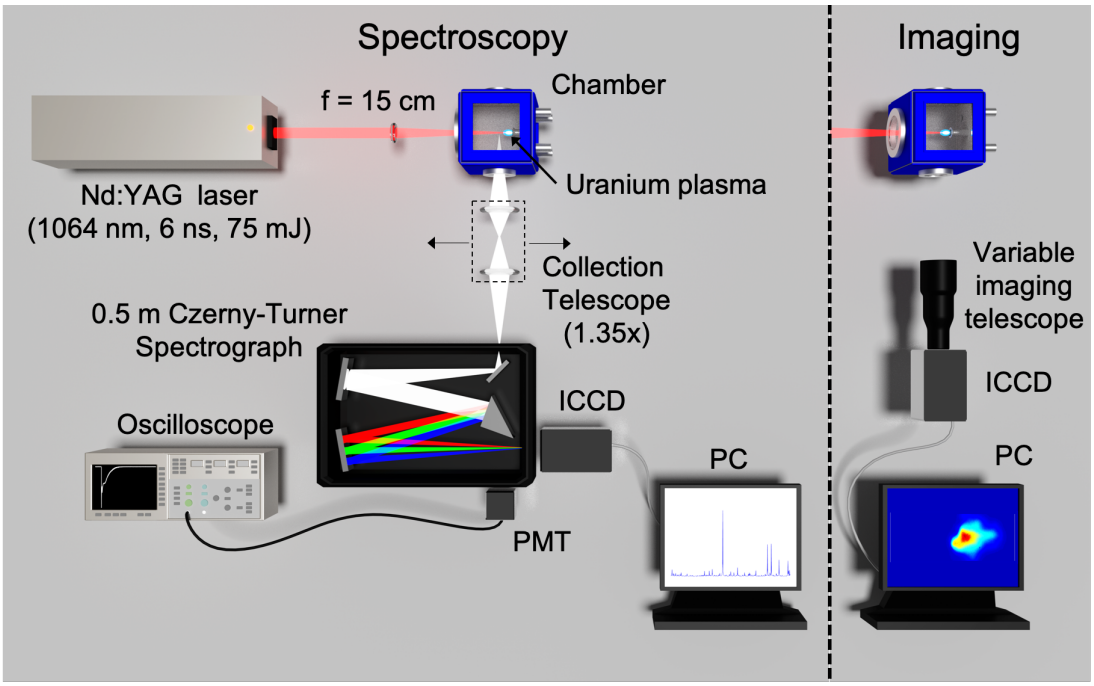

Figure 3.1: A natural isotopic concentration U target is ablated in various inert and reactive environments using a Nd:YAG laser (1064 nm, 6 ns, 75 mJ) focused using a 15-cm FL lens to a spot diameter ($1/e^2$) of approximately 1 mm. Non-invasive methods which track emission are used to study the plasma. Imaging with a variable magnification telescope and ICCD (min. gate width 3 ns), with or without narrow-line filters to isolate specific species, provides information about the macroscopic evolution of the plasma and its constituents. The plasma is imaged using a fixed 1.35×-magnification telescope onto the slit of a variable grating 0.5-m Czerny-Turner spectrograph coupled to both an ICCD and PMT (rise time 2 ns) for OES and OTOFS, respectively. The PMT is coupled to a fast oscilloscope (1 GHz, 50 Ω termination) [220].

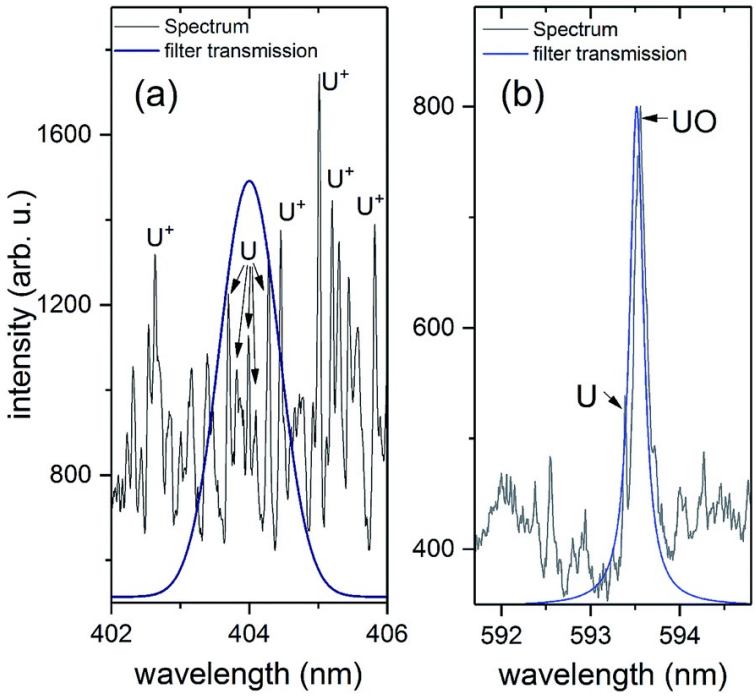

Figure 3.2: Transmission spectra for (a) atomic U filter at 404 nm with 1-nm bandwidth (FWHM) and (b) UO filter at 593.55 nm with 180-pm bandwidth (FWHM). The U emission spectra were recorded in a 5% oxygen concentration in a background of pure argon, with (a) 1 µs ICCD gate delay and 1 µs gate delay for the 404-nm window and (b) 20 µs gate delay and 20 µs gate delay for the 593-nm window, respectively. The transmission window shape was adjusted arbitrarily to match the intensity of the spectrum, and is not representative of the actual transmissivity of the filter [125].

ing narrow-line filters, a variable-magnification telescope was coupled directly to an ICCD (Princeton Instruments, PiMAX, min. gate width 3 ns, square pixel size 13 µm). Measurements were synchronized to the laser pulse using the digital delay generator integrated within the ICCD. Figure 3.2 shows the transmission bands of the narrow-line filters used to isolate the emission from (predominantly) UI and UO species. Evidently, there is some overlap of UII lines with the targeted UI lines in the 404-nm filter; however, the emission from ionic species is limited to the earliest times in the plasma evolution and is not expected to contribute significantly at later times $\gtrsim$1 µs.

For spectroscopy, the plasma emission was imaged using a fixed 1.35×-magnification telescope onto the slit of a 0.5-m Czerny-Turner spectrograph (Acton, Spectrapro 2500i) coupled to the ICCD used for imaging as well as a PMT (Hamamatsu, R929, 2-ns rise time) for OTOFS. A slit width of 30 µm was used for spectroscopy measurements. A Voigt profile was found to be well suited for modeling the instrumental profile, and also corresponds to the late time emission spectral profiles of both uranium and oxygen lines. Three interchangeable gratings were used in various experiments: (1) high-resolution, 2400 l/mm, 40-pm linewidth resolution at 404.6 nm (calibrated using an Hg I transition from an Hg-Ar lamp); (2) intermediate resolution, blazed for longer wavelengths, 1200 l/mm, 70-pm linewidth resolution at 632.8 nm (calibrated using He-Ne laser line); and (3) low-resolution, used for viewing broad spectral windows, 300 l/mm, 300-pm linewidth resolution at 404.6 nm. Since the emission is averaged along the line of sight, the quantitative results presented in Sec. 3.2 should be interpreted with caution. For OES measurements, results from 10 ablation laser shots were averaged unless otherwise noted. OTOFS involves using the spectrograph in a monochromator configuration, in which the exit aperture coupled to the single-pixel PMT detector is used to select a narrow range of wavelengths corresponding to the transition(s) from an individual species in the plasma. The entrance slit width

used for OTOFS was 50 µm, and the exit aperture width was 100 µm. The PMT is coupled to a fast oscilloscope (1 GHz, 50-Ω DC termination) to record the temporal evolution of the selected range of wavelengths. The plasma image is translated horizontally along the entrance slit, so that the spatial variation along the laser axis in the emission could also be tracked. The spatial resolution for PMT measurements is estimated to be $\frac{50\ \mu\text{m}}{1.35} = 37$ µm limited by the entrance slit of the spectrometer. For OTOFS measurements, results from 16 ablation laser shots were averaged unless otherwise noted. The vertical entrance slit size was ∼2 mm, and the slit was centered at the laser axis for both OES and OTOFS.

Experiments were conducted at a pressure of 100 Torr with different fill gases (air, nitrogen, argon) as well as air at low pressure (∼5 mTorr). The 100-Torr pressure was experimentally determined to simultaneously yield the emission features of uranium and its oxides in the presence of oxygen. Further studies, presented in Sec. 3.4 and 3.5, investigate the effects of oxygen on uranium and uranium oxide signatures by varying the partial pressure of oxygen (99.99% pure) in a background of argon (99.99% pure). Oxygen concentrations were varied from $\sim 3.2\times10^{13}$ (5 mTorr) to 7.2×10^{17} cm^{-3}. It must be noted that, because the fill gas was not continuously cycled through the experimental chamber, the oxygen concentration in "pure" gas or low pressure conditions cannot be predicted with certainty. The ambient oxygen concentration is expected to increase slowly from both target ablation as well as leaks in the chamber. However, using a stationary fill gas and periodic sample translation to prevent excessive drilling ensures minimal shot-to-shot fluctuations in the plume morphology. The maximum variation which was observed in the plume length along the laser axis (from imaging experiments) was ∼6% between five laser shots. The fluctuation of the maximum intensity in the image was observed to be the greatest ∼8% at the earliest times ($\lesssim$1 µs), similarly for five laser shots. At late times ($\gtrsim$10 µs), the fluctuation was observed to be ∼5%.

3.2 Characterization of uranium plasma properties using optical emission spectroscopy

Non-invasive means to determine the thermodynamic properties of uranium-containing LPPs are important for applications such as analytical spectroscopy and when using the LPP as a laboratory-scale surrogate for nuclear detonations. Only one previous work employs uranium emission lines (in the 385.8–391.9 nm spectral window) for experimental determination of thermodynamic properties of such plasmas [213]. Previously, we used other impurity lines for determination of uranium-containing plasma properties [215, 222]. The lack of available literature which performs such quantitative analyses with uranium lines epitomizes the difficulties in working with the complex uranium spectrum. Further, spectral line information for uranium transitions is limited, and knowledge of the Stark coefficients, which are used to estimate electron density and ionization degree, among other parameters, can benefit development of modeling, diagnostic, and analytical techniques to further understand the physical processes within the plasma. In this section, a meticulous analysis of the uranium emission spectra following ns-LA of uranium metal in low-pressure (5 mTorr) conditions is conducted to determine spatiotemporal thermodynamic properties of the plasma, and the Stark broadening parameters of U I 499.01 nm and U II 500.82 nm transitions are reported. Methods for determining the spatiotemporally varying plasma temperatures of the plasma include using Boltzmann plots [Eq. (2.17)] and the Saha-Eggert equation [Eq. (2.18)]. Electron density distributions were determined via analysis of Stark broadening [Eq. (2.23)] of the O I 777.19 nm line. The validity of the LTE assumption is assessed by comparing the temperatures of successive ionization states and the McWhirter criterion [Eq. (2.19)]. The Stark widths of selected U transitions were measured by comparing their linewidths with the broadening of O I 777.19 nm line. The temperatures were determined to be in

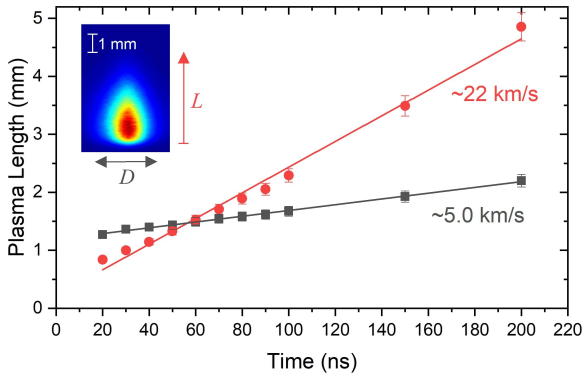

Figure 3.3: Estimated expansion velocities of the plasma under low-pressure conditions in axial (L, along laser axis) and radial (D, perpendicular to laser axis) direction. Distances were determined in the axial (red) direction from the target surface to 5% of the maximum emission observed in each image. Diameters (black) were determined similarly, using 5% of the maximum emission in each image as the measurement threshold [28].

the range of 3000–9000 K, and electron densities were determined to be on the order of 10^{16} cm^{-3}.

3.2.1 Spatiotemporal evolution, thermodynamic properties, and equilibrium in the uranium plasma formed in a low-pressure environment

Knowledge of the morphology of the LPP is vital in conjunction with other diagnostics to determine the plasma's thermodynamic properties. Figure 3.3 shows the expansion of the uranium-LPP in a low-pressure environment fit with a free (linear) expansion model. The axial (along the laser axis) expansion rate is determined to be ∼22 km/s, while the radial (perpendicular to laser axis) expansion rate is slower, at ∼5.0 km/s. The spatiotemporal emission contours presented in Fig. 3.4(a–c) provide the particle distributions that can be linked to electron density and excitation temperature. Figure 3.4(a–c) shows the emission contours for neutral atomic and ionic uranium species as well as an oxygen impurity, whose origin is dominantly attributed to the target surface, evidenced by its expansion behavior (away from the target surface alongside uranium species) shown in Fig. 3.4(c). From the emission contours,

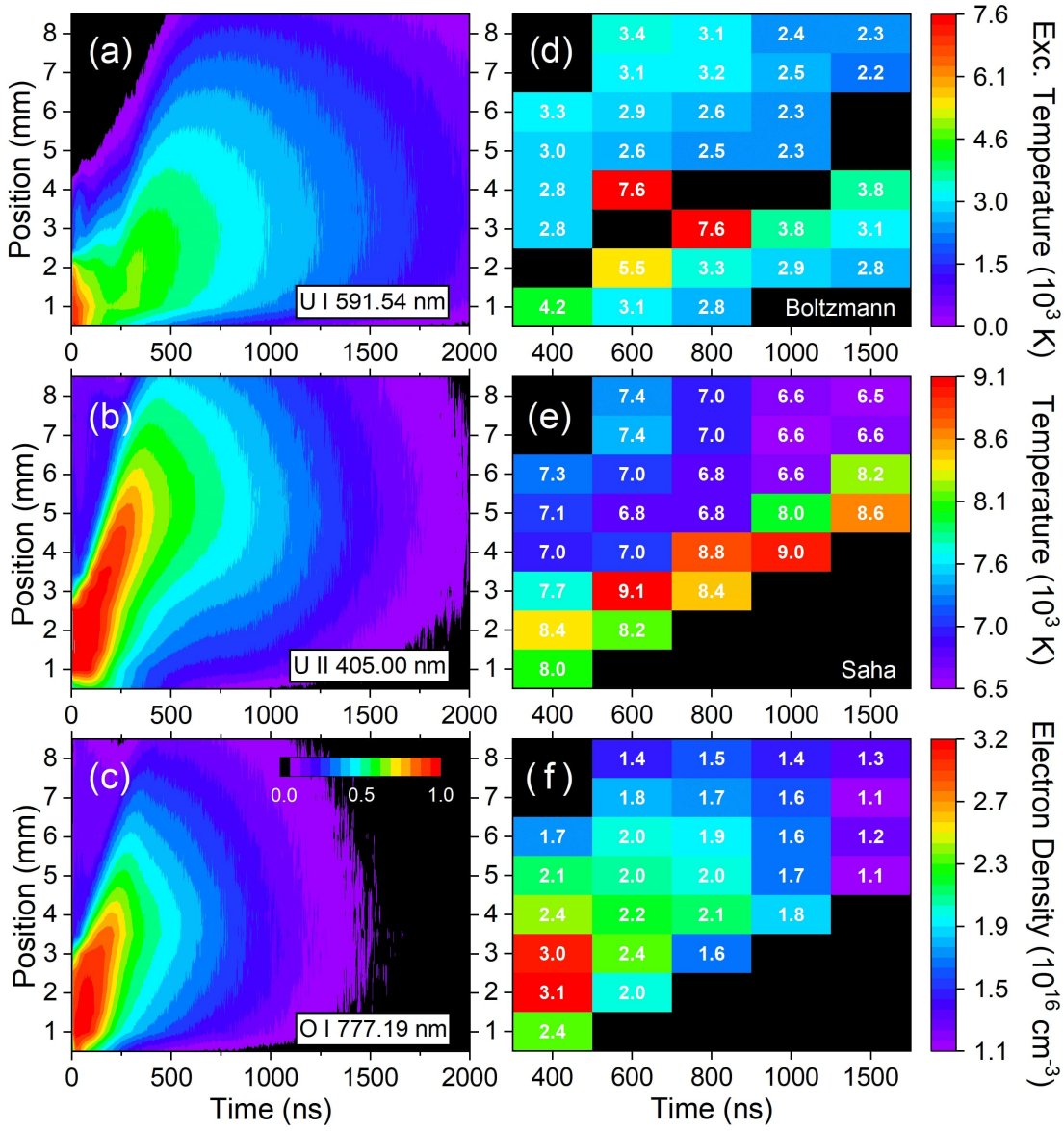

Figure 3.4: (a) U I 591.54 nm, (b) U II 405.00 nm and (c) O I 777.19 nm spatiotemporally resolved emission contours using OTOFS. Temperature distribution obtained via (d) Boltzmann plot method and (e) Saha-Eggert equation and (f) electron density at various time delays and axial positions with respect to the target surface (along the laser axis). The absence of values along the diagonal in (d) is due to inability to clearly observe majority of spectral lines at corresponding positions and time delays, indicating a possible departure from equilibrium [28].

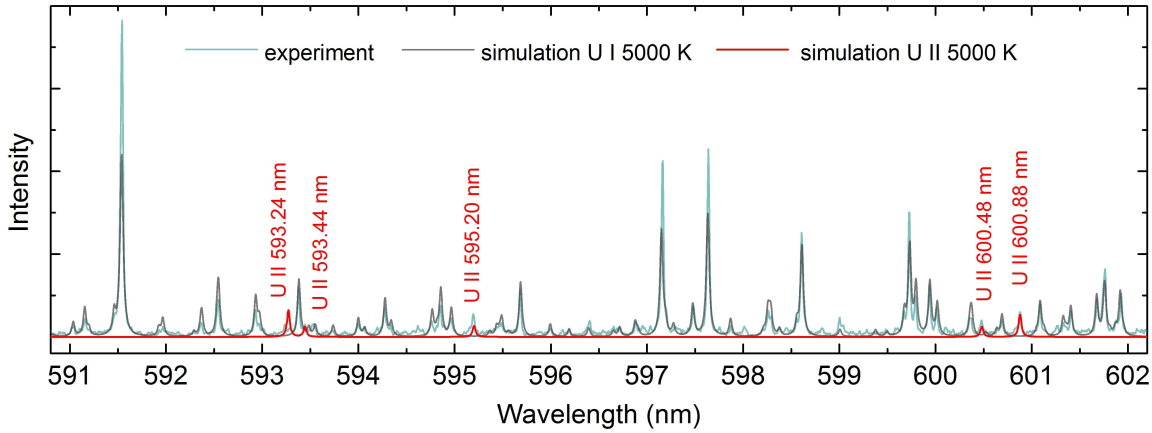

Figure 3.5: The experimental spectrum is recorded at a delay of 1 µs and gate width of 0.2 µs at a distance of 2 mm from the target. The simulated spectrum incorporates the majority of transitions used in the Boltzmann plot and Saha-Eggert equation analyses and is simulated for an excitation temperature of 5000 K [28].

the particle velocities are determined by tracking the time at which the emission profile peaks at each spatial position. U I species exhibits the slowest axial expansion rate of ∼4.0 km/s, corresponding to a kinetic energy (KE) of ∼20 eV. U II species has a greater velocity of ∼16 km/s (KE ∼320 eV) and appears to dissipate more quickly via recombination. The O I species exhibits a velocity of ∼13 km/s and a similar kinetic energy to atomic U of ∼15 eV. The similar kinetic energies of U I and O I species from the target help justify the use of the O I line for comparison with uranium-line broadening in the latter determination of Stark broadening parameters.

OES is used to determine the thermodynamic plasma properties; an example spectrum from this series of experiments is shown in Fig. 3.5 alongside a simulated spectrum for an excitation temperature of 5000 K. The simulated spectrum features the majority of transitions used in the Boltzmann plot and Saha-Eggert equation analyses. The Boltzmann plot analysis assumes PLTE is satisfied, and the intensity of a spectral line can be determined by Eq. (2.16) which assumes a Boltzmann energy distribution characterized by a single excitation temperature value. Only U I lines are considered. Lines are chosen to avoid those which are prone to self-absorption, like those featuring ground-state transitions. The lines used for the Boltzmann plots

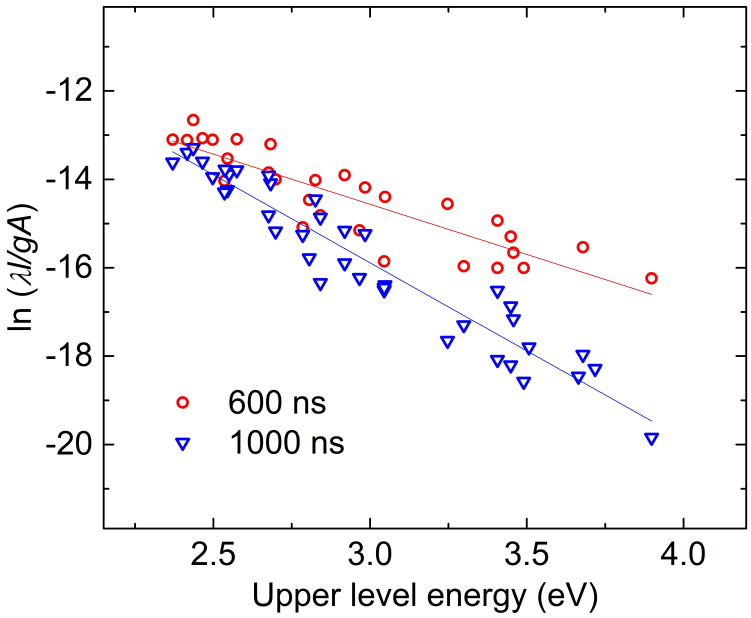

Figure 3.6: The Boltzmann plots are generated from spectra recorded at 2-mm distance from the target for two different gate delays. The U I transition information was retrieved from the Palmer Spectral Atlas [179] and is listed in Table A.1 in Appendix A [28].

are listed in Table A.1 in Appendix A, with the atomic parameters obtained from the Palmer Spectral Atlas [179]. Figure 3.6 shows examples of Boltzmann plots generated for spectra recorded at a distance of 2 mm from the target at different gate delays. Secondly, the Saha-Eggert equation [Eq. (2.18)] is used to determine the electronic temperatures by comparing the intensities of successive ionization states (U I and U II). Lines were similarly chosen to avoid overlap with adjacent features as well as self-absorption. The Saha-Eggert equation was solved iteratively using the electron densities determined via analysis of Stark broadening of the oxygen 777.19 nm line discussed later. The first standard deviation of the twelve line pair combinations ranged from 10% to 15% at different spatiotemporal positions. Figure 3.4(d) and (e) show the excitation temperature distribution from the Boltzmann plots and the electronic temperature distribution from averaging the twelve U I-U II line pair combinations using the Saha-Eggert equation, respectively. Comparing the excitation and electron temperatures can be done to ascertain the validity of LTE conditions.

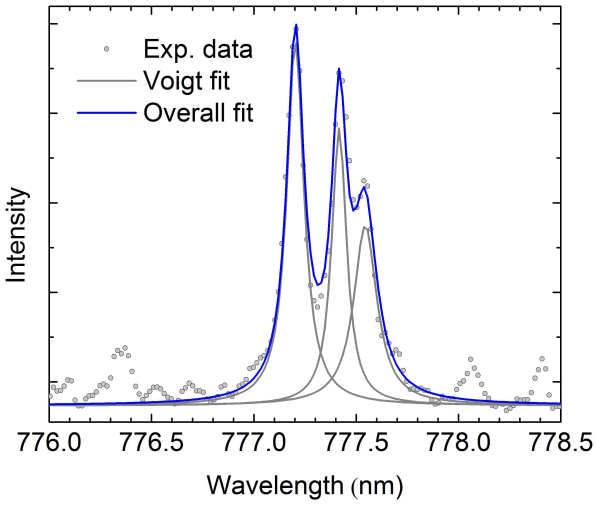

Figure 3.7: Typical profiles of oxygen lines at 777.19, 777.42, and 777.54 nm fit with a cumulative Voigt profile. Stark-broadened widths are determined by deconvolution of other mechanisms including instrumental and Doppler broadening [28].

The electron temperatures obtained with this method are notably greater than those obtained by the Boltzmann plot method, indicating a departure from absolute equilibrium. This difference is even more pronounced at the plasma periphery. However, partial equilibrium for individual species may still exist.

The electron density distribution shown in Fig. 3.4(e) is determined via analysis of the spectral line broadening of the O I 777.19 nm line, which is sufficiently resolvable from its neighboring lines in the triplet, O I 777.42 nm and O I 7777.54 nm. An example cumulative Voigt fit of the triplet is shown in Fig. 3.7. Stark broadened line widths are determined by deconvolution of the Voigt profile to consider the instrumental and Doppler contributions to broadening. Typical Doppler widths [Eq. (2.24)] for the O I 777.19 nm line ranged between 10 pm and 14 pm for plasma temperatures of 5000 K and 10000 K, respectively. The Stark broadening parameter is 16.6 pm for the temperature of $\sim$0.5 eV [18].

We evaluate the McWhirter criterion [Eq. (2.19)] for the largest energy gap of $\Delta E \approx 2$ eV and peak plume temperature of 8400 K for a lower limit of the electron

density of 1×10^{15} cm^3. The observed densities are always greater than this lower bound. Although the criterion is satisfied, it is not sufficient to verify absolute LTE, because of the plasma inhomogeneity as indicated by the discrepant excitation and electronic temperatures. The discrepant temperatures may occur because the ionic species travel much faster than the neutral species as shown in Fig. 3.4(a–c), and the efficiency of three-body recombination is reduced in the plasma periphery. Consequently, equilibration between excited electronic levels and the ground state is slower than the equilibration between translational energies of the free electrons and heavy particles. This leads to pronounced species segregation in the periphery, reducing the collision frequency. Previous work warns about discrepant thermodynamic properties when comparing line-of-sight averaged spectral data with Abel-inverted data which accounts for radial symmetry in the plume [7]. Therefore, the temperatures reported here should be considered with caution. Ultimately, these measurements present a step towards higher-fidelity determination of thermodynamic properties of uranium plasmas.

3.2.2 Determination of Stark widths for selected U I and U II transitions

Prior to this work, it appears that no Stark broadening parameters have been reported in available literature for uranium species. This section presents the first experimentally determined U I and U II parameters which may be used in certain situations to estimate free electron density and the degree of ionization in uranium-containing plasmas. The main difficulties in asserting the conditions for deduction of the Stark parameters arise from the congestion of the uranium spectrum. The criteria for a candidate spectral line include that the line should be: (i) isolated, (ii) sufficiently broadened, (iii) intense, and (iv) optically thin. The latter two are opposing requirements, which *a priori* preclude the use of lines associated with a ground-state transition. The most intense spectral lines in the uranium spectrum include a ground-

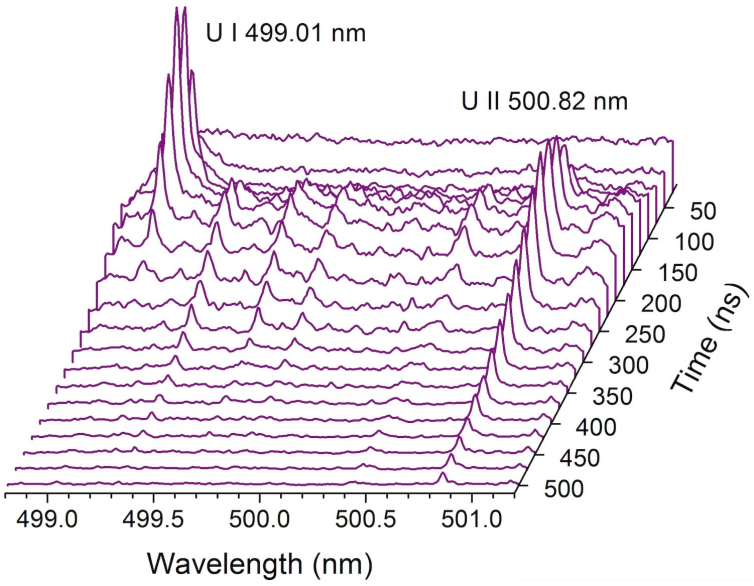

Figure 3.8: The temporal evolution for the spectral window featuring both U I 499.01-nm and U II 500.82-nm is shown for a distance of 1.5 mm from the target. A gate width of 50 ns was used for each delay [28].

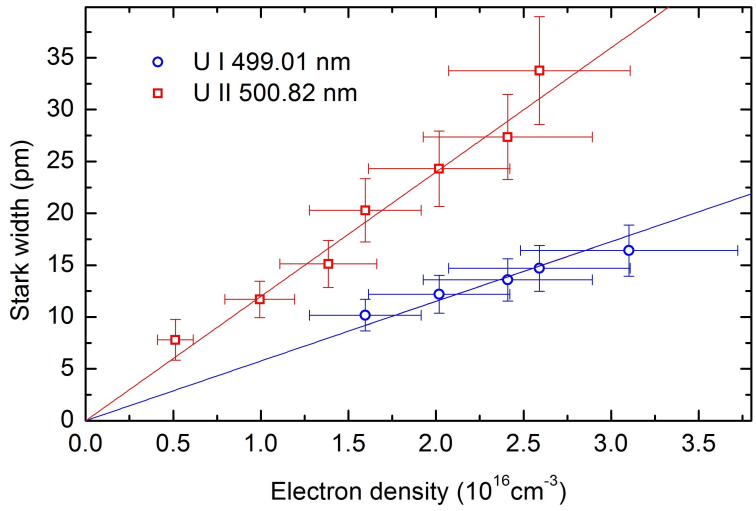

Figure 3.9: The linearity of the experimentally determined Stark widths as a function of electron density is assessed according to Eq. (2.23) to validate the determination of the Stark broadening parameters given in Table 3.1 [28].

state transition, and many other sufficiently intense lines are overlapped with weaker features, even in the low-pressure environment with reduced continuum radiation from sources such as uranium oxides. Nevertheless, two lines were selected satisfying the aforementioned criteria: U I 499.01-nm and U II 500.82-nm. The same Voigt fitting procedure was employed for these uranium lines as the O I lines in the previous section. The Gaussian width (influenced by instrumental and Doppler broadening) was deconvolved from the Voigt profile, leaving the Lorentz width. The Doppler width [Eq. (2.24)] for the nearby transitions was calculated to be 2.3 pm for a temperature of 10000 K. Subsequently, the instrumental Lorentz width was subtracted, leaving the Stark contribution to broadening. The validity of the determination of Stark widths was asserted by confirming the linear behavior comparing measured Stark widths with the electron densities from O I profiles. That is to say, the deconvolved widths should exhibit a linear dependence with the free electron density according to Eq. (2.23) if indeed other contributions to broadening are appropriately subtracted. Different gate delays, shown in Fig. 3.8, supplied the varying electron densities in order to assert the linear dependence of the deconvolved widths, presented in Fig. 3.9. Indeed, the Stark widths demonstrate a linear dependence with electron density, in accordance with Eq. (2.23), and the Stark parameters were consequently determined from the slope of the linear fits shown in Fig. 3.9. The measured Stark broadening parameters normalized to $1\times10^{16}\text{cm}^{-3}$ are presented in Table 3.1. A direct comparison of the measured parameters is impossible because of the lack of data in the literature; however, the order of magnitude of values reported here is consistent with typical values for other elements in the literature spanning from several tens to several hundreds of pm for densities on order of 10^{17} cm^{-3}. These measurements provide the first reference for further investigations of uranium Stark coefficients and enable the capability to estimate electron densities in uranium-containing plasmas using uranium lines under certain conditions.

Table 3.1: Atomic parameters [179] of U I 499.01 nm and U II 500.82 nm spectral lines together with experimentally determined Stark widths normalized to 10^{16}cm^{-3} [28].

Species	λ (nm)	E_u (eV)	J_u	E_l (eV)	J_l	λ_S (pm)
U I	499.01	3.49	7	1.01	7	6
U II	500.82	2.69	6.5	0.22	6.5	12

3.3 Uranium laser-produced plasma emission and morphology in inert and reactive environments

The dynamics of expansion, thermodynamics, and chemical reactions in LPPs are of broader interest for various laser ablation applications. For example, reactive processes [208] which may occur in LPPs are of general interest for understanding combustion physics [3, 258] and general LA physics, particularly that related to nanoparticle formation and kinetics [141], pulsed laser deposition [177], and analytical techniques. The morphology and reactive processes occurring in uranium-containing LPPs are of further interest for analytical techniques, especially considering the prospects for using uranium oxide bands for isotopic identification. In this section, an exploratory investigation of the complex morphological behavior of uranium plasmas formed following LA in inert (pure nitrogen or argon) and reactive (those containing oxygen, *e.g.* air) environments is conducted. The results presented here, which demonstrate interesting behavior of the uranium plasma and significant quenching of atomic uranium species persistence in air in contrast to the behavior observed in nitrogen and argon, motivate a more comprehensive experimental study isolating the potential uranium-oxygen interactions. That study is presented in Sec. 3.4 and 3.5.

Time-resolved, single-shot images of the uranium-LPP are compared between a control, low-pressure (5 mTorr) environment, two more chemically inert gases, pure nitrogen and argon, and air in Fig. 3.10. Characterization of the plume morphology takes into consideration three important parameters: (i) plume shape, (ii) size, and (iii) intensity. The low-pressure reference expands adiabatically with negligible

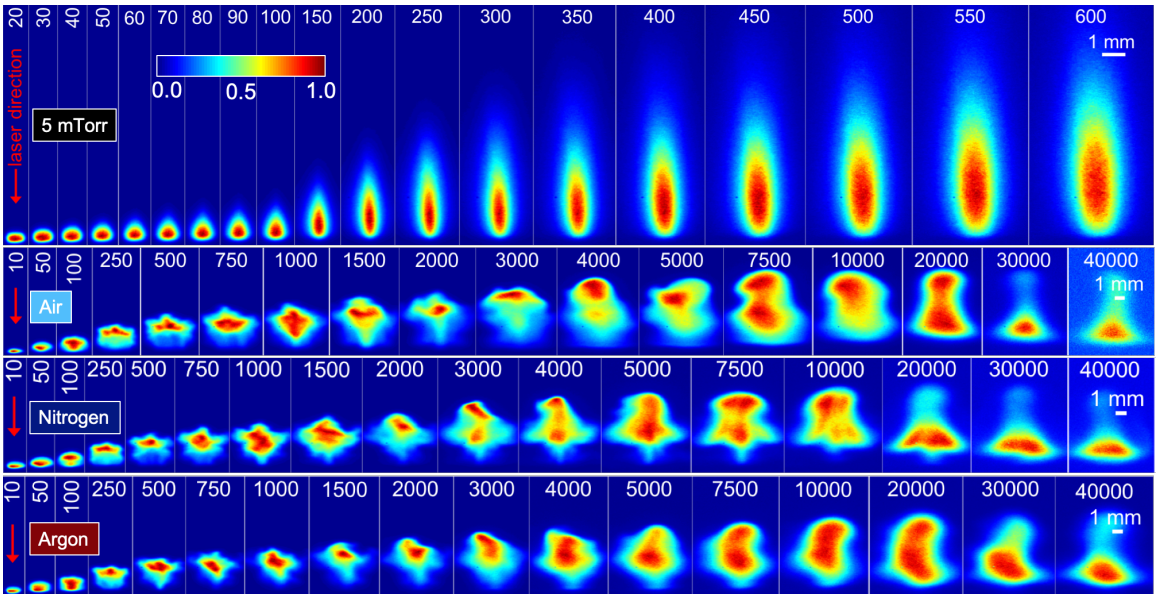

Figure 3.10: Time-resolved images of total plasma emission taken 5 mTorr (low pressure), 100 Torr nitrogen, air, and argon. The total emission corresponds to the spectral region between 200 and 900 nm. The red arrow marks the incident laser direction in the earliest time frame. Delays are given in ns (wrt. the ablation laser pulse). Each image is normalized to its own maximum [220].

confinement. The shape and size of the plume are summarized from Fig. 3.10 in Fig. 3.11 showing (a) representative intensity profiles along the center of the plume on the laser axis and (b) plume lengths measured from the target, along the laser axis as a function of time. In the low-pressure environment, the plume expands according to a linear free-expansion model $R \propto t$ with a goodness of fit $R^2 = 0.957$.

A transition from a collisionless to a collisional regime occurs around ∼100 mTorr [96]. In the collisional regime, expansion becomes increasingly complex, leading to macroscopic morphological behavior like plume splitting, sharpening, and confinement indicated by the formation of a sharp boundary between the plume periphery and ambient and increased temperature and density of the plasma which yield greater total emission at early times [11, 57]. Sharpening has been previously observed for other high-Z targets like tungsten at pressures of ∼1 Torr and is caused by a greater kinetic energy of target species in the target normal direction [96]. Notable sharpening is not observed in the results presented in Fig. 3.10; however, from Fig. 3.11(a), dra-

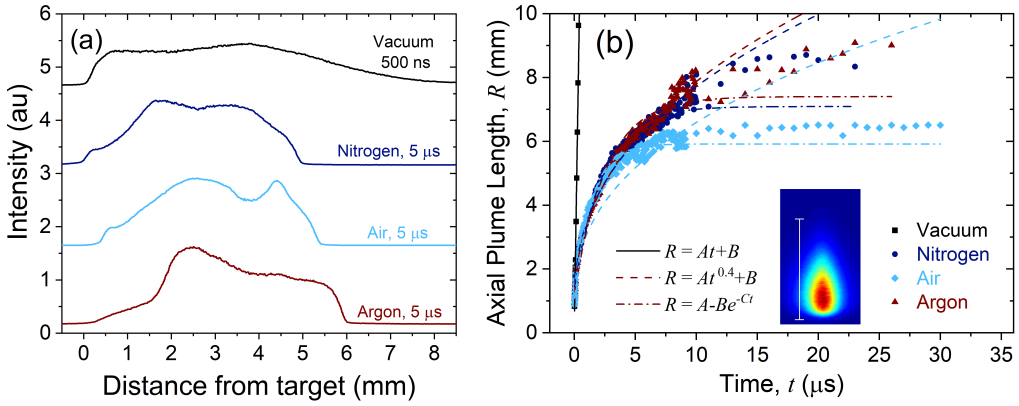

Figure 3.11: (a) Intensity profiles along the center of the laser axis taken from plasma images in Fig. 3.10 in 5 mTorr, and 100 Torr pure nitrogen, air, and pure argon. Delays for each case are given in the figure: 500 ns for low pressure; 5 μs for each of the 100-Torr cases. (b–d) Maximum plume length along the laser axis as a function of time. The inset plasma image for 5 mTorr with a delay of 500 ns indicates how the plume length was measured, from the target plane to 5% of the maximum emission along the laser axis. The red arrow marks the incident laser direction. Low pressure data are fit with a linear free expansion model (solid line). The 100-Torr cases are each fit with both the blast (dashed line) and drag models (dash-dot line). The equation for each model is given in the figure; A,B, and C are fit parameters; R and t are the dependent and independent variables denoting plume length and time, respectively [220].

matic plume splitting is observed in air, exists to some degree in the case of nitrogen, and is least pronounced in argon. Oscillatory behavior described by Raleigh-Taylor and Richtmyer-Meshkov instabilities in the plume shape is observed from the images recorded at 100-Torr pressure [96]. These instabilities arise from interactions of the expanding plume with the steady-state ambient gas and could contribute to the plume splitting observed in nitrogen and air. Further, shock expansion governs the plume morphology at the earlier delays in nitrogen and argon as shown in Fig. 3.11(b); the spherical blast model $R \propto t^{0.4}$ agrees well with the plume size up to $\sim$10 µs in both nitrogen and argon; beyond 10 µs the expansion rate lies between the blast and drag models $R \propto (1 - e^{-\beta t})$, indicating the weakening of the shock. In the case of air, weakening shocks or detachment of the shocks at the target surface may allow reactive species like oxygen to penetrate the plume resulting in chemical reactions with plasma species. The penetration of reactive species is evidenced by the agreement between the plume size in air and the drag model which describes primarily collisional deceleration mechanisms (including the contribution of inelastic collisions such as reactions). These reactions are believed to significantly contribute to plume splitting observed in air, in contrast to the smaller degree of splitting observed in nitrogen and argon. It must be noted that the insights on plume morphology should be regarded with caution considering the limitation of probing only the emitting excited state populations in these measurements.

Spectroscopy, similarly, shows an interesting difference in the case of air compared to nitrogen and argon. Figure 3.12 shows early-time emission spectra at visible wavelengths for (a) the low-pressure and (b) higher pressures of nitrogen, air, and argon. The most prominent emission lines in the spectrum are the U I resonance lines at 436.20, 556.41, and 591.54 nm. The spectrum in air shows further evidence of confinement and increased collisional excitation with an elevated background and atomic line intensities, which is different from both pure nitrogen and argon. The

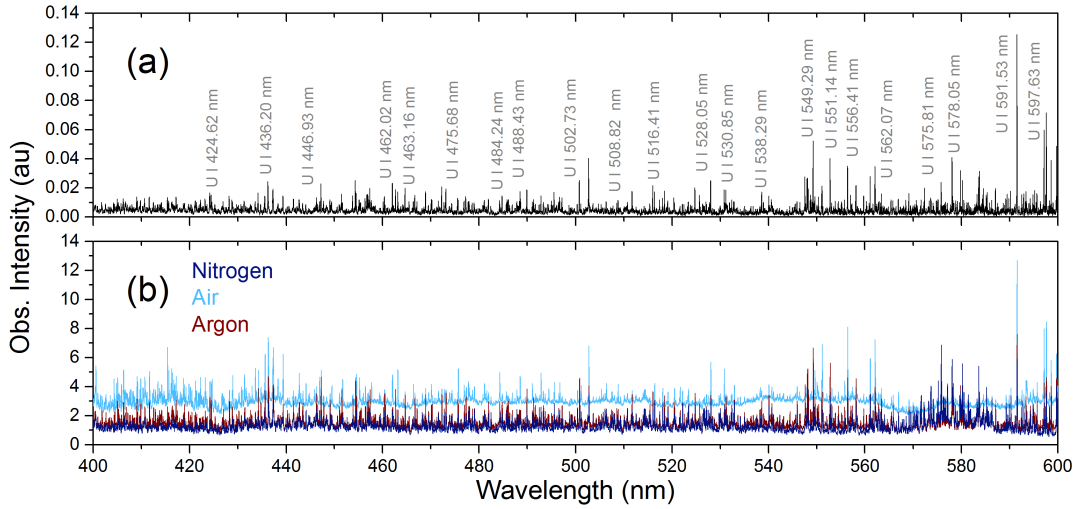

Figure 3.12: (a) Representative spectra recorded in 5 mTorr (low-pressure) and (b) 100 Torr air, nitrogen, and argon. The gate delay and width for the low-pressure spectrum were 1 µs and 0.5 µs, respectively. The low-pressure spectrum was recorded at a distance of 3 mm from the target. The gate delays and widths for the 100-Torr spectra were 1 µs and 0.2 µs, respectively. The 100-Torr spectra were recorded at a distance of 2.5 mm from the target [220].

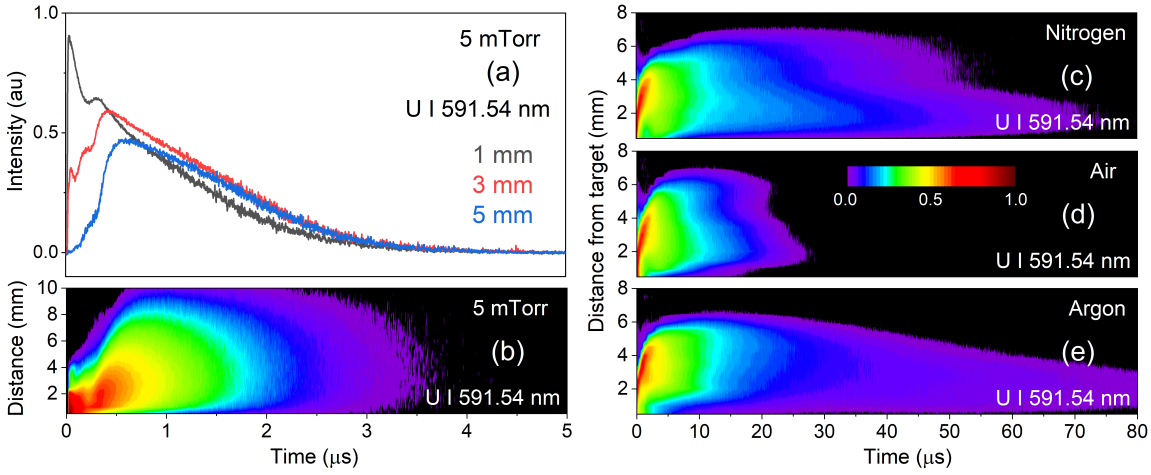

Figure 3.13: (a) Normalized time-evolution profiles for U I 591.54 nm line at various distances from the target; these profiles were stitched together for various positions of the plasma image along the slit to form the contours in (b–e). Contours are recorded in (b) low pressure (5 mTorr) and 100 Torr (c) nitrogen, (d) air, and (e) argon [220].

continuum radiation (bremsstrahlung and recombination) from LPP is more pronounced at early times ($\lesssim$500 ns) and is not expected to contribute considerably to the observed spectral features, so the dominant contribution to the elevated background in air is believed to originate from overlapping, unresolved spectral features from uranium oxides [98]. The results from OTOFS tracking the U I 591.54 nm line, shown in Fig. 3.13, provide further evidence that suggests uranium-oxygen reactions in the plasma formed in air cause the interesting morphological behavior including pronounced plume splitting and confinement as well as dramatic reduction in the persistence of the emission from U I species suggest frequent uranium-oxygen reactions. These results agree with previous studies [138, 222] that employed LA-LIF and LA-LAS to probe, instead, the unexcited U I populations. The differences between the inert nitrogen and argon environments can plausibly be explained by nitrogen having a greater density of states than argon due to its ro-vibrational levels, more quickly quenching the emission from U I species via inelastic collisions [139]. Additionally, molecular nitrogen is more readily ionized than argon, and the specific heat of nitrogen is approximately twice that of argon [74]. Recent work demonstrated that greater plasma temperatures from these contributions in an argon background gas can be used to provide a uniform radiation source from LPPs [108]. The contrast between nitrogen and air implies that the presence of oxygen causes depletion of the U I population. Although uranium oxides and nitrides may form in air, the extremely high bond dissociation energy of nitrogen molecules in comparison with that of oxygen makes the formation of uranium nitrides less probable [156]. Previous work reported that the addition of oxygen has a dramatic effect in reducing the emission of Pb I species [22], agreeing with other results showing reduction of Hg I line intensities in air compared to a pure nitrogen background [87]. These studies highlight that the oxygen-initiated plasma chemistry may lead to a reduction of the excited state population, supporting the results shown here.

3.4 Tracking formation and evolution of uranium and its oxides in the plume

The results from Sec. 3.3 motivate a dedicated investigation into the formation and evolution of uranium oxides in the LPP. Clearly from these results and those presented in Refs. [138, 222], formation of uranium oxides is inevitable during LA of uranium-containing targets in air and leads to substantial quenching of atomic uranium signals. Signal quenching poses challenges for *in-situ* or in-field LIBS, among other analytical techniques, conducted in air. Moreover, uranium oxides are especially interesting considering the prospects to use LAMIS to distinguish uranium-isotopes [104, 155]. Improved understanding of the uranium-LPP chemistry may be translated to comprehension of the similar physics occurring at larger scale in nuclear fireballs. In this section, uranium-oxygen reaction pathways leading to the formation and evolution of various uranium oxide species are isolated by varying the concentration of oxygen in a background of inert argon with a fixed total pressure of 100 Torr.

Figure 3.14 shows emission contours from OTOFS of U I 591.54 nm and UO 593.55 nm species in the uranium-LPP for various oxygen concentrations in the range $\sim 3.2 \times 10^{13}$ cm^{-3} ('pure' argon) and $\sim 7.2 \times 10^{17}$ cm^{-3} (18% oxygen). The emission contours in pure argon show uniform species distributions with no evidence of plume splitting or species segregation. Notably, there is some concentration of the UO species present in the LPP, perhaps originating in part from the target as evidenced by the expansion behavior. The addition of even trace amounts of oxygen (3.2×10^{16} cm^{-3}, 1%) causes quenching of the emission (persistence) of U I. From the contours in Fig. 3.14, UO emission nearer the target persists by up to approx. 10 µs longer than in the pure argon case. This may be caused by oxygen species penetrating the weaker shock regions at the target surface interface. These results indicate a trace amount of oxygen is sufficient for gas-phase oxide formation. Figure 3.15 shows similar coexistence of

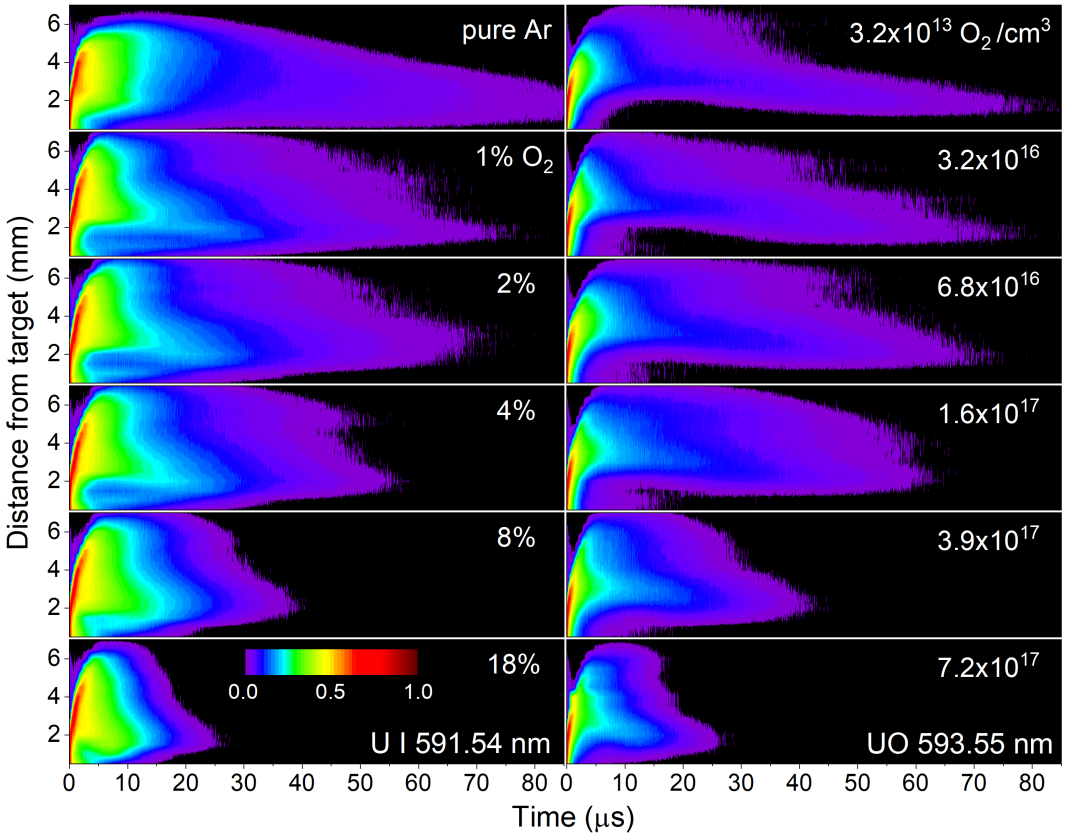

Figure 3.14: Normalized spatiotemporal emission contours from OTOFS for U I 591.54 nm (left) and UO 593.55 nm (right). All data were recorded at 100 Torr total pressure varying the partial pressures of oxygen in a background of pure argon. The oxygen percentages and number densities are provided in the figure [220].

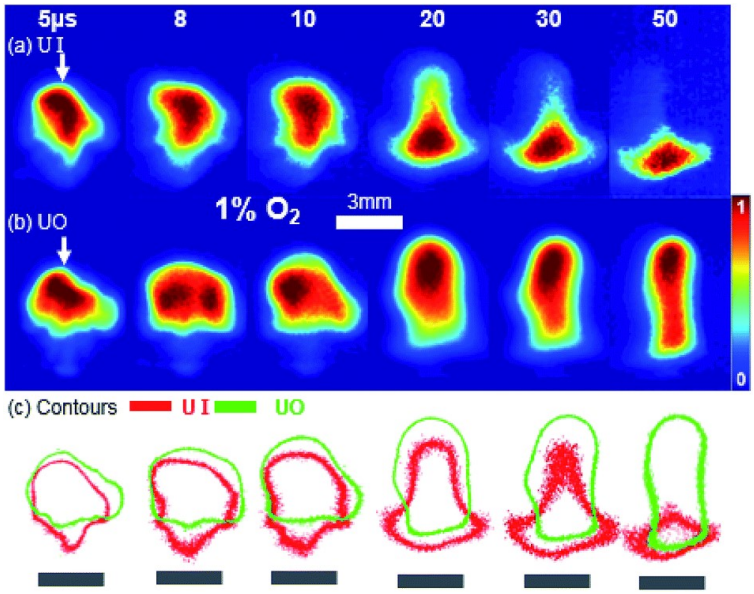

Figure 3.15: Narrowline transmission filters (Fig. 3.2) are used to isolate the emission of (a) U I and (b) UO species in order to directly image their distributions in the LPP formed with 1% oxygen partial pressure in a total pressure of 100 Torr backed with pure argon. Each image is obtained from a single ablation laser shot. The white arrow in the first frame denotes the ablation laser direction. Each image is normalized to its own maximum intensity. (c) Overlapped shape contours (at a threshold of 25% of the maximum intensity) for both U I and UO species. The dark boxes denote the target location [125].

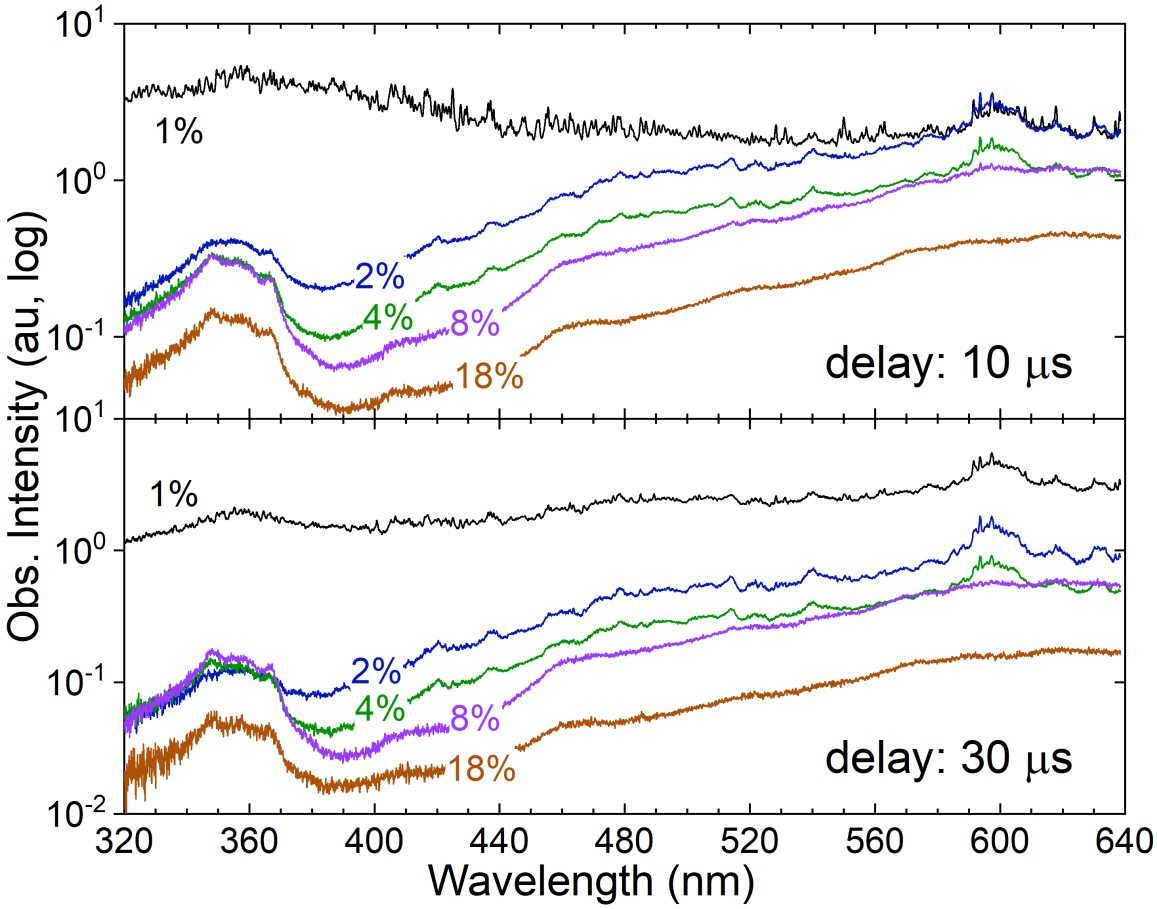

Figure 3.16: Low-resolution spectra recorded at a distance of 2 mm from the target at 10-(top) and 30-µs (bottom) delays at various partial pressures of oxygen (denoted as percentages) in a background of pure argon with a constant total pressure of 100 Torr. Gate widths were 5 µs and spectra were accumulated for 10 laser shots [220].

U I and UO species at early times via selective imaging using narrowline filters (see Sec. 3.1). At later times, segregation of the U I and UO species becomes prevalent as seen in Fig. 3.15(c) indicating preferential formation of the uranium oxide in the peripheral regions of the plasma, where temperatures are presumed to be cooler (see Sec. 3.2.1). The regions of segregated uranium and uranium oxide species coincide with the split plume regions for the air ambient observed in Sec. 3.3, indicating that, indeed, uranium-oxygen chemistry in the LPP causes the interesting morphological behavior of the plasma in air.

A peculiar observation is that increasing the oxygen concentration has similar

effects on the persistence of emission from both U I and UO. The emission lifetime from both species decreases nearly fourfold in 18% oxygen when compared to the pure argon environment. Both species seem to react with ambient oxygen, depleting their excited state populations at similar rates. Similar depletion rates for both U I and UO with increasing oxygen points to possible pathways for the formation of heavier gas-phase uranium oxide species (denoted U_xO_y, $x \geq 1$ and $y > 1$), like UO_2, UO_3, and U_2O_2. However, as discussed in Sec. 2.2, existing literature lacks information about the emission features from these heavier gas-phase uranium oxides in the visible spectral range, with the exception of a few works comparing experimental results from resonantly enhanced multiphoton ionization (REMPI) [94] and LIF [152] and numerical solutions of multiconfigurational wavefunctions [79] for UO_2 species. These works predict two intense regions for the electronic spectrum of UO_2 in the range of 312–370 nm and 526–600 nm.

Figure 3.16 shows late-time emission spectra over a broader spectral range from the uranium-LPP in varying partial pressures of oxygen, looking for possible signatures from heavier uranium oxide species. Table B.1 in Appendix B lists the most probable thermochemical $U \leftrightarrow UO \leftrightarrow U_xO_y$ reaction pathways, summarized from Ref. [69]. The forward reaction rate coefficients show the temperature dependence for each pathway, predicting that U_xO_y tend to form at lower temperatures. Emission from U I is typically observed at plasma temperatures in the range ∼4000–10000 K, while UO features are prevalent at lower temperatures in the range ∼3000–6000 K [98]. Heavier uranium oxides like UO_2 are expected to form at temperatures below ∼4000 K [69, 120]. The lower temperature conditions occur at later times in the LPP in the peripheral regions of the plasma as demonstrated in Sec. 3.2.1, prompting OES investigation at later delays (Fig. 3.16). From Fig. 3.16, greater oxygen partial pressures (≥1%) diminish U I and U II lines, exposing broad features likely corresponding to uranium oxides whose higher density of states results in unresolved fine emission lines which

appear as bands. Two such features grow in prominence with increasing oxygen concentration: the spectral band between 320 and 380 nm and the broad feature near 600 nm. These broad features may originate from heavier uranium oxide species, as their band positions agree with the locations predicted for the electronic transitions of UO_2 [79, 94, 152]. The assignment of these features is discussed more in Section 3.5.

3.5 Identification of emission from heavier uranium oxides

Information about heavier uranium oxide species (U_xO_y) beyond UO and the chemical reaction pathways which lead to formation of U_xO_y in LPPs is still limited. The results presented in Sec. 3.4, which show similar depletion of both U I and UO species with increasing oxygen concentration, suggest both species may be precursors for U_xO_y. Albeit U_xO_y transitions have been extensively studied in the infrared spectral region via Raman or vibrational spectroscopy methods [150], visible-range transitions have not been previously identified experimentally from LPPs. Here, the band locations and morphological behavior of the emission from the broad 355 nm band shown in Fig. 3.16 are compared to those predicted by numerical methods for UO_2. The agreement between the predicted band locations [79] and morphology [68, 69] with experimental data supports the assignment of the 355 nm band as comprised, in part, by the emission from UO_2 species. Identifying the broad emission features from heavier uranium oxides may enable the use of the LAMIS technique for distinction of uranium-isotopes with a less stringent resolution requirement. Moreover, these features may be additionally useful in forensics of nuclear fireballs.

Figure 3.17 shows the predicted line and band locations for U I and U II (Palmer [179]), UO (Kaledin & Heaven [120]), and UO_2 (Gagliardi *et al.* [79]) in the broad spectral range between 320 and 640 nm. The feature positions are compared to a late-time (10 µs gate delay and 20 µs gate width) experimental spectrum from the uranium-LPP with a 4% oxygen partial pressure in 100 Torr total pressure backed with pure

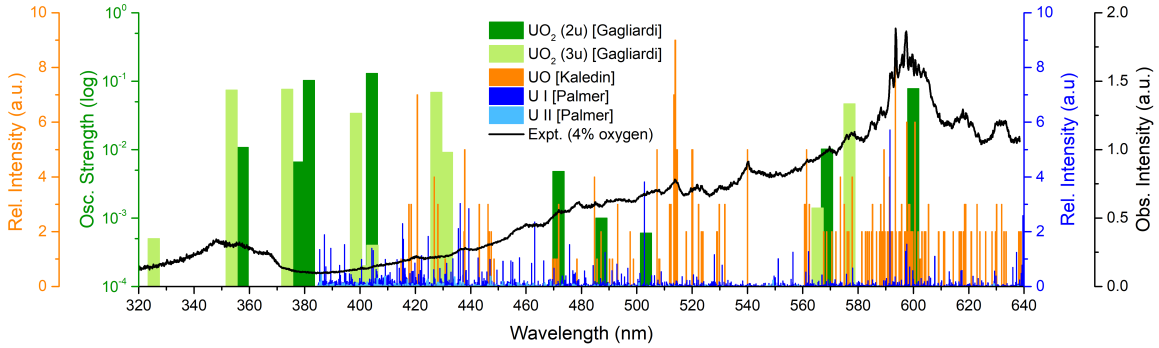

Figure 3.17: The predicted line and band locations for U I and U II (Palmer [179]), UO (Kaledin & Heaven [120]), and UO_2 (Gagliardi *et al.* [79]) in the broad spectral range between 320 and 640 nm is compared to an experimental spectrum from the U-LPP with a 4% oxygen partial pressure in 100 Torr total pressure backed with pure argon. The ICCD recording parameters were 10 µs gate delay and 20 µs gate width, respectively.

argon. Focusing on the 2u and 3u electronic transitions from UO_2, as predicted by solving multiconfigurational wavefunctions by Gagliardi *et al.* [79], several clusters of transitions are present including several overlapped with the prominent band at 355 nm and several near the prominent band around 600 nm. The numerical predictions from Ref. [79] are supported by experimental results from REMPI [94] and LIF [152]. This comparison implies that the observed band features at 355 nm and 600 nm may originate from electronic de-excitation transitions of UO_2 species.

Figure 3.18 summarizes the results from Sec. 3.4, showing confluent decreasing persistence of U I and UO with the increasing prominence of the 355-nm band attributed to U_xO_y. The persistence of U I decreases monotonically with increasing oxygen partial pressure; however, the persistence of UO peaks at a particular oxygen concentration and then decreases like for the U I species. The prominence of the 355-nm band is defined as the ratio of the area beneath the band (between 310 and 380 nm) to the total area beneath the entire spectral range (between 310 and 640 nm), as shown in the inset of Fig. 3.18 (c). The monotonic decrease of U I persistence and the optimal oxygen concentration for UO persistence imply the existence of competing reaction pathways for varied oxygen concentrations, leading to the formation of dif-

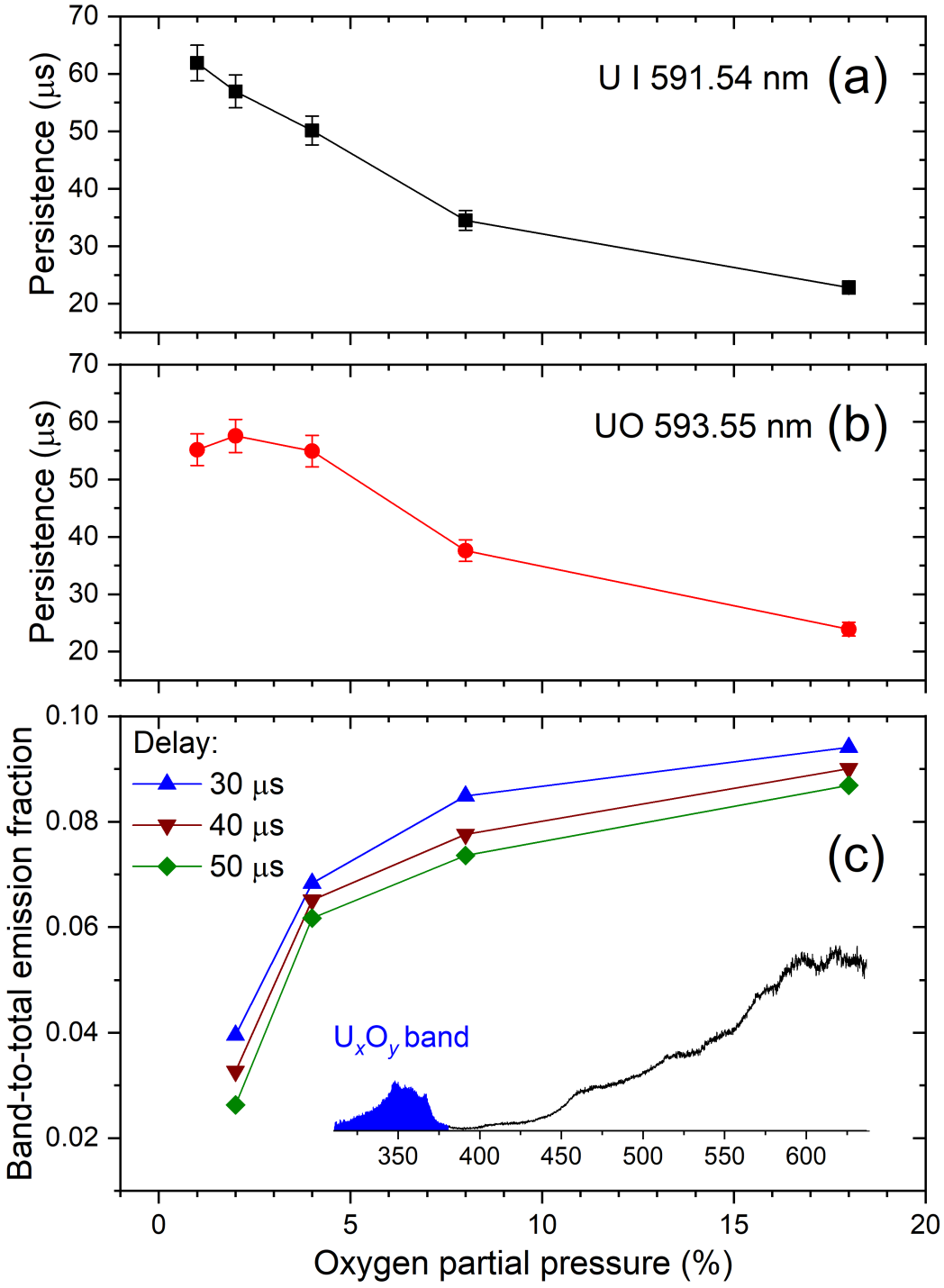

Figure 3.18: The observed persistence of (a) U I 591.54 nm and (b) UO 593.55 nm emission decreases with increasing oxygen concentration; (c) the fractional emission of the broad feature between 310 and 380 nm to the observed emission between 310 and 640 nm as shown in the inset. Three different late delays are shown to show that the trend with oxygen partial pressure is invariant with time [220].

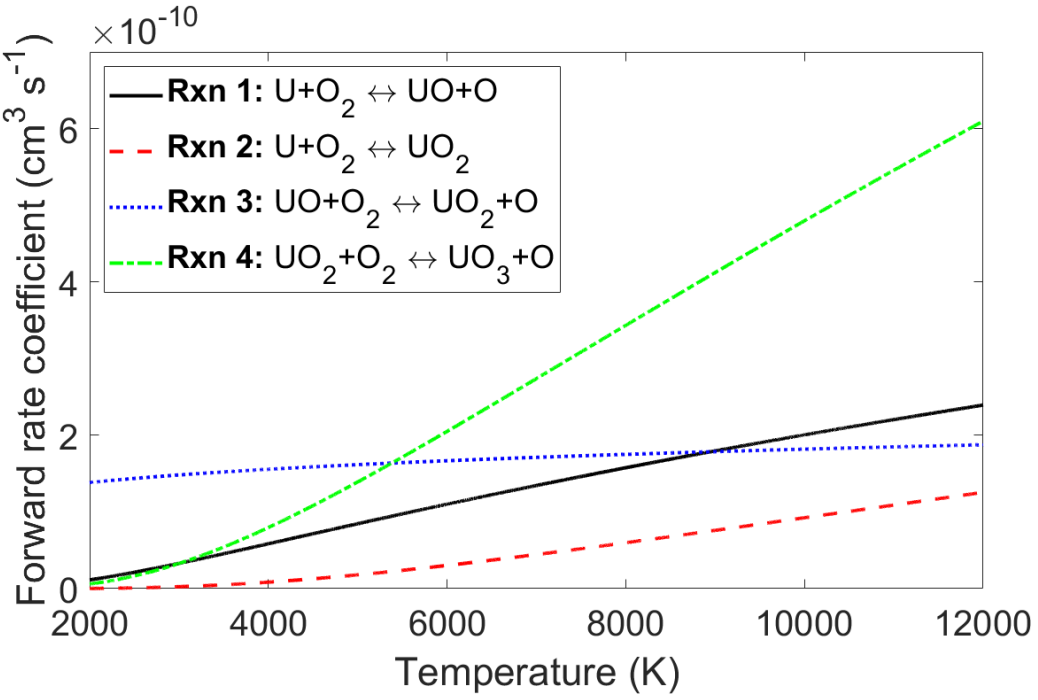

Figure 3.19: The forward rate coefficients are plotted as a function of temperature in the range relevant for typical U-LPPs for the exothermic U↔UO↔U_xO_y reactions (denoted Rxn in the legend). Reactions 1–4, for which the rate coefficients are plotted here, are presented in Table B.1 in Appendix B and taken from Ref. [69].

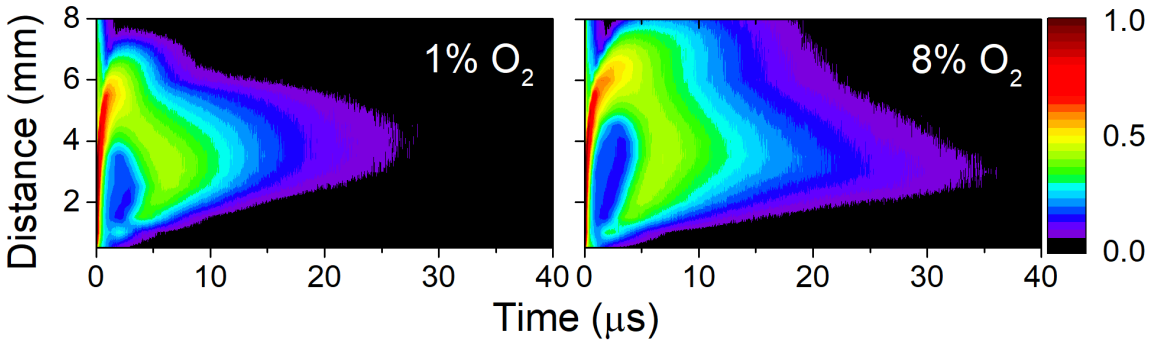

Figure 3.20: U_xO_y 355 nm emission contours from OTOFS for 1% (left) and 8% (right) oxygen partial pressures in 100 Torr total pressure (backed with argon gas) [219].

ferent U oxide states. Lower oxygen concentrations promote reaction pathways which consume U I to form UO, and greater concentrations promote formation of heavier uranium oxide species via combustion of U I. The weaker temperature-dependence of the rate coefficient for Reaction 2 than that for Reaction 1 in Table B.1 is consistent with this observation, as shown in Fig. 3.19. Comparison of the reaction rates for Reactions 1 and 3 further supports the observation that UO concentration is sensitive to the local temperature and oxygen concentration, because depletion of UO (Reaction 3) via combustion to form UO_2 has a weaker temperature dependence than formation of UO via combustion (Reaction 1). The temperature dependence of Reaction 3 implies also that depletion of UO to form UO_2 occurs over a greater temperature span, while UO is more likely to form at larger temperatures (Reaction 1). Indeed, previous work demonstrates that greater oxygen concentrations, which also foster the formation of heavier oxides, lead to lower average plasma temperatures [99]. In summary, the contrasting behavior of 355-nm band to that of U I and UO is consistent with expected reaction pathways which imply lower temperatures and greater oxygen concentrations lead to UO2 formation from combustion of both U I and UO, further supporting the assignment of the 355-nm to the emission from UO_2, in part, among other oxides.

Figure 3.20 shows the emission contours from OTOFS of the 355-nm band, and

likewise demonstrates that this emission exhibits contrasting behavior to that of U I and UO. The persistence of this emission increases with increasing oxygen concentration, implying that the species from whom the emission originates forms from the reaction of U I and UO with ambient oxygen. Moreover, the spatiotemporal dependence of the emission in Fig. 3.20 is consistent with the morphology of the UO_2 species predicted from the fluid model simulation in Ref. [68] for ultrashort-pulse LA of uranium. The simulation predicts the expansion of a dense layer of UO_2 away from the target at the earliest times which overlaps with UO behavior. At these times, the core of the plume is (mostly) devoid of UO_2, consistent with the empty emission region in Fig. 3.20. After $\sim$5 µs, the UO_2 region is predicted to broaden, while the core UO_2 concentrations diminish further due to increased dissociation rates caused by elevated temperatures; again, this behavior is observed in similar timescales in Fig. 3.20 for the 8% oxygen case. At later times, the simulation predicts that turbulence transports the cooler region where UO_2 formation takes place toward the core region, resulting in the the macroscopic reverse motion toward the target which is consistent with the late-time behavior observed in experiments. At later stages as the plasma cools and condenses further, even heavier gas-phase oxides like UO_3 begin to form. Ultimately, the agreement between the morphology predicted for UO_2 in Ref. [68] and the emission contour observed in Fig. 3.20 further supports the assignment of the U_xO_y feature partially to UO_2.

3.6 Summary and future work

This chapter presents a comprehensive experimental investigation of the evolution of uranium-containing LPPs. Section 3.2.1 provides the thermodynamic properties and discusses equilibrium in a uranium-LPP formed in a low-pressure environment following a meticulous analysis of the uranium emission spectrum. These results add to the extremely limited literature which conducts non-invasive, emission-based diagnos-

tics of uranium-containing plasmas. Further, the first Stark broadening parameters for uranium lines are reported, enabling future electron density measurements using uranium lines as opposed to impurity lines. Section 3.3 demonstrates the dramatic quenching of atomic uranium signal and effects on the macroscopic morphology of the uranium-LPP in the presence of ambient oxygen, motivating the dedicated study presented in Sec. 3.4–3.5 which isolates uranium-oxygen chemistry. Section 3.4 shows peculiar decreasing persistence of UO species with increasing oxygen concentration, similar to that observed for U I, implying that greater ambient oxygen concentrations lead to the formation of heavier uranium oxides. Sections 3.4–3.5 address the lack of information in existing literature about heavier uranium oxide species, identifying plausible broadband emission features in the visible spectral range, for the first time, from heavier oxides like UO_2. The results presented in this chapter have implications for better understanding of the physics of uranium-plasmas, applicable to analytical spectroscopy methods like LIBS and LA-LAS for direct measurements of uranium as well as forensics of nuclear fireballs.

For either application, further work studying uranium-plasmas is necessary to understand early- and late-time ejecta and agglomeration. Early-time micron-scale ejecta may form from subsurface boiling, recoil ejection, and exfoliation mechanisms [250] and could contribute to the continuum emitting hot body radiation [Eq. (2.15)], relevant to LIBS in which such continuum may contribute to background limiting analytical capabilities. Late-time agglomeration is thought to involve heavier uranium oxide species, and the agglomerates can simulate debris from nuclear explosions in forensics. A plausible non-invasive technique for recording micron-scale ejecta or agglomerates is shadowgraphy; all-optical Rayleigh scatter has also been previously proposed to observe nanoparticles [129]. Future work is required to confirm the assignment of the 355-nm band to emission from UO_2 and identify other gas-phase uranium oxides. Further work should explore the isotopic shift of the 355-nm

band, perhaps looking at oxygen-isotopes as a more convenient, safer alternative to uranium-isotopes. These efforts may help lessen the stringent resolution requirement for LAMIS with uranium-isotopes.

CHAPTER 4

Remote Sensing Enabled by Ultrashort Laser Filamentation

Ultrashort laser-driven filamentation is of considerable interest for applications which require long-scale delivery of optical pulses [194]. The propagation of an intense, fs-duration laser pulse in air incurs a third-order nonlinear response, causing an intensity-dependent change in the refractive index and self-focusing of the beam followed by plasma formation. Propagation through the plasma causes de-focusing of the laser pulse, and the dynamic balance between self-focusing, plasma de-focusing, and diffraction results in extended beam propagation. The filament sustains a high intensity over distances which significantly exceed the Rayleigh length [20]. This chapter discusses the phenomena which enable filamentation as well as the prospects for combining filamentation with analytical spectroscopy techniques, like LIBS and LIF, for remote detection applications, specifically in the context of nuclear security, safeguards, and nonproliferation.

4.1 Nonlinear propagation and filamentation of intense laser pulses

4.1.1 Linear polarizability

The classical formulation which describes light-matter interaction and the propagation of electromagnetic fields is given by Maxwell's equations [228]:

$$\nabla \cdot \mathbf{D} = \rho, \tag{4.1a}$$

$$\nabla \cdot \mathbf{B} = 0, \tag{4.1b}$$

$$\nabla \times \mathbf{E} + \frac{\partial \mathbf{B}}{\partial t} = \mathbf{0}, \tag{4.1c}$$

$$\nabla \times \mathbf{H} - \frac{\partial \mathbf{D}}{\partial t} = \mathbf{j}, \tag{4.1d}$$

where $\mathbf{E}$, $\mathbf{B}$, $\mathbf{D}$, and $\mathbf{H}$ represent the electric, magnetic, displacement, and magnetizing fields, respectively; ρ is the free charge density; and $\mathbf{j}$ is the current density. The displacement field is related to the electric field by the polarization ($\mathbf{P}$) response of the medium $\mathbf{D} = \varepsilon_0 \mathbf{E} + \mathbf{P}$; and the magnetizing field is similarly related to the magnetic field by the magnetization ($\mathbf{M}$) response $\mathbf{H} = \frac{1}{\mu_0}\mathbf{B} - \mathbf{M}$. Here, ε_0 and μ_0 are the permittivity and permeability of free space, respectively.

The reaction of bound electrons to a weak electromagnetic field manifests as the macroscopic linear polarization response of the medium. This interaction introduces the linear susceptibility [114, 142]:

$$\chi^{(1)}(\omega) = \frac{Ne^2}{m_e \varepsilon_0} \left(\sum_j \frac{f_j}{\omega_{0,j}^2 - \omega^2 - i\gamma_j \omega} \right), \tag{4.2}$$

where N is the number density of molecules, each with f_j electrons with natural frequencies $\omega_{0,j}$ and damping coefficients γ_j [228]. For crystalline materials, the susceptibility is a second-rank tensor which describes an orientation-dependent response;

whereas, for gases whose species have random orientation, the susceptibility is treated as a scalar. The frequency dependent refractive index is derived from the relationship between the electric and displacement fields $\tilde{\mathbf{D}}(\omega) = \varepsilon_0\tilde{\mathbf{E}}(\omega) + \tilde{\mathbf{P}}(\omega) = \varepsilon(\omega)\tilde{\mathbf{E}}(\omega)$ where $\varepsilon_R(\omega) = \varepsilon_0(1 + \chi_R^{(1)}(\omega))$ is the frequency-dependent permittivity, giving the relation for the index considering the real part of the susceptibility $n(\omega) = \sqrt{\frac{\varepsilon_R(\omega)}{\varepsilon_0}} = \sqrt{1 + \chi_R^{(1)}(\omega)}$. The refractive index can be used to predict propagation and boundary interactions for electromagnetic waves in the linear regime. The complex part of the susceptibility similarly varies with frequency and describes absorption $\alpha(\omega) = \frac{\omega\chi_I^{(1)}(\omega)}{n(\omega)c}$.

The homogeneous wave equation describes propagation in the linear regime and can be modified to include nonlinearities. Starting with Maxwell's equations [Eq. (4.1)], we can derive the wave propagation equation assuming no macroscopic magnetization in the nonconducting, electrically-neutral dielectric medium:

$$\nabla^2\tilde{\mathbf{E}}(\mathbf{r},\omega) - \frac{n(\omega)^2}{c^2}\frac{\partial^2}{\partial t^2}\tilde{\mathbf{E}}(\mathbf{r},\omega) = \mathbf{0}. \tag{4.3}$$

Equation (4.3) yields the plane wave solution:

$$\tilde{\mathbf{E}}(z,t) = \hat{e}A_0 \exp\left(-\frac{\alpha z}{2}\right) \exp\left[i(kz - \omega t)\right] + \text{c.c.}, \tag{4.4}$$

where A_0 is the amplitude of the wave at $z = 0$; $\hat{e}$ represents the polarization; and the wave vector obeys the dispersion relation $k(\omega) = n(\omega)\frac{\omega}{c}$. The monochromatic plane wave solution, given by Eq. (4.4), propagates with a phase velocity $v_p = c/n$. For real, polychromatic waves it is useful to define the group velocity $v_g = \left(\frac{dk}{d\omega}\right)_{\omega_0}^{-1}$ which describes the propagation of a group of superimposed monochromatic waves with carrier frequency ω_0 (*e.g.*, an ultrashort optical pulse). In experiments, the intensity envelope must be measured because of the slow response of electronic detectors (for example, silicon-based photodiodes or CCDs discussed in Chapter 2) compared to rapidly-varying optical carrier frequency. The intensity I is related to the field

amplitude by

$$I(z,t) = 2\varepsilon_0 nc|A(z,t)|^2, \tag{4.5}$$

The optical power is the integral of the intensity over the entire area of the pulse $P = \int_A I dA$. Equation (4.3) and its plane wave solution in Eq. (4.4) provide the framework for understanding the linear propagation regime in isotropic media described by concepts such dispersion, refraction, reflection, and linear absorption. Section 4.1.2 introduces the framework for the nonlinear propagation regime, important for understanding the phenomena associated with filamentation.

4.1.2 Nonlinear polarizability

The nonlinear polarizability response results from small nonlinear corrections to the susceptibility and yields the comprehensive polarization response given by the expansion:

$$\tilde{\mathbf{P}} = \tilde{\mathbf{P}}^{(1)} + \tilde{\mathbf{P}}^{(2)} + \tilde{\mathbf{P}}^{(3)} + ... = \varepsilon_0 \chi^{(1)} \cdot \tilde{\mathbf{E}} + \varepsilon_0 \chi^{(2)} \cdot \tilde{\mathbf{E}} \cdot \tilde{\mathbf{E}} + \varepsilon_0 \chi^{(3)} \cdot \tilde{\mathbf{E}} \cdot \tilde{\mathbf{E}} \cdot \tilde{\mathbf{E}} + ..., \tag{4.6}$$

where $\tilde{\mathbf{P}}^{(N)}$ is the N^{th}-order ($N > 1$) nonlinear polarization; and $\chi^{(N)}$ is the nonlinear susceptibility tensor of rank $N + 1$. The expanded polarizability given by Eq. (4.6) provides the framework for understanding various nonlinear phenomena. The wave equation [Eq. (4.3)] for a nonlinear medium considering N^{th}-order effects becomes:

$$\nabla^2 \tilde{\mathbf{E}} - \frac{n^2}{c^2} \frac{\partial^2}{\partial t^2} \tilde{\mathbf{E}} = \frac{1}{\varepsilon_0 c^2} \frac{\partial^2}{\partial t^2} \tilde{\mathbf{P}}^{(N)}. \tag{4.7}$$

The nonlinear term becomes a driver for solutions of the homogeneous wave equation.

Processes that rely on the second-order susceptibility $\chi^{(2)}$ include frequency effects

such as second harmonic generation (SHG) and sum- and difference-frequency generation, asymmetric polarization and optical rectification, and the electro-optic effect. The i^{th} cartesian component of the second-order nonlinear polarization is generally expressed as [228]:

$$P_i^{(2)}(\omega_3) = \varepsilon_0 D^{(2)} \sum_{jk} \chi_{ijk}^{(2)}(-\omega_3; \omega_1, \omega_2) E_j(\omega_1) E_k(\omega_2), \tag{4.8}$$

for a field oscillating at ω_3 due to the presence of fields oscillating at ω_1 and ω_2, where $D^{(2)}$ is the degeneracy which describes the ability to distinguish the fields (by frequency or direction).

Third-order processes include the optical Kerr effect, third-harmonic generation, various stimulated scattering phenomena (Brillouin and Raman), and two-photon absorption. The i^{th} Cartesian component of the third-order polarization for a wave oscillating at $\omega_4 = \omega_1 + \omega_2 + \omega_3$ is [228]:

$$P_i^{(3)}(\omega_4) = \varepsilon_0 D^{(3)} \sum_{jkl} \chi_{ijkl}^{(3)}(-\omega_4; \omega_1, \omega_2, \omega_3) E_j(\omega_1) E_k(\omega_2) E_l(\omega_3), \tag{4.9}$$

where the degeneracy $D^{(3)}$ is 1 for all fields indistinguishable, 3 for two fields indistinguishable, and 6 for all fields distinguishable. The optical Kerr effect caused by the third-order nonlinear polarization gives rise to self-focusing among other processes, which is especially relevant for filamentation.

4.1.3 The optical Kerr effect and self-focusing

The optical Kerr effect arises from the third-order susceptibility $\chi_{iiii}^{(3)}(-\omega; \omega, \omega, -\omega)$ (where $i = x, y, z$), and for a isotropic (or centrosymmetric) medium the third-order polarization becomes the first important nonlinear term. Recalling Eq. (4.9), the i^{th}

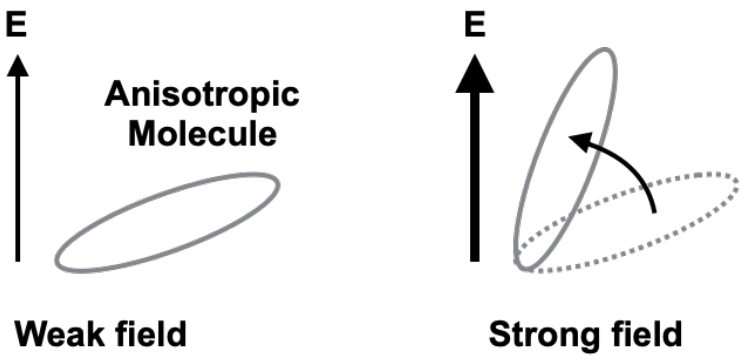

Figure 4.1: An anisotropic molecule realigns in response to the polarization of a strong electric field, which leads, macroscopically, to an index change quantified as n_2 in the optical Kerr effect.

component of the polarization becomes

$$P_i^{(3)}(\omega) = 3\varepsilon_0 \sum_{jkl} \chi_{ijkl}^{(3)}(-\omega;\omega,\omega,-\omega_3)E_j(\omega)E_k(\omega)E_l^*(\omega), \tag{4.10}$$

where for like dimensions $j,k,l = i$ (linear polarization and isotropic medium), $P_i^{(3)}(\omega) = \frac{3}{4}\varepsilon_0\chi_{iiii}^{(3)}(-\omega;\omega,\omega,-\omega)|E_i(\omega)|^2E_i(\omega)$. Considering the linear and third-order terms, the effective susceptibility for the linearly polarized field is $\chi_{\text{eff}} = \chi_{ii}^{(1)}(-\omega;\omega) + \frac{3}{4}\chi_{iiii}^{(3)}(-\omega;\omega,\omega,-\omega)|E_i(\omega)|^2$ which leads to the effective refractive index $n = \sqrt{1+\chi_{\text{eff}}} \approx n_0 + n_2 I(\omega)$, where $n_0 = \sqrt{1+\chi_{ii}^{(1)}(-\omega;\omega)}$, from Eq. (4.5), the spectral intensity is $I(\omega) = \frac{1}{2}\varepsilon_0 n_0 c|E_i(\omega)|^2$, and the Kerr intensity coefficient is $n_2 = \frac{3}{4\varepsilon_0 n_0^2 c}\chi_{iiii}^{(3)}(-\omega;\omega,\omega,-\omega)$. The optical Kerr effect, thus, leads to an intensity-dependent change to the refractive index expressed as:

$$\Delta n = n_2 I. \tag{4.11}$$

Here, the Kerr coefficient is the intensity coefficient although this should be distinguished from the field-squared coefficient often used in literature $\Delta n = 2n_2^E|E|^2$, where $n_2^E = \frac{3}{4n_0}\chi_{iiii}^{(3)}(-\omega;\omega,\omega,-\omega)$. Microscopically, the optical Kerr effect results from reorientation of an anisotropic molecule in response to the polarization of a

strong electric field, leading to an index change quantified by n_2. This is shown as a diagram in Fig. 4.1. The molecular polarizability of gases, relevant for filamentation, is highly transient consisting of a fast electronic response followed by rotational relaxation. For the nitrogen molecule near the ionization threshold, the electronic response occurs on the order of several tens of femtoseconds, and molecular relaxation occurs over several hundreds of femtoseconds [240].

The optical Kerr effect causes modulations in both phase and spatial domains. The phase effect leads to a frequency shift and is referred to as self-phase modulation (SPM). The frequency shift from propagation over a distance L is $\Delta\omega(t) = -\frac{d\phi}{dt} = -\frac{d}{dt}[kn_2I(t)L]$ [228]. For a Gaussian-shaped optical pulse in the time-domain, the rising edge causes a red-shift, and the falling edge causes a blue-shift. In the spatial domain, the nonlinear change in the index follows the shape of the intensity profile. For a Gaussian beam and positive Kerr coefficient, the index change is greater near the beam axis than away from axis, leading to the formation of a positive Kerr lens which tends to focus the beam. This is referred to as self-focusing.

The effective FL, f, of a Kerr lens formed in a thin medium with length L in response to a plane wave with Gaussian amplitude distribution (width w_0) is $f = \frac{n_0 w_0^2}{4n_2 I_0 L}$, under the paraxial approximation [228]. In a thick medium, the beam can come to focus within the medium, and the analysis is more complicated. Self-trapping occurs when self-focusing balances diffraction and depends on power rather than intensity because both self-focusing and diffraction are area-dependent and tend to offset one another. The critical power for self-trapping of a Gaussian beam under the paraxial approximation is $P_{\mathrm{cr},2} = \frac{(1.22\lambda)^2\pi\varepsilon_0 c}{32n_2}$. The critical power for catastrophic self-collapse of a Gaussian beam is $P_{\mathrm{cr},1} = \frac{\varepsilon_0 c\lambda^2}{8\pi n_2}$ [228]. The critical power for self-collapse with a general beam profile is

$$P_{\mathrm{cr}} = C\frac{\lambda^2}{4\pi n_2 n_0}, \tag{4.12}$$

where C is a shape factor in the range between 3.72 and 6.4 (3.72 for Townes profile and 3.77 for Gaussian profile) [162, 176, 231]. In reality, beam collapse is arrested because increasing intensity triggers other nonlinear phenomena such as absorption/ionization, breakdown, and plasma formation.

4.1.4 Ionization and excitation of the propagation medium and plasma de-focusing

Self-focusing in gaseous media which results in filamentation is arrested by competing MPI and tunneling ionization mechanisms, discussed in Chapter 2 (Section 2.1), yielding a distribution of free electrons. For most gases at atmospheric pressure (density $\sim 10^{19}$ cm^{-3}), in the range of laser intensities relevant to filamentation (10^{13} W.cm^{-2}), IB and cascade ionization mechanisms are unlikely to occur because the ultrashort pulse duration is significantly shorter than the mean free time of a liberated electron given by $\langle \Delta t \rangle = \frac{1}{\sigma N v_e}$, (derived from Eq. 2.12 and 2.13) where σ is the electron-neutral collisional cross-section, N is the medium density, and v_e is the electron velocity. For an electron energy on order of 1 eV, gas density $\sim 10^{19}$ cm^{-3}, and cross-section on the order of 10^{-15} cm^{-2}, the mean free time for an electron is $\sim$1 ps [38], significantly longer than the typical pulse duration (several tens of femtoseconds) for which filamentation is usually observed.

The free electron (or plasma) susceptibility $\chi_e(\omega)$ is determined by substituting $\omega_{0,j=0} = 0$ and $N_e = f_{j=0}N$ into Eq. 4.2, and recalling the definition of the plasma frequency ω_p (Eq. 2.7):

$$\chi_e(\omega) = \frac{-\omega_p^2}{\omega(\omega + i\gamma)}. \tag{4.13}$$

Considering a radial distribution of free electrons following ionization by a bell-shaped beam profile, the magnitude of the induced phase is greatest along the central axis,

which leads to de-focusing because the plasma susceptibility is negative. The plasma-induced index change can be related to the free electron distribution:

$$(\Delta n)_e(r,t) = -\frac{4\pi e^2 N_e(r,t)}{2m_e\omega_0^2}. \tag{4.14}$$

In filamentation, the plasma de-focusing mechanism, alongside diffraction, balances focusing contributions including self-focusing and optionally external focusing, for example, with a lens or spherical mirror.

4.1.5 Filamentation of ultrashort laser pulses in gases

The net contributions to the macroscopic polarization relevant for filamentation of high-peak-power optical pulses in gases include the linear term, the third-order nonlinear term which gives rise to the optical Kerr effect, and the plasma term:

$$\tilde{\mathbf{P}}(\mathbf{r},\omega) = \varepsilon_0 \left(\chi^{(1)}(\mathbf{r},\omega) + \frac{3}{4}\chi^{(3)}(\mathbf{r},\omega)|\tilde{\mathbf{E}}(\mathbf{r},\omega)|^2 + \chi_e(\mathbf{r},\omega) \right) \tilde{\mathbf{E}}(\mathbf{r},\omega). \tag{4.15}$$

Considering diffraction and the optional contribution of an external focusing lens, when inserted into the nonlinear wave propagation equation [Eq. (4.7)], the balance $(\Delta n)_{\text{focus}} = (\Delta n)_{\text{defocus}}$ yields an extended mode of propagation, referred to as a filamentation:

$$n_2 I(+\Delta n_{\text{lens}}) = \frac{4\pi e^2 N_e}{2m_e\omega_0^2} + \frac{1.22\lambda_0^2}{8\pi n_0 w_0^2}. \tag{4.16}$$

Here, the first term on the right-hand side represents plasma de-focusing and the second term diffraction. The sequence of mechanisms whose combination results in filamentation of high-peak-power optical pulses begins with self-focusing. The Kerr coefficient for gases is typically three orders of magnitude smaller than that for solid-density dielectric media, on the order of 10^{-19} cm^2 W^{-1} [198, 241]. Eventually, the

peak intensity grows enough to overcome diffraction which would lead into catastrophic collapse if not for arrest through the ionization mechanisms. Filamentation then describes the dynamic competition of self-focusing and de-focusing which results in an extended mode of propagation of an intense core region over distances greatly exceeding the Rayleigh length [20].

4.1.6 Intensity clamping

Maintaining a sufficiently high intensity is important for applications which require remote excitation or even ablation/breakdown of a target, like analytical spectroscopy techniques including LIBS and LIF. As ionization begins, self-focusing continues so long as $n_2 I > \frac{4\pi e^2 N_e}{2m_e\omega_0^2}$. However, the electron density increases rapidly since tunneling ionization is a highly nonlinear process which can be approximated from experimental observations by a power law $N_e \propto I^m$ [38, 229]. When self-focusing balances the negative plasma-induced index change

$$n_2 I = \frac{4\pi e^2}{2m_e\omega_0^2}\zeta I^m, \tag{4.17}$$

the peak intensity reaches a maximum, because the beam starts to diverge after the plasma index change overcomes the self-focusing term. This clamped intensity has been measured for free-propagating filaments in air at atmospheric pressure with a typical pulse of duration ~100 fs from a Ti:sapphire system (~800 nm) to be on order of 10^{13}–10^{14} W.cm^{-2} [38, 232].

4.1.7 Filament core and reservoir structures

A classical model of filamentation includes the concept of a peripheral energy reservoir, an intensity pedestal, which propagates alongside the intense (central) core region. The core region is vaguely defined by the radius in which ionization of the

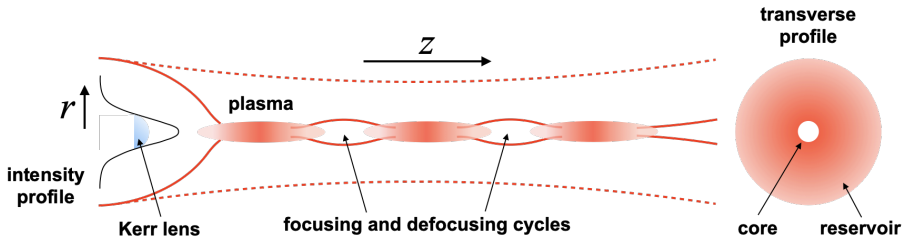

Figure 4.2: Filamentation of high-peak-power lasers in gases begins with self-focusing enabled by the optical Kerr effect which leads to the formation of a positive Kerr lens due to the transverse intensity profile of the incident Gaussian beam. Eventually, plasma formation mechanisms arrest the collapse of the beam and cause subsequent de-focusing because of the free electron distribution. Filamentation ensues wherein self-focusing and de-focusing cyclically compete to sustain a high intensity along an extended propagation distance, significantly exceeding the Rayleigh length. The transverse profile of the filament shows a central, intense core region which sits upon and propagates alongside an intensity pedestal referred to as the energy reservoir. Adapted from Ref. [98].

propagation medium tends to occur. Figure 4.2 shows a diagram of the filament structure depicting initial self-focusing followed by ionization and several self-focusing, defocusing cycles, as well as a transverse profile labeling the core and reservoir regions. The peripheral reservoir has been observed to support the replenishing of the energy lost from the core due to ionization [146, 147]. Further, the reservoir was observed to revive the core following collision with water droplets [45, 113]. The reservoir was found to be of importance for applications involving ablation/breakdown, such as LIBS, because external focusing of the filament dictates the contribution of the intensity pedestal toward ablation and eventually signal formation [102]. The recent concept of spatiotemporal optical vortices provides a more accurate model which describes the energy flow between the core and peripheral regions of the filament. A shear-like boundary forms in the spatiotemporal phase front of the propagating beam between the intense core region and the weaker periphery, generating toroidal vortices of opposite topological charge. Simulation results suggest these vortices govern energy flow in the propagating beam [116].

4.1.8 Spectral broadening and self-steepening in filaments

The high peak-intensities as well as the ultrashort pulse durations typically associated with the filamentation phenomenon drive significant spectral broadening and associated self-steepening. SPM in the filament is manifested by the self-generated extra phase $\Delta\omega = -kz\frac{d}{dt}(\Delta n(t))$ for a pulse propagating along z. The front of the pulse (rising edge with positive slope $I_+(t)$, $\frac{dI_+(t)}{dt} > 0$) sees a neutral medium, and ignoring the plasma contribution yields $\Delta\omega = -kzn_2\frac{dI_+(t)}{dt} < 0$, resulting in primarily red (Stokes) shift and broadening. The back, falling edge of the pulse $I_-(t)$ ($\frac{dI_-(t)}{dt} < 0$) sees a partially ionized medium which results in predominant blue shift and broadening due to low ionization fraction $\Delta\omega = -kzn_2\frac{dI_-(t)}{dt} > 0$. Eventually, the contribution of the plasma-induced index change similarly causes a blue shift $\Delta\omega = \frac{2\pi ze^2}{cm_e\omega_0}\frac{dN_e(t)}{dt} > 0$ [38, 78].

The continuous spatiotemporal self-transformation of the pulse also gives rise to self-steepening. The laser pulse propagates with a phase velocity $v_p = c/n$, where from Eq. (4.16) $n = n_0 + (\Delta n)_{\text{Kerr}} - |(\Delta n)_e|$. The front, rising edge of the pulse sees a greater index $n_+ = n_0 + (\Delta n)_{\text{Kerr},+} = n_0 + n_2 I_+(t)$ than the central, most-intense of the pulse, which experiences at the clamped intensity point $n_c \approx n_0$ because $(\Delta n)_{\text{Kerr}} = |(\Delta n)_e|$. The back, falling edge sees a weak plasma and experiences the smallest index $n_- = n_0 + (\Delta n)_{\text{Kerr},-} - |(\Delta n)_e|$. Hence, self-steepening describes stretching of the rising edge and compression of the falling edge of the pulse because $n_- < n_c < n_+$. Net pulse compression has been observed from the total contributions of spectral broadening and self-steepening mechanisms [226].

4.1.9 Conical emission

SPM taking into consideration the real curvature of the laser wave front during self-focusing gives rise to radially-redistributed frequencies referred to as conical emission. The wave vector $\mathbf{k}$ may be broken into axial $k_z\hat{z}$ and transverse $k_r\hat{r}$

components, and the total wave vector includes the contributions of SPM, $\Delta k_{z,r} = \int_0^{\zeta,\rho} \int_0^{\tau} \frac{\Delta\omega}{z,r} dtd(z,r)$. Further, we can similarly separate the neutral (Kerr) contribution $\Delta k_z^+ = -\frac{\omega_0 n_2}{c} \int_0^{\zeta} \int_0^{\tau} \frac{d}{dt} I_+(t) dtd(z,r) < 0$ and the plasma contribution $\Delta k_{z,r}^- = \frac{2\pi e^2}{cm_e\omega_0} \int_0^{\zeta,\rho} \int_0^{\tau} \frac{d}{dt} N_e(z,r,t) dtd(z,r) > 0$. The free electron distribution in the transverse direction results in radial divergence of the radiation, whereas the Kerr contribution acts predominantly along the axial direction [38].

4.1.10 Multiple filamentation

Multiple filamentation becomes prominent for high incident laser peak powers ($\gtrsim 10P_{cr}$) [17] in which modulational instabilities nucleate several intense cores. For real beams which do not have a smooth spatial profile, microscopic distortions which lead to breakup into several filaments have a critical size of $\Lambda_{\mathrm{cr}} = \sqrt{4P_{\mathrm{cr}}/\pi I_0}$ [228]. These distortions can arise from traversing an optical system, seeded by inhomogenities in the beam profile or propagation medium, or can also be influenced by external perturbations such as air turbulence [263]. Consequently, natural multiple filamentation is rather sporadic [17], but can be seeded, for example, with phase manipulation techniques using deformable optics [63]. The peak power for a single filament core in multiple filamentation is approximately $P_{\mathrm{fil}} \approx \frac{\pi^2}{4} P_{\mathrm{cr}}$ [260]. The cores compete for the energy from the reservoir, and each core radiates conical waves which interfere with those from other cores and the reservoir [38].

One of the most attractive features for remote sensing applications of filamentation is the possibility of long distance propagation in air. A major challenge for this feature is multiple filamentation; available laser technology limits propagation to relatively short distances on the order of several hundred meters, not because of the peak power, but because of the beam quality [38]. Poor beam quality causes nucleation of multiple competing filament cores, making it difficult to sustain high intensities at long distances. A contribution presented in this dissertation is the experimental

investigation of propagation and interaction of multiple filaments with a solid target.

4.2 Remote delivery of laser excitation source using filamentation for analytical spectroscopy applications

Filamentation has been combined with various analytical spectroscopy techniques [25, 48, 49, 84, 102, 103, 110, 119, 126, 148, 196, 209, 210, 225, 233, 256, 257] and sensing methods [48, 56, 123, 145, 259] in order to extend the excitation distance. This dissertation focuses on FIBS with solid targets which may be applied to direct detection of exposed uranium. Earlier works established the potential of long-range FIBS with various low-Z metal targets (Al, Cu, steel) from standoff distances of approx. 90 m [196, 225]. Since, several studies explored various experimental parameters which could influence signal formation, for example controllable filament laser parameters including wavelength [233], temporal phase [196, 262], spatial phase [48, 63], external focusing conditions [102, 110, 233], and external parameters such as the ambient environment in which ablation occurs [102, 126, 257]. FIBS has been found to be useful in various applications including detection of pollutants and aerosols in the atmosphere [49], biological materials [256], explosive material [209, 210], and even more unconventional areas such as cultural heritage monitoring [233] and agricultural monitoring [75]. FIBS detection limits can reach ppm concentrations; for example, Daigle *et al.* [49] predict detection limits for Na-containing aerosols to be ∼3 ppm at a 5-m distance or 33 ppm at 50 m.

The emission signal produced following filament ablation of solids depends critically on the laser intensity. The ablation threshold for most metals, $\mathcal{O}$(10-100 mJ.cm^{-2}) [106, 172], is comparatively low for dielectric or ceramic targets. Generally, both short- and ultrashort pulsed beams easily exceed these thresholds via focusing. A major advantage of filamentation is that high intensities, on the order of the clamped

intensity (10^{13} [43, 149] to 10^{14} W.cm^{-2} [144, 163, 227]), can be sustained in the core region(s) along several Rayleigh lengths in contrast to focused short- or ultrashort pulses. A major consideration for filament ablation, however, is the contribution of the intensity pedestal, the energy reservoir, toward ablation. External focusing increases the intensity of the reservoir locally [130]; therefore, target placement with respect to the external focusing lens may dramatically influence ablation and consequent signal formation [102]. Comparison between externally-focused and free-propagating filament ablation suggests less target material removal [237] and lower thermodynamic parameters of produced plasma [102] which lead to weaker emission signal in the case of free propagation. However, the free-propagating scheme offers precise control and scalability to extended distance, because the optimal target placement zone is reduced to near the focal position of the external focusing optic in the other scheme. Filament placement has been demonstrated by control of the second-order dispersion (chirp) of the ultrashort laser pulse to compensate for the negative dispersion of air [194]. Further, for longer-scale applications, greater laser peak-powers are required considering attenuation from ionization, diffraction of the reservoir, and interaction with obstacles. In this regime, multiple filamentation becomes another concern because the competition between several filament cores may lead to more rapid attenuation along the path, but also during ablation, as each core may lead to an individual detonation site. The interactions of several LPPs and their shocks in close proximity may lead to complicated signal formation. The following chapters present experimental investigations of multiple filament ablation and the resultant FIBS signals.

4.3 Remote collection of optical signal

Besides remote excitation, collection of optical signal from large distance is an equally vital part of emission-based remote sensing using techniques like FIBS. This section introduces the typical components and considerations of a remote spectro-

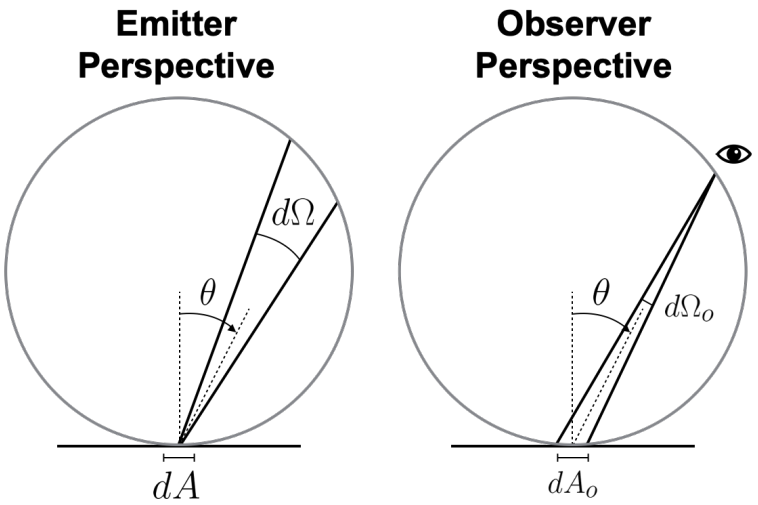

Figure 4.3: The Lambertian emitter strength decays with the cosine of the angle with respect to the normal $S'(\theta) = S_0 \cos(\theta) d\Omega dA$. From the perspective of the observer, the signal is $S'_{\text{obs}}(\theta) = \frac{S'(\theta)}{|\cos(\theta) d\Omega_o| dA_o}$.

scopic detection system. Starting with the signal source S_0, the angular dependence of the emission is considered. The simplest emitter is isotropic. The inverse square law describes how the isotropic source strength is distributed uniformly across the sphere with radius R which also denotes the distance of the observer from the point, $S' = \frac{S_0}{4\pi R^2}$. LPPs formed in gases can be considered nearly isotropic. Another simple emitter is one which follows Lambert's law, for example an LPP formed at the surface following ablation of a solid target. As shown in Fig. 4.3, the emission strength for a Lambertian source decays with the cosine of the angle θ with respect to the normal $S'(\theta) = S_0 \cos(\theta) d\Omega dA$. From the perspective of the observer, the signal is $S'_{\text{obs}}(\theta) = \frac{S'(\theta)}{|\cos(\theta) d\Omega_o| dA_o}$ where $d\Omega$ and dA are the solid angle and area elements subtended by the emitted (or observed, denoted by the subscript o) portion. Other sources may have steeper angular dependence; for example the emission from the filament plasma is cylindrically isotropic, and induced or stimulated emission sources may be even more directional.

In long-range measurements, atmospheric optical scattering and absorption may become significant. Aerosols, small water droplets, or atmospheric density perturba-

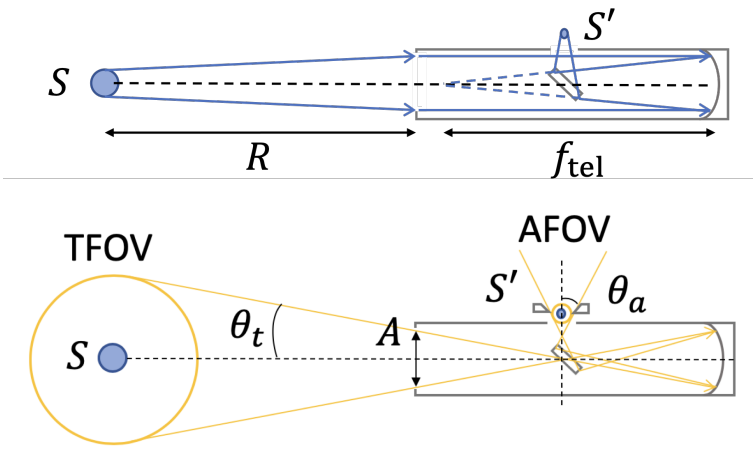

Figure 4.4: The Newtonian reflector telescope design is used to show important factors for designing a collection system including geometrical attenuation considerations like the inverse square law and solid angle, coupling considerations like the numerical aperture (or f-number, f_{tel}), and unwanted signal rejection described by the true (TFOV) and apparent fields-of-view (AFOV).

tions may contribute to optical scattering phenomena. Scattering is parameterized by the ratio of the particle size r to the wavelength $\Lambda_{\text{sc}} = \frac{2\pi r}{\lambda}$. Small particles $\Lambda_{\text{sc}} \ll 1$ cause Rayleigh scattering, while larger particle scattering $\Lambda_{\text{sc}} \gtrsim 1$ can be described by general Mie theory. The attenuation caused by scattering may be generalized by a single transmission efficiency term f_{sc}; this term depends on factors including observation distance and angle, particle size, density, refractive index, and the wavelength of the scattered radiation. Similarly, the atmospheric absorption is generalized by a single transmission efficiency term f_{abs}. Notable absorbing species in air include its major constituents, nitrogen and oxygen, as well as species with varying local concentrations like water vapor and carbon dioxide [88]. Macroscopic absorption is described by the Beer-Lambert law [Eq. (2.30)] and depends strongly on the wavelength-dependent cross-section, absorbing species density, and path length.

Next, the components of the collection system are considered. In most experiments described in this dissertation, a large lens or set of lenses (telescope) is used for collection of the source emission. For simple collection systems, like a lens or series

of lenses, the most significant factor for collection efficiency is the solid angle of the observation area with respect to the angular dependence of the source. For an arbitrarily oriented observation surface A looking at a point source at a distance R, the solid angle Ω can be determined by the surface integral

$$\Omega = \iint_{S_A} \frac{\hat{r} \cdot \hat{n} dS_A}{R^2}, \tag{4.18}$$

where $\hat{n}$ denotes the normal direction of the surface. This relation gives the inverse square law when the surface is the entire sphere. Collection of unwanted signals, such as backgrounds, is an additional consideration for designing the collection system. Figure 4.4 shows a Newtonian reflector telescope design to introduce the true and apparent field-of-view (FOV) concepts which can be used to describe background collection. The true FOV (TFOV) describes the range of accepted angles θ_t by the collection optic(s), described by the numerical aperture which sees the range of angles θ, NA $= n \sin(\theta)$ or f-number $f/_{\#} = \frac{f}{D} = \frac{1}{2\text{NA}}$ of the optic, where f is the effective FL of the collection optic with aperture size D. The TFOV angle of acceptance is given by

$$\theta_t = 2 \arctan\left(\frac{A}{f_{\text{tel}}}\right), \tag{4.19}$$

where A is the area of the collection optic ($A = \pi D^2$ for circular aperture), and f_{tel} is the f-number of the collection optic. The TFOV describes the entire field observed by the collection optic(s), including the background field which may include sources like solar radiation, room or street lights, etc. The user may choose an aperture like an iris or slit at the eyepiece of the telescope to limit the collection of background; the apparent FOV (AFOV) describes the limited range of angles θ_a accepted by the

eyepiece aperture described by the f-number f_{aper}:

$$\theta_a = \frac{A}{f_{\text{aper}}}. \tag{4.20}$$

A notable advantage of pulse-based spectroscopy discussed here is the added capability to discriminate between the rapidly-varying time signatures of the typical source terms (LPPs) from slow-varying or steady-state backgrounds via temporal gating.

The collection optic(s) are coupled with the detector system, which in most experiments described in this dissertation is comprised of a Czerny-Turner spectrograph and (intensified) CCD. In some cases, an optical fiber is used to transmit light from the collection optic(s) to the detector system. The coupling efficiency is described by the ratio of numerical apertures from the first component denoted by subscript 1 to the coupled component denoted 2:

$$\frac{S'}{S} = \left(\frac{\text{NA}_1}{\text{NA}_2}\right)^2. \tag{4.21}$$

General considerations for the effectiveness of the collection system are described in more detail in Chapter 2, Sections 2.1.4.2 and 2.1.4.3. Briefly, the net efficiency of the collection and detection apparatus considers inclusively the geometry of the collection optic(s) with respect to the source, atmospheric attenuation like scattering and absorption, TFOV and AFOV as well as subsequent coupling and transmission of the collection and detection subsystems.

4.3.1 Filament guiding mechanisms

Clearly, there is a large number of factors to consider for design of an efficient collection system for distant optical signals. In most circumstances relevant to this dissertation, the distance is the most significant contributor to signal losses. Filamentation poses an interesting solution to overcoming the inverse square law: the

transient structures associated with filamentation in gases have been demonstrated to be useful for guiding of optical beams [117, 137, 143, 197] and microwaves [34]. These guiding methods may be applied not only to collection of distant optical signal but also to the delivery of the excitation source.

The filament may be structured to form a waveguide analogous to an optical fiber, with a depressed outer clad index and elevated central core index to support total internal reflection (TIR). TIR is characterized by the critical angle θ_c which describes the range of angles which are reflected at an interface between the core n_{core} and clad n_{clad}:

$$\theta_c = \arcsin\left(\frac{n_{\text{clad}}}{n_{\text{core}}}\right). \tag{4.22}$$

The range of accepted angles for an optical fiber (or analogous structure) that satisfy the critical angle criterion is given by the numerical aperture NA_{fiber}:

$$\text{NA}_{\text{fiber}} = \frac{1}{n_0}\sqrt{n_{\text{core}}^2 - n_{\text{clad}}^2}, \tag{4.23}$$

where n_0 is the index of the propagation medium before the fiber. The V-number of the fiber describes the number of supported propagation modes given by

$$V = \frac{2\pi a}{\lambda}\text{NA}_{\text{fiber}}, \tag{4.24}$$

where a is the fiber core size. Single-mode guiding occurs below the cutoff $V \leq 2.405$.

Three temporal regimes of filament guiding have been investigated in the past: (1) ns-scale plasma guiding [8, 249], (2) ns–µs-scale acoustic guiding [117, 137, 143, 197], and (3) ms-scale thermal guiding [117, 197]. Plasma guiding has been demonstrated with an annular input beam pattern to form a cylindrical plasma. This structure exhibits a refractive index profile in which the central core has a greater

index, and the outer ring has a lower index due to the greater free electron density of the plasma. Several methods for achieving the annular structure include the use of a series of half-pellicles [116, 197], deformable optics [34], and Bessel beams [249]. However, these waveguides typically last only several nanoseconds due to the recombination time of the plasma. Acoustic guiding has been demonstrated using (near) Gaussian input beam profiles [137, 143, 197] with lifetimes on the order of several nanoseconds [143] to several tens of microseconds [117, 137]. The shockwave which forms along with the plasma channel generates an annular refractive index profile required for guiding. Finally, thermal guiding occurs in the wake of the filament lasting several hundreds of microseconds enabled by the long thermal relaxation of the medium [117]. Thermal guiding relies on the elevated temperature in the gas left in the wake of the plasma, and, similar to the plasma guiding regime, requires and annular plasma structure and consequently initial beam shaping.

CHAPTER 5

Experimental Investigation of Propagation and Ablation in the Multiple Filament Regime

Multiple filamentation arises for incident laser peak powers greatly exceeding the critical power for self-focusing. The critical power for self-focusing in air [Eq. (4.12)] is ∼3 GW for the standard 800-nm beam from Ti:sapphire chirped-pulse amplification (CPA) laser systems. For remote sensing applications which require the extended delivery of the filament excitation source, this critical power is easily exceeded by an order of magnitude or more; for example, a 100 fs pulse from a typical Ti:sapphire-based CPA system, like the Lambda Cubed laser facility used most frequently in this dissertation, requires only 0.3 mJ to reach the critical power, while normal operation involves energies in the range 1–20 mJ. Further, commercially available CPA lasers routinely exceed even this energy range. Multiple filament cores are seeded by modulational instabilities in the beam profile which can arise from the beam traversing and optical system or external perturbations like air turbulence, water droplets, etc., and each core sustains a high intensity on the order of the clamped intensity. However, the competition of multiple filaments as discussed in Sec. 4.1.10 may be a hindrance to extended propagation; therefore, a better understanding of propagation in the multiple filament regime is essential for remote sensing applications. Moreover, existing literature lacks mature understanding of the filament-target interaction in

the multiple filament regime, for example filament ablation of metals in LIBS (also referred to as FIBS). Besides remote sensing, other filament application areas which may benefit from improved understanding of multiple filamentation include the use of filaments as transient conductive wires [195, 234], as radio-frequency antennae [21], for water condensation [252] and discharge guiding [251], and for air lasing [153, 188].

This chapter discusses recent experimental investigations of propagation in the multiple regime as well as multiple filament ablation of metals with direct implications for analytical methods like FIBS. In Sec. 5.1, invasive and non-invasive probing diagnostics are used to measure the properties of the multiple filament air plasma in the energy range in which the onset of multiple filamentation is observed. The work presented in this section fills gaps in current literature by conducting an experimental investigation of the spatial dependence of air plasma properties during multiple filamentation. The results shed light on the possible mechanisms that lead to spatial localization of excited and ionized species in the plasma, and demonstrate a transition region in the macroscopic conductivity of the plasma between single- and multiple-filament regimes. Section 5.2 similarly explores the transition between single- and multiple filament regimes during ablation of a metal target. In Sec. 5.2.1, a non-invasive probing method is used to determine the energy deposited in the target, and a novel approach to induce multiple filamentation with a split focusing optic is presented to investigate scaling of the detonation energy into the multiple filament regime. The indirect method described here overcomes challenges in direct measurement of the deposited energy because the high peak intensities observed during filamentation are prone to cause damage to the measurement device. The energy deposited in the target is a critical parameter to aid understanding of this interesting and complex ablation mode. Finally, Sec. 5.2.2 investigates filament ablation of metal with varying filament laser wavelength from the near-UV to the mid-IR spectral regions. The mid-IR spectral range around 2 µm laser wavelength is interesting because

another gap in the atmospheric transmission window exists in this region, and the longer wavelength that requires a greater critical power for self-focusing also results in a greater threshold for the onset of multiple filamentation. This chapter includes edited portions from Refs. [29, 30, 72, 218].

5.1 Characterization of the multiple filament plasma in air

5.1.1 Direct probing of the multiple filament plasma conductivity

In this section, a direct probing method is used to determine the conductivity of the filament air plasma during the transition between single- and multiple filamentation. The conductivity of the air plasma is related to its free electron distribution, and these measurements provide insights into the plasma formation mechanisms during multiple filamentation. In addition to improving fundamental understanding of the multiple filamentation regime, these results have implications for using filaments as transient, configurable conductive wires that are impervious to mechanical stresses and melting caused by Joule heating among other related applications [73, 122, 160, 182]. Previous works demonstrated that shorter laser wavelengths yield more conductive filament plasmas in the single filament regime [165, 206, 235], and other works investigated using a second beam [203, 205, 264], external bias [10, 50], or low-AC current [186] for improving conductivity. Here, multiple filamentation is found to enhance the conductive properties of the plasma structure in air, presenting an attractive domain through which greater current can be transmitted. This section includes edited portions from Ref. [30].

5.1.1.1 Experiment

Figure 5.1 shows a diagram of the equivalent circuit used to measure the filament conductive properties as well as a photograph of the filament plasma traversing two

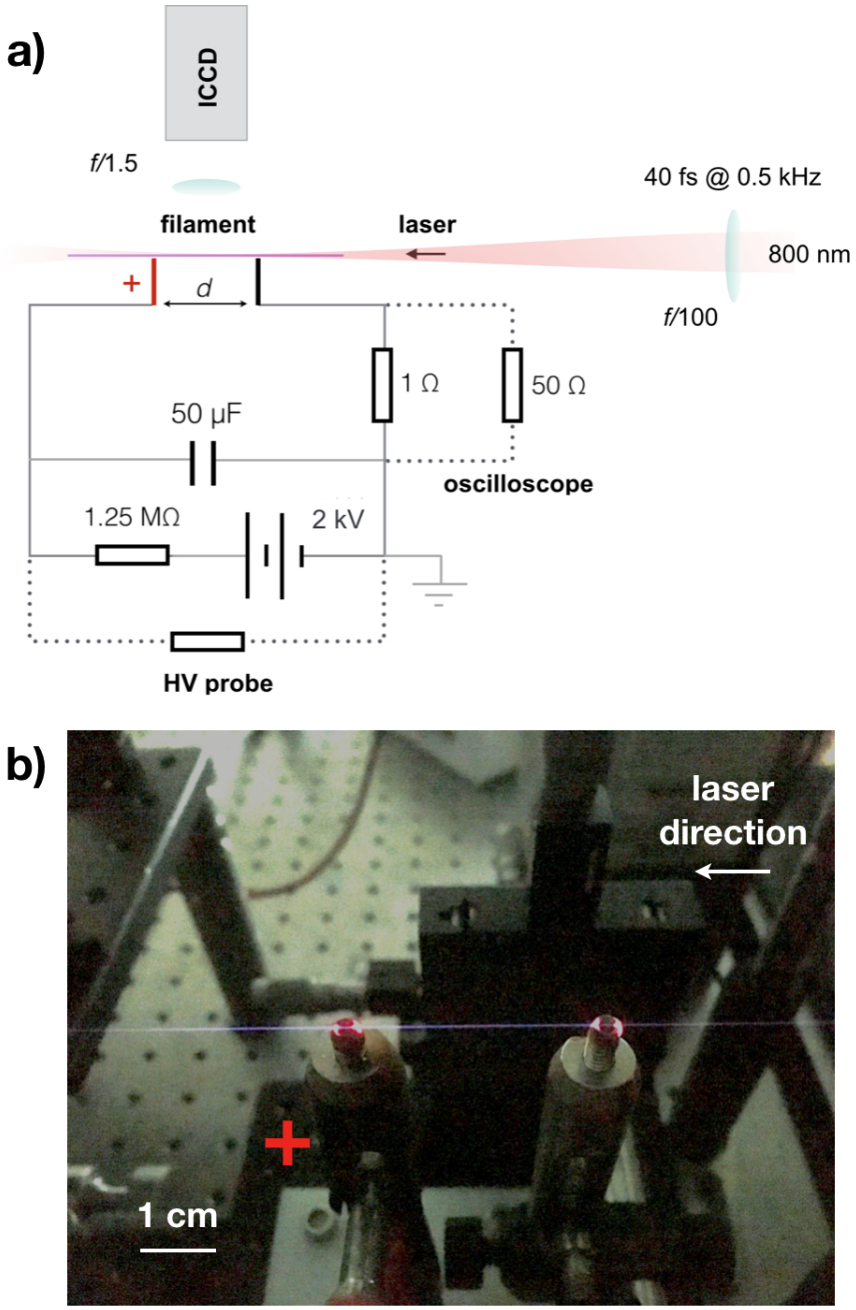

Figure 5.1: (a) Circuit diagram for the experiments measuring DC conductive properties of the filament air plasma between single- and multiple filament regimes; (b) photograph of the filament plasma propagating over two electrodes. The arrow depicts the incident laser direction, and the red plus symbol denotes the positive electrode in the photograph [30].

electrodes. The Lambda Cubed CPA laser system (central wavelength 800 nm, pulse duration 40 fs, and repetition rate 480 Hz) at the University of Michigan Gèrard Morou Center for Ultrafast Optical Science was used for these (and subsequent) filament experiments. A lens with 1-m FL ($f/100$) was used to form the filament in air. DC electrical current was guided through the filament plasma using two stainless steel electrodes with adjustable distance between 30 and 40 mm. The filament was used to ablate the electrodes, so that it could propagate unperturbed across the electrode gap. The current was maintained below the spark discharge threshold of air $\lesssim$0.6 kV/cm and varied using a high-voltage source and 50 µF capacitor which discharged current through the filament using a load resistor. An oscilloscope (LeCroy, Waverunner 604Zi, 400 MHz) was used to measure signal averaged over 1000 laser shots.

5.1.1.2 Results & Discussion

Example current waveforms for different laser energies spanning the transition region between single- and multiple-filamentation are shown for different electrode separation distances in Fig. 5.2. The current profiles shown here represent the average profile from 1000 laser shots; shot-to-shot fluctuation was found to be approx. 7%. These current profiles exemplify the transient nature of the filament plasma; collisional processes and electronic recombination occur on timescales on order of several nanoseconds in such plasmas [205]. Figure 5.3 shows the results from further analysis of the current profiles shown in Fig. 5.2. The transmitted charge as given in Fig. 5.3(a) is determined by integrating the area under the first (positive) half-wave of the current profile during the first 10 ns of the filament. The conductivity of the filament plasma is determined from the plasma resistivity given by

$$\rho_f = \frac{\pi r^2}{L} R_f, \tag{5.1}$$

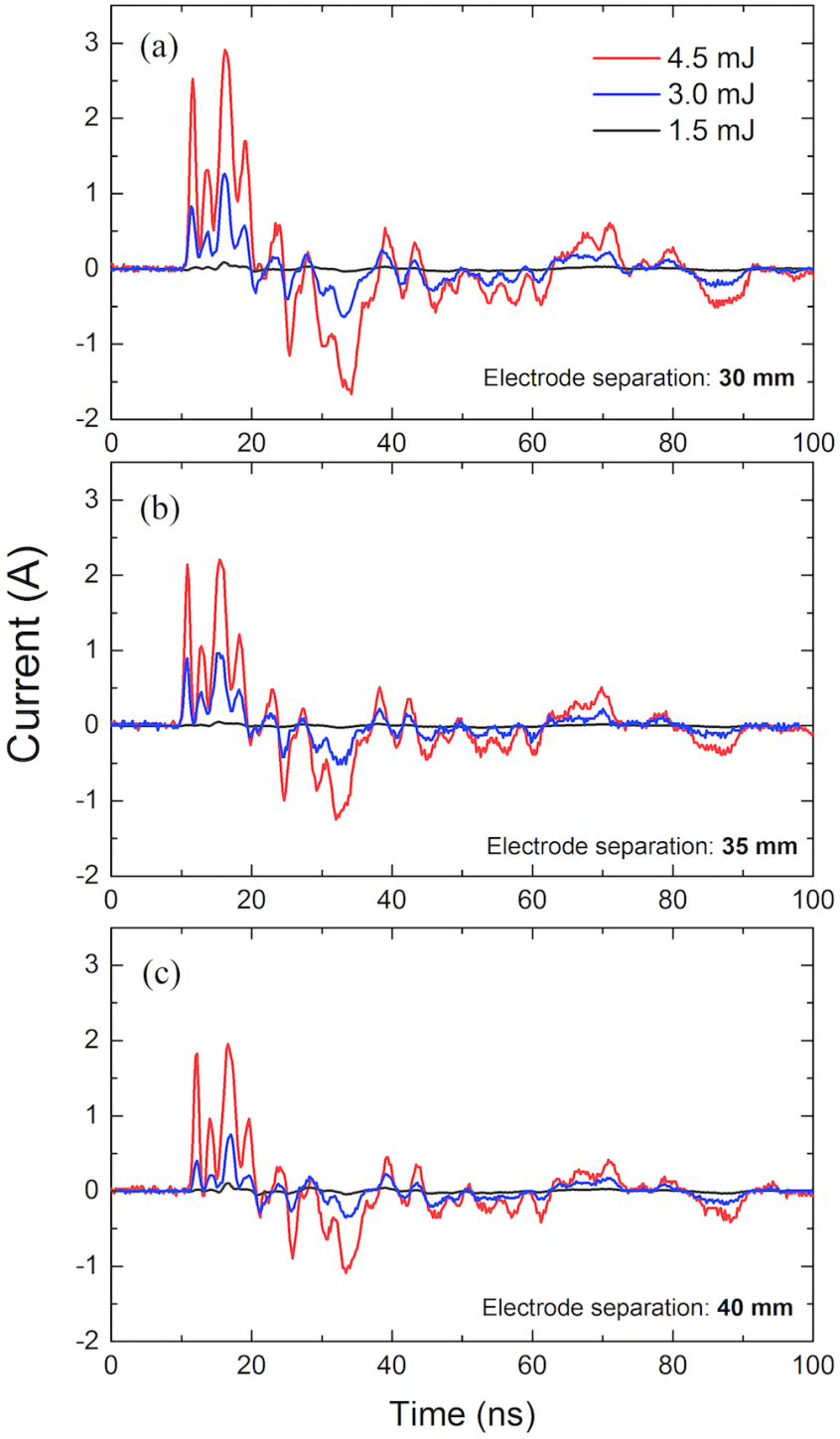

Figure 5.2: Current waveforms are recorded through the filament plasma varying the laser energy from the single- to multiple filament regimes with different electrode separation distances of (a) 40-mm, (b) 35-mm, and (c) 30-mm. A 2-kV bias voltage was used for all measurements [30].

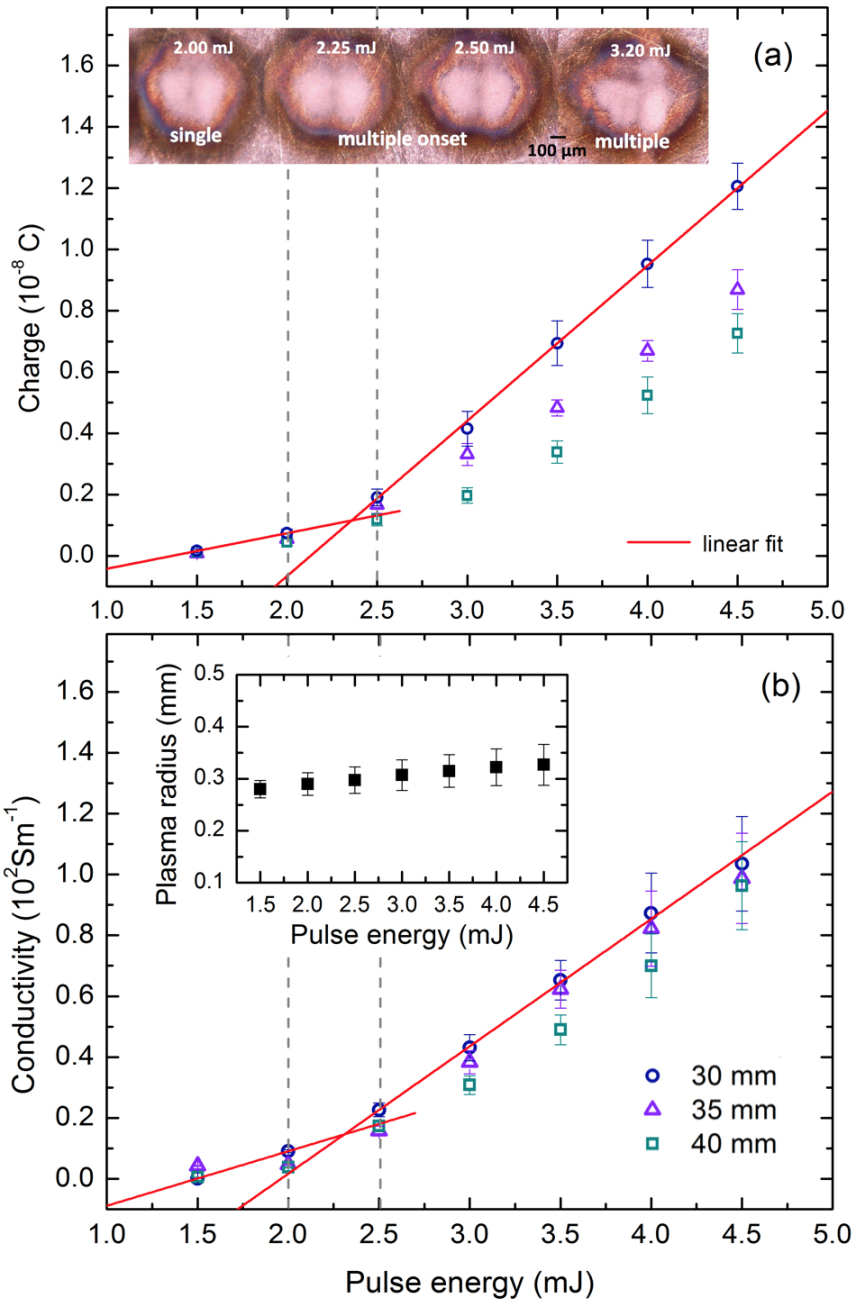

Figure 5.3: (a) Integrated charge transmitted during the first 10 ns, and (b) peak electrical conductivity of the filament plasma. The range of laser energies describes the transition region between single- and multiple filamentation as shown by the inset in (a). The conductivity depends on the area of the conductive element, so the inset in (b) shows the plasma radius measured by observing the optical emission using a 1:1 imaging scheme with an ICCD for the relevant range of pulse energies. Dashed lines indicate the single- to multiple-filament transition energies. The red line is a linear fit to the data points demonstrating a deviation in the trend between regimes [30].

where r and L are the conductor radius and length, respectively; and R_f is the filament resistance. The resistance is estimated by using Ohm's law $R_f = V/I_m$ assuming cylindrical symmetry in the plasma, where V is the applied bias and I_m is the measured current through the plasma, respectively. The filament conductivity is then determined by $\sigma_f = 1/\rho_f$.

Both quantities, charge and conductivity, exhibit linear behavior with incident laser energy in both single- and multiple-filament regimes, where the transition occurs in the energy range between ∼2 and 2.5 mJ. The inset in Fig. 5.3(a) shows evidence of the transition from single- to multiple-filamentation; several damage spots appear on the surface of the copper target following filament ablation for greater pulse energies. Notably, the multiple filament regime for pulse energies beyond ∼2.5 mJ demonstrates an increased rate of change over the single filament regime for both quantities. The change in the slope of the transmitted charge between single- and multiple filament regimes, quantified by the slope ratio ∼29.9, is substantially larger than that of the conductivity, slope ratio ∼2.3.

The charge Q depends on the conductance G of the filament $Q = VtG$, where V is the bias voltage, and t represents the time through which the charge traverses the plasma; and the conductance depends on the free electron density N_e, electron-neutral collision rate ν_{en}, and plasma dimensions r and L, given by $G = \frac{e^2 N_e \pi r^2}{m_e \nu_{en} L}$. The electron-neutral collision rate for a Boltzmann energy distribution characterized by the electron temperature T_e is $\nu_{en} = \sigma_{en} N \sqrt{\frac{8 k_B T_e}{\pi m_e}}$, where σ_{en} is the collision cross-section and N is the neutral particle density. Therefore, the transmitted charge varies strongly with free electron density and plasma geometry and weakly with electron temperature. The conductivity, on the other hand, is independent on geometry as an inherent property of the conducting medium. During multiple filamentation, the nucleation of several plasma cores results in a larger effective cross-sectional area of the macroscopic plasma channel as evidenced by the inset in Fig. 5.3(b). The ra-

dius, here, is measured by observing the emission from the plasma; it must be noted that the plasma size measured in this way may not be representative of the size of the plasma, because only excited state populations are studied, nor the radial intensity profile of the beam. The plasma radial dimension and free electron density is expected to vary more slowly than the plasma length and total number of free electrons. The changing geometry of the filament plasma during multiple filamentation causes the larger change in slope of the charge with increasing pulse energy in contrast to that for the conductivity. Additionally, the free electron density and electronic temperature of the plasma may contribute to the transmitted charge; the scaling of these plasma properties in the multiple filament regime is investigated experimentally in the following section (Sec. 5.1.2). The conductivity is believed to increase during multiple filamentation because of the formation of additional conductive channels. These results suggest that multiple filamentation could be an attractive means to transmit current in air, and the geometric dependence of conductance offers a new parameter space for improving charge transfer through filament plasma structures via control of multiple filament arrangement, for example using adaptive optics [63].

5.1.2 Non-invasive optical emission spectroscopy of the multiple filament plasma

The work presented in this section uses non-invasive diagnostics based on the optical emission from the multiple filament plasma in order to determine the spatial dependence of plasma properties along the propagation axis. Understanding the spatiotemporal plasma characteristics in the multiple filament regime is vital for practical applications like remote sensing, and experimental determination of such properties like free electron distribution and temperature in this regime is lacking in current literature, unlike the single filament regime [18, 35, 64, 107, 148, 180, 233]. Moreover, such experimental studies as that presented here, may benefit computational

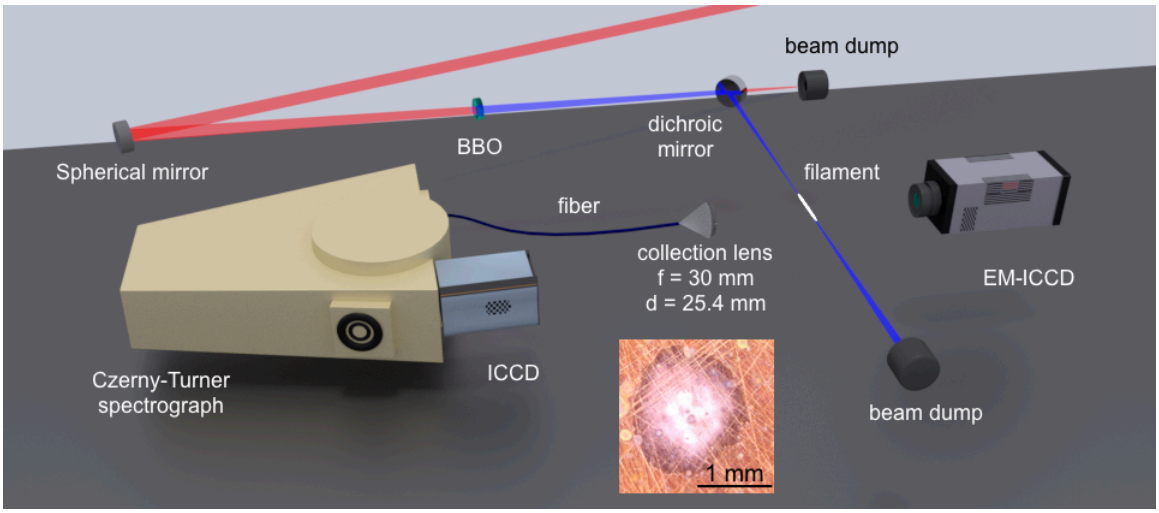

Figure 5.4: A 0.55-m Czerny-Turner spectrograph is used in conjunction with an ICCD to measure the optical emission from the air plasma formed during multiple filamentation. Multiple filamentation is investigated for laser wavelengths of 400 nm and 800 nm. A 100-µm-thick BBO crystal is used to create 400-nm pulses from the fundamental 800 nm wavelength from a Ti:sapphire CPA laser system, and the residual 800-nm light is rejected using a high-pass dichroic mirror. The OES collection system is translated along the filament propagation axis to determine the axially-dependent plasma properties. The inset shows evidence of damage from multiple filament cores following single-shot 400-nm filament ablation of a copper sample (placed at the geometric focus of the spherical focusing mirror, with 1-m focal length) [72].

modeling of the complex physical processes that occur during filamentation, like those relevant to ionization and excitation of the medium and filament propagation through the ionized medium. This section includes edited portions from Ref. [72].

5.1.2.1 Experiment

Figure 5.4 shows the scheme for OES of the air plasma formed during multiple filamentation. Both the fundamental 800-nm and second-harmonic 400-nm wavelengths from a Ti:sapphire CPA laser system (Lambda Cubed facility) were investigated. SHG involves the use of a 100-µm-thick β-$Ba(BO_2)_2$ (BBO) crystal to generate the 400-nm light, and residual 800-nm light is rejected using a high-pass dichroic mirror. The 800-nm pulse duration is measured using frequency-resolved optical gating (FROG) to be 50 fs, and calculated for the 400-nm beam [223] to be 41 fs.

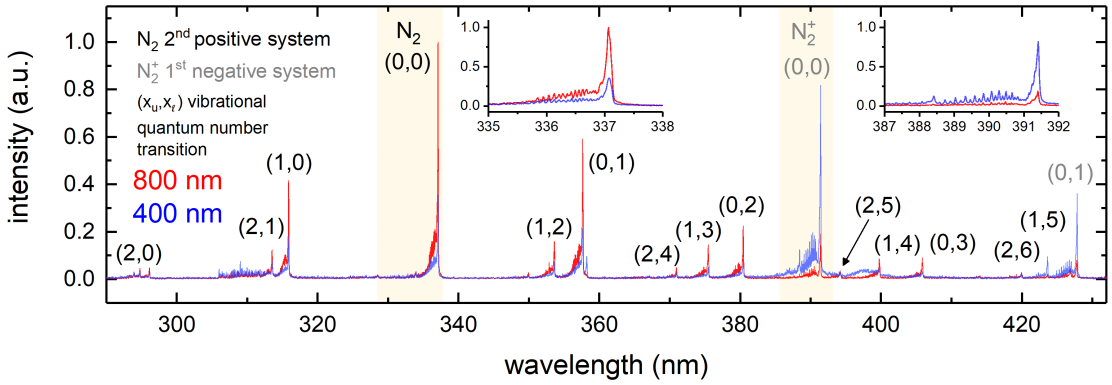

Figure 5.5: Experimental spectra showing the N_2 second positive system and the N_2^+ first negative system are compared for air plasmas formed using 400- and 800-nm filament laser wavelengths in the multiple filament regime. The recording parameters included ICCD gate delay of 0 ns and gate width of 10 ns, respectively. The position 0 mm denotes geometric focus of the spherical mirror, and negative positions mark the region before focus, and positive after focus [72].

Both beams are focused to form filaments using a 1-m FL spherical mirror ($f/40$). OES involves the use of an ICCD (Andor, iStar 334T) coupled to a 0.55-m Czerny-Turner spectrograph (Horiba Jobin Yvon, iHR550) with linewidth resolution of 40 pm at 632.8 nm (calibrated using a He-Ne laser source). The collection apparatus (1"-diam., 30-mm FL lens coupled to 400-µm optical fiber) is translated along the filament propagation axis (referred to as the *axial* dimension). Peak powers in the range of 20–80$\times P_{cr}$ ($P_{cr} \approx 3$ GW) for the 800-nm wavelength are compared to 140$\times P_{cr}$ for the 400-nm wavelength ($P_{cr} \approx 0.5$ GW).

5.1.2.2 Results & Discussion

The emission spectrum from the filament air plasma is dominated by the N_2 second positive system ($C^3\Pi_u \rightarrow B^3\Pi_g$) and the N_2^+ first negative system ($B^2\Sigma_u^+ \rightarrow X^2\Sigma_g^+$) as shown by Fig. 5.5. N_2 is excited indirectly following electronic recombination of N_4^+ species [255], while MPI and tunneling ionization mechanisms directly contribute to formation of N_2^+ species. The increased contribution of MPI for the shorter wavelength

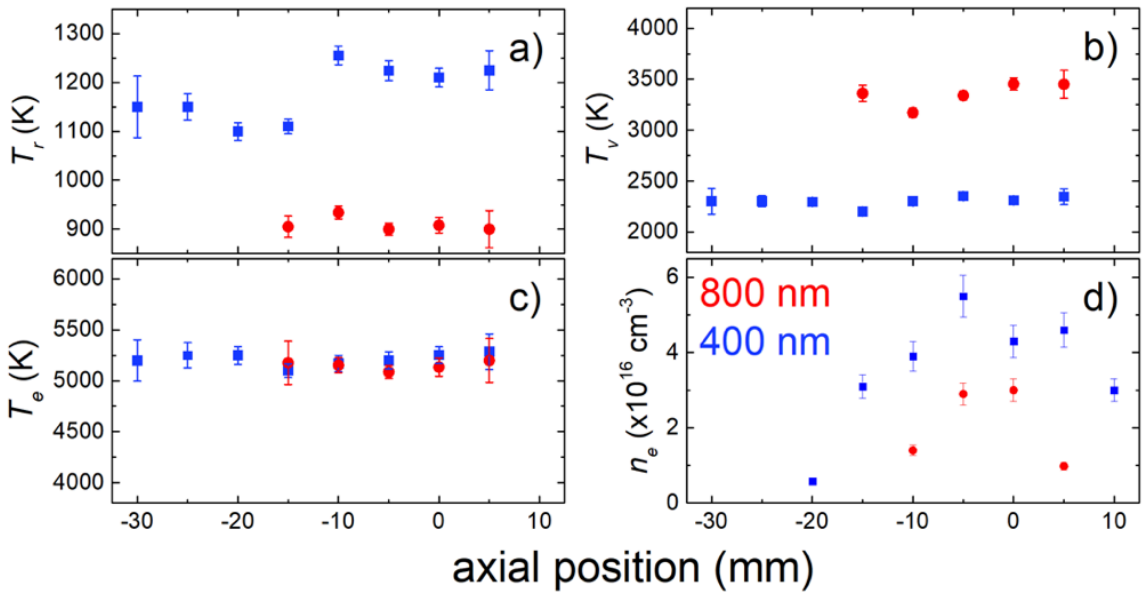

Figure 5.6: Measured multiple filament air (a–c) plasma temperatures and (d) free electron densities are determined for 400- and 800-nm laser wavelengths along the propagation axis. The properties are compared for 3 mJ laser energies for both wavelengths [72].

as shown in Fig. 2.1 (refer to Sec. 2.1.1) results in greater absolute emission strength of the 391-nm (0,0) band of the N_2^+ first negative system for 400-nm compared to 800-nm; whereas, the 337-nm (0,0) band of the N_2 second positive system is the most prominent feature in spectrum from 800-nm. The optical emission is further used to evaluate plasma properties including rovibrational molecular temperatures, and electron temperature and density. This analysis and example data and fits are presented in more detail in Appendix C. The results from this analysis are summarized in Fig. 5.6 and Table 5.1.

The temperatures are found to vary weakly along the propagation axis, while the free electron density is found to have a steeper axial variation, as shown in Fig. 5.6. The discrepant rotational, vibrational, and electronic temperatures imply a departure from LTE; however, the lower limit of electron density of 6.4×10^{14} cm^{-3} imposed by the McWhirter criterion [Eq. (2.19)] is satisfied in all measured positions, suggesting a PLTE condition may still exist. Further work is necessary to verify the local

Table 5.1: The intensity ratios ($I_{N_2}/I_{N_2^+}$), peak intensities (I_{peak}), peak electronic temperatures (T_e, K), and peak free electron densities (N_e, cm^{-3}) are compared for different 800-nm laser energies and an energy of 3 mJ for the 400-nm case [72].

$E_{800\ nm}$ (mJ)	$I_{N_2}/I_{N_2^+}$	I_{peak} (counts)	T_e (K)	N_e (cm^{-3})
3	5.5	9.9×10^5	5180±120	1.2×10^{16}
6	5.4	2.2×10^6	5160±100	2.2×10^{16}
9	5.2	3.3×10^6	5230±110	2.2×10^{16}
12	4.9	4.1×10^6	5290±120	2.7×10^{16}
$E_{400\ nm}$ (mJ)	$I_{N_2}/I_{N_2^+}$	I_{peak} (counts)	T_e (K)	N_e (cm^{-3})
3	0.5	9.6×10^5	5100±70	3.9×10^{16}

equilibrium conditions in the transient and inhomogeneous filament plasma. The temperatures reported here for the multiple filament air plasma are in a similar range to those previously reported for single filament plasmas [18, 110, 148]. The 400-nm wavelength forms a longer plasma region where the emission is measureable, and exhibits greater rotational temperature and electron density and lower vibrational temperature than the 800-nm filament. These differences between 400- and 800-nm are consistent with the expectation that MPI and tunneling ionization compete to ionize the propagation medium between the two wavelengths, but also imply there competing excitation mechanisms also follow. For example, the lower vibrational temperature for the 400-nm plasma implies higher-lying vibrational transitions like those leading to the emission of the N_2 (2,5) band are less probable. These differences between 400- and 800-nm cases are reiterated in Table 5.1 by comparing the intensity ratios for the (0,0) bands for N_2 and N_2^+ and the electron densities. The weak spatial variation of the temperatures in contrast to the electron density is consistent with previous studies of single filament plasmas [148]. The free electron distribution implies that plasma collisional processes may contribute significantly to dissociation and ionization of molecular oxygen species (O_2 and O_2^+) to form O I species, because photo-dissociation of molecular oxygen is much more likely for laser wavelengths below 400 nm [66], and electronic plasma temperatures of ∼5000 K allow dissociation via oxygen-oxygen and electron-oxygen collisions, with the dissociation energy for O_2

being 5.1 eV.

The peak electronic temperature and peak free electron density increases slowly with increasing laser energy as shown in Table 5.1. The slow increase in temperature with more rapidly increasing peak intensity, also given in Table 5.1, may indicate the formation of additional plasma cores, each with a similar temperature but an greater absolute number of emitters. This observation is consistent with the increasing effective plasma size as seen in the inset of Fig. 5.3(b) in Sec. 5.1.1.2. Furthermore, the slowly increasing temperatures agree with the concept of the clamped intensity. The clamped intensity depends weakly on the free electron density, and the free electron density may be approximated by a power-law dependence with the incident intensity and, consequently, energy according to Eq. (4.17). The increasing ionization fraction for increasing laser energy is consistent with the trend of electron density and can be explained by the increasing contribution of MPI of N_2 for larger laser intensities.

The results presented in this section add to the limited existing literature on experimentally measured air plasma properties in the multiple filament regime. Fundamental understanding of multiple filament propagation is crucial toward remote sensing applications, where large laser peak powers are required to reach long distance propagation. The measured plasma properties reported here can also aid computational modeling capabilities for this regime of propagation.

5.2 Ablation of metals in the multiple filament regime

5.2.1 Determination of multiple filament detonation energy

Filament ablation is relevant to analytical spectroscopy techniques like FIBS (discussed in more detail in the following chapter, Chapter 6), and existing literature lacks mature understanding of the filament-target interaction in the multiple filament regime. Several prior studies investigated ultrashort- and filament ablation un-

der various external focusing conditions by studying the target plasma [102, 237, 256], and another work used *ex-situ* methods to study filament-target interactions by measurement of ablation craters [247]. Here, a non-invasive pump-probe shadowgraphy scheme and OES are used to study ablation during the transition between single- and multiple filamentation. Further, the Sedov blast model [Eq. (2.14)] is used to estimate energy deposited in the target; and a novel approach is presented in which a split lens is used to seed reproducible multiple filamentation to investigate deposited energy scaling into this regime. An interesting combination of fast and slow mechanisms unique to filament ablation is revealed and discussed. Ultimately, the results indicate favorable scaling of the deposited laser energy despite multiple filamentation, which bodes well for remote sensing. This section contains edited portions from Ref. [218].

5.2.1.1 Experiment

The pump-probe shadowgraphy scheme and interchangeable imaging setup is shown in Fig. 5.7. The Lambda Cubed CPA system (center wavelength 790 nm, pulse duration 40 fs, repetition rate 80 Hz) is used to form filaments and ablate a copper metal sample. The beam is externally focused using a 1-m FL lens ($f/100$). All experiments are conducted in air. The sample was periodically polished and translated to prevent excessive drilling which would affect the filament-target interaction. For both shadowgraphy and imaging diagnostics, a 7.5-cm-FL achromatic lens was used with a 1:1 object-image magnification. A flippable mirror was used to change between each diagnostic. The probe beam for shadowgraphy was an Nd:YAG (10 mJ, 10 ns pulse duration, 10 Hz repetition rate) synchronized to the filament and incident on a CMOS camera (Mightex, CGE-B013-U, 3.75 µm square pixel dimension). A 532-nm laserline filter was used to reject plasma emission. Imaging of the plasma emission used an ICCD (Andor, iStar 334T, 13 µm square pixel dimension), and narrow bandpass filters were used to isolate the emission from different plasma species.

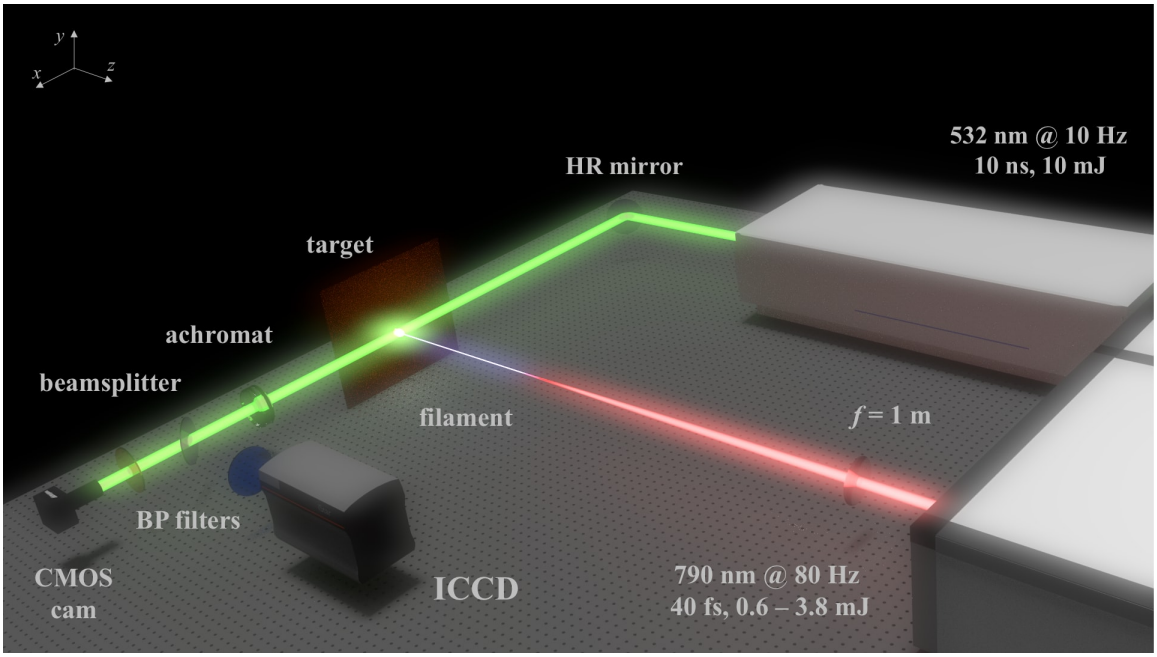

Figure 5.7: The filament/ablation laser (center wavelength 790 nm, pulse duration 40 fs, repetition rate 80 Hz) is focused using a 1-m-FL lens to form a filament. The filament ablates a copper target placed at geometric focus of the lens. The pump-probe shadowgraphy scheme for imaging the filament-target interaction uses an Nd:YAG (532 nm, 10 ns, 10 Hz) probe laser and a CMOS camera. A flippable mirror allows for interchangeable imaging of the emission from the plasma formed at the target using an ICCD. The emission from different species is imaged using narrow bandpass (BP) filters [218].

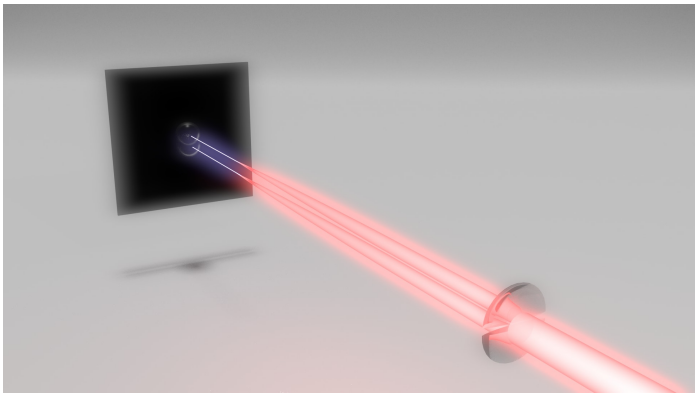

Figure 5.8: The beam is focused using a split lens to reproducibly form two filament cores, each yielding its own detonation site during target ablation [218].

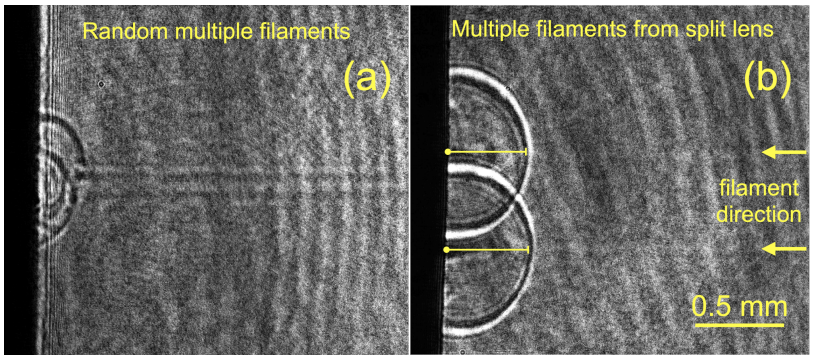

Figure 5.9: (a) Example shadowgraph showing natural, sporadic multiple filament ablation of a copper target (pulse energy 3.1 mJ, gate delay 200 ns); (b) shadowgraph of the seeded, reproducible multiple filament detonation using the split lens approach (energy 3.1 mJ, delay 400 ns) [218].

The lines for selective species imaging of copper species were Cu I 521.82 nm and Cu II 490.97 nm. Each image was integrated for an ICCD gate width of 3 ns and averaged over 30 laser shots.

The Sedov blast model [Eq. (2.14)] was used assuming spherical symmetry and a point detonation in order to estimate the energy deposited in the target during filament ablation. The model was fit to the time-dependent shock dimension for a range of laser energies spanning the single- to multiple filament regimes, as shown by the inset of Fig. 5.3(b) and discussed in Sec. 5.1.1.2. In the multiple filament regime, the blast model was found to no longer accurately describe the expansion of the shocks, considering approx. 90% of the recorded data showed evidence of multiple detonation sites, each caused by individual filament cores. An example is shown in Fig. 5.9(a). Consequently, a split lens, as shown in Fig. 5.8, was used to reproducibly form two filament cores, each yielding its own, distinct detonation site during target ablation, shown in Fig. 5.9(b). In this scheme, the blast model was fit to the shock dimensions for each detonation site to determine deposited energy. The total deposited energy is the sum of the individual energies for each site. Notably, although laser energy is measured after the lens, the sharp boundary between the halves of the split lens causes diffraction that reduces the energy reaching the target

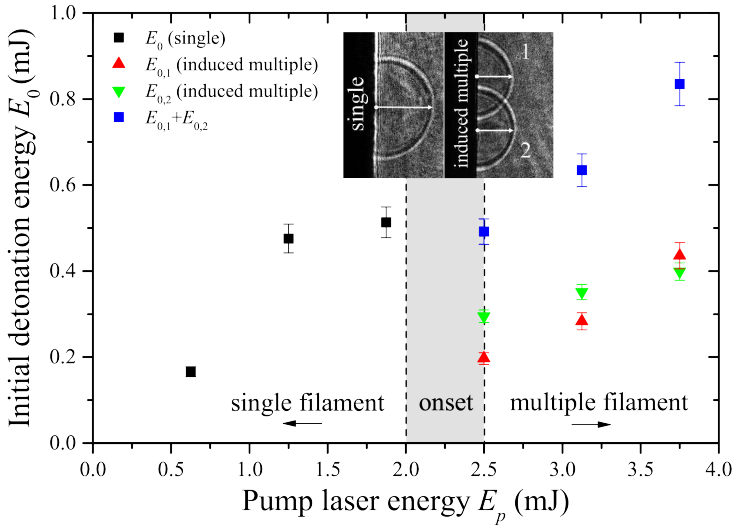

Figure 5.10: The detonation energy is determined using the spherical Sedov blast model, and the energies are shown comparing the single- and multiple filament regimes. The scaling into the multiple filament regime was determined using the split lens to form two reproducible filament cores and detonation sites, and the total energy deposited is the sum of the individual contributions from each site [218].

by a small fraction that cannot be fully accounted.

5.2.1.2 Results & Discussion

Figure 5.10 summarizes the results from pump-probe shadowgraphy used to measure the shock rate of expansion. Example shadowgraphs and blast model fits to the shock dimension are provide in Fig. D.1 and Fig. D.2 in Appendix D, respectively. For laser energies in the single filament regime, $\lesssim$1.9 mJ here, shot-to-shot fluctuations of the shock dimensions are found to be insignificant, and the blast model is used to determine the trend of the deposited energy with incident (pump) laser energy. For laser energies $\gtrsim$1.9 mJ, shadowgraphy provided evidence of multiple filamentation, because several detonation sites formed at the target surface, as shown in Fig. 5.9(a). The location of these sites varied significantly for different ablation laser shots. As discussed in Chapter 4, Sec. 4.1.10, multiple filamentation is caused by modulational

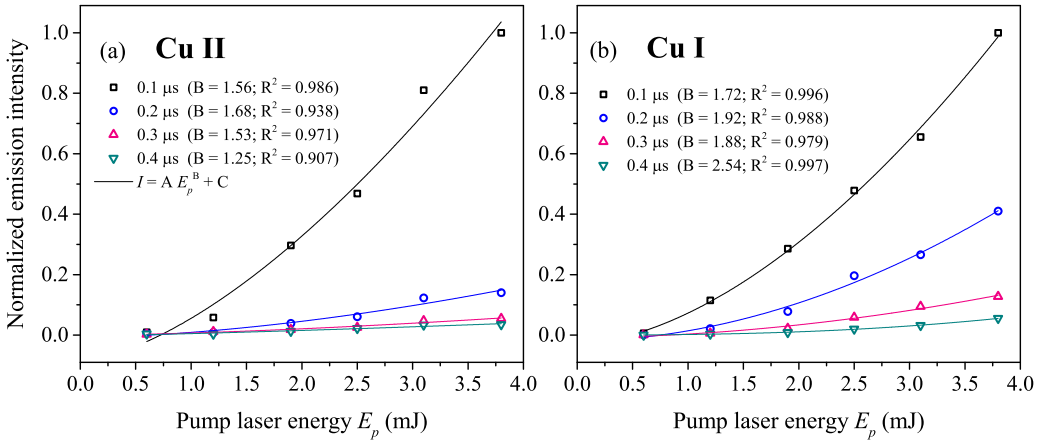

Figure 5.11: Total emission from selective imaging of (a) Cu II and (b) Cu I target species as a function of pump laser energy fit with a power-law to identify the trend [218].

instabilities in the spatial intensity profile of the beam, and as such, is sporadic in nature, because these instabilities may be seeded by defects in the optical system as well as external factors like air turbulence. Consequently, the blast model analysis used here which compiles shock dimensions from different ablation laser shots and requires high shot-to-shot reproducibility, is not appropriate for measurements of the multiple filament regime. The split lens approach is adopted to reproducibly seed two sufficiently separated detonation sites from shot-to-shot, so the blast model analysis may be applied also in the multiple filament regime. The total energy deposited in the target is determined by the sum of the detonation energies from the two sites, shown in Fig. 5.10. The total energy deposition exhibits a positive trend despite the onset of multiple filamentation with incident laser energy which agrees with the trend observed for the total emission of both Cu I and Cu II species in Fig. 5.11. Figure 5.11 summarizes the results from selective species imaging shown in Fig. D.3 in Appendix D. The agreement observed between detonation energy and total target plasma emission affirms that the split lens approach for induced multiple filamentation is a viable method to mimic the sporadic multiple filamentation for which the

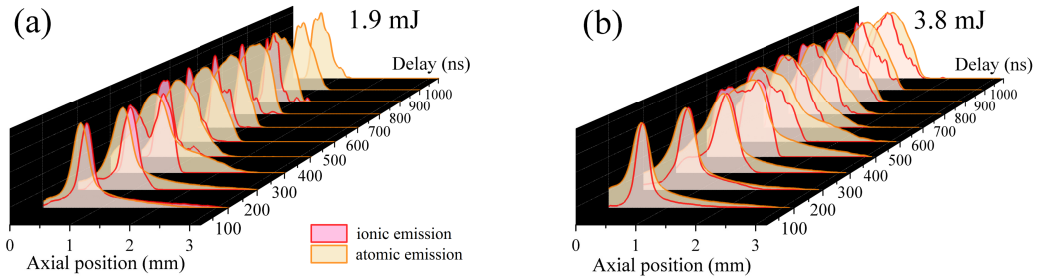

Figure 5.12: Time-resolved, normalized emission distributions along the central axis of each image recorded using narrow bandpass filters isolating (red) Cu II and (orange) Cu I species at pulse energies of (a) 1.9 mJ and (b) 3.8 mJ representative of the single and multiple filament regimes, respectively [218].

emission is measured in Fig. 5.11. This comparison further implies that multiple filamentation has insignificant detrimental effects to total signal generated following ablation in this range of energies, relevant to remote-FIBS applications; however, further work is necessary to confirm this scaling for freely-propagating filaments and for greater laser peak powers. The power-law scaling observed for net Cu line emission in Fig. 5.11 agrees with the scaling predicted for the tunneling ionization mechanism $N_e \propto I^m$ where $N_e \approx \frac{N_\mathrm{I}}{N_\mathrm{II}} f(T)$ by the Saha equation [Eq. (2.18)] and $I \propto E$ [229], suggesting the prevalence of tunneling ionization for seed electron generation during ablation. Here, N_I and N_II represent neutral atom (Cu I) and ion (Cu II) number densities, respectively; and $f(T)$ represents the functional dependence on the plasma temperature.

The distributions of emitting species from the plasma formed from the copper target, shown in Fig. 5.12, provide further insights into the filament ablation mechanisms. In both single- and multiple filament ablation regimes, ionic species (Cu II) travel faster, with peak velocity along the laser axis of 2.4 km s^{-1}, than neutral (Cu I) species, peak velocity 1.7 km s^{-1}. For comparison, the maximum observed shock ex-

pansion velocity is 2.2 km s^{-1}. The segregation between ions and neutrals is consistent with the behavior typically observed for ultrashort-pulsed LA, and similar observations were reported in past studies for filament ablation [103, 225]. Ultrashort-pulse LA mechanisms are discussed in Chapter 2. The larger velocity of the ions may be caused in part by enhanced Coloumb explosion, because the filament air plasma with free electron densities on order of 10^{16} cm^{-3} lasts on order of several nanoseconds, as discussed in Sec. 5.1.2, and creates a Coloumbic field gradient which pulls positively charged ions into the channel. Preferential expansion of the ions along the laser axis shown in Fig. D.3 provides additional evidence of the enhanced Coloumb explosion mechanism unique to filament ablation. Dissipation of the emission from ions may be aided by interactions of the plume with the shock boundary layer, because the ions travel faster than the expanding shock. Although the degree of species bifurcation observed here is consistent with ultrashort-pulse ablation mechanisms including Coloumb explosion and a direct solid-vapor transition (atomization), evidence from Fig. D.1 and D.3 suggests longer-lived mechanisms occur, including phase explosion related to the interaction of the filament air plasma with the lattice and enhanced Coloumb explosion from the interaction of the filament air plasma and the target plasma. These mechanisms are well-separated in time and evidenced by the formation of internal shock fronts and the ionic emission track along the laser axis. These results highlight a unique combination of fast and slow mechanisms that contribute to filament ablation and the formation of the target plasma, and improve understanding of signal formation relevant for FIBS. The following section expands on this effort, investigating the effect of laser wavelength on filament ablation of copper.

5.2.2 Wavelength-dependent filament ablation of copper

Numerous works investigate filament ablation using the fundamental 800-nm wavelength from Ti:sapphire laser systems [49, 84, 103, 247, 256]; however, fewer groups

have studied the near-UV and mid-IR wavelength regions. This section presents recent work investigating the effects of filament laser wavelength on metal ablation, comparing wavelengths ranging from the near-UV (400 nm) to the mid-IR (2-µm) spectral domains. The reflectivity of metal targets, like the copper sample used here, varies signficantly with wavelength and temperature during the ablation process; and for the intensity range relevant for filamentation, the target is expected to better absorb shorter wavelengths [131, 191]. However, previous work that investigated filamentation using the second-harmonic 400-nm wavelength from a Ti:sapphire system demonstrated an increased ionization fraction in the filament air plasma, as discussed in Sec. 5.1.2, results in a lower clamped intensity on order of 10^{13} W.cm^{-2} [47] than that for the 800-nm wavelength. The 2-µm filament air plasma is expected to differ even more considering the tunneling ionization overcomes MPI in the mid-IR spectral region, as shown by Fig. 2.1. Additionally, the critical power for self-focusing varies significantly with the wavelength [Eq. (4.12)] considering also the wavelength dependence of the linear (n_0) and nonlinear indices (n_2). In particular, the nonlinear index varies from 4–5$\times10^{-19}$ W^{-1} cm^2 for 400 nm to 3$\times10^{-19}$ W^{-1} cm^2 for 800 nm [48, 80] and is not expected to vary significantly between 800-nm and 2 µm [92]. The critical power for the 400-nm wavelength is, therefore, considerably lower at 0.5 GW than that for 800-nm, 3 GW, and 2 µm, 20 GW. The critical power provides an ambiguous threshold for the onset of multiple filamentation, indicating that the longer wavelength is less likely to exhibit multiple filamentation for equivalent peak powers. Notably, the 2-µm wavelength used in this study lies within a favorable gap in the atmospheric absorption spectrum so may be interesting for extended propagation with decreased atmospheric attenuation. In summary, target absorption, filament peak intensity, the interaction of the filament plasma with the target, multiple filamentation, and atmospheric transmission present a complex set of factors that depend on laser wavelength and may influence filament ablation. This section presents experimental investigation

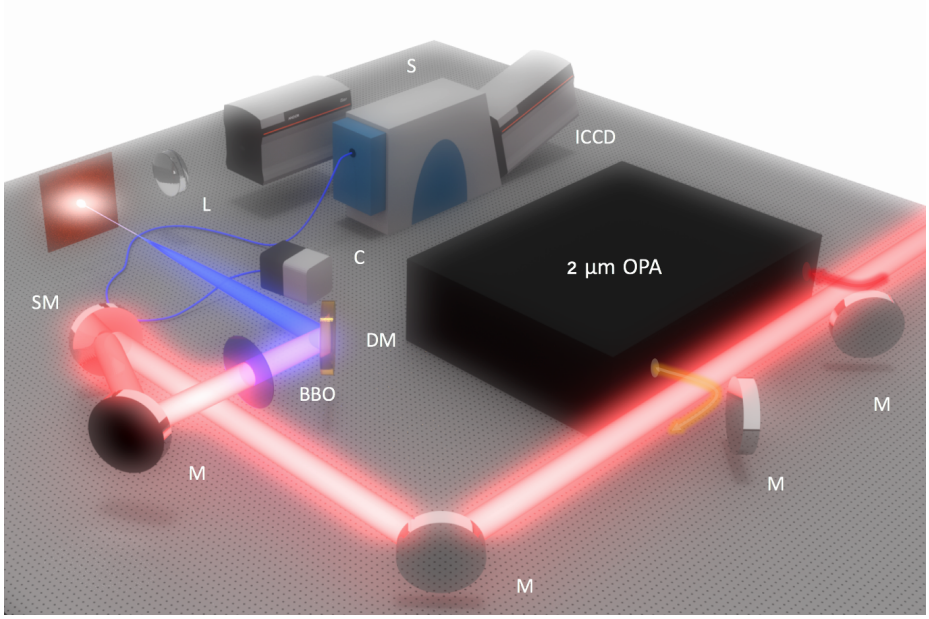

Figure 5.13: Experimental setup for OES and imaging of the target plasma formed following 0.4-, 0.8-, and 2-µm filament ablation of copper. The 0.4-µm wavelength is made via SHG through a BBO crystal with the 0.8-µm beam from the Ti:sapphire-based CPA system, and the fundamental beam is rejected using a dichroic mirror (DM). The 2-µm wavelength is generated in an optical parametric amplification (OPA) system. A spherical mirror (SM) is used to externally focus the laser. OES involves an ICCD coupled to an Echelle spectrograph (S) that collects the emission from the plasma through a collimator and optical fiber. For imaging, an achromatic lens (L) is used for 1:1 object-image maginification onto the ICCD [29].

of these confluent effects on the target plasma formed via filament ablation with laser wavelengths spanning the near-UV to mid-IR regions. The results have implications for remote sensing using analytical spectroscopy methods like FIBS. This section includes edited portions from Ref. [29].

5.2.2.1 Experiment

Figure 5.13 shows the experiment investigating the aggregate effects of laser wavelength on the target plasma signal, morphology, and thermodynamic properties following filament ablation of copper. The primary laser was the Ti:sapphire-based Lambda Cubed CPA system. The laser parameters used in this study include a pulse duration of 50 fs and repetition rate of 80 Hz. All experiments were performed in

air. The 0.4 µm wavelength was generated via SHG as described in Sec. 5.1.2.1. The 2.0-µm pulses were produced in a non-degenerate optical parametric amplifier (OPA) pumped with the 0.8-µm [254], and the pulse duration was predicted to be 43 fs. Filaments were formed for each wavelength with a 2"-diam., 1-m-FL spherical mirror, and the copper target was placed at the geometric focus of the mirror to ensure the target plasma was formed at the same location for imaging and OES. The copper sample was translated continuously during the experiments with a rotating stage. A 2"-diam., 7.5-cm-FL achromatic lens was used to image (1:1 object-image magnification) the target plasma onto an ICCD (Andor, iStar 334). The plasma images were accumulated for 50 laser shots and recorded with a gate width of 5 ns. For OES, an $f/2$ collimator (Andor,CC52) collected the emission from the target plasma into a 400-µm optical fiber coupled to an Echelle spectrograph (Andor, ME5000, slit size: 25×50 µm^2 yielding resolving power of $\sim$3000). The detector for OES was the same ICCD that was used for imaging, and spectra were accumulated for 150 laser shots unless otherwise stated. The spectrograph was wavelength-calibrated with an Hg-Ar lamp (Oriel, Pen Light) and intensity-calibrated using a radiometric source (Ocean Optics, DH-2000).

5.2.2.2 Results & Discussion

First, the morphological behavior of the copper target plasma is compared between the three different laser wavelengths for filament ablation. These results are summarized in Fig. 5.14; the plume dimensions are determined from imaging of the target plasma [29]. The 0.4- and 0.8-µm plasmas expand more quickly in the axial dimension (along the laser propagation axis) than the radial dimension, similar to that observed for multiple filament ablation with 0.8-µm in the previous section (Sec. 5.2.1.2, Fig. D.3), indicative of the enhanced Coloumb explosion mechanism in which the Coloumbic field gradient formed by the filament air plasma pulls pos-

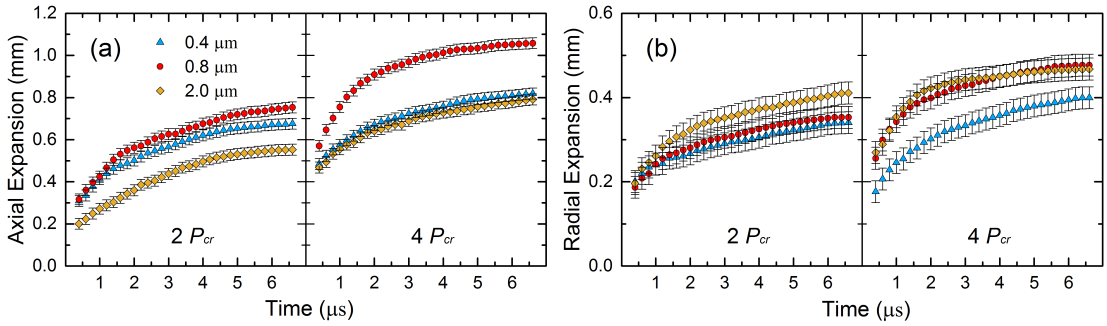

Figure 5.14: Expansion of the target plasma formed following 0.4-, 0.8-, and 2-μm filament ablation (a) along the laser propagation axis (*axial* dimension) and (b) perpendicular to the laser propagation axis (*radial* dimension) for filament laser peak powers equivalent to $2\times P_{\mathrm{cr}}$ and $4\times P_{\mathrm{cr}}$. The plume dimensions are determined from imaging of the target plasma emission as described in [29].

itively charged species into the channel. The 2-μm target plasma expands at more similar rates in both axial and radial dimensions, perhaps because the filament air plasma is expected to have a lower ionization fraction and free electron density, as predicted by the trends presented in Sec. 5.1.2.2. Enhanced Coloumb explosion is expected to be less prominent for lower ionization fraction and free electron density. Further discrepancies between the expansion rate of the 0.4- and 0.8-μm plumes may arise from the complex temperature- and wavelength-dependent reflectivity of copper during ablation. Interestingly, the size of the plasma is found to be well correlated with the peak power ratio to the critical power, considering the absolute peak powers vary drastically between 1 GW for 0.4 μm, 6 GW for 0.8 μm, and 40 GW for 2 μm, respectively.

Next, the thermodynamic properties of the target plasma are compared for the different laser wavelengths following analysis of the emission spectra shown in Fig. 5.15. The excitation temperatures are determined using Boltzmann plot analyses [Eq. (2.17)]. The Cu I lines used in these analyses are identified in Fig. 5.15 and listed along with relevant line parameters in Table D.1 in Appendix C. The free electron densities are determined by deconvolution of the Stark broadening mechanism to observed spectral

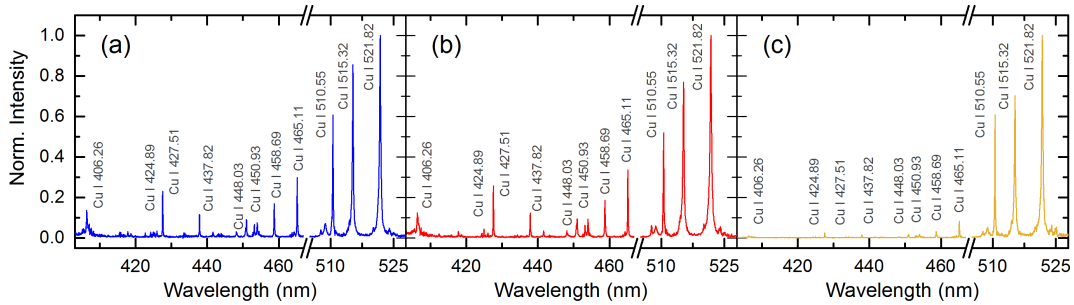

Figure 5.15: Optical emission spectra are compared for filament ablation using laser wavelengths of (a) 0.4 µm, (b) 0.8 µm, and (c) 2.0 µm with 2 mJ pulse energy [29].

line widths [Eq. (2.23)]. The electron density was determined as the average from analysis of three Cu I lines, 510.55, 515.32 and 521.8 nm. The corresponding Stark broadening parameters are taken from Ref. [134]. Instrumental and Doppler broadening contributions are considered. The Doppler width is estimated using Eq. (2.24) and the temperatures from the Boltzmann plot analyses to be 8 pm. Furthermore, the limiting electron density is evaluated using the McWhirter criterion [Eq. (2.19)] for each laser wavelength. The measured plasma properties are given in Table 5.2; it must be noted that these properties are averaged over time and space due to the OES collection scheme. In each case, the measured electron densities satisfy the McWhirter criterion implying the existence of quasi-LTE which justifies the Boltzmann plot analysis. The temperature and electron density of 2-µm plasma are notably lower than those of the 0.4- and 0.8-µm plasmas. These lower plasma parameters are attributed to a decreasing contribution of MPI during ablation for the longer wavelength. Previous works similarly reported lower thermodynamic properties for ultrashort-pulse LA with tight-focusing (without filamentation) for longer wavelengths in the mid-IR [13, 41]. On the other hand, the temperatures for 0.4- and 0.8-µm plasmas were found to be similar, and the electron density of the 0.4-µm plasma was found to be lower than that for 0.8 µm. Evidently, the decreased contribution of MPI during ablation between 0.4 and 0.8 µm does not account for the measured target plasma

Table 5.2: Time- and space-averaged target plasma excitation temperatures (T_e), free electron densities (N_e), and minimum electron densities to satisfy the McWhirter criterion ($N_e^{\min}$) are compared for different filament laser wavelengths (λ) [29].

λ (µm)	$k_B T_e$ (eV)	N_e (10^{16} cm^{-3})	$N_e^{\min}$ (10^{16} cm^{-3})
0.4	0.80±0.06	5.59±1.12	1.14
0.8	0.83±0.06	7.57±1.51	1.16
2.0	0.72±0.09	4.47±1.34	1.02

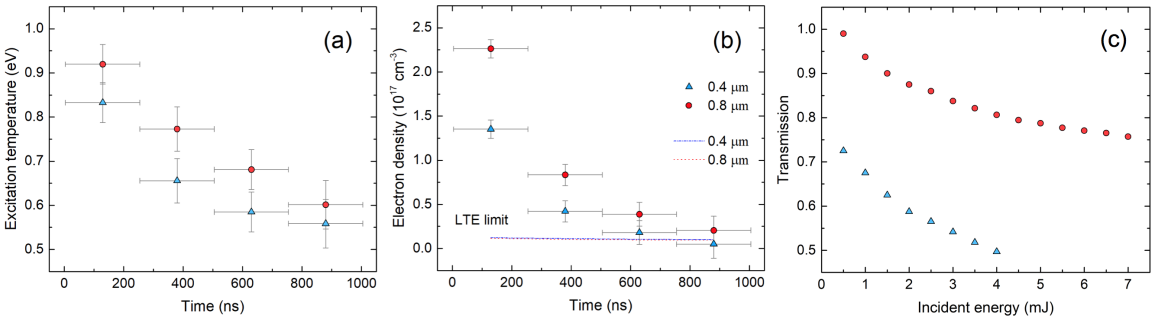

Figure 5.16: Time-resolved target plasma properties including (a) excitation temperature and (b) electron density are compared for 0.4- and 0.8 µm filament ablation. (c) Scaling of the energy transmitted through the filament for 0.4- and 0.8 µm laser wavelengths entering the multiple filament regime [29].

parameters, motivating further investigation of other parameters which may vary for different wavelengths. These factors, as previously discussed, include target absorption, filament peak intensity, the interaction of the filament plasma with the target, multiple filamentation, and atmospheric transmission.

Figure 5.16(a) and (b) show the temporal evolution of the copper plasma temperature and electron density, respectively, for 0.4- and 0.8-µm filament ablation. These results reiterate the peculiar lower thermodynamic properties of the target plasma formed using the shorter wavelength. The intensity threshold for filamentation can be evaluated for 0.4- and 0.8-µm wavelengths considering a predominant MPI mechanism by [38]

$$I_{\text{th}} \approx \left(\frac{0.76 n_2 N_c}{\tau_L \sigma_K N} \right)^{1/(K-1)}, \tag{5.2}$$

where N_c and N are the plasma critical density and neutral atom density, respectively; τ_L is the laser pulse duration; and σ_K is the MPI cross-section for K-photons required to reach the ionization potential. For an ionization potential of 12 eV (molecular oxygen) [201], the 0.4-µm wavelength has a lower threshold of 1.0×10^{13} W.cm^{-2} than that for 0.8-µm, 1.5×10^{13} W.cm^{-2}. MPI further attenuates the laser energy propagating through the filament more for the shorter wavelength. Figure 5.16(c) shows evidence of MPI reducing the transmitted energy through the filament comparing the 0.4- and 0.8 µm laser wavelengths spanning into the higher energy regime in which multiple filamentation is observed. Multiple filamentation is observed for $\sim$10-15$\times P_{\mathrm{cr}}$ for both the 0.4- and 0.8 µm wavelengths, at peak powers of $\sim$5 GW (0.2 mJ pulse energy) for 0.4 µm, and 40 GW (2 mJ pulse energy) for 0.8 µm, respectively. These results are consistent with the greater ionization fraction and electron density observed for the 0.4 µm filament air plasma when compared to those of the 0.8 µm discussed in Sec. 5.1.2.2. Ultimately, the increased attenuation due to MPI in the 0.4-µm filament causes less energy to reach the target and contributes to the lower target plasma temperatures and densities than those observed for 0.8-µm filament ablation.

Finally, the scaling of the spatially-integrated emission from the target plasma is compared for the three laser wavelengths in Fig. 5.17. The emission scales comparably for 0.4- and 0.8-µm, despite the transition into multiple filamentation. The trend for 0.8-µm agrees with that observed in the previous section (Fig. 5.11, Sec. 5.2.1.2). A positive trend is similarly observed for the 2-µm case, although the emission is notably weaker than that for both 0.4- and 0.8-µm, as predicted by the lower target plasma properties in Table 5.1. Notably, multiple filamentation is not observed for the 2-µm laser wavelength for the range of energies in Fig. 5.17. Consequently, 2-µm filamentation may be viable for remote FIBS considering the positive scaling of target plasma emission, greater threshold for multiple filamentation, and the favorable atmospheric transmission window for this wavelength. The results in this section

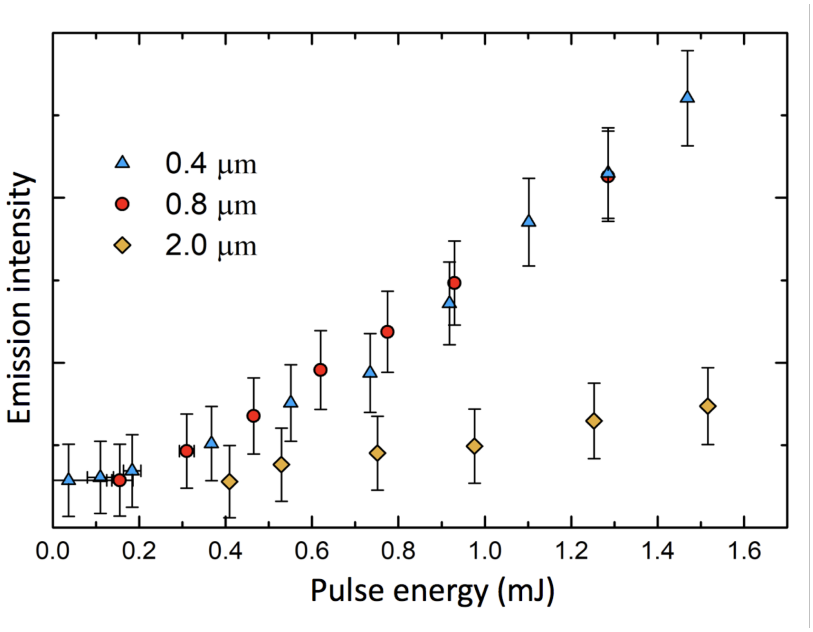

Figure 5.17: The spatially-integrated emission from the copper target plasma is compared for filament ablation using 0.4-, 0.8-, and 2-µm laser wavelengths with increasing pulse energies. The emission is integrated over the image of the target plasma recorded at a delay of 200 ns and gate width of 5 ns, respectively [29].

elucidate which wavelength-dependent factors most significantly influence ablation of metals, relevant to FIBS applications.

5.3 Summary

Section 5.1 in this chapter presents an extensive experimental investigation of propagation in the multiple filament regime, concentrating on the formation of the air plasma. In Sec. 5.1.1, transmitted charge is found to increase faster with increasing energy than the air plasma conductivity. The transmitted charge depends on the geometry and free electron density of the plasma; while, the conductivity is an inherent property of the plasma that is independent of geometry but varies with the number of free electrons. Both these quantities are influenced by multiple filamentation, because the formation of additional plasma cores influences the overall geometry of the conductive channel as well as the free electron density. From these

results, the multiple filament regime is encouraging for transmission of greater current magnitudes through transient structures, with relevance to development of novel circuitry and devices. Section 5.1.2 complements the direct probing of the filament air plasma to qualitatively assess the free electron density in Sec. 5.1.1 using non-invasive measurements based on OES to determine plasma properties. The experimentally-determined plasma properties measured in Sec. 5.1.2 fill gaps in current literature and may benefit computational modeling of propagation in the multiple filament regime. Understanding propagation in the multiple filament regime has direct implications for long-distance sensing which may require high laser peak powers.

Section 5.2 likewise presents an extensive experimental investigation of filament ablation, studying specifically the transition into the multiple filament regime. Understanding filament-target interactions is vital for FIBS, in which the signal depends strongly on the filament-target coupling. In Sec. 5.2.1, a novel technique for reproducing multiple filamentation using a split lens is presented, and a combination of fast and slow mechanisms unique to filament ablation is observed and discussed. Section 5.2.2 expands on the experiments in Sec. 5.2.1, studying the influence of laser wavelength on target plasma properties and total signal. In both sections, the total signal is found to scale positively for increasing laser energy despite the transition into the multiple filament regime (for 0.4- and 0.8-µm laser wavelengths), which bodes well for remote FIBS applications. The 2-µm filament results in lower signal but may be applicable when propagation in the single filament regime is desirable, especially considering the favorable atmospheric transmission window for this wavelength. The complex interplay of wavelength-dependent factors that influence filament ablation is also discussed in Sec. 5.2.2. The next chapter (Chapter 6) applies the understanding developed from these results for direct detection of uranium using standoff FIBS.

CHAPTER 6

Standoff Detection of Uranium Using Filament-Induced Breakdown Spectroscopy

Filamentation may be combined with analytical techniques like LIBS (referred to as FIBS) to enable excitation of a target over long distances, paving the pathway to remote sensing. Chapter 5 investigated filament propagation and ablation with high incident laser peak powers, in the range where multiple filamentation occurs. High peak powers are required for long-distance applications to overcome the loss mechanisms such as atmospheric absorption, ionization of the propagation medium, diffraction of the reservoir, and competition of multiple filaments. In Chapters 1–3, the importance of uranium is discussed in the context of the nuclear fuel cycle and power generation as well as global nuclear nonproliferation efforts. Further, Chapters 2 and 3 describe the advantages of LIBS among other techniques for detection of uranium. Examples of such advantages are sensitivity to various forms of the target including isotopes, simplicity of the collection and spectroscopy scheme, and prospects for long-distance detection. In previous work, Chinni *et al.* [39] demonstrated ns-LIBS with uranium from a standoff distance of 30 m; however, FIBS has been demonstrated with other metallic samples from distances of ∼90 m [148, 196]. Evidently, the FIBS technique shows prospects for longer-distance detection than standard ns-LIBS, because filamentation can sustain high intensities sufficient for target excitation and ablation

over distances significantly exceeding the Rayleigh length [20], overcoming the limits of diffraction. However, the congested uranium spectrum, compounded by the formation of uranium oxide species, poses challenges for remote-FIBS, because the noisy signal starts to resemble detector and background noise in remote collection. Elements of the collection setup which contribute to degradation of the signal and signal-to-background are discussed in Sec. 2.1.4.2 and 4.3.

This chapter demonstrates the combination of filamentation and LIBS for excitation and direct detection of uranium and UO at a standoff distance of 10 m. FIBS measurements are compared between loose-focused and free-propagating filaments. Single-shot detection is demonstrated in the loose-focusing scheme; while, controlling the second-order dispersion [group delay dispersion (GDD)], here often referred to as *chirp*, promises scalability to greater delivery distances in the free-propagating scheme. In either case, rapid detection of both uranium and UO signatures is demonstrated with high certainty enabled by accumulating over several ablation laser shots at high laser repetition rates. This chapter contains edited portions from Refs. [27, 71].

6.1 Experiment

Figure 6.1 shows the experiment for both loose-focused and free-propagating FIBS of a depleted U (DU) metal target. The Lambda Cubed Ti:sapphire-based CPA system was used for these experiments (800 nm, 35 fs, 480 Hz, Gaussian beam diameter of 11 mm prior to filamentation with or without the external focusing lens). All experiments were conducted in air. For loose-focusing experiments, 10-m FL lens was used, and the DU target was placed at a distance of 10 m from the lens (geometric focus). For free-propagation, the target was placed 10 m after the final mirror in the 0.5× telescope which was used to shrink the beam to 11 mm diam. In both experiments, the target was periodically translated to prevent excessive drilling. The insets of Fig. 6.1 show (a) the 4-m long filament air plasma used in free-propagation

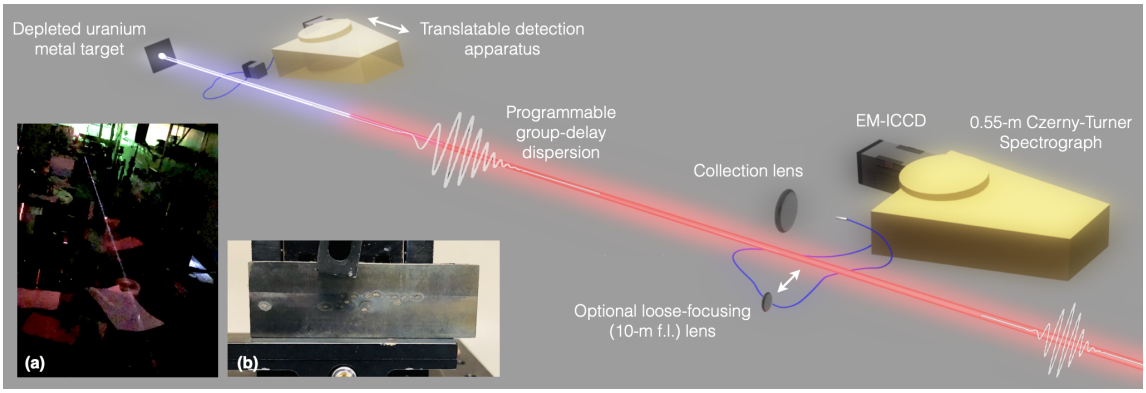

Figure 6.1: Filamentation was used in both loose-focusing (with 10-m FL lens) and free-propagating configurations to ablate a depleted U metal sample at a standoff distance of 10 m. For free-propagation experiments, a programmable acousto-optic modulator was used to control the GDD and optimize FIBS signal. The detection apparatus, consisting of a collection optic, optical fiber, Czerny-Tuner spectrograph, and EM-ICCD, was translated for near and far measurements with respect to the target. Near measurements were used to optimize GDD and characterize the target plasma. The insets show photographs of (a) a long (∼4 m) plasma channel formed in the free-propagating scheme and (b) the depleted U metal target after ablation. Adapted from Ref. [27].

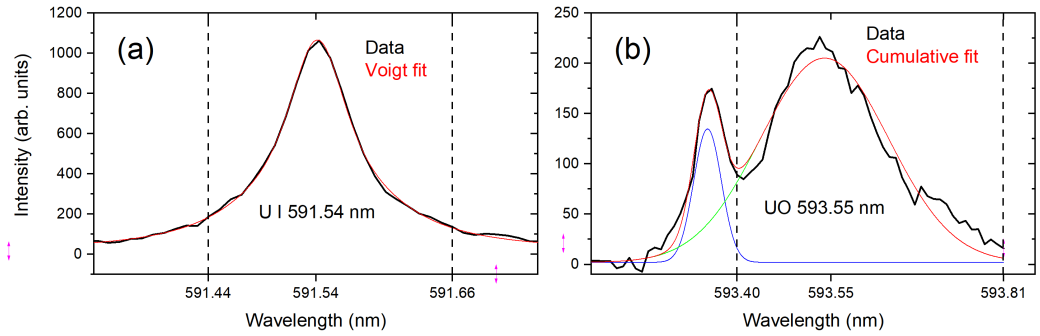

Figure 6.2: The measured spectra here are recorded 1 m away from the U target in order to identify the peak locations and integration limits for further analysis. (a) The U I 591.54 nm line is fit with a Voigt profile to determine the limits of integration for standoff signal analysis. The limits are determined from the $1/e^2$ level of the maximum peak intensity. (b) The UO 593.55 nm band is fit with a cumulative Gaussian profile to distinguish from the overlapping U I 593.33 nm line, and limits are chosen accordingly to avoid the overlap. Adapted from Ref. [71].

ablation and (b) the DU target after ablation. For free-propagation, the initial spectral phase of the laser was controlled using a programmable acousto-optic dispersive filter (Fastlite, Dazzler V370f). The radial filament core structure (shown in Fig. 6.9) was determined by placing a compact-disc at the position of the target.

The collection system was comprised of a collimator (Andor, CC52), 400-µm optical fiber, 0.55-m Czerny-Turner spectrograph (Horiba Jobin Yvon, iHR550), and electron multiplying-ICCD (EM-ICCD, Princeton Instruments, PI-Max 4). For standoff detection, a 4"-diam., 20-cm FL lens replaced the collimator in order to improve the solid angle efficiency (discussed in more detail in Chapter 7, Sec. 7.2.3). An 1800-l/mm grating was used for spectroscopy (resolving power $\sim 10^4$). Both the U I 591.54 nm and UO 593.55 nm spectral signatures were identified and studied. For determining the detection probabilities of each signature, the background-subtracted spectra were integrated in the regions shown by Fig. 6.2. The U I 591.54 nm line was fit with a Voigt profile, and the UO 593.55 nm band was fit with a Gaussian profile to determine the limits of integration. The integration limits were determined for when the signal reached the $1/e^2$ level of the peak maximum.

6.2 Results from loose-focusing scheme for standoff FIBS with uranium

The principal challenge for standoff FIBS with uranium-containing targets arises from the complexity and density of the uranium spectrum. As discussed in Chapter 2 and 3, the uranium emission spectrum is comprised of 10^5 atomic and ionic spectral lines necessitating comparably high spectral resolution to analytes previously studied using FIBS. Past works demonstrated FIBS measurements on order of several tens of meters with metallic targets such as copper and steel (iron) [225], aluminum [196], and sodium [49]. These targets exhibit a comparably lower density of

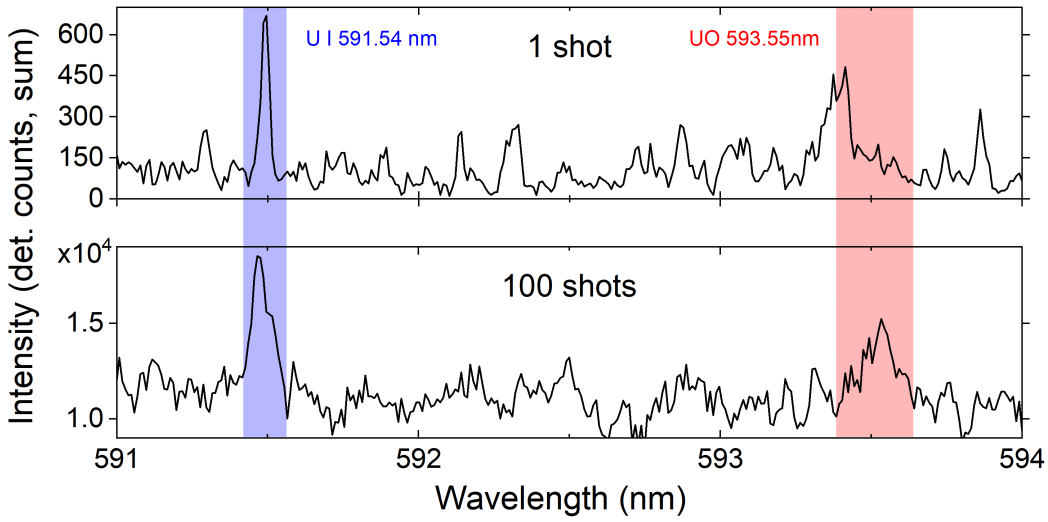

Figure 6.3: Representative spectra for (top) a single shot and (bottom) 100 integrated shots showing the U I 591.54 nm and UO 593.55 nm signatures and regions. Here, the loose-focus FIBS scheme is used at a distance of 10 m (filament propagation and collection). Adapted from Ref. [71].

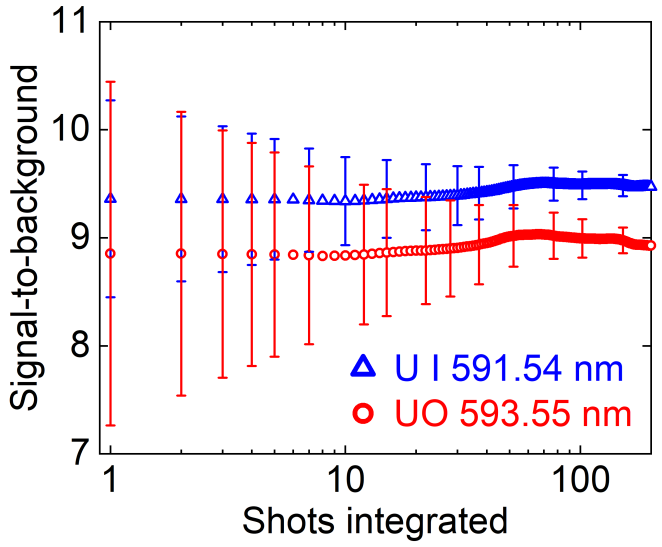

Figure 6.4: The signal-to-background ratio is compared for both U I 591.54 nm and UO 593.55 nm signatures with increasing number of filament ablation shots integrated. Here, the loose-focus FIBS scheme is used at a distance of 10 m (filament propagation and collection). Adapted from Ref. [71].

atomic and ionic spectral lines in the visible region. For uranium, weaker lines, even with high-resolution spectroscopic instruments, tend to look like noise. Furthermore, the uranium spectrum becomes considerably more complex in environments, like air, with even small concentrations of oxygen as demonstrated in Chapter 3. The emission from uranium oxides contributes to the broad continuum and looks like background. The fine and hyperfine rovibrational lines from uranium oxide transitions cannot be easily resolved using emission-based techniques. Nevertheless, this section demonstrates direct detection of U I and UO signatures using FIBS at a standoff distance of 10 m.

In this section, filamentation involves the use of a 10-m-focal length (NA $\approx 5 \times 10^{-4}$) loose-focusing lens. The DU target is placed at the geometric focus of the lens. In this scheme, the reservoir is expected to come to focus at the target position and contribute during target ablation. Previous works have demonstrated that loose-focusing results in greater signals and thermodynamic properties of the target plasma during filament ablation [102, 237]. Example spectra are shown for a single shot and integrated for 100 shots in Fig. 6.3. As shown in Fig 6.2, a moderate resolving power of $\sim 10^4$ is sufficient to be able to distinguish the U I 593.33 nm line from the UO 593.55 nm band.

An important quantity for practical standoff detection is the signal-to-background ratio. In following analyses, the analytical capability to distinguish signal (U I 591.54 nm and UO 593.55 nm signatures) from background is assessed, and the origin of the background is ignored. It should be noted that the background for the uranium spectrum may be comprised of emission from unresolved heavier uranium oxide species as discussed in Chapter 3 among other external sources. Other internal (those arising from the plasma) background contributions such as hot-body or other continuum emissions are rejected by appropriate time-gating. The temporal evolution of the spectrum and procedure for selecting appropriate time-gating windows are discussed

in more detail in Ref. [71]. The gate delay used in all measurements is 50 ns, and the gate width is 2 µs, respectively. A major advantage of laser-based excitation, like FIBS, is the availability of high laser repetition rates on order of kHz. The typical lifetimes for target plasmas formed during FIBS measurements are on order of µs to several tens of µs, enabling rapid successive measurements limited by the available repetition rates so that detection statistics may be improved. In current experiments, the data acquisition limits the rate of the measurements to 80 Hz.

Figure 6.4 shows the evolution of the signal-to-background ratio for both U I and UO signatures with increasing number of integrated laser shots. The signal is defined as the integral area between the limits shown in Fig. 6.2 for each signature, and the background is determined by the area under a polynomial curve fit to the spectrum. As expected, the signal-to-background remains nearly constant; however, the uncertainty decreases with increasing shot number. The uncertainty is determined by $(\sigma_{\mathrm{SBR}}/\mathrm{SBR})^2 = (\sigma_{\mathrm{S}}/\mathrm{S})^2 + (\sigma_{\mathrm{B}}/\mathrm{B})^2$, where SBR, S, and B represent the signal-to-background ratio [$\mathrm{SBR} = (\mathrm{S} - \mathrm{B})/\mathrm{B}$], signal, and background, respectively. σ denotes the uncertainty. A relative uncertainty of 5% is attained for U I in 7 shots (0.09 s), and for UO in 28 shots (0.35 s), respectively. The relative uncertainty falls to 1.2% for U I and 2.0% for UO in 100 shots (1.25 s).

Receiver operating characteristic (ROC) curves are standard tools which are used to characterize the limits of detectability of a counting system, such as the standoff FIBS measurement described here [132]. In a field scenario, a user must make a binary (yes or no) decision whether a given measurement constitutes a true detection or a false alarm. ROC curves may be used to define a pass or fail criterion for this decision. Constructing an ROC curve begins with generating a probability distribution of the signal+background $P(N_S)$ and background $P(N_B)$ counts, as shown in Fig. 6.5(a) for U I and UO signatures. Here, the contribution of external background sources such as room lights and detector dark current is measured to be 575±1.2 counts and

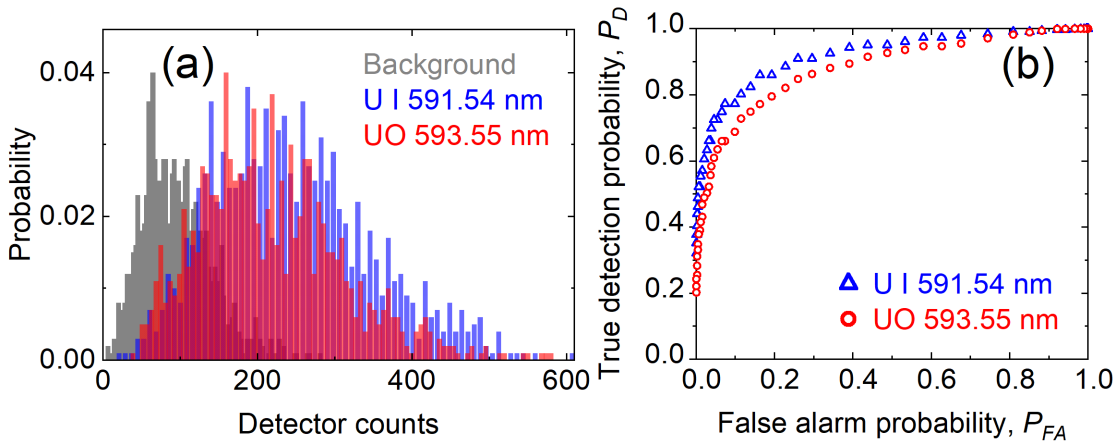

Figure 6.5: (a) Single-shot probability distributions for the U I 591.54 nm and UO 593.55 nm signatures compared to that for the background. The distributions are integrated to form the receiver operating characteristic curves for both signatures in (b). Here, the loose-focus FIBS scheme is used at a distance of 10 m (filament propagation and collection). The true detection probabilities for a single-shot measurement (1% P_{FA}) are 52.2% and 39.0% for U I and UO signatures, respectively. Adapted from Ref. [71].

subtracted. The mean background and its variation including this contribution is 708±41.5 counts. Next, a critical level L_C (or alarm level) is chosen such that if a subsequent measurement is made, $N_S < L_C$ means the measurement is representative only of background, and $N_S > L_C$ means a source is present. In a scenario where $P(N_S)$ and $P(N_B)$ overlap, the choice for L_C is not clear, so an ROC curve is generated by defining the true detection P_D and false alarm P_{FA} probabilities

$$P_D = \int_{L_c}^{\infty} P(N_S) dN_S \tag{6.1}$$

and

$$P_{FA} = \int_{L_C}^{\infty} P(N_B) dN_B. \tag{6.2}$$

The ROC curve is then constructed by plotting P_D as a function of P_{FA} for different choices of L_C. The L_C is typically varied from several standard deviations

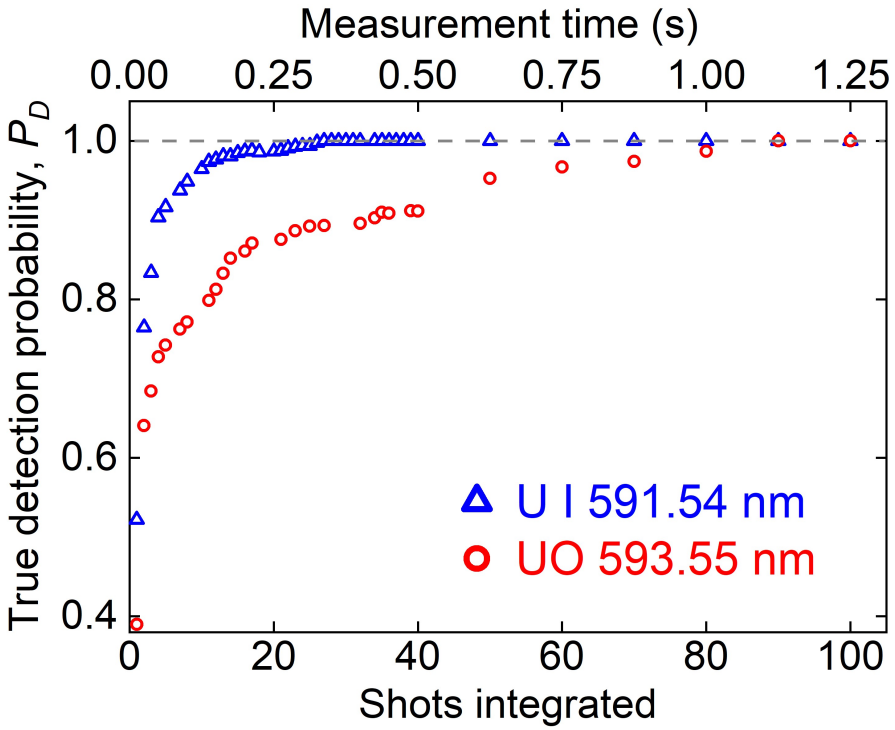

Figure 6.6: The true detection probability is determined for a 1% false alarm rate and compared to the integral number of filament ablation shots and measurement time for a laser repetition rate of 80 Hz and matching data acquisition rate. Here, the loose-focus FIBS scheme is used at a distance of 10 m (filament propagation and collection). True detection probabilities reach 100% (1% P_{FA}) in 24 shots (0.3 s) and 90 shots (1.1 s) for U I and UO signatures, respectively. Adapted from Ref. [71].

below the average background $\bar{N}_B$ to several standard deviations above the average signal+background $\bar{N}_S$. Here, 50 evenly-spaced L_C are chosen in the range between $(\bar{N}_B - 3\sigma_B)$ and $(\bar{N}_S + 3\sigma_S)$ to construct the ROC curve in Fig. 6.5(b). From the ROC curve, the true detection probability may be ascertained for a chosen false alarm rate. For a single-shot measurement, the true detection probabilities for U I and UO signatures are 52.2% and 39.0%, for a chosen false alarm rate of 1%, respectively. Single-shot detection is limited in practice by shot-to-shot variability of the signal and background. The background variation of 41.5 counts is greater than that predicted by a Poisson model ($\sigma_{\text{Poisson}} = \sqrt{N}$, $\sqrt{708} = 26.6$ counts) indicating overdispersion is present. Fluctuations in laser energy, turbulence of the propagation medium, multiple filamentation, and deformities in the target surface and matrix are examples of plausible sources of overdispersion from the experiment. Further, the contribution of uranium oxide emission to the observed background may be another source of overdispersion.

Detection probability, as defined by the ROC curve, may be improved similarly by integrating over several laser shots. Figure 6.6 shows the true detection probability (1% false alarm rate) for an increasing number of integrated shots. For each shot number, a new ROC curve is constructed to determine the detection probability. The advantage of high laser repetition rate and data acquisition rate is clear: 100% true detection probability is reached in just 24 shots (0.3 S) for U I and 90 shots (1.1 s) for UO signatures, respectively.

In summary, efficient detection of both U I and UO signatures is demonstrated using the loose-focusing FIBS scheme from a standoff distance of 10 m in this section. Single-shot true detection probabilities of 52.2% and 39% for U I and UO signatures, respectively, are determined for a 1% false alarm rate. Experimental sources of variability that hinder single-shot detection are also discussed. Finally, such measurements offer rapid measurement capability enabled by high laser repetition rate

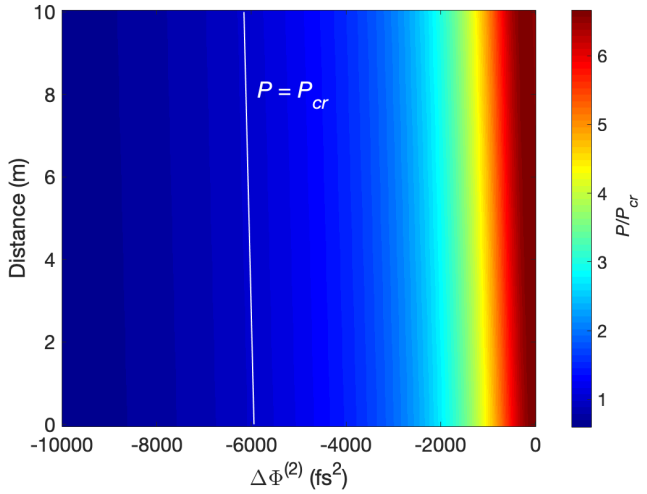

Figure 6.7: Incident laser peak power is compared to the critical power for self-focusing for a range of GDD values and propagation distances. The critical power is determined for that of an 800-nm pulse propagating in air, $P_{\mathrm{cr}} \approx 3$ GW. The GVD of air at 800 nm is 0.021233 fs^2 mm^{-1}. The pulse has an initial (Gaussian) pulse duration of 50 fs, and peak energy of 1 mJ.

and data acquisition rate, and 100% true detection probabilities (1% false alarm) can be reached on the time-scale of 1 s with a data acquisition rate of 80 Hz. The results from this section reveal the potential of FIBS for detection of uranium in the context of nuclear safeguards, security, and nonproliferation. The next section compares the results shown here to results from FIBS of the DU target with a free-propagating filament ablation scheme.

6.3 Results from free-propagation scheme for standoff FIBS with uranium

In Sec. 6.2, the reservoir is expected to contribute to ablation and formation of the signal in the loose-focusing scheme. In the free-propagation scheme presented in this section, the reservoir is expected to contribute less toward ablation as discussed in previous works [102, 237]. However, free propagation allows scalability to larger excitation distances with the capability to delay the onset of self-focusing and conse-

quent filamentation. By applying a negative GDD to pre-compensate for the positive dispersion experienced by the pulse propagating through air, the user can effectively control filament placement. Air has a positive group velocity dispersion (GVD) of 0.021233 fs^2 mm^{-1} for 800 nm, so that a pulse propagating through 10 m of air experiences a GDD of +212.33 fs^2. For a Gaussian temporal profile with duration τ_i, the resultant pulse duration τ_f experiencing a net GDD of $\Delta\Phi^{(2)}_{\text{net}}$ can be predicted by

$$\tau_f = \frac{\sqrt{\tau_i^4 + \left[(4\ln 2)\Delta\Phi^{(2)}_{\text{net}}\right]^2}}{\tau_i}, \tag{6.3}$$

where the net GDD here considers the contributions of user-controlled GDD, $\Delta\Phi^{(2)}_{\text{in}}$, and that experienced through propagation in air, $\Delta\Phi^{(2)}_{\text{air}}$, such that

$$\Delta\Phi^{(2)}_{\text{net}} = \Delta\Phi^{(2)}_{\text{in}} + \Delta\Phi^{(2)}_{\text{air}}. \tag{6.4}$$

Figure 6.7 shows the ratio of the incident laser peak power determined as $P = E/\tau_f$ to the critical power for self-focusing for a relevant range of input GDD and propagation distance (in air). Here, the critical power is 3 GW [Eq. (4.12)], the incident Gaussian pulse duration is 50 fs, and the peak energy is $E = 1$ mJ. As discussed in Chapter 4, filamentation involves a complex interplay of more mechanisms than just self-focusing, and previous work demonstrates that an applied negative chirp can successfully delay the onset of filamentation in a free-propagation configuration, even if initial peak power exceeds the critical power for self-focusing [158]. In this section, the DU target position is fixed with respect to the total propagation distance, and the FIBS signal for both U I and UO signatures is used as the feedback for optimization of the applied negative chirp.

Figure 6.8 shows the results from optimization of the applied chirp. The FIBS signals shown here are recorded at a (close) distance of 1 m from the target, while the

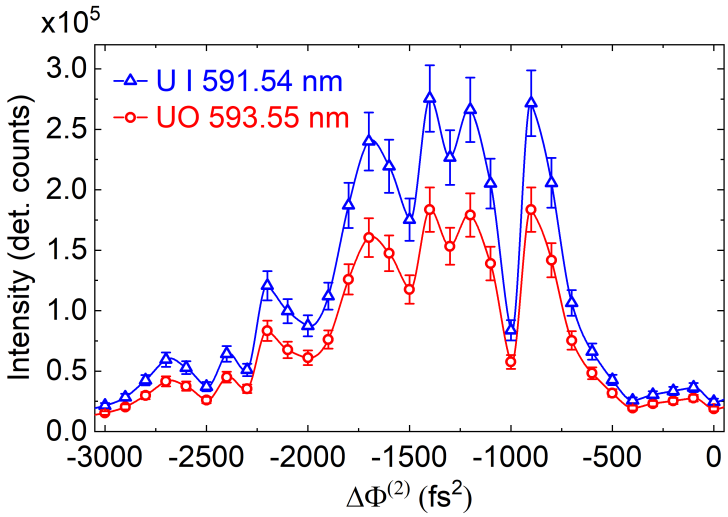

Figure 6.8: Quadratic phase is varied using an acousto-optic dispersive filter prior to forming free-propagating filaments. The intensities of U I 591.54 nm and UO 593.55 nm are measured at a distance of 1 m following filament ablation at 10 m and used as figures of merit for optimization of the quadratic phase. Adapted from Ref. [27].

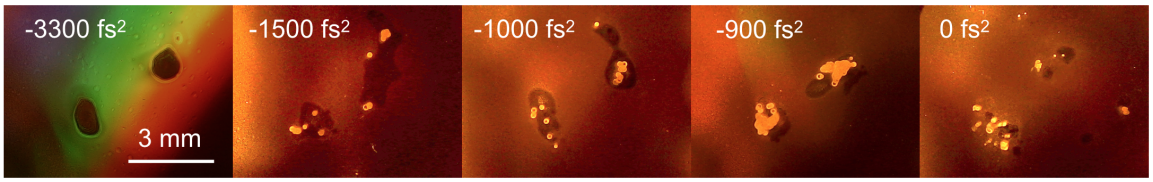

Figure 6.9: Damage profiles are recorded on the surface of a compact disc for various settings of the quadratic phase prior to formation of free-propagating filaments. The discs are exposed to 40 laser shots at the position of the DU target. Evidence of multiple filamentation is observed [27].

total filament propagation distance is 10 m. U I and UO signatures are integrated as shown in Fig. 6.2 and serve as the figures of merit for optimization. Interestingly, the optimal chirp does not occur for the negative applied GDD which pre-compensates for the positive dispersion propagating through 10 m of air (+212.33 fs^2). The oscillatory behavior observed in Fig. 6.8 is instead consistent with the interplay of temporal self-transformation mechanisms that occur during filamentation, as discussed in Chapter 4, Sec. 4.1.8. Furthermore, damage profiles were recorded on a compact disc surface at the position of the DU target, shown in Fig. 6.9. These profiles display two clusters of multiple filament cores whose local density varies with applied chirp. The two clusters may originate from an imperfect intensity profile of the beam prior to filamentation. Notably, however, the damage pattern observed for an applied chirp of -900 fs^2 shows convergence of the multiple filament cores in the two clusters, coinciding with one of the optimal signals. These results imply that spatial effects in addition to temporal self-transformation also influence FIBS signal during free-propagation. Spatial self-transformation results from the competition of cyclical self-focusing and de-focusing and includes other consequences like multiple filamentation. Next, the standoff detection capability is assessed for (one of) the optimal GDD settings of -900 fs^2.

Figure 6.10 shows the single-shot probability distribution for both U I 591.54 nm and UO 593.55 nm signatures (signal+background) compared to the background. As expected, the true detection probabilities (at 1% false alarm rate) for single-shot measurements are significantly lower ($\lesssim$8%) than those for the loose-focusing scheme because of the contribution of the reservoir to ablation and consequent signal formation. This comparison is consistent with previous results which measured lower mass removal [237] and thermodynamic properties of the target plasma [102] for free-propagating filament ablation than those for loose-focusing. In this measurement, the data acquisition rate was improved to 240 Hz by selecting a narrower region

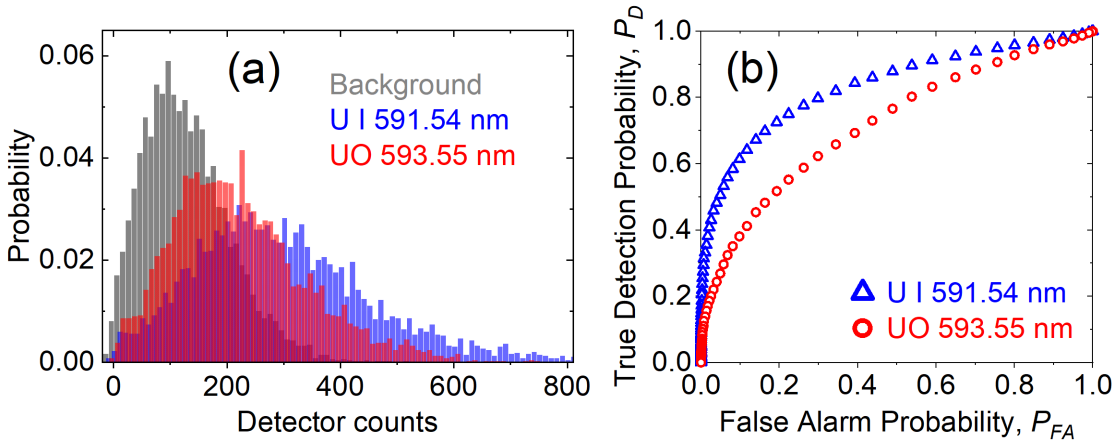

Figure 6.10: (a) Single-shot probability distributions for the U I 591.54 nm and UO 593.55 nm signatures compared to that for the background. The distributions are integrated to form the receiver operating characteristic curves for both signatures in (b). Here, the free-propagation FIBS scheme is used at a distance of 10 m (filament propagation and collection). Adapted from Ref. [27].

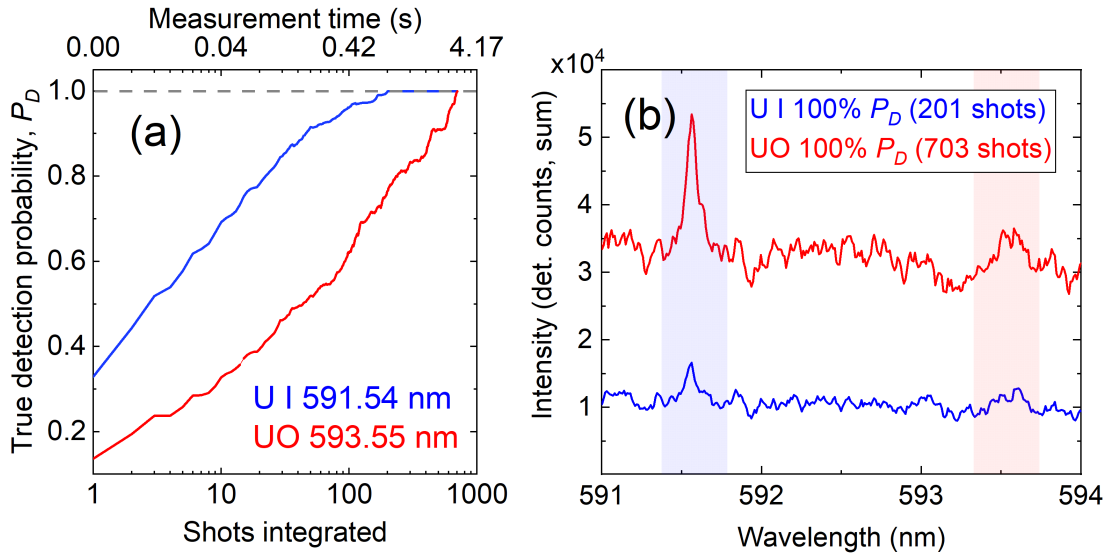

Figure 6.11: (a) The true detection probability is determined for a 1% false alarm rate and compared to the integral number of filament ablation shots and measurement time for a laser repetition rate of 80 Hz and matching data acquisition rate. Here, the free-propagation FIBS scheme is used at a distance of 10 m (filament propagation and collection). True detection probabilities reach 100% (1% P_{FA}) in 201 shots (0.8 s) and 703 shots (2.9 s) for U I and UO signatures, respectively. (b) Example integrated spectra for the 100% true detection probabilities. Adapted from Ref. [27].

of interest on the EM-ICCD for spectroscopy. Consequently, 100% true detection probabalities (1% false alarm) are reached for U I and UO with 201 shots (0.8 s) and 703 shots (2.9 s), respectively, as shown in Fig. 6.11. These results demonstrate that controlling the chirp is an effective means to optimize FIBS signal and bode well for scaling filament excitation to farther distances.

6.4 Summary

Effective standoff detection of a DU target is demonstrated using FIBS in this chapter. The loose-focusing scheme is promising for single-shot detection based on the criteria defined by constructing an ROC curve. Single-shot true detection probabilities for a 1% false alarm rate are 52.2% and 39.0% for U I and UO signatures, respectively. In these measurements, 100% true detection probabilities can be reached for U I in 24 shots (0.3 s) and for UO in 90 shots (1.1 s), respectively, limited by a data acquisition rate of 80 Hz. In free-propagation, spatial self-transformation is found to contribute alongside temporal effects like self-steepening and self-compression to formation of the FIBS signal. Although single-shot standoff detection probabilities are comparably lower than that for the loose-focusing scheme, even following chirp optimization, improvements to the data acquisition rate yield similar rapid detection capability. 100% true detection probabilities are reached for U I in 201 shots (0.8 s) and for UO in 703 shots (2.9 s) with the improved data acquisition rate of 240 Hz. The wide availability of laser systems with kHz repetition rates is encouraging for further improving detection rates. Ultimately, the ability to control the onset of filamentation and optimize FIBS signal bodes well for extending the excitation distances even farther. These results have additional implications for nuclear safeguards, security, and nonproliferation. Standoff FIBS of a uranium-containing target is shown to be feasible with a moderate resolving power of 10^4, and both U I and UO signatures were sufficiently resolved and detected. Applications to the nuclear fuel cycle

may include prospecting for uranium-containing ores or safe, standoff-surveillance of uranium-isotope concentrations in conversion or enrichment processes. In the next chapter, filamentation is combined with LIF for detection of another uranium compound relevant to the nuclear fuel cycle, uranyl fluoride.

CHAPTER 7

Filament-Induced Fluorescence Spectroscopy of Uranyl Fluoride

Enrichment of uranium is a cornerstone activity in both the nuclear fuel cycle as well as nonproliferation as discussed in Sec. 1.1. Consequently, novel technologies for measuring those uranium compounds like uranium hexafluoride (UF_6) and its derivatives in the fuel cycle could benefit nuclear safeguards in the energy industry. In the context of security, a clandestine enrichment facility operating outside the authority of the International Atomic Energy Agency may pose a threat to global nonproliferation efforts [52, 128]. Here, innovative means are likewise required to detect or monitor illicit enrichment activities.

Uranyl fluoride (UO_2F_2) forms readily from the hydrolysis of UF_6 which is widely used for uranium enrichment:

$$UF_{6(g)} + 2\ H_2O_{(g)} \rightarrow UO_2F_{2(s)} + 4\ HF_{(g)}. \tag{7.1}$$

Of the products from Eq. (7.1), UO_2F_2 exhibits a negligible natural background; therefore, its presence implies active operation of nearby enrichment or conversion facilities. For this reason, detection and audits of UO_2F_2 concentration may be applicable to safeguards as well as nonproliferation. As an example, UO_2F_2 may be used

to guide remediation efforts around enrichment facilities which experience a leak or another, more serious, catastrophic accident [128].

Several prior studies have demonstrated detection of compounds related to conversion and enrichment in the nuclear fuel cycle (namely, UF_6, HF, and UO_2F_2) using remote LIDAR [212], air sampling methods that use particle filtration [128, 238], air sampling with LA-laser absorbance ratio spectrometry (LAARS) [19, 91], LIBS [211], and LIF [15, 83, 91, 242, 243]. UO_2F_2, besides its near-zero natural background, is the most promising compound for aforementioned applications because of its chemical stability. UO_2F_2, unlike UF_6, remains as an aerosol for periods on the order of several days, limited by its solubility in water [128]. LIF is advantageous for detection of UO_2F_2 over the other proposed methods for two reasons: (1) the standoff detection distance of LIF is greater than that of the air sampling methods, especially when combined with filamentation which enables extended delivery of the excitation source; and (2) LIF involves direct excitation of the molecular rovibrational states, whereas those methods involving LA may require nontrivial stoichiometric analysis and consideration of the natural backgrounds of oxygen and fluorine species to infer the presence of UO_2F_2, since larger compounds tend to dissociate during breakdown. The luminescence spectrum of uranyl compounds has been extensively studied following cw- or short-pulse excitation [4, 9, 14, 33, 46, 54, 55, 60, 61, 77, 81–83, 121, 159, 166–171, 199, 242–244]. As suggested by these works, an additional prospect for using LIF is the lower energy requirement to excite rovibrational modes of molecules, and the resultant luminescence is typically longer lived than the emission from LPPs, $\mathcal{O}$(ms) [15].

This chapter demonstrates how filamentation can extend the distance at which the luminescence of UO_2F_2 may be induced using LIF, presenting another example how filamentation combined with analytical spectroscopy may be used for nuclear safeguards or security. Also, interesting luminescence dynamics, unique to ultrshort-

pulse excitation, are discovered and discussed herein. This chapter includes edited portions from Refs. [216, 217].

7.1 Experiment

7.1.1 Sample Preparation

UO_2F_2 samples were prepared at the University of Nevada Las Vegas. The facility was designed for chemical synthesis using efficient HEPA-filtered fume hoods and glove boxes, and the methods described here followed locally approved radioisotope handling and monitoring procedures.

Sample production began with preparation of anhydrous UO_2F_2 according the procedure outlined in Ref. [31]. First, $UO_2(NO_3)_2.6H_2O$ was converted to $UO_4.2H_2O$ by treatment with concentrated HNO_3 and H_2O_2. Second, the resulting $UO_4.2H_2O$ was dissolved in 24% HF in a Teflon flask which was connected to a Schlenk line and treated at 110 °C for 1 hr under flowing argon. Third, a yellow solid (UO_2F_2) was obtained and subsequently placed in a desiccator over concentrated H_2SO_4 for one week. Finally, the solid was dissolved in 3 mL 0.05 M HF/0.05 M KF to make a 0.05 M UO_2F_2 solution. The sample was then shipped to the University of Michigan for spectroscopy experiments described in Sec. 7.1.2.

7.1.2 Ultrafast laser- and filament-induced fluorescence spectroscopy of uranyl fluoride

Figure 7.1 shows the experimental scheme for filament-induced fluorescence spectroscopy. Relevant laser parameters (Lambda Cubed facility) include the pulse duration of 50 fs, repetition rate of 80 Hz, and pulse energies spanning 1–1.6 mJ. Experiments were conducted in air. The second-harmonic wavelength was generated via SHG as described in Chapter 5, Sec. 5.1.2.1. The 400-nm pulses are well-aligned

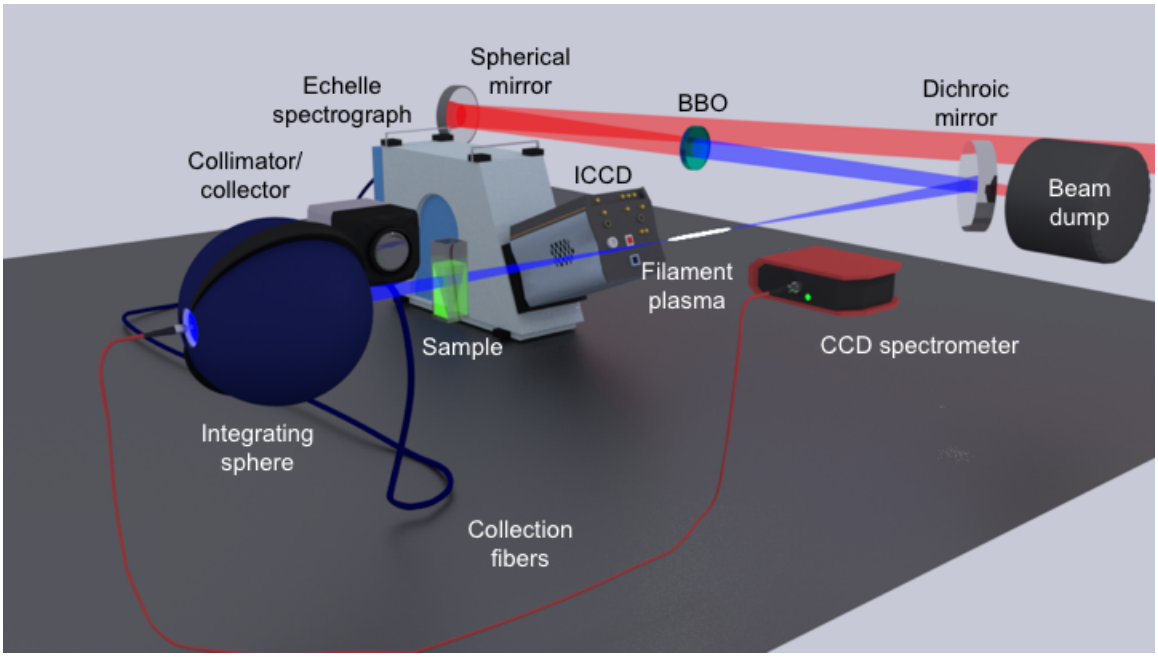

Figure 7.1: A 1-m FL ($f/40$) spherical mirror is used to form a filament following SHG through a 100 µm-thick BBO crystal to create 400-nm pulses; residual 800-nm light is rejected using a high-pass dichroic mirror. The 0.05 M UO_2F_2 solution is placed 30 cm after the geometrical focus of the spherical mirror. The conical emission from the filament excites sample luminescence collected with an $f/2$ collimator and transported through a 400-µm diameter optical fiber into an Echelle spectrograph coupled to an ICCD detector. Filament spectra are collected using an integrating sphere and directed into a compact CCD spectrometer via optical fiber [216].

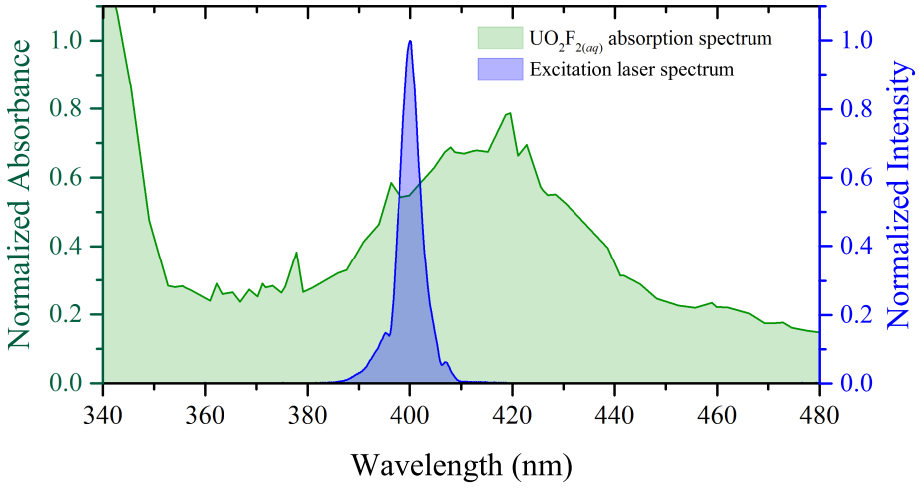

Figure 7.2: The absorption spectrum of UO_2F_2 in solution is measured using a UV/VIS spectrophotometer (green) and compared to the experimental SHG laser spectrum, prior to filamentation (blue) [216].

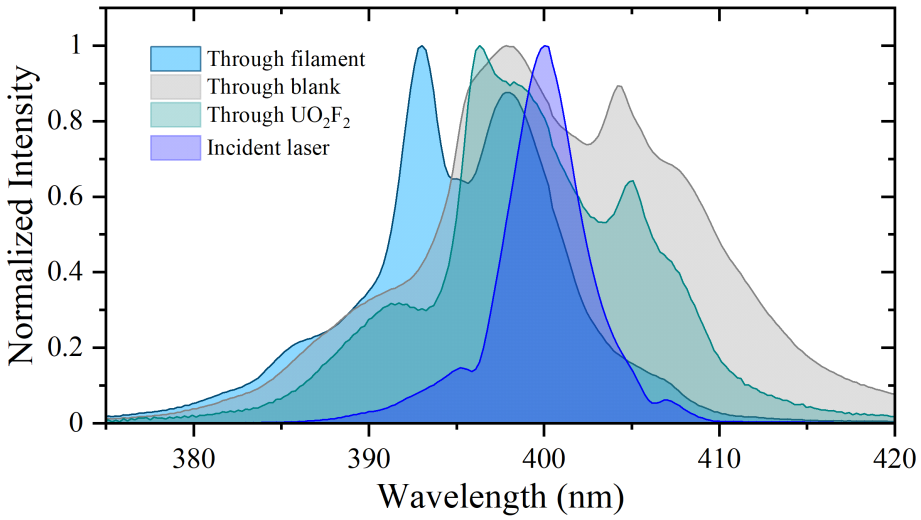

Figure 7.3: The incident laser spectrum (blue) is compared to the broadened spectrum experiencing SPM, among other mechanisms, in the filament (light blue) as well as blank HF sample (gray) and absorption and SPM in the UO_2F_2 sample (cyan) [216].

with the absorption spectrum of UO_2F_2, as shown by Fig. 7.2. The absorption spectrum was measured using a UV/VIS spectrophotometer. Residual 800-nm light was rejected using a high-pass dichroic mirror with reflectance $\mathcal{R}(800\text{ nm})<0.2\%$. The sample was contained in a 1-cm×1-cm PMMA cuvette with transmission measured to be $\mathcal{T}(>300\text{ nm})>80\%$. Transmission measurements were compared to solution of 0.05 M HF/0.05 M KF contained in an identical cuvette, referred to as the *blank*. The total absorption length included 2 mm of PMMA and 8 mm of solution [Eq. (2.30)]. The transmission of the blank was measured to be $(8\bar{0}\pm3)\%$. SPM, among other mechanisms described elsewhere [154], through the filament as well as cuvette and sample results in notable spectral broadening as shown in Fig. 7.3; however, the broadened laser spectrum is not expected to adversely affect excitation because its extents are still within the favorable absorption range of the analyte.

The laser was focused using a 50-mm diameter, 1-m FL spherical mirror ($f/40$), and a filament plasma with ∼4-cm length was observed near the geometric focus of the mirror. The sample was placed 30 cm after geometric focus of the mirror, and the conical emission from the filament was used to excite sample luminescence. Laser

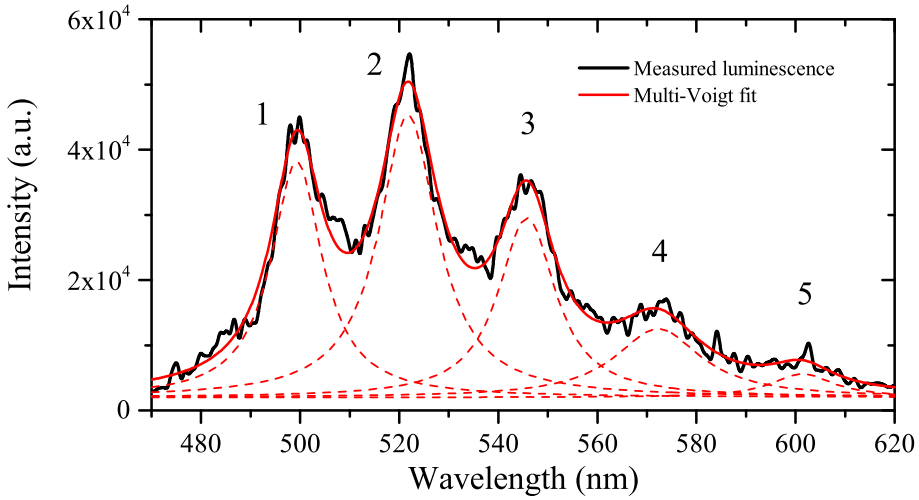

Figure 7.4: Example of a cumulative Voigt fit (red) of the measured luminescence from aqueous UO_2F_2 (black) following excitation with 1-mJ incident energy.

spectra shown in Fig. 7.2 were recorded with an integrating sphere using a compact CCD spectrometer (CCS200, Thorlabs). Sample luminescence was collected with a $f/2$ collimator (Andor, CC52) coupled into a 400-µm diameter optical fiber. The spectroscopy system is comprised of an Echelle spectrograph (Andor, ME5000) and ICCD (Andor, iStar 334T). The spectrograph slit dimensions are 50 µm × 50 µm providing a resolving power of ∼5000. Spectra were averaged over several excitation laser shots. The spectrograph was wavelength-calibrated with an Hg-Ar lamp (Oriel, Pen Light) and intensity-calibrated using a radiometric source (Ocean Optics, DH-2000).

7.2 Results and discussion

7.2.1 Luminescence of UO_2F_2

Uranyl compounds luminesce from magnetic dipole transitions from the lowest triplet $^3\Delta_g$ excited state to five vibrational levels in the singlet $^1\Sigma_g^+$ ground state, resulting in four to six characteristic bands in the spectral range between ∼450 nm and ∼650 nm [127, 242]. The luminescence mechanism is primarily phosphorescence

Table 7.1: Experimentally determined decay rates of the luminescence of aqueous UO_2F_2 following ultrashort- and filament excitation [216].

Peak	Decay rate, γ ($\times 10^4$ s^{-1})	Filament-excited decay rate, γ_f ($\times 10^4$ s^{-1})
1	4.7±0.1	4.7±0.2
2	4.3±0.1	4.4±0.2
3	5.6±0.5	4.7±0.2
4	5.3±0.2	4.6±0.4
5	4.8±0.8	5.5±0.4

which involves inter-system crossing, yielding longer-lived decay described by

$$I_1(\lambda, t) = \sum_i A_i S_i(\lambda) \exp(-\gamma_i t), \tag{7.2}$$

where A_i and $S_i(\lambda)$ describe the strength and spectral band shape, respectively; and γ_i is the characteristic decay rate for the uranyl complex i [23].

Figure 7.4 shows an example measured luminescence spectrum from aqueous UO_2F_2 fit with a cumulative Voigt profile following excitation with the ultrashort 400-nm SHG source, as described in Sec. 7.1.2. The spectrum exhibits five broad peaks, labeled 1–5. The cumulative Voigt fit uses least squares with a Nelder-Mead simplex algorithm to optimize fit parameters and accounts for the natural (Lorentz) [127] shape of the transitions as well as instrumental (Gaussian) broadening. Table E.1 in Appendix E summarizes the fit parameters including the measured centroid locations and widths for each of the five peaks. The denotation for the peaks (labeled 1–5) presented in this section is continued in the following sections.

7.2.2 Fast luminescence dynamics of UO_2F_2 in response to ultrashort- and filament-excitation

The temporal character of the UO_2F_2 luminescence may be a useful component of the signature for analytical measurements, especially for remote sensing applications, because time-gating may be used to isolate the rapidly-varying signal from

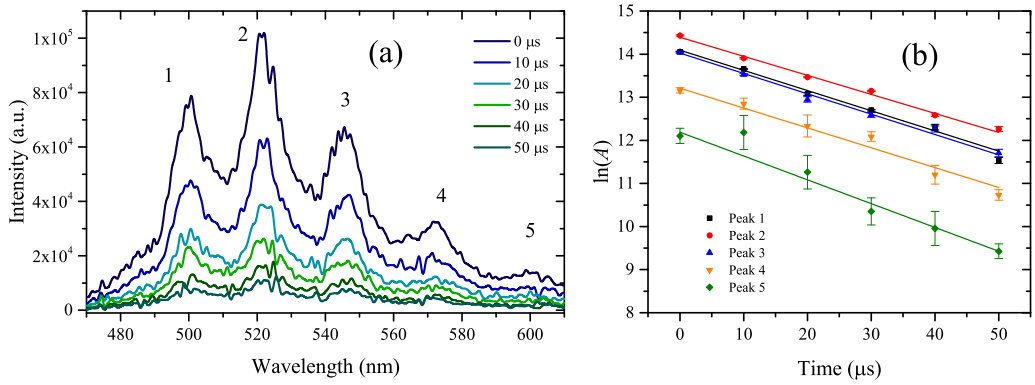

Figure 7.5: (a) The time-dependent luminescence of aqueous UO_2F_2, excited by the conical emission from filamentation with 1-mJ energy at the cuvette face, is accumulated for 300 laser shots for each ICCD delay. (b) The logarithm of the individual peak areas A is fit with a linear model to determine the decay constants γ_f [216].

slowly-varying backgrounds. Figure 7.5 shows the time-dependent UO_2F_2 luminescence spectrum following excitation with the conical emission from the filament. The conical emission was used for excitation, because the greater intensities near the geometric focus of the spherical mirror (within the filament plasma zone) would damage the cuvette containing the sample. For comparison, the luminescence and its temporal profile are recorded also without formation of the filament, with just ultrashort-pulse excitation with similar excitation intensities at the entrance face of the cuvette to those used with filament excitation; those results are presented in Fig. E.1 in Appendix E and summarized in Table 7.1. The range of laser and filament intensities (determined at the entrance face of the cuvette) used for excitation is $1.0–1.6\times10^{11}$ W.cm^{-2}. Figure 7.5(b) [and Fig. E.1(b)] measures the rate of decay $\gamma_{(f)}$ of the luminescence assuming an exponential character according to Eq. (7.2). The adjusted R^2 values for each fit are greater than 0.96. The measured decay rates are on the order of 10^4 s^{-1} and given in Table 7.1. The rates are similar between each of the five peaks and similar between ultrashort-pulse and filament excitation schemes. Strangely, the decay rates measured here are an order of magnitude greater than those previously observed with ns-pulse excitation [15]. The rates measured in this

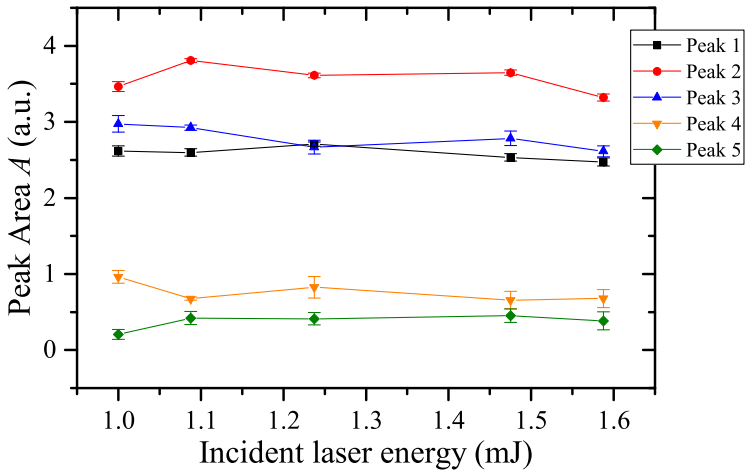

Figure 7.6: Peak area for each of the five major peaks observed in the luminescence spectrum for varying incident laser energies (translating to the range of peak intensities 1.0–1.6 $\times$ 10^{11} W.cm^{-2})) [216].

work are more comparable to those determined with ns-pulse excitation, though with higher excitation laser intensities on the order of 10^7 W.cm^{-2} [23]. The greater luminescence decay rates observed in Ref. [23] are attributed an increased contribution of the triplet-triplet annihilation mechanism.

The timescale of excitation is on order of picoseconds, and the fs-pulse durations used here are believed to cause nearly simultaneous excitation. The increased local excited state density (in time) in turn increases the likelihood of the triplet-triplet annihilation mechanism, because the collision rate, ergo the annihilation rate $f_{33\mathrm{A}}$, varies with the square of the particle density

$$f_{33\mathrm{A}} = N_{\mathrm{UO_2F_2^*}} N_{\mathrm{UO_2F_2^*}} \sigma_{33\mathrm{A}} v, \tag{7.3}$$

where $N_{\mathrm{UO_2F_2^*}}$ is the excited state density of UO_2F_2 ; $\sigma_{33\mathrm{A}}$ is the triplet-triplet annihilation cross-section; and v is the particle velocity. For interactions between particles A and B, the rate would be proportional to the product of each density $f \propto N_A N_B$; here $N_A = N_B = N_{\mathrm{UO_2F_2^*}}$. Longer pulse excitation (with lower laser intensities) results in prolonged distribution of the excited state in which annihilation occurs less fre-

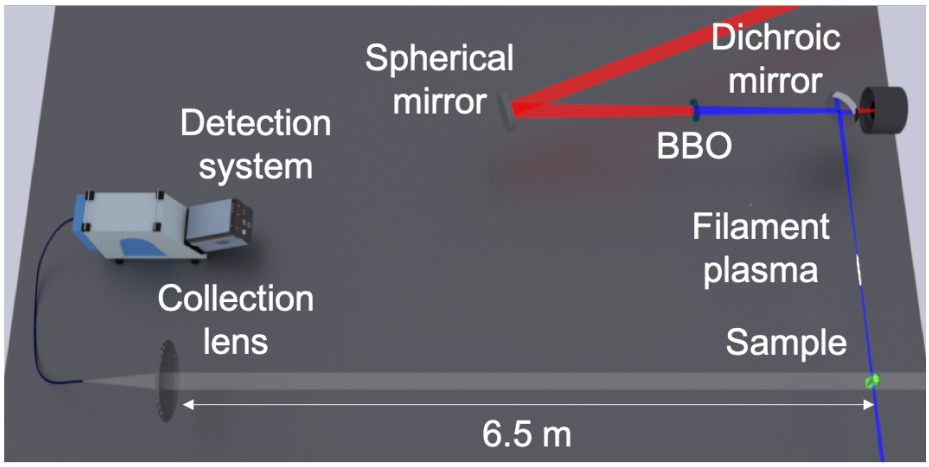

Figure 7.7: The experiment is modified to detect the luminescence of UO_2F_2 from a standoff distance of 6.5 m; the sample is still excited at a distance of 1.3 m from the focusing optic [217].

quently, and the primary luminescence mechanism is instead phosphorescence which is typically longer-lived. Moreover, for the relevant range of laser energies used in the present study (translating to the range of peak intensities 1.0–1.6 $\times$ 10^{11} W.cm^{-2}), the total luminescence appears saturated as shown in Fig. 7.6. These results may indicate saturation of the local excited state density, such that the rate of the annihilation mechanism is at a maximum. Ultimately, the saturated contribution of annihilation to the measured decay rate may bode well for analytical measurements, in which the time-signature is more reproducible using filamentation with the relevant range of peak intensities. Further work is necessary to confirm that triplet-triplet annihilation is more prevalent for ultrashort-pulse excitation and to explore the effect of concentration and laser intensity on the occurrence of this phenomenon in more detail.

7.2.3 Scaling the detection distance for filament-induced fluorescence spectroscopy of UO_2F_2

Further work is necessary to explore the trend of the signal for greater intensities ($\gtrsim$ 10^{11} W.cm^{-2}). These intensities are easily exceeded by the typical filament

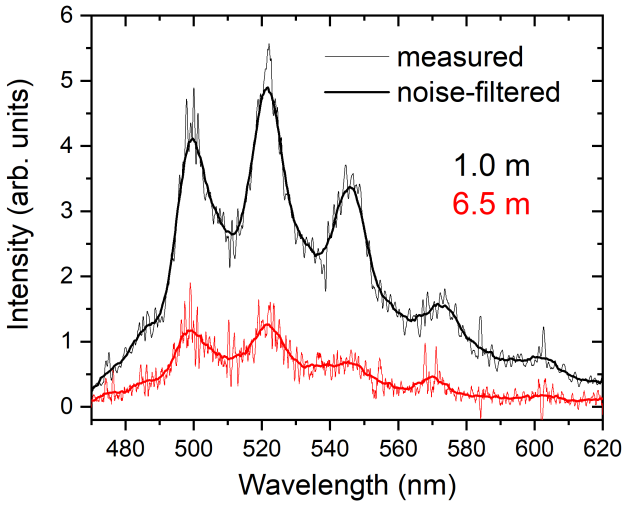

Figure 7.8: UO_2F_2 luminescence spectra are compared between the 1-m and 6.5-m standoff detection schemes. A noise-filtering method is used to help guide the eye to the shape of the luminescence [217].

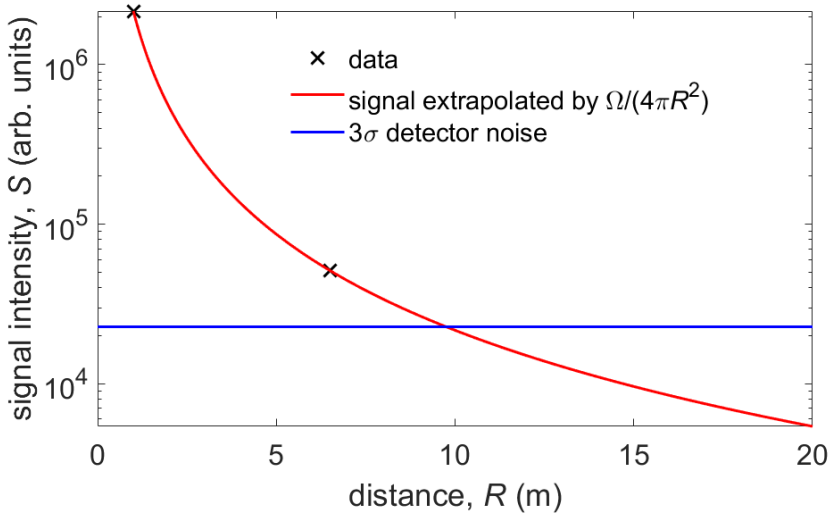

Figure 7.9: UO_2F_2 luminescence is extrapolated considering the solid angle $\Omega/4\pi$ of the collection optic and the inverse square law $1/R^2$ to predict the maximum detection distance. A detection distance of 9.7 m is predicted for when the extrapolated signal reaches the 3σ detector noise level.

clamped intensities, on the order of 10^{13} W.cm^{-2} as discussed in Sec. 4.1.6. In the present case, the limitation of sample damage prohibited investigating this range of greater intensities. In this section, the feasibility of standoff detection is demonstrated and limits of the detection range are discussed. The results shown here may be scalable for extended excitation distances also, if the trend of saturated signal level continues for larger intensities.

Figure 7.7 shows a standoff detection scheme, in which the collection optic and detector are moved to a distance of 6.5 m away from the sample. In this scheme, the collection optic is changed to a 4"-diam., 20-cm FL lens to increase the solid angle efficiency. The solid angle for a circular aperture with radius r_{coll} and at a distance R is derived from Eq. (4.18)

$$\Omega = 2\pi \left(1 - \frac{R}{\sqrt{r_{\text{coll}}^2 + R^2}} \right). \tag{7.4}$$

The solid angle efficiency from the 1-m detection scheme is 1.6×10^{-4}, and the larger collection optic for the 6.5-m detection preserves the efficiency 1.5×10^{-4}. Notably, the 400-µm fiber with numerical aperture of 0.2 accepts the entire range of angles from the collection optic with numerical aperture 0.25, as described by Eq. (4.21). However, the small fiber aperture size limits the coupling efficiency to 0.33 by comparing the AFOV [Eq. (4.20)] of 58° to the TFOV [Eq. (4.19)] of 177°. The coupling between the fiber and detector and other instrument losses remains the same between both schemes. Atmospheric attenuation is also ignored. The luminescence spectra recorded using both collection schemes are compared in Fig. 7.8. Luminescence is accumulated for 300 excitation laser shots, like in the 1-m collection experiments. In the current setup, the clear limiting factor toward detection is detector noise. Major contributors to detector noise include detector dark current (0.1 photoelectron/pixel/second) and background leakage. This noise is determined experimentally with the same number

of accumulations (300 shots) as the signal to have a mean number of counts 1.4×10^4 (47 counts per shot, ∼10.5 of these are predicted to arise from dark current with a 1024×1024 pixel array and integration time of 100 µs) and standard deviation 2.9×10^3. A maximum detection distance of ∼9.7 m is predicted by extrapolating the total signal measured in both collection schemes with the inverse square law and accounting for the differences in geometric attenuation (solid angle, coupling), as shown in Fig. 7.9. The 4"-diam., 20-cm FL lens is chosen as the collection optic for this prediction, and a third-standard deviation (3σ) noise cutoff is set as the lower limiting factor toward detection. These results demonstrate practical standoff detection of UO_2F_2, though further work is necessary to explore different analyte concentrations and the scalability of filament excitation distance.

7.3 Summary

The results presented in this chapter demonstrate a novel standoff detection method for UO_2F_2 by combining filamentation with LIF. Unique, fast decay rates are discovered for fs- and filament-excitation schemes and attributed to an increased likelihood of prompt triplet-triplet annihilation as opposed to longer-lived phosphorescence. The saturated emission for the range of excitation laser intensities on order of 10^{11} W.cm^{-2} used in this study bode well for scaling the excitation distance using filamentation, which can sustain clamped intensities on the order of 10^{13} W.cm^{-2} over significant distances. Here, a standoff detection distance of 6.5 m is demonstrated, and a maximum detection distance of 9.7 m is predicted for the same collection scheme. Nevertheless, further work is necessary to explore the scaling of excitation distance and determine the analyte concentration limits for minimum detection. The contribution of the annihilation decay mechanism should also be investigated for lower analyte concentrations. Finally, other forms of UO_2F_2, for example as an aerosol or solid particulate, should be interrogated in order to simulate field applications.

Such applications of the proposed method include guiding remediation around uranium conversion and enrichment facilities as well as monitoring declared or detecting undeclared enrichment activity.

CHAPTER 8

Millisecond-Duration Suppression of Optical Signals Using Filamentation

Chapters 6 and 7 demonstrate that filamentation can be used to extend the propagation distance of the excitation source used in various analytical spectroscopy methods including LIBS (FIBS) and LIF. In these previous chapters, the standoff collection of optical signals formed following excitation was optimized: first, by temporal gating to reject unwanted backgrounds; and second, by maximizing the collection efficiency via solid angle, coupling, FOV, etc. Chapter 4, Sec. 4.3, discusses in more detail the components that must be considered when constructing a collection system. Section 4.3.1 in Chapter 4 describes an approach to use the structures associated with filamentation for waveguiding optical signals. In particular, the thermal waveguiding mechanism relies on the relaxation of the gas temperature and density in the wake of the filament plasma occuring over several milliseconds and was shown to enhance the collection of spectroscopic signal from an air LPP [117]. Thermal waveguiding involves structuring the filament in such a way that an annular region of greater gas temperature and pressure is created. The thermal relaxation of the propagation medium can also be used as a means to reject time-varying optical signals in the wake of an unstructured (Gaussian), single filament plasma.

This chapter presents a novel approach that uses the ms-timescale thermal relax-

ation of air left in the wake of a single filament plasma in combination with imaging to reject a temporal slice of the optical signal. The thermal relaxation of air in the wake of the filament has been extensively studied in both experiments and simulations [36, 115, 118, 135, 137, 174, 187, 197], and the idea that the depressed index region in the wake of a single filament could be used as an *anti-guide* has been proposed [44]. However, filament anti-guiding of spectroscopic optical signal, such as the signal produced in LIBS or FIBS, has not yet been reported. In Sec. 8.2, the ms-time-scale index change of air is reconstructed from shadowgraphic imaging of the filament structure and compared to index change predicted by an analytical model. The results from the experimental determination of the refractive index change using shadowgraphy agree well with previous interferometric measurements [36] and simulations [174]. Shadowgraphy presents a simpler means to experimentally measure such index changes, requiring only a single arm of the probe beam in contrast to interferometry, which compares the probe arm to a reference arm via interference. In Sec. 8.3, ms-duration anti-guiding of both a CW beam and time-varying spectroscopic signal is demonstrated using the thermal relaxation mechanism in the wake of a single filament. The boundary of the anti-guiding structure causes significant reflection and refraction, inhibiting the propagation of the signal. These results bode well for remote sensing applications using techniques like FIBS, where early-time signal suppression may be used to reject continuum, or late-time signal suppression may be used to reject molecular or agglomerate hot-body emissions.

8.1 Experiment

Figure 8.1 shows the experiment for probing and testing the filament anti-guide structure that includes multiple diagnostics. The Lambda Cubed laser system is used in this study with an energy of 1 mJ, pulse duration of 50 fs, central wavelength of 800 nm, and 480 Hz repetition rate. The 11-mm Gaussian diameter beam is focused

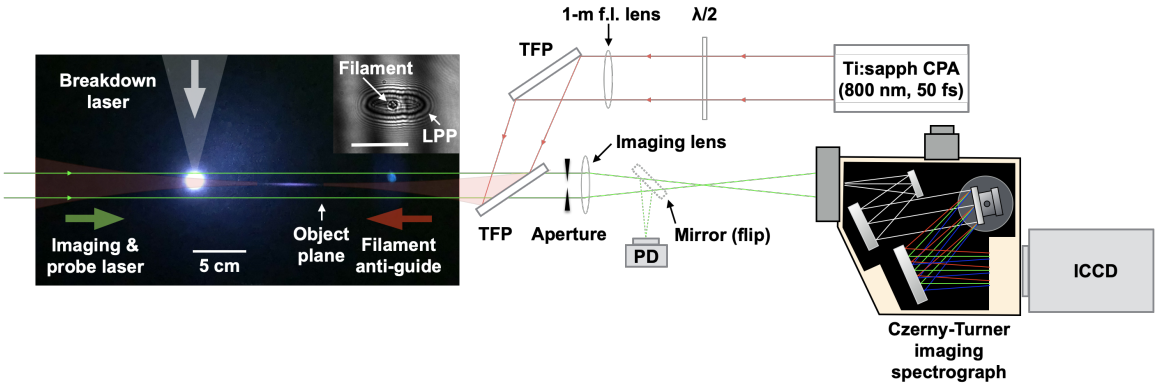

Figure 8.1: Multi-diagnostic scheme for probing and testing of anti-guiding using a single filament structure. Two counterpropagating probes are used interchangeably: a 10-ns, 532-nm Nd:YAG pulse and a CW 632.8-nm He-Ne laser. A pair of thin-film polarizers (TFP) is used to attenuate the 50-fs, 800-nm Ti:sapphire beam in combination with a half-wave plate ($\lambda/2$) which forms the filament and separate it from the probe. The filament beam is focused with a 1-m FL lens. The *exit plane* of the filament anti-guide is imaged onto an imaging Czerny-Turner spectrometer coupled to a camera (ICCD or CCD, interchangeably). A removable mirror is used to direct the probe onto a photodiode (PD) to determine temporal evolution of the anti-guided He-Ne signal. For anti-guiding spectroscopic signals, a 10-ns, 1064-nm Nd:YAG pulse is used to breakdown air or ablate an aluminum-containing alloy target, as shown in the photograph. An iris is used to select the region of interest in the image for anti-guiding. The inset shows alignment of an air breakdown spark with the filament anti-guide using the shadowgraphic imaging diagnostic; the scale in the inset denotes 1 mm.

to form a filament using a 1-m FL lens ($f/90$). A pair of thin-film polarizers is used to attenuate the 800-nm beam in combination with a half-wave plate and also to separate it from the counterpropagating, cross-polarized probe beam. Two probes are used interchangeably: a 10-ns, 532-nm Nd:YAG pulse and a 632.8-nm CW He-Ne laser. The exit plane of the filament anti-guide is imaged onto the slit of an imaging Czerny-Turner spectrometer (Horiba Jobin Yvon, MicroHR) coupled to a camera (ICCD or CCD, interchangeably). The ICCD (Andor, iStar 334T) is used in combination with the CW probe, while the CMOS (Mightex, CGE-B013-U) is used in combination with the pulsed probe. The *exit plane* of the anti-guide is defined as the point along the propagation axis where the filament plasma begins to form, determined experimentally by the appearance of a "hole" in the image by varying the image plane along the propagation axis. A removable mirror is used to direct the probe onto a photodiode (Thorlabs, DET36A, 14 ns rise time) to determine temporal evolution of the anti-guided He-Ne signal. For anti-guiding spectroscopic signals, a 10-ns, 1064-nm beam from an Nd:YAG laser is focused using a 15-cm FL lens to either breakdown air or an aluminum alloy target placed at geometric focus. The imaging diagnostic allows for alignment of the pump, probe, and LPP as shown by the inset of Fig. 8.1. For anti-guiding of the spectroscopic signal, the LPP is formed 10 cm after geometric focus of the 1-m FL lens used for filamentation, as shown by the photograph in Fig. 8.1.

8.1.1 Finite-difference method for reconstruction of the refractive index change from shadowgraphy

As discussed in Chapter 2, Sec. 2.1.3, shadowgraphic imaging can be used to reconstruct the change in refractive index of a perturbed medium. Here, the finite difference method is used to reconstruct the index [53]. Equation (2.29) may be

rewritten as

$$\Delta I = \frac{d^2}{dy^2}\delta N, \tag{8.1}$$

where $\Delta I = \frac{1}{L_{\text{det}}}\frac{I_0 - I_m}{I_0}$ and $\delta N = \int_L \delta n dz$. The measured change in intensity at point i is

$$\Delta I_i = \frac{\frac{\delta N_{i+1} - \delta N_i}{\Delta y} - \frac{\delta N_i - \delta N_{i-1}}{\Delta y}}{\Delta y} = \frac{\delta N_{i-1} - 2\delta N_i + \delta N_{i+1}}{\Delta y^2}, \tag{8.2}$$

where Δy, here, is the pixel size of the detector. The measured intensity pattern (along of two principal axes) is then related to the index change by the matrix A with elements $a_{ij} = \frac{1}{\Delta y^2}$ and $a_{ii} = -\frac{2}{\Delta y^2}$:

$$\Delta I = A\delta N. \tag{8.3}$$

In this work, an iterative Jacobi algorithm is used to reconstruct the one-dimensional (1D) refractive index change from shadowgraphic imaging of the filament and its remnants. The Jacobi algorithm is outlined in more detail in Ref. [53].

8.2 Forming the filament anti-guiding structure

This section investigates the ms-timescale change in refractive index of air following the formation of a single filament via experiment and modeling. Shadowgraphy is used with a counterpropagating probe to determine the refractive index change. Figure 8.2 shows example shadowgraphs of the evolution of the gas in the wake of a single-filament plasma formed from a near-Gaussian beam profile. The changes in gas temperature and pressure in the wake of the filament plasma cause the observed change in refractive index of the medium. The counterpropagating probe consequently undergoes reflection and refraction at the interface of the air and thermal anti-guide.

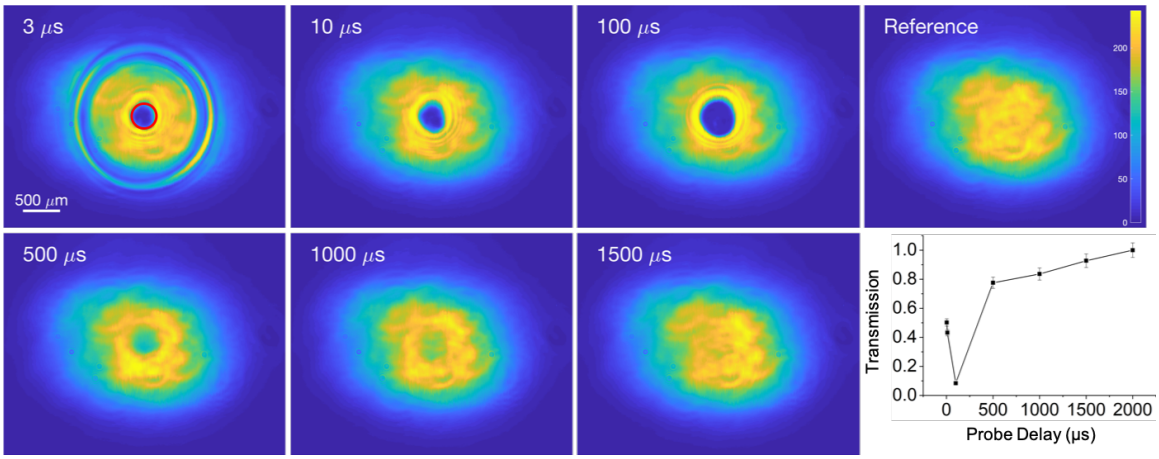

Figure 8.2: Time-resolved shadowgraphic images using the 10-ns, 532-nm Nd:YAG probe. The probe beam is used to image the exit plane of the filament as described in Sec. 8.1. The probe delays are shown in each image, and determined with respect to the arrival of the filament laser pulse. A reference beam profile is also shown. The red circle denotes the region of interest in which the probe transmission is measured, as shown in the plot [221].

The shockwave is still within the probe beam in the earliest frame; however, the shock expands beyond the image region by the time of arrival of the second probe. Another noteworthy feature in the earliest frames is the dark region, or "hole", at the center of the probe beam in the wake of the plasma. The plasma dissipates within several tens of nanoseconds as discussed in Chapter 5, Sec. 5.1. The graph in Fig. 8.2 shows the ratio of the energy in the marked region of interest and the energy over the entire reference beam profile as a function of time, as determined by image analysis. The transmitted signal in the region of interest drops to ∼5% at a delay of 100 µs after the filament pulse, and the hole persists for nearly 1.5 ms.

Cheng *et al.* [36] demonstrated that the behavior of the gas in the wake of the filament may be approximated by an analytical model which is derived as a solution to the thermal diffusion equation. Here, the evolution of the peak change in temperature and pressure of the gas is investigated. From Ref. [36], the peak gas temperature T_p

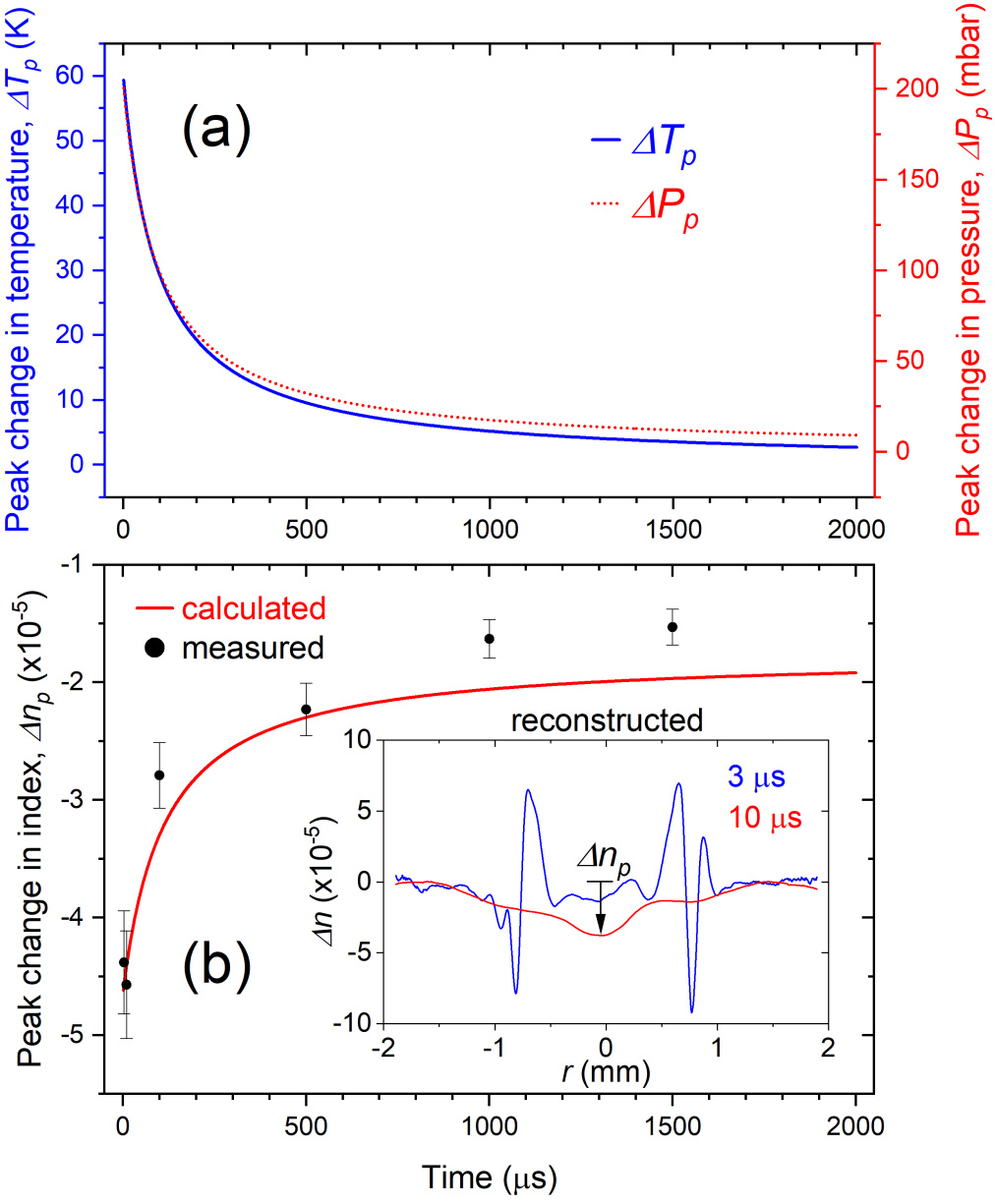

Figure 8.3: (a) The temporal evolution of the peak change in air temperature (left) and pressure (right) is predicted using an analytical model [36]. (b) Temperature- and pressure-dependent Sellmeier equations [178] are used to predict the peak change in the refractive index from the results of the analytical model in (a). The calculated change in index is compared to measurements. A 1D finite-difference reconstruction is used to determine the change in index from shadowgraphy with $L_{\text{det}} = 10^7$ µm. The peak index change is determined from each profile as shown by the inset.

evolves as a function of time t according to

$$\Delta T_p(t) = T_p(t) - T_b = \Delta T_{\max} \frac{R_0^2}{R_0^2 + 4\alpha t}, \tag{8.4}$$

where $\Delta T_{\max}$ and T_b are the maximum temperature change and the background temperature of the gas, respectively; R_0 is the initial (Gaussian, $1/e$) radius of the perturbed region of the medium; and α is the ratio of the thermal conductivity κ and specific heat capacity of the gas c_p, $\alpha = \kappa/(c_p\rho)$. The peak change in pressure is determined by the ideal gas law, $P = \rho RT$, where ρ is the gas density and R is the gas constant, resulting in the model:

$$\Delta P_p(t) = P_b \frac{\Delta T_{\max}}{T_b} \frac{R_0^2}{R_0^2 + 4\alpha t}, \tag{8.5}$$

where P_b is the background gas pressure. The calculated temperature and pressure of air in the wake of the filament are used to predict the peak change in the refractive index of the gas and for comparison with measurements. Here, the maximum temperature change $\Delta T_{\max}$ is a free parameter that is used to match the change in index to that measured from shadowgraphy. The initial radius R_0 of the perturbed region is also determined from measurements to be 50 µm. The background temperature and pressure of air are 300 K and 1013.25 mbar, respectively. The change in refractive index is calculated using temperature- and pressure-dependent Sellmeier equations for air [178]. A 1D finite-difference reconstruction is used to determine the refractive index change from shadowgraphy, as described in Sec. 8.1. The finite-difference reconstruction is performed along the centerline of pixels from the images shown in Fig. 8.2. The peak change in index is determined at the center of the reconstructed radial profile, as shown by the inset of Fig. 8.3(b). The peak index change is iteratively compared to that predicted by varying $\Delta T_{\max}$ in the model. A maximum temperature change of 60 K yields a good match for the measured change in index in

the range -5×10^{-5} to -1×10^{-5}. The measured and predicted change in index are comparable to those reported in Ref. [36], in which a maximum temperature change of ∼100 K was determined, and the change in index was measured to be in the range -6×10^{-5} to -1×10^{-5} using interferometry. Further, these results agree with computational results in Ref. [174]. Shadowgraphy involves simpler implementation than interferometry by requiring only a single beam arm without the need for a reference and is demonstrated as an alternative means to quantitatively measure change in the refractive index of the filament propagation medium even over long timescales, with similar sensitivity to interferometry, $\mathcal{O}(\Delta n \sim 10^{-5})$. The following section presents a practical demonstration of the filament anti-guide used for rejection of CW and time-varying optical signals.

8.3 Demonstration of anti-guiding of spectroscopic signal using filamentation

The efficacy of anti-guiding is demonstrated with a CW signal as shown in Fig. 8.4. In these measurements, the counterpropagating CW He-Ne probe is coupled into the anti-guide structure with a 4-m FL lens ($f/400$), as shown in Fig. 8.4(a) and (b), in order to determine the extent to which such optical signal may be rejected. A photodiode is used to measure the time-dependent He-Ne signal transmitted through the anti-guide. The transmitted signal returns to its original level after ∼1.5 ms between subsequent laser pulses for a filament laser repetition rate of 480 Hz. The relaxation timescale is consistent with that determined in Sec. 8.2, as shown by the plot in Fig. 8.2 and Fig. 8.3. The maximum signal attenuation is ∼8% in this configuration. Following experiments demonstrate the practical application of the anti-guide in combination with imaging to reject spectroscopic optical signal from an LPP.

The emission from an LPP formed following ns-pulsed LA of an aluminum-containing

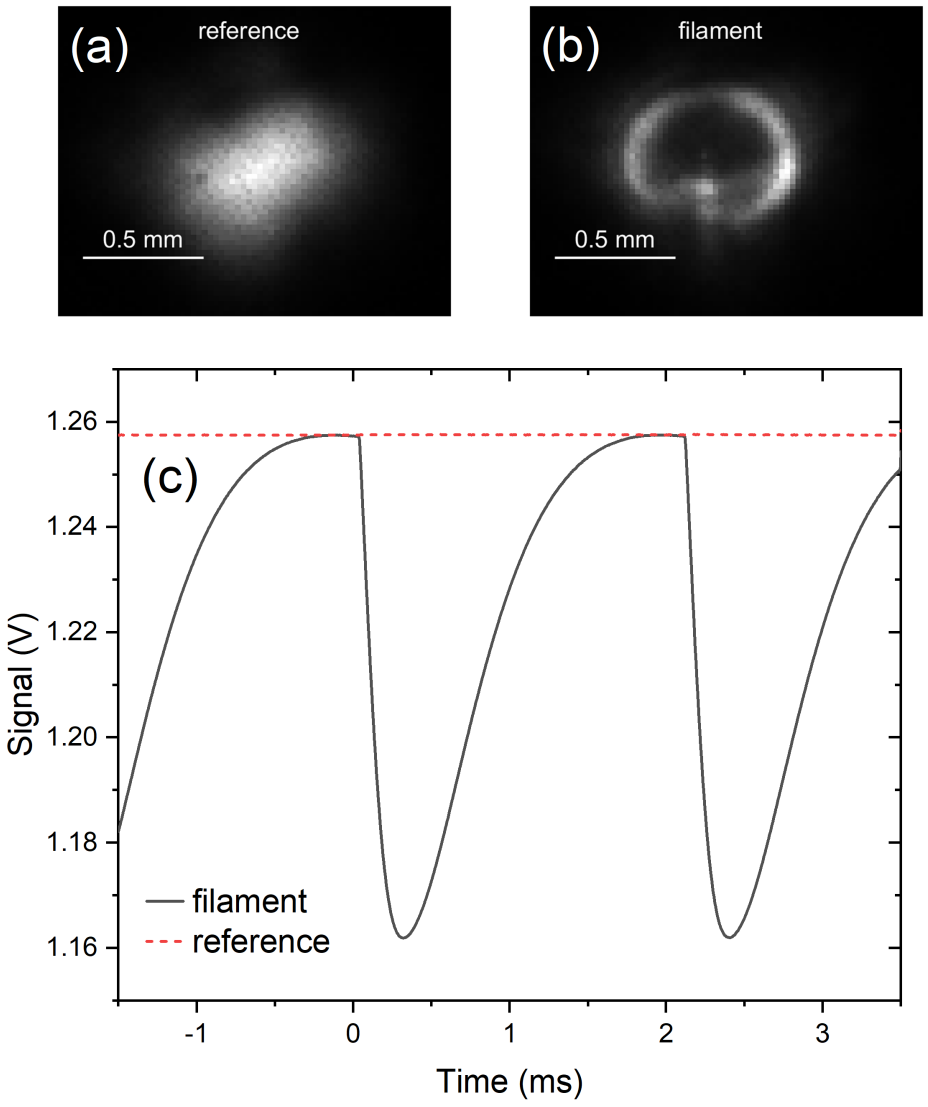

Figure 8.4: (a) Reference He-Ne spot focused into the filament anti-guide structure using a 4-m FL lens. (b) Example filament anti-guide structure illuminated with the focused He-Ne probe. Both reference and filament images were recorded using an ICCD with a gate delay of 0 µs and width of 200 µs. (c) Temporal evolution of the transmitted focused He-Ne probe through the filament anti-guide measured with a photodiode. Effects from several subsequent filament laser pulses are shown in the window; the laser repetition rate is 480 Hz. The dashed line shows the unperturbed (CW) He-Ne signal.

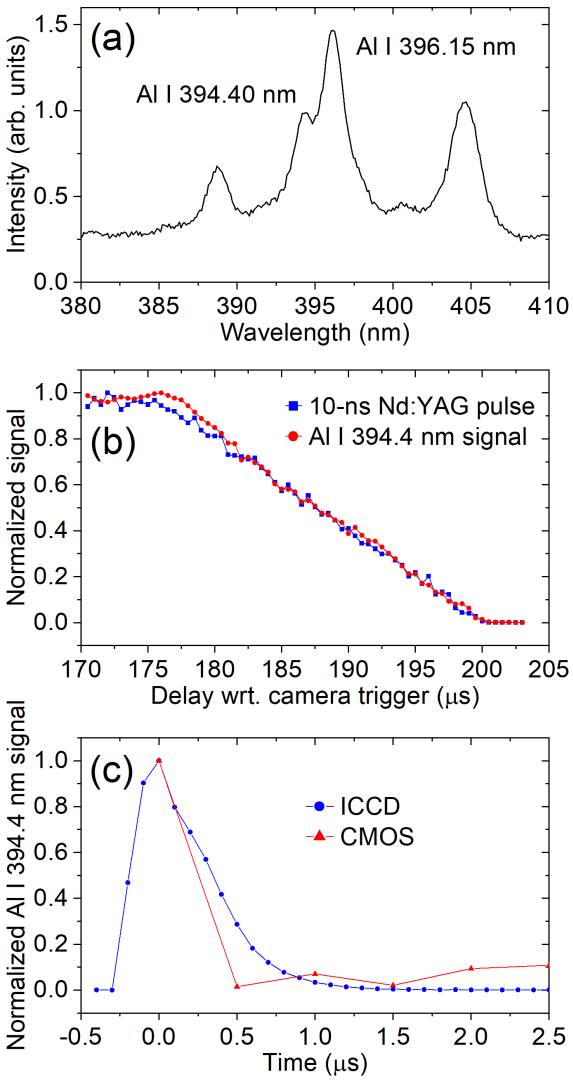

Figure 8.5: (a) Example spectrum from an LPP formed following ns-pulsed LA of an aluminum target. The spectrum is recorded with an ungated CMOS camera, with a trigger delay of 1 µs with respect to the ablation laser. (b) Time-varying signal is convolved with the slow falling edge of the CMOS exposure window. A 10-ns pulse from an Nd:YAG laser is used to determine the temporal shape of the falling edge, and Fourier transform deconvolution is used to determine the temporal dependence of the Al I 394.40 nm line, shown in (c). The results of the deconvolution are compared to a fast-gated measurement of the Al I signature using an ICCD.

alloy target is studied. The relevant spectral and temporal signatures from the Al-LPP are shown in Fig. 8.5. Anti-guiding of Al I 394.40 nm and Al I 396.15 nm signatures, shown in Fig. 8.5(a), is investigated. For standoff or remote sensing especially, the temporal signature may be equally important to the spectral signature, because temporal gating is an effective means to distinguish signal from background. The filament anti-guide may be used as an all-physical gate to suppress unwanted early- (*e.g.* plasma continuum) or late-time optical signal (*e.g.* molecular or agglomerate hot-body emission) as an alternative to using a time-gated detector. In these experiments, a triggerable but ungated CMOS camera is used as the detector to demonstrate using the anti-guide as a physical (as opposed to electronic) gate. The CMOS detector has a relatively long exposure window of ∼0.2 ms, with a slow falling edge. The falling edge of the exposure window is measured in Fig. 8.5(b) using a 10-ns laser pulse from an Nd:YAG. A similar measurement is made with the emission from the Al-LPP, and discrete Fourier transform deconvolution is used to determine the decay of the signal from the LPP. The slower decay of the LPP emission f is convolved with the falling edge of the exposure window g, $f * g = h$, where h is the measured signal. The signal is deconvolved in the frequency domain following a Fourier transform $F = H/G$ where F, H, and G are the Fourier transforms of f, h, and g, respectively. Here, the falling edge measured with the short-pulse laser is used to determine the response function. The results of the deconvolution are shown in Fig. 8.5(c). The deconvolved decay of the emission from the Al-LPP measured with the CMOS camera matches that measured using a fast, electronically-gated ICCD. The Al I 394.40 nm line emission persists over ∼1 µs. This procedure demonstrates that despite the long exposure window and slow falling edge of the CMOS camera, a comparably fast time signature may be deconvolved using a scanning measurement.

Figure 8.6(a–c) shows the imaging method used for alignment of the LPP to the filament anti-guide and iris aperture to isolate the anti-guide region of interest.

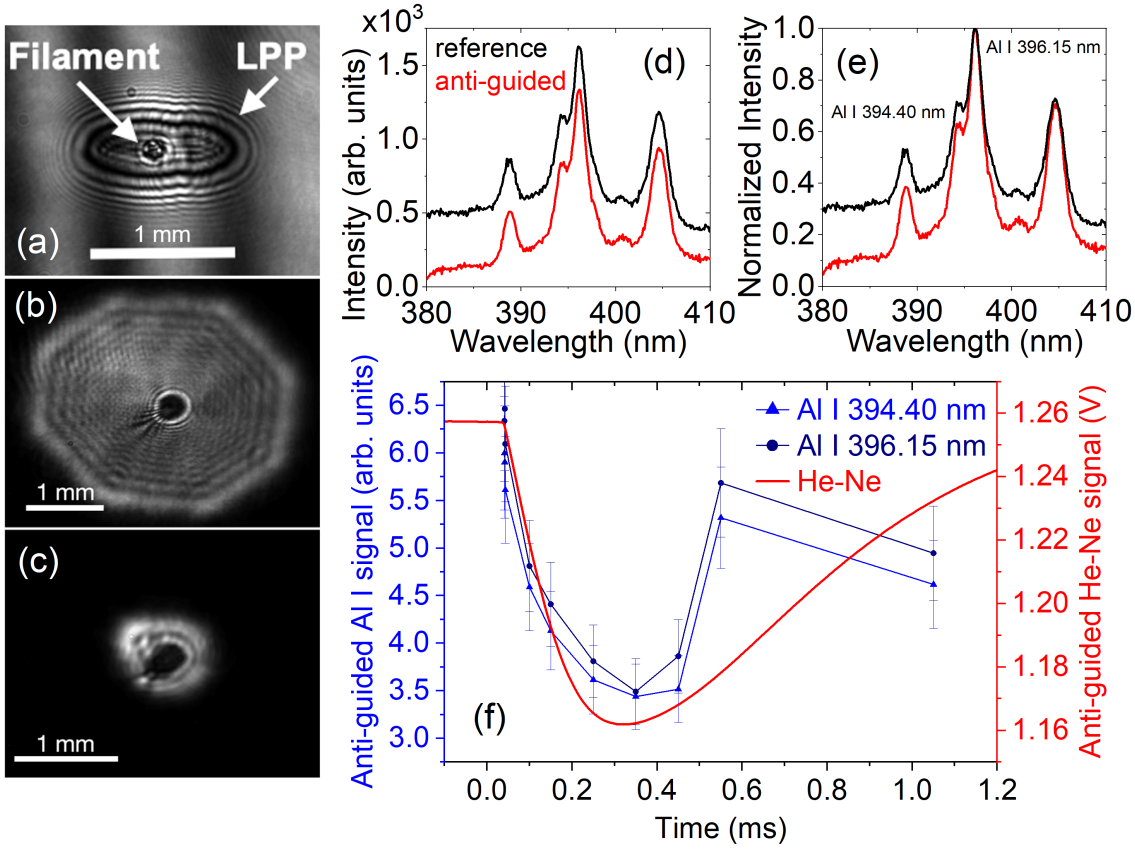

Figure 8.6: Imaging was used for (a) alignment of the LPP signal source to the filament anti-guide and (b–c) isolating the anti-guiding region. (d) Example anti-guided spectrum from the Al-LPP compared to a reference spectrum without the anti-guide. (e) Normalized spectra. (f) The anti-guiding timescale for Al signatures is compared to that of a counterpropagating CW He-Ne probe, from Fig. 8.4.

Figure 8.6(a) shows the alignment of an air breakdown plasma as a surrogate for the solid-target (Al) plasma which was actually used for anti-guiding measurements. For solid-target ablation, an aluminum plate is placed at the geometric focus of the 15-cm FL lens, whose location was not changed from the measurements with the air LPP. The iris aperture is a physical means to narrow the FOV, though a post-processing procedure may similarly be used, as shown in Fig. 8.2. Here, the ungated CMOS detector, with an exposure window of ∼0.2 ms, is used. The ablation laser and CMOS trigger are synchronized, such that the laser fires 0.1 ms after the CMOS trigger ensuring the entire plasma emission (which persists for ∼1 µs as shown in Fig. 8.5) is integrated. The ablation laser and CMOS trigger are delayed with respect to the filament laser pulse. After alignment of the LPP, anti-guide, and iris via imaging, the spectrograph slit is closed to 50 µm and grating is rotated to resolve the Al I lines. An example anti-guided spectrum from the Al-LPP is shown in Fig. 8.6(d) and (e); evidently, both identified Al I spectral signatures are suppressed, and the background is suppressed more improving prospects for analytical measurements. The signal-to-background is improved from ∼2.3 in the reference to ∼9.0 in the anti-guided spectrum. In this study, the early-time continuum is integrated alongside the spectral line signatures, because of the use of the ungated CMOS detector. Figure 8.6(f) shows the measured transmission of the Al I spectral signatures for delays through the filament anti-guide. Notably, the anti-guiding timescale is similar to that observed in previous configurations using a counterpropagating probe laser (unfocused, pulsed probe in Fig. 8.2 and focused CW probe in Fig. 8.4). In contrast to the ns-pulsed or CW collimated probes, the LPP is an omnidirectional source with a ∼µs-long temporal signature. The directionality of the emission from the LPP complicates measurements in addition to spectrally-resolving the image of the exit plane of the anti-guide. Nevertheless, the anti-guide is shown to suppress Al I signatures by ∼46%. These results have implications for standoff or remote detection of emission from LPPs

relevant to FIBS. It is demonstrated that the filament may be used in combination with imaging as a physics-based means to suppress spectroscopic signature with a time dependence that could allow improved measurements with ungated detectors such as the CMOS cameras, as used in this demonstration. For example, a user may want to reject early-time continuum or late-time molecular emission from an LPP.

8.4 Summary

Previous works demonstrated that the thermal relaxation of the gaseous propagation medium in the wake of the filament plasma may be structured to form waveguides, which can be useful for guiding optical signals. The residual temperature and pressure changes in the gas cause a change in the refractive index on order of 10^{-5} in air which lasts on order of milliseconds. This chapter demonstrates that this change in refractive index could be useful for anti-guiding optical signals. First, in Sec. 8.2, it is shown that shadowgraphy can be used as an alternative quantitative technique to measure the residual refractive index left in the wake of a single-filament plasma with similar sensitivity to interferometry, $\mathcal{O}(\Delta n \sim 10^{-5})$. The method is used to determine the temporal dependence of the peak change in index on the ms-timescale, and results agree with the analytical model which predicts that the index change is influenced by variations upwards of 20% in the air temperature and pressure. These results similarly agree with previous interferometric measurements [36] and simulations [174]. Further work should be done to investigate larger laser repetition rates $\gtrsim$1 kHz which may cause lasting effects on the gas properties, because relaxation is found to occur between 1–1.5 ms. Section 8.3 discusses a practical application of the filament anti-guide for suppressing counterpropagating CW signal from a He-Ne probe as well as spectral line signatures from an Al-LPP. The spectral signatures from the Al-LPP are shown to be suppressed by ∼46% when using an iris to isolate the region of interest. These results demonstrate that the filament anti-guide can be

used as an physics-based method to reject time-varying spectral signatures, for example the unwanted early-time continuum from an LPP, as an alternative to using a fast-gated detector. The anti-guiding technique, therefore, may have implications for standoff or remote FIBS. The following chapter discusses concatenation of filament-driven thermal waveguides as another means to enhance analytical performance of the remote FIBS technique.

CHAPTER 9

Concatenation of Filament-Driven Thermal Waveguides

Previous works demonstrated that filamentation can be tailored to form a waveguide in a gaseous medium like air [34, 117, 137, 143, 197]. Such gas plasmas have been shown to be able to guide microwaves [34] and laser beams [143] when arranged into annular structures; this form of waveguiding persists only for several nanoseconds because the peripheral clad region, comprised of the plasma, dissipates rapidly as electron recombination occurs [8, 143, 249]. The free electron distribution in the plasma depresses the refractive index of the gas, described by Eq. (2.8), forming the equivalent of a waveguide clad. Annular plasma structures were produced using deformable optics, controlling the phase and intensity pattern of the filament-driver beam [34]. A modified Bessel-Gaussian intensity pattern was also proposed as a method to shape the annular plasma structure [249]. The refractive index change induced by the steep pressure gradient in the shockwave formed alongside the filament can also be used for waveguiding. Acoustic waveguiding was demonstrated with an unaltered Gaussian input intensity pattern [137] as well as with symmetric arrangements of several plasma filaments by shaping the phase pattern of the input beam [117, 197]. This waveguiding mechanism persists for several microseconds, corresponding to the rate of shockwave expansion. Thermal guiding relies on the longer-lived relaxation of temperature and

pressure of the gas in the wake of filament plasma, as discussed in Chapter 8. Prior work demonstrated notable improvement in the collection of optical signals enabled by filament-driven thermal waveguiding, including spectroscopic emission from an LPP [117, 197]. Thermal waveguiding relies on shaping the filament-driver beam in order to form an annular region with an elevated temperature and pressure, creating a clad region with depressed index. In previous work, a series of half-pellicles was used to seed and symmetrically arrange multiple filament cores [117]; other means to control the arrangement of multiple filaments have been proposed and demonstrated, for example the use of deformable optics [63] or a split lens, as described in Chapter 5, Sec. 5.2.1. This chapter demonstrates that two filament-driven thermal waveguides may be concatenated to extend the total waveguide length and increase the collection efficiency of optical signal and thereby improve analytical performance of the LIBS/FIBS method.

Concatenation of single- and multiple-filaments has been modeled [42, 80] and experimentally demonstrated [181, 236] for extending the filament plasma channel length. Other methods for extending the channel length that have been explored include a nested-phase configuration of filament driver pulses [151], externally "refuelling" the channel with a secondary laser pulse [16, 203], and modifying the input beam intensity and phase patterns [67, 76, 109, 189]. In the method explored in this dissertation, simultaneous elongation and control over the seeding and arrangement of multiple filament cores is necessary in order to extend the thermal waveguide length. A lens split into thirds is used to seed and control the arrangement of three filament cores, which form the equivalent of a clad of the thermal waveguide after plasma dissipation. Two such waveguides are formed and concatenated on the same axis, and the efficacy of signal collection is measured for each individual waveguide as well as the concatenated structure. The concatenated filament-driven thermal waveguide provides an enhancement of injected signal from a continuous-wave probe laser, as

well as enhancement of the signal-to-background ratio of characteristic line emission from an LPP, when compared to waveguiding with individual component structures.

9.1 Experiment

Figure 9.1 shows the experiment for forming and testing the individual and concatenated filament-driven thermal waveguides. The filament driver is an 800-nm, 55-fs pulse (480 Hz) from the Lambda Cubed Ti:sapphire-based CPA system. A half-wave plate is used to rotate the linear polarization of the beam, so it may be separated into two legs with a thin-film polarizer. The pulse energy for the reflected (s-polarized) leg is measured to be 5.2 mJ, and the pulse energy for the transmitted (p-polarized) leg is measured to be 5.6 mJ. A 2-m FL ($f/80$) lens is split into thirds and used to focus the reflected leg. The transmitted leg is focused using a 2.5-m FL ($f/100$) split lens. The transmitted leg is delayed by 20.5 ns with respect to the first leg using a delay stage; the delay ensures that this second pulse may propagate through the region in which the filament air plasma is formed by the first pulse and experience negligible perturbation from the free electron density, because electron recombination is expected to occur over several nanoseconds. The transmitted leg is recombined with the reflected leg through a second thin-film polarizer. The long-exposure photographs in Fig. 9.1 show the alignment of the two filament structures along the propagation axis. The focal plane of the 2.5-m FL lens is positioned 25 cm after the focal plane of the 2-m FL lens. A counterpropagating (632.8 nm) CW He-Ne probe is used for imaging and alignment of the filaments. This probe is later coupled into the 2.5-m filament-driven thermal waveguide using a 2.5-m FL ($f/250$) lens. The focal plane of the coupling lens, denoted as the *coupling plane*, is 12 cm after the focal plane of the 2.5-m FL split lens. The probe is first separated from the reflected leg of the filament-driver using the thin-film polarizer and then from the transmitted leg using a short-pass dichroic mirror with a cutoff wavelength of 638 nm. A series of 632.8-nm narrowband

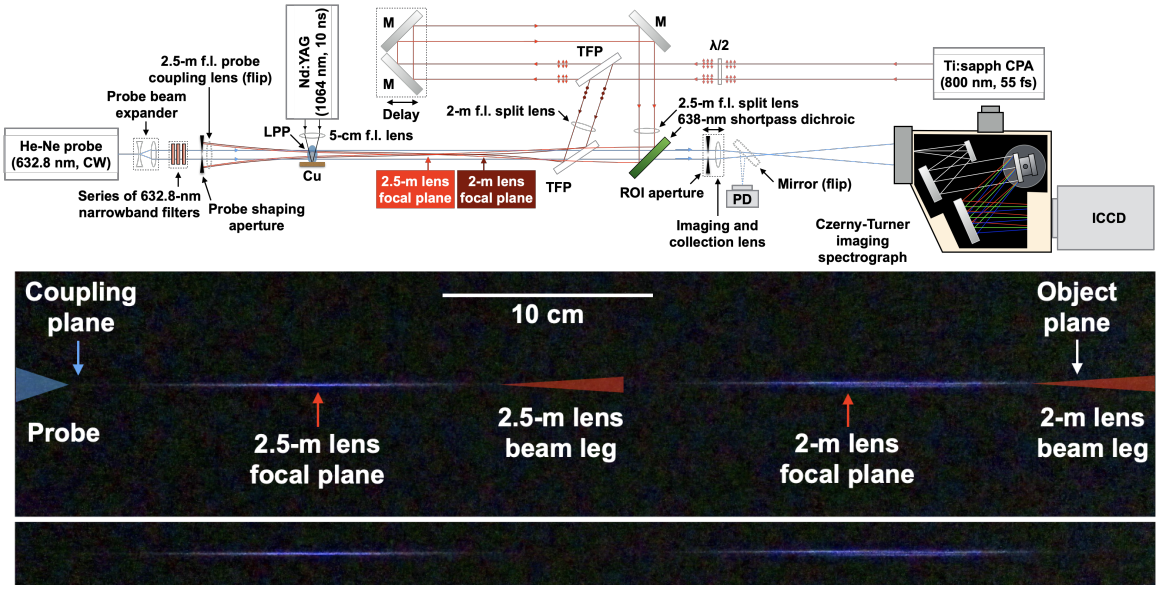

Figure 9.1: Multi-diagnostic scheme for probing and testing the concatenation of two filament-driven thermal waveguides. A counterpropagating CW 632.8-nm He-Ne laser is used interchangeably for shadowgraphic imaging of the waveguides and testing of guiding. A pair of thin-film polarizers (TFP) in combination with a half-wave plate ($\lambda/2$) is used to separate the 55-fs, 800-nm Ti:sapphire beam into two cross-polarized legs. The first leg is focused using a 2-m FL lens split into thirds to form the first thermal waveguide, while the second leg is delayed and focused using a 2.5-m FL split lens to form the second thermal waveguide. For guiding measurements, the He-Ne beam is coupled into the 2.5-m and concatenated waveguide structure using a 2.5-m FL lens; the *coupling plane*, denoted in the photograph, is located one focal distance from the coupling lens. The *object plane*, denoted in the photograph, of the 2-m and concatenated structures is imaged onto an imaging Czerny-Turner spectrometer coupled to an ICCD. The He-Ne and spectroscopic signals are separated from the filament-driver by a TFP and short-pass dichroic mirror with a cutoff wavelength of 638 nm. An aperture is used to select the region of interest (ROI) in the image for waveguiding. A removable mirror is used to direct the probe onto a photodiode (PD) to measure the temporal evolution of the guided He-Ne signal. For guiding spectroscopic signals, a 10-ns, 1064-nm Nd:YAG pulse is focused using a 5-cm FL lens in order to ablate a copper (Cu) target, such that the LPP is positioned at the coupling plane.

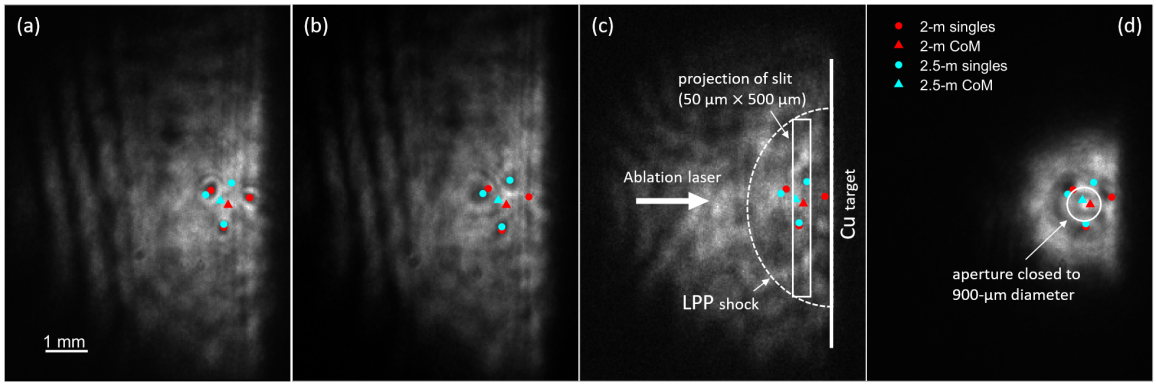

Figure 9.2: For guiding spectroscopic signal from a Cu-LPP, the counterpropagating He-Ne is used in an imaging configuration to align (a–b) each waveguide structure, (c) the target and LPP, and (d) the partially-closed aperture which is used to select the ROI in which the guided signal enhancement is observed. The circle markers denote the center of mass (CoM) for single-filament cores, while the triangle markers denote the CoM of the three cores. These markers are overlaid onto each image to compare the locations of each waveguide structure. The box in (c) is the projection of the 50-µm-wide slit onto the image for spectroscopic measurements (slit height is 500 µm), and the circle shows the size of the fully-closed aperture (900 µm-diameter) for He-Ne guiding measurements.

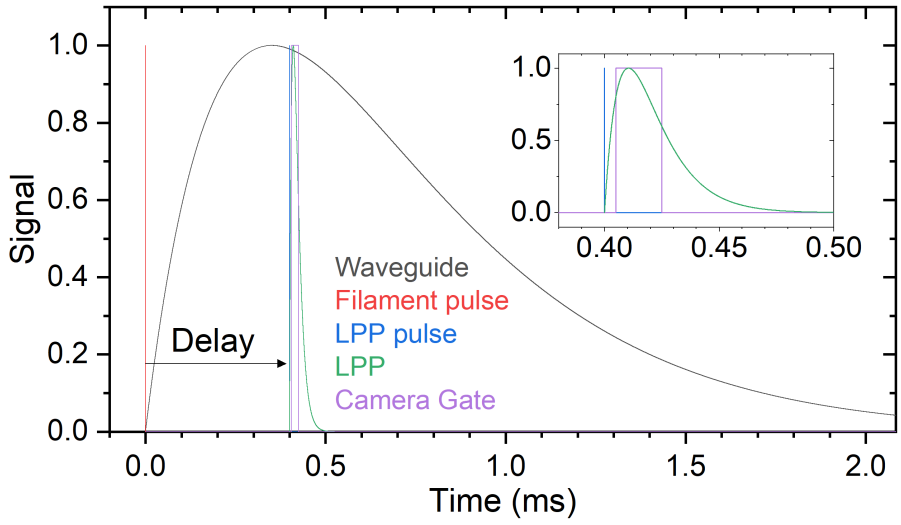

Figure 9.3: The camera gate is synchronized to the ablation laser with a delay of 1 µs and width of 20 µs, so that it integrates the emission from atomic species in the Cu-LPP while rejecting early-time continuum. The ablation laser and camera are then delayed arbitrarily with respect to the filament-driver pulse. An illustrative thermal guiding timescale is shown for comparison.

interference filters are used in combination with an iris to reject transmitted light from the filament driver and protect the He-Ne and other downstream optics. A 1"-diam., 40-cm FL lens is used to image the filaments and collect the signal transmitted through the waveguides. The imaging/collection lens is mounted on a stage so that the object plane may be translated along the propagation axis. The object plane for observing the exit mode of the guided He-Ne beam and measuring the guiding efficacy is denoted in the photograph in Fig. 9.1. This object plane is 10 cm before the focal plane of the 2-m FL split lens. An aperture whose opening size is adjustable is placed in front of the imaging lens to physically narrow the region-of-interest to that in which greatest guiding signal enhancement can be observed. A flip mirror is used to interchangeably direct the probe to either a photodiode (Thorlabs, DET36A, 14 ns rise time) or an imaging Czerny-Turner spectrometer (Horiba Jobin Yvon, MicroHR) coupled to an ICCD (Andor, iStar 334T). For imaging the filament structure and the exit mode of the guided He-Ne beam, an ICCD gate width of 100 µs is used. During imaging measurements, the spectrometer grating is rotated to view the first order diffraction image of the monochromatic He-Ne at 632.8-nm, aiding rejection of unwanted scatter from the filament, driver, and other sources. A narrowband 632.8-nm interference filter placed before the photodiode is used similarly for this purpose.

For guiding spectroscopic signals from an LPP, a 10-ns, 1064-nm, 100-mJ pulse from an Nd:YAG laser (Quantel, Evergreen^2) is focused with a 5-cm FL ($f/5$) lens onto a copper target. The focusing configuration is arranged so that the LPP is centered on the coupling plane for the He-Ne probe. Figure 9.2 shows the alignment of two filament waveguides formed with the 2-m and 2.5-m split lenses with respect to one another. The mean separation between filament cores in the 2-m split lens structure is ∼900 µm, and the mean separation for the 2.5-m split lens case is ∼800 µm. The distance between the centers-of-mass of the structures is ∼200 µm. Subsequently, the copper target and LPP are aligned with respect to the waveguides, and then the

aperture is similarly aligned. Due to the rapid timescale of the LPP evolution, a 2-μs gate width is used to record the image the LPP; whereas the other images were recorded with a longer gate width of 100 μs. The target is translated periodically to avoid excessive drilling or cratering which may influence LPP formation. Figure 9.3 shows a diagram which outlines the synchronization of the filament driver, ablation laser and LPP, and camera gate. For spectroscopic measurements of the emission from the Cu-LPP, the spectrometer slit is closed to 50 μm, and the grating is rotated to view the spectral region centered at ∼515 nm. The camera gate is synchronized to the ablation laser pulse with a delay of 1 μs and width of 20 μs. In this way, the early-time continuum emission from the LPP is avoided. The ablation laser and camera are then delayed with respect to the filament driver pulse. Illustrative profiles of the filament-driven thermal waveguide and evolution of the LPP are shown in Fig. 9.3 for comparison.

9.2 Guiding continuous optical signal with a concatenated filament-driven thermal waveguide

Figure 9.4 shows images of the filament-driven waveguide structures formed using the 2-m FL split lens and the 2.5-m FL split lens, respectively. The object plane is changed in each case by translating the imaging lens. The elevated gas temperature and pressure in the wake of the filament plasma are expected to decay according to Eqs. (8.4) and (8.5), respectively, causing a change in the refractive index as described in Sec. 8.2. In previous work, the "hole" diameter (FWHM, $d_{1/2}$), that describes the size of the perturbed index region, was found to increase as a function of time according to [36]

$$d_{1/2} = \sqrt{R_0^2 + 4\alpha t}. \tag{9.1}$$

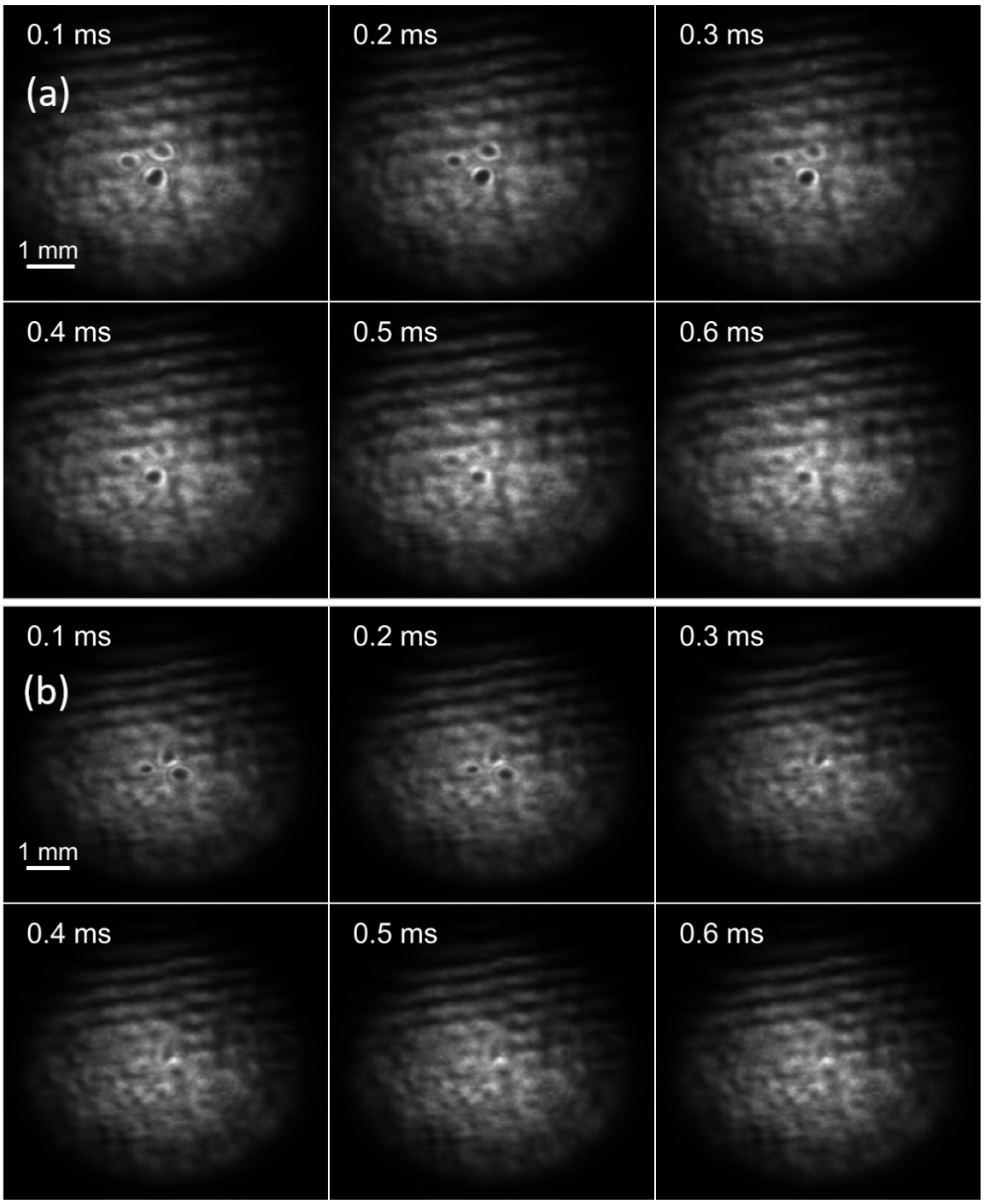

Figure 9.4: Shadowgrams showing the temporal evolution of the filament-driven thermal waveguide formed using the (a) 2-m- and (b) 2.5-m-FL split lenses.

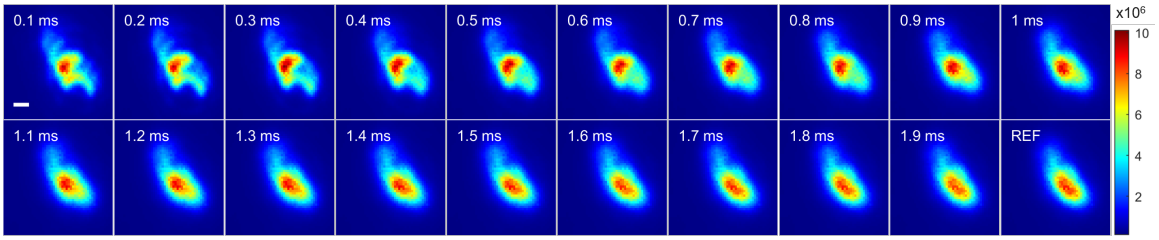

Figure 9.5: Images showing the temporal evolution of the exit mode profile of the He-Ne signal transmitted through the concatenated filament-driven thermal waveguide. Astigmatism is induced in the initial He-Ne profile to provide better contrast between the guided and unguided profiles. The scale is 200 µm. The color scale represents intensity measured by the ICCD (counts).

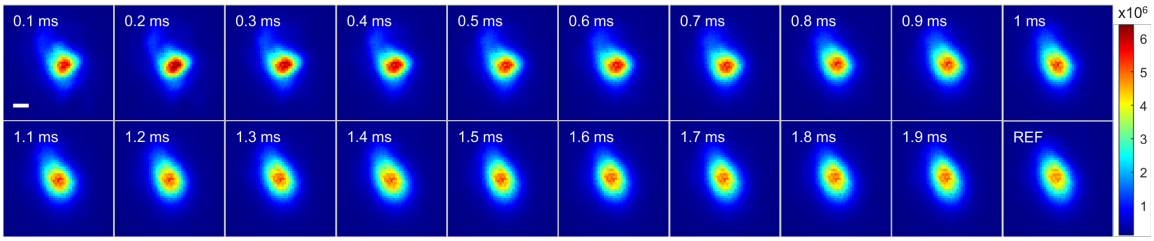

Figure 9.6: Images showing the temporal evolution of the exit mode profile of the corrected He-Ne beam transmitted through the concatenated filament-driven thermal waveguide. The astigmatism in the initial He-Ne profile is corrected in order to improve the probe coupling into the waveguide. The scale is 200 µm. The color scale represents intensity measured by the ICCD (counts).

As the peak change in refractive index of the perturbed region decreases in time, the waveguide structure simultaneously changes because of the increasing hole diameter. The evolving index and hole sizes cause both the coupling and waveguiding efficiencies to vary in time.

Figure 9.5 shows the exit mode of the guided He-Ne signal through the filament-driven concatenated waveguide at various delays with respect to the filament-driver. Astigmatism is induced in the initial unguided He-Ne beam profile (shown in the reference probe image) by rotating one of the lenses by a small angle in the probe beam expander. This imperfect initial beam profile provides better contrast when compared to the guided profile, visible at earlier delays. A brighter spot is evident during waveguiding at earlier delays; as the gas relaxes, the astigmatic initial He-Ne

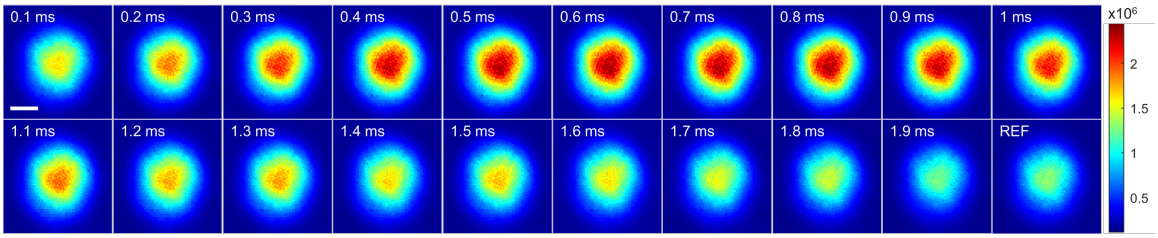

Figure 9.7: Images showing the temporal evolution of the He-Ne signal transmitted through the concatenated filament-driven thermal waveguide. An aperture is used to isolate the region of interest in which optimal guiding is observed to determine the maximum signal enhancement, shown in Fig. 9.8. The signal transmitted through the aperture and imaging/collection lens forms an Airy pattern. The aperture diameter is set to 0.9 mm, and the expanded probe beam diameter on the aperture is 1 cm. The scale is 500 µm. The color scale represents intensity measured by the ICCD (counts).

profile becomes clearer. However, in order to optimize coupling into the concatenated waveguide, the astigmatism in the He-Ne beam profile was corrected; the exit mode of the corrected He-Ne beam transmitted through the concatenated waveguide is shown in Fig. 9.6. Figure 9.7 provides images of this guided He-Ne signal transmitted through the concatenated structure using an aperture to physically select the region of interest in which the greatest enhancement of the guided signal is observed. The aperture diameter is 0.9 mm, and the expanded probe beam diameter on the aperture is 1 cm. The small aperture size and the imaging lens form an Airy pattern when imaged onto the camera. These images are integrated to provide the data points in Fig. 9.8.

Figure 9.8 compares the enhancement of the guided He-Ne signal through the individual and concatenated filament-driven thermal waveguides as a function of time. The data points in the plot result from integration of the images provided in Fig. 9.7. Each image is an accumulation of 200 shots, and the error is determined by $\sigma = \sqrt{N}$, where N is the sum of the counts in the accumulated image. The data recorded with the ICCD are compared to signal traces recorded with a photodiode. The photodiode traces and error represent the average and one standard deviation from 1200 measurements. The alignment and aperture size are not changed between the two mea-

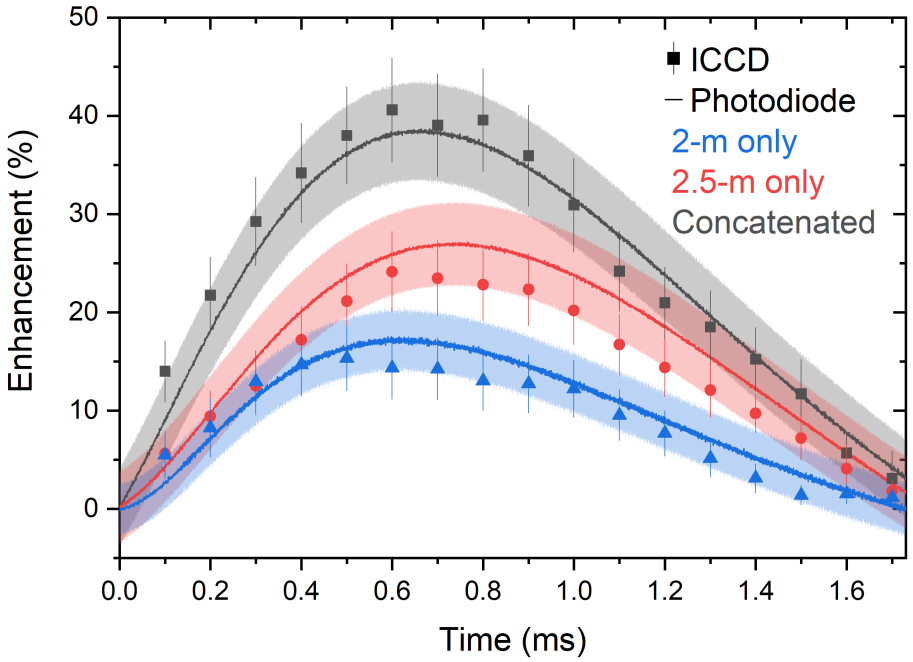

Figure 9.8: Guided He-Ne signal enhancement transmitted through the concatenated filament-driven thermal waveguide (gray) compared to the individual, shorter waveguide segments formed using a 2-m-FL split lens (blue) and a 2.5-m-FL split lens (red). Two detectors are compared: an ICCD (markers) and a photodiode (lines). The error in the photodiode measurement represents the one standard deviation from 1200 measurements, while the error from the ICCD measurement is determined by $\sigma = \sqrt{N}$, where N is the sum of the counts in the accumulated image. An aperture was used to select the region-of-interest in which the greatest enhancement is observed.

surements. The enhancement E is determined by first subtracting the background B_S from the signal S and then comparing it to a reference R recorded without the filament waveguide(s); the background B_R is similarly subtracted from the reference:

$$E = \frac{(S - B_S) - (R - B_R)}{(R - B_R)}. \tag{9.2}$$

The error σ is determined from the measurements as follows:

$$\sigma_E^2 = \left(\frac{(S - B_S)\sigma_{(R-B_R)}}{(R - B_R)^2} \right)^2 + \left(\frac{\sigma_{(S-B_S)}}{R - B_R} \right)^2, \tag{9.3}$$

where $\sigma^2_{(S-B_S)} = \sigma_S^2 + \sigma_{B_S}^2$ and $\sigma^2_{(R-B_R)} = \sigma_R^2 + \sigma_{B_R}^2$. Both the coupling plane for the focused probe beam and the object plane of the imaging/collection lens were kept constant between the tests of individual legs and the test of concatenated waveguide, as shown in the photograph in Fig. 9.1. In this configuration, the filament-driven thermal waveguide formed with the 2-m FL split lens alone provides ∼15% signal enhancement at a delay of ∼0.6 ms after the driver pulse; the 2.5-m case provides a higher peak enhancement of ∼25% at a slightly later delay of ∼0.8 ms. The different levels of signal enhancement are largely influenced by the configuration of the coupling and imaging/collection; whereas, the different peak enhancement times result from the evolution of the waveguide structure. Different initial conditions, for example the focusing geometry of the filament driver, which contribute to air plasma formation, may influence the guiding timescales. The concatenated structure provides the best enhancement of ∼40% at a delay of ∼0.7 ms. The timescale of the concatenated structure results from the convolution of the individual waveguide timescales.

The alignment of the two individual waveguides is critical, and external factors such as air currents which may shift the position of one or more filament cores were found to strongly contribute to the error shown in Fig. 9.8. Figure 9.8 demonstrates that waveguide structure and, consequently, coupling the probe into the waveguide

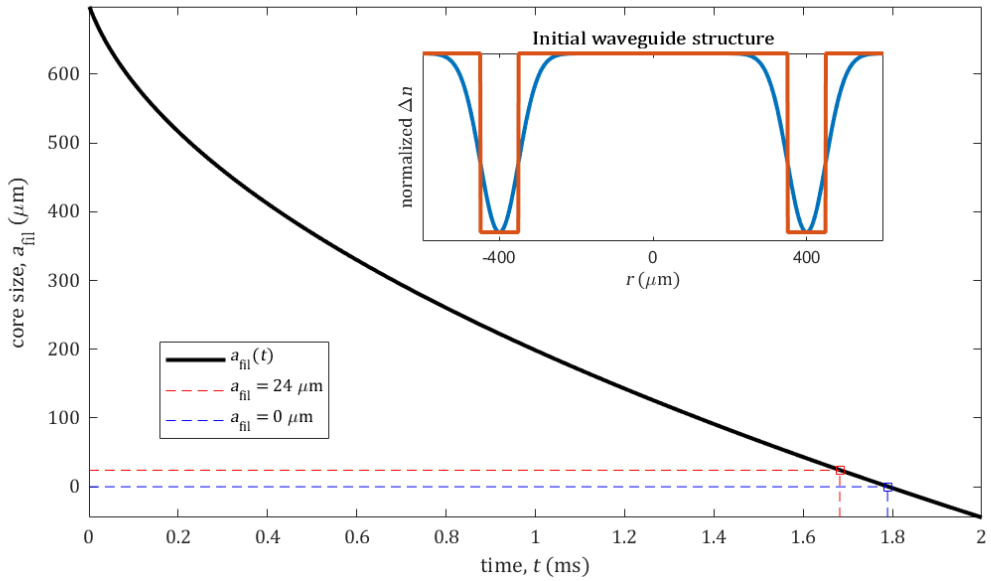

Figure 9.9: Simulated temporal evolution of the concatenated filament-driven thermal waveguide approximated by a step-index fiber with clad size equivalent to the FWHM-diameter of the refractive index hole caused by changes in the gas temperature and pressure. The inset shows the initial waveguide structure (blue) and the step-index approximation (orange). Red-dashed line shows the time at which the waveguide collapses to single-mode guiding for $V = 2.405$ determined for a peak refractive index change of $\Delta n \approx -1 \times 10^{-5}$. Blue-dashed line shows the time at which the waveguide collapses to a core size of 0 µm.

vary significantly in time. The diffraction-limited spot size of the focused He-Ne is calculated to be 100 µm at the coupling plane, and the Rayleigh length using Eq. (1.2) is 2.6 cm, with a numerical aperture of 2×10^{-3}. The length of the concatenated waveguide structure is estimated to be ∼47 cm; the lengths of the individual waveguides formed using the split 2-m and 2.5-m lenses are ∼19 cm and ∼28 cm, respectively. These lengths are determined experimentally by translating the object plane along the propagation axis observing the appearance and size of the holes as well as observing the emission of the air plasma. The lengths of the visible emission from the air plasmas at early times, observed in the photograph in Fig. 9.1, are ∼16 cm and ∼23 cm for the 2-m and 2.5-m legs, respectively.

In the subsequent analysis, the filament-driven thermal waveguide is approximated

as a step-index fiber with core size a_{fil} equal to the separation of the holes, whose diameter $d_{1/2}$ is given by Eq. (9.1):

$$a_{\text{fil}}(t) = d_0 - 2d_{1/2}(t) = d_0 - 2\sqrt{R_0 + 4\alpha t}, \tag{9.4}$$

where d_0 is the initial peak-to-peak core separation. The change in the refractive index of the air is expected to vary from Sec. 8.2 between $\Delta n \approx -5 \times 10^{-5}$ at early times and $\Delta n \approx -1 \times 10^{-5}$ at late times. Using Eq. (4.23), the numerical aperture of the filament-driven thermal waveguide lies in the range between 10×10^{-3} (early times) and 4×10^{-3} (late times). These numerical apertures correspond to acceptance angles in the range between 0.25° and 0.55°. It is expected that multimode guiding occurs until late times ($V > 2.405$), because the maximum waveguide core diameters required for single-mode guiding lie in the range between 54 µm (early times) and 24 µm (late times), calculated using Eq. (4.24). The initial mean (peak-to-peak) separation of the filament cores is significantly larger, on order 800–900 µm, as discussed in Sec. 9.1. In Fig. 9.9, Eq. (9.4) is used to estimate the core size of the waveguide as a function of time. For an initial filament core size $R_0 = 50$ µm and separation $d_0 = 800$ µm, a waveguide core diameter of 24 µm required for single-mode guiding at late times ($\Delta n \approx -1 \times 10^{-5}$) is reached after 1.67 ms, and the core collapses (to a size of 0 µm) after 1.78 ms. These calculations agree well with the observations in Fig. 9.8, where enhancement reaches the reference level at a delay of ∼1.7 ms. Moreover, the thermal waveguiding timescales observed here agree with those reported in Refs. [117] and [197]. Future comprehensive numerical investigation should be done in order to better understand the evolution of the coupling and waveguide structure.

Ultimately, these results demonstrate the successful concatenation of two filament-driven thermal waveguides. The concatenated structure is significantly longer than either of the individual waveguides, and provides notable improvement in enhance-

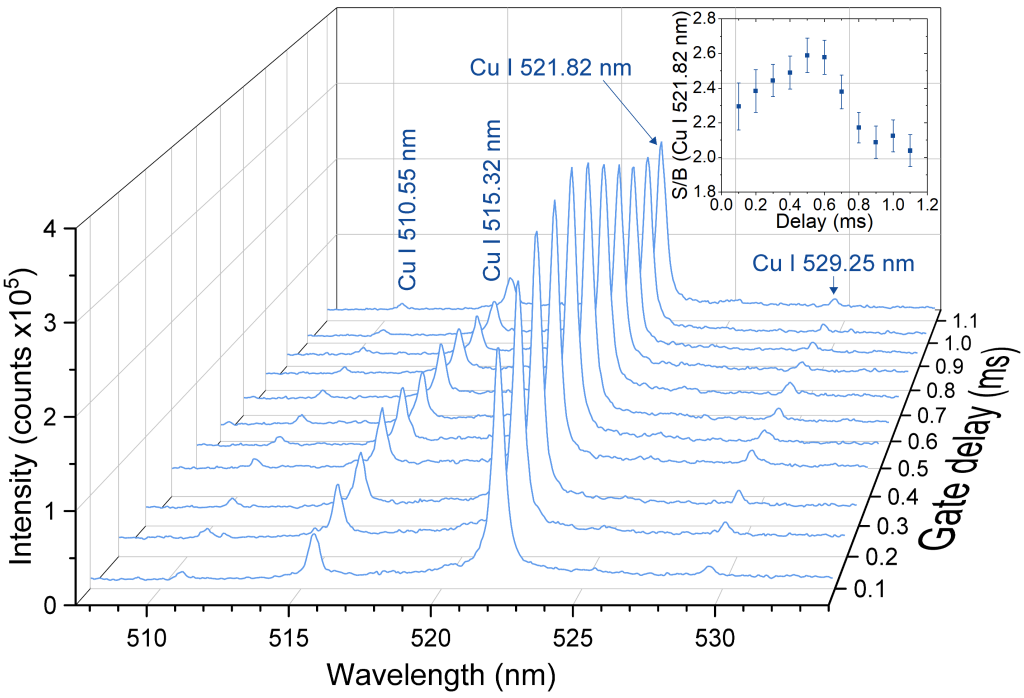

Figure 9.10: Temporal evolution of the spectroscopic signal from a Cu-LPP transmitted through the concatenated filament-driven thermal waveguide. The ablation laser pulse and camera gate are delayed with respect to the filament-driver. The spectra were accumulated for 300 laser shots for each time step.

ment of the guided CW probe signal in the present configuration of the coupling and imaging/collection. These results indicate that several such structures may be concatenated to farther scale the effective length of the waveguide, possibly enabling long-distance transmission of optical signals. In the following section, the concatenated filament-driven thermal waveguide is used to improve the collection of spectroscopic emission signatures from an LPP, which is of interest for LIBS/FIBS applications.

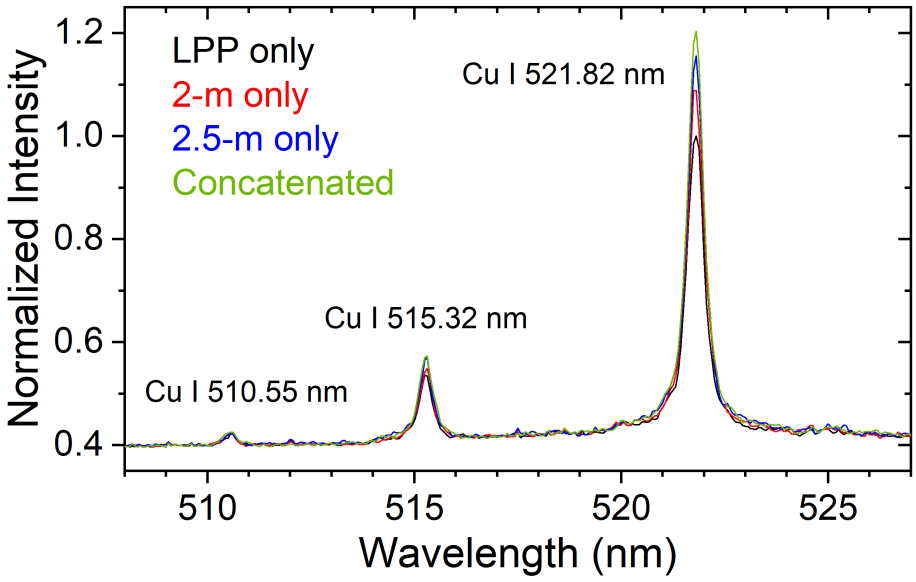

Figure 9.11: Spectra from the Cu-LPP comparing transmission through the individual and concatenated filament-driven thermal waveguides. The spectra represent the average from 1000 measurements. The spectra were recorded for a delay of 0.5 ms with respect to the filament driver pulse.

9.3 Guiding spectroscopic emission from an LPP with a concatenated filament-driven thermal waveguide

Collection of the spectroscopic emission from a Cu-LPP was found to be very sensitive to the alignment of the source and individual filament-driven thermal waveguides. The alignment procedure is discussed in more detail in Sec. 9.1, and illustrated in Fig. 9.2. Briefly, the ablation laser is aligned perpendicular to the axis of the waveguide(s) in such a way that the LPP is formed at the coupling plane along the axis in which the filament and He-Ne propagate. As discussed in previous chapters, the LPP is a highly dynamic system which expands rapidly away from the target. Influential factors that govern the expansion rate include ablation laser energy, target surface character, mass of the target species, ambient pressure which contributes to plume confinement, and the nature of the ambient gas (*e.g.* reactive or inert). The center of mass of the three cores for each waveguide is aligned to be ~1.3 mm away from

the target surface, so that the filaments may propagate unimpeded by the target but still align with the LPP emission.

For spectroscopic measurements, the aperture is fully opened, but the spectrometer slit, which is closed to a width 50 µm, acts in a similar manner, selecting the region in which optimal guiding is observed. The slit size is comparable to the core size of the waveguide when imaged onto the slit, as shown in Fig. 9.2(c). The results from using the concatenated filament-driven thermal waveguide to improve collection of emission from the Cu-LPP are shown in Fig. 9.10. In these measurements, the ablation laser and camera gate are delayed with respect to the filament driver pulse. The camera gate delay with respect to the ablation pulse is 1 µs in order to avoid early-time continuum from the LPP, and the gate width is 20 µs. Signal-to-background is assessed for the strongest line in this spectral region, Cu I 521.82 nm. The best signal-to-background $S/B = (S-B)/B$ is observed at delays of 0.5–0.6 ms, as shown by the inset of Fig. 9.10. Signal-to-background is improved by ∼25% at the optimal delay compared to later delays. The weaker lines in the spectrum, labeled in Fig. 9.10, follow a similar trend.

Figure 9.11 compares the Cu-LPP spectra recorded for each individual filament-driven thermal waveguide to that from the concatenated structure. Spectra are recorded at a delay of 0.5 ms, corresponding to the time at which peak signal-to-background is observed in Fig. 9.10. Guided spectra are normalized to the unguided spectrum, and the background is not subtracted in order to assess the analytical performance of each waveguide. The signal-to-background ratio, that compares the peak line intensity to the background, for the Cu I lines shown in the spectrum is enhanced by ∼10–15% for the waveguide formed with the 2-m FL split lens, ∼23–26% for the 2.5-m FL case and ∼27–34% for the concatenated case. Similarly, total peak area after background subtraction is increased by ∼10–12% for the 2-m FL split lens, ∼22-25% for the 2.5-m case, and ∼27–32% for the concatenated case. These

levels of signal enhancement are mostly comparable with those observed in Sec. 9.2 for guiding the coupled CW probe. However, the enhancement for the concatenated structure is lower than that observed for the He-Ne; the most probable cause is a slight misalignment of the two individual waveguides between the different experiments. Nevertheless, the concatenated structure still provides the best enhancement which is consistent with the results in Sec. 9.2. Ultimately, these results suggest that the concatenated filament-driven thermal waveguide provides an effective means to improve analytical performance of the LIBS/FIBS techniques. Furthermore, successful concatenation of two filament-driven thermal waveguides foreshadows that the effective length of these structures may be scaled farther by concatenation of a longer series of filaments.

9.4 Guided signal redirection with a filament-driven concatenated thermal waveguide

Although there exist many scenarios in which the LIBS/FIBS and LIF methods may be applied for detection of a substance in the field, one remaining notable drawback is the requirement for an open line of sight to the target. In a situation where shielding is used or an obstacle is encountered, the segments of the concatenated waveguide, demonstrated herein, may potentially be steered to avoid the obstruction. In this section, the segment of the waveguide formed using the 2.5-m split lens is steered by translating and rotating the dichroic mirror, so that this segment is angled by $\sim 0.5^{\circ}$ with respect to the original propagation axis. This configuration is shown in Fig. 9.12. The He-Ne probe is focused and steered into the "entrance" of the angled waveguide, such that the unguided signal is blocked from the field of view of the imaging system by the mount of the dichroic mirror, as shown in Fig. 9.12(d). Instead, a reflection of the transmitted probe from the back face of the polarizer which

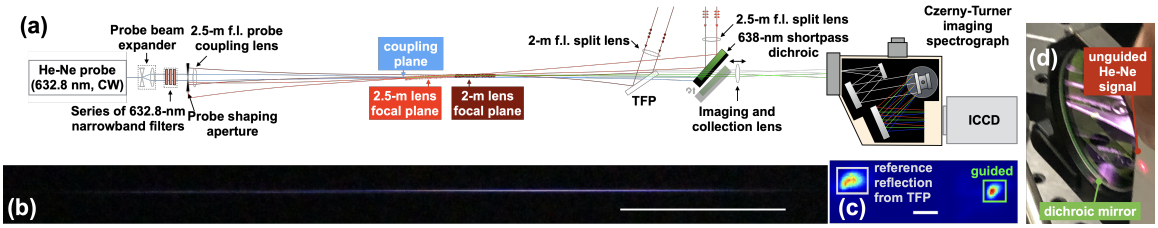

Figure 9.12: (a) The dichroic mirror which steers the p-polarized leg focused using the 2.5-m FL split lens is translated and rotated in order to angle the second thermal waveguide $\sim$0.5° with respect to the other structure. (b) The long-exposure photograph shows the concatenated structure with the 2.5-m waveguide angled by $\sim$0.5° with respect to the other structure; the scale in the photograph is 10 cm. The probe is focused and steered into the entrance of the angled waveguide, such that the unguided signal (blue) is blocked by the mount of the dichroic mirror and is not in the field of view of the imaging system. Instead, a reflection (gray) of the transmitted probe from the thin-film polarizer (TFP) that recombines the filament-driver legs is used as a reference. (c) The image identifies the reference reflection and guided signal (green) in the ICCD image; the scale in the image is 500 µm. (d) Photograph of the main unguided He-Ne signal blocked by the mount of the dichroic mirror. The guided signal is steered around this obstruction in order to be visible to the imaging apparatus.

recombines the filament-driver legs serves as a reference within the field of view.

Figure 9.13 shows the results from steering the guided signal with the individual segments. The probe is misaligned with respect to the waveguide segment formed using the 2-m FL split lens; consequently, no guided signal is observed. The angled segment, formed using the 2.5-m FL split lens, captures and redirects the probe; however, the guided signal is weak, because less light is collected by the imaging apparatus which is misaligned with respect to the angled waveguide. The straight segment in the concatenated structure redirects the signal guided through the angled segment onto the imaging axis. The guided signal through the concatenated structure is shown in Fig. 9.14 and compared to a reference signal in the same image frame. The guided signal exhibits a distinct temporal evolution on the millisecond timescale, corresponding to the thermal relaxation of air in the wake of the filament plasma. Figure 9.15 compares the integrated counts in the guided spot to those in the reference spot in the images from Fig. 9.14, as illustrated by the inset. As the total guided

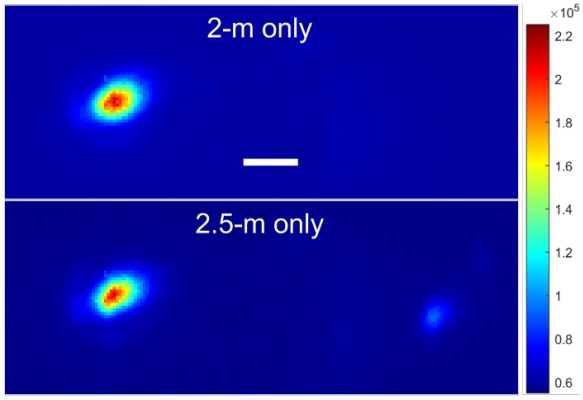

Figure 9.13: Reference (left spot) and guided signals (right spot) through the (top) straight thermal waveguide formed with the 2-m FL split lens and (bottom) angled thermal waveguide formed with the 2.5-m FL split lens. Both images are recorded with an ICCD gate delay of 0.1 ms after the filament-driver pulse and gate width of 0.1 ms, and 100 shots are accumulated. The scale is 500 µm.

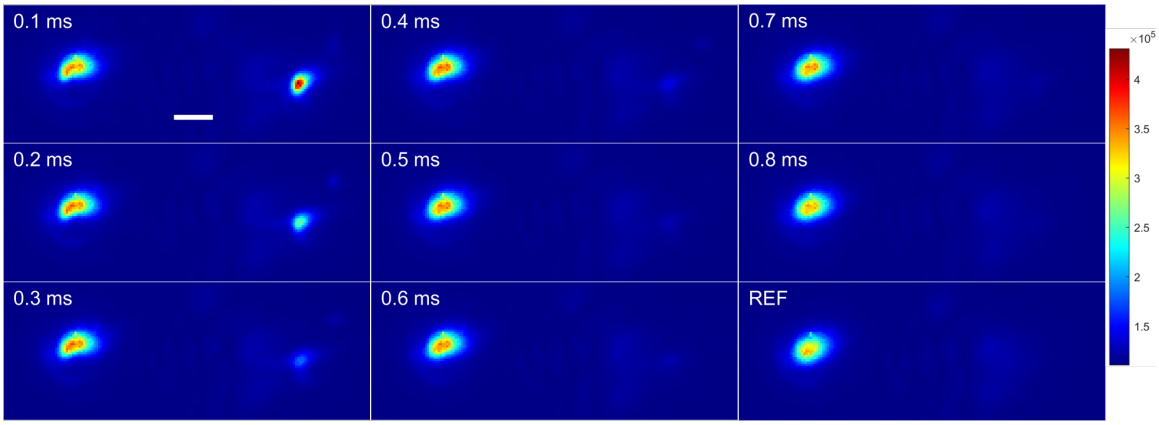

Figure 9.14: Temporal evolution of reference (left spot) and guided signals (right spot) through the concatenated filament-driven thermal waveguide with one waveguide leg at a ∼0.5° angle with respect to the other. Each image is recorded with an ICCD gate width of 0.1 ms, and 200 shots are accumulated. The scale is 500 µm.

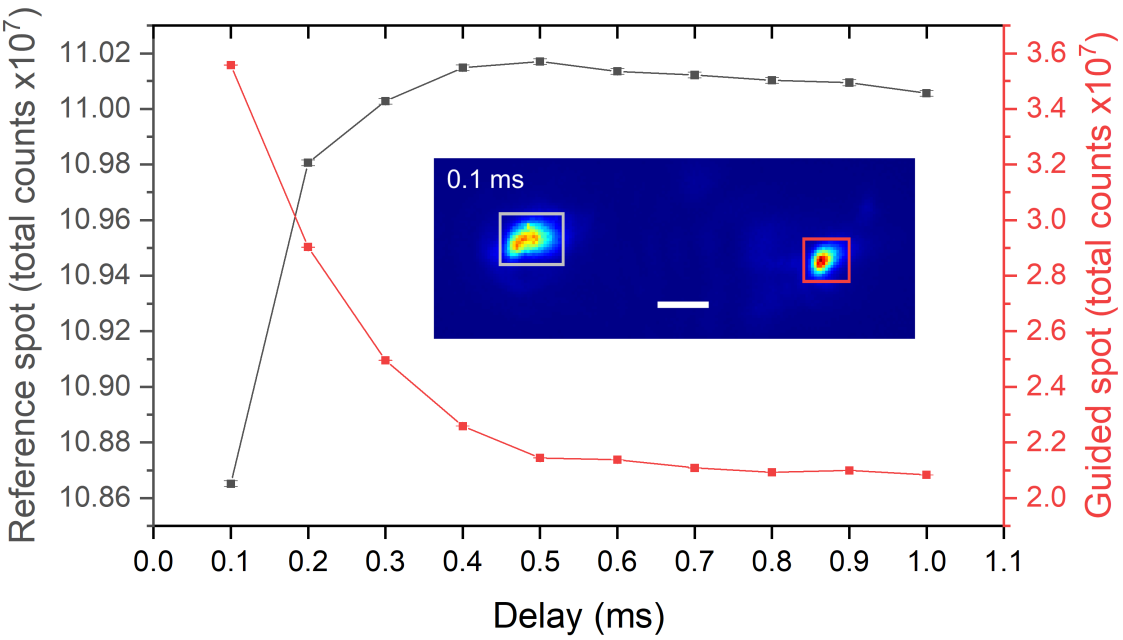

Figure 9.15: Integrated counts in the reference and guided probe profiles. The integration regions are shown by the inset. The scale in the inset is 500 µm.

signal decreases with time, the total reference signal displays an inverse trend. The contrasting temporal behaviors of the guided signal and reference indicate that the guided signal is indeed redirected away from the path of the unguided probe by the concatenated structure. The signal is redirected to avoid the mount of the dichroic mirror, such that it falls within the field of view of the imaging system. These results demonstrate that the segments of the concatenated filament-driven waveguide may be arranged to overcome obstructions in the line of sight.

Interestingly, this configuration of the concatenated waveguide behaves differently in time than the waveguide that consists of concatenated segments on the same axis. Waveguiding efficiency for both individual segments as well as the concatenated structure was found to depend on both the effective core size as well as the peak index change in the clad region. These effects lead to an optimal timescale in which the largest signal enhancement is observed, evident as a peak in Fig. 9.8. In other words, waveguiding efficiency does not depend strongly on the acceptance angle when the

waveguides are arranged on the same axis as the signal source. From Sec. 8.2, the peak index change is expected to vary between $\Delta n \approx -5 \times 10^{-5}$ at early times and $\Delta n \approx -1 \times 10^{-5}$ at late times. These peak changes in the index correspond to effective acceptance angles of the waveguide between 0.55° at early times and 0.25° at late times determined solely by the peak change in index described by

$$\theta_{\text{acc}} = \arcsin\left(\frac{1}{n_{0,\text{air}}}\sqrt{n_{0,\text{air}}^2 - (n_{0,\text{air}} + \Delta n)^2}\right), \tag{9.5}$$

which is derived from Eq. (4.23). In the current configuration with one segment angled ∼0.5° with respect to the other, the waveguiding efficacy is dominantly influenced by this acceptance angle. The resemblance in the waveguide trend in time with the expected decay of the peak index change shown in Fig. 8.3(c) further supports this claim. Here, an angular tolerance is demonstrated up to ∼0.5°, which agrees well with the predicted range of effective acceptance angles.

Ultimately, these results demonstrate that the segments in the concatenated filament-driven thermal waveguide may be arranged to redirect or steer optical signals to improve collection or transmission. These measurements also illustrate the sensitivity of such waveguides to the acceptance angle. Here, the arrangement of waveguide segments is demonstrated to tolerate an angle of ∼0.5°, which corresponds to the predicted range of acceptance angles. These results have notable implications for scenarios where shielding is used or an obstacle is encountered: the segments of the concatenated waveguide may be steered to avoid the obstruction to improve collection or transmission of optical signals, relevant to remote LIBS/FIBS and LIF.

9.5 Summary

In filament-driven thermal waveguiding, the filament air plasmas are shaped or arranged to form an annular clad-like region. Thermal relaxation of the gas temperature

and pressure, well-described by diffusion [36], in the wake of the plasma depresses the refractive index, forming the clad. Previous works show these waveguides may be used to transmit optical signals, including the emission from an LPP with implications for LIBS/FIBS [117, 197]. This chapter demonstrates the successful concatenation of two such filament-driven thermal waveguides. Split lenses are used to seed and arrange three filament cores in each waveguide. In Sec. 9.2, a counterpropagating CW probe beam is coupled to the individual and concatenated waveguides. The concatenated structure provides the best signal enhancement of ∼40%, while the individual 2-m and 2.5-m FL lens waveguides provide peak enhancement of ∼15% and ∼25%, respectively. The waveguides are observed to evolve on the millisecond timescale, consistent with that reported in Refs. [117] and [197] with optimal signal enhancement observed between 0.6 and 0.8 ms for the CW probe signal. The guiding duration is consistent with the analytical model which predicts the step-index-equivalent core size of the waveguide reaches the threshold for single-mode guiding at 1.67 ms and collapses at 1.78 ms. In Sec. 9.3, the concatenated structure is found to similarly enhance the total signal and signal-to-background of spectroscopic emission from a Cu-LPP. The best signal-to-background enhancement of ∼34% is observed for the Cu I 521.82 nm line, greater than those for the individual 2-m and 2.5-m FL lens waveguides, ∼15% and ∼26%, respectively. Finally, in Sec. 9.4, the individual segments of the concatenated filament-driven thermal waveguide are steered in order to redirect a counterpropagating probe. The signal is redirected to avoid an obstruction in the line of sight (the mount of the dichroic mirror), such that it falls within the field of view of the imaging system. Therefore, the concatenated filament-driven thermal waveguide may be an effective means to overcome obstacles in the line of sight or direct signals to a desired location. Furthermore, the successful concatenation of two waveguides foreshadows that a series of filaments may be concatenated to even farther extend the length and improve the efficacy of waveguiding. These results have implications for improving

distant collection of optical signals relevant to remote detection/sensing as well as extending the delivery range of optical signals with potential significance in free-space telecommunications.

CHAPTER 10

Conclusion and Future Work

10.1 Summary and conclusion

Laser-based optical spectroscopy methods have features that can complement the existing technology used for safeguards in the nuclear energy industry and nuclear security. In particular, the methods discussed herein facilitate rapid measurements, sensitivity to all states of matter as well as both radioactive and nonradioactive species, sensitivity to atoms, ions, compounds, and even isotopes, long detection range, and simplicity of the excitation and detection schemes. The present work applies methods including LIBS, LA-LAS, and LIF for characterization and detection of uranium and its compounds. Uranium is central to both civilian and military uses of nuclear technology; for example, uranium is the main component of fuel in most reactor types. Furthermore, this dissertation explores nonlinear propagation of intense, ultrashort laser pulses which lead to filamentation as a means to extend the detection range of analytical spectroscopic techniques like LIBS and LIF.

The work presented in Chapter 3 develops emission-based spectroscopy as a tool for direct detection of uranium. Moreover, Chapter 3 addresses the gaps in fundamental understanding of the formation and evolution of uranium oxides in uranium-containing LPPs. Uranium oxide emission signatures have been shown in previous work to be useful for discrimination of U isotopes [104, 155], *e.g.* fissile U-235 and

fissionable U-238, as a complementary method to observing atomic or ionic signatures or a standalone method. For example, the shift in the 593.55-nm UO signature between U-235 and U-238 isotopes is significantly larger than the average atomic shift of 7.5 pm [98]. OES and OTOFS are used to experimentally identify the effects of increasing ambient oxygen concentration on the formation of UO; increasing oxygen is found to similarly deplete both U I and UO populations. Further, potential emission signatures from heavier gas-phase uranium oxide species are discovered and tracked using OTOFS, and likely reaction pathways which lead to the formation of such species including UO_2, UO_3, and U_3O_8 are discussed. Additionally, the uranium-containing LPP is investigated as a laboratory-scale surrogate for the nuclear fireball, relevant to simulating the forensic signatures of nuclear detonations. Emission spectroscopy of uranium is used to study the spatiotemporal evolution of plasma temperature, free electron density, bulk and impurity species distributions, as well as assess local equilibrium conditions. U I and U II Stark broadening parameters are reported for the first time, enabling direct determination of free electron densities using U lines in the future and advancing computational capability of the uranium-LPP environment.

Later chapters investigate the fundamental aspects of filamentation and its application to remote sensing and detection of nuclear materials. Chapter 5 explores propagation in the multiple-filament regime. For laser peak powers greatly exceeding the critical power for self-focusing, like those required for extending the propagation distance, the modulation instability nucleates several filament cores. Multiple filamentation may have detrimental effect on FIBS, including inhibiting distant propagation and diminishing the efficacy of remote excitation or ablation of a target. Section 5.1 presents experimental investigations of the multiple filament air plasma. In Sec. 5.1.1, the air plasma conductivity is found to scale favorably despite multiple filamentation. In Sec. 5.1.2, OES is used to identify the local temperature, free

electron density, and excited species distributions in the multiple filament air plasma. These results elucidate excitation and ionization mechanisms in such plasmas and may aid the modeling and simulation of this propagation regime. Section 5.2 demonstrates the effects of multiple filament ablation on the formation of the solid-target LPP and analytical signals. A unique combination of ultrashort and thermal ablation mechanisms is reported and discussed in Sec. 5.2.1. Moreover, in Sec. 5.2.1, a split lens is used to induce stable and reproducible modes of multiple filamentation, and the total emission from the LPP is found to scale favorably with incident laser energy despite the onset of multiple filamentation. On the other hand, the results from Sec. 5.2.2 imply that longer driving laser wavelengths, which impede the formation of multiple filaments, may have implications for extended delivery of laser energy to a solid target: similar LPP temperatures, free electron densities, and total emission are reported for the 2-μm filament driver wavelength to those using 0.4- and 0.8-μm wavelengths.

Chapters 6 and 7 demonstrate that filamentation can be used to extend the detection distance for uranium using FIBS and UO_2F_2 using LIF. In Chapter 6, loosely-focused and freely-propagating filaments are compared with standoff excitation and collection distances of 10 m. In the loose-focusing scheme, the contribution of the energy reservoir during ablation causes stronger emission from the LPP in contrast to the freely-propagating case. Single-shot detection is achieved with the loose-focusing scheme with 10 m standoff excitation and collection. Despite comparably lower single-shot detection probability in the freely-propagating scheme, the high repetition rate of the excitation laser and data acquisition system still enable rapid detection within just a few seconds. Additionally, the ability to control the onset of filamentation and optimize FIBS signal in the freely-propagating scheme bodes well for extending the excitation distances even farther. In Chapter 7, LIF is used in combination with filamentation to detect UO_2F_2 at standoff. UO_2F_2 forms from the hydrolysis of UF_6, a

compound widely used during uranium enrichment, and exhibits a near-zero natural background. Therefore, the presence of UO_2F_2 implies active operation of nearby uranium enrichment or conversion facilities, and detection and audits of UO_2F_2 concentration is of interest for safeguards and nonproliferation. The results presented in Chapter 7 show a fast decay rate of UO_2F_2 luminescence following filament excitation, which may be useful for distinguishing UO_2F_2 emission from slowly-varying backgrounds in addition to discerning its spectral signature. Ultimately, standoff detection of UO_2F_2 at a distance of 6.5 m is achieved, and the proposed method in which LIF is augmented with filamentation may be a practical means for standoff or remote surveillance of uranium enrichment activities.

Significant challenges remain in efficient collection of distant optical signals, like the emission from LPPs formed during FIBS or the luminescence excited during filament-LIF, presented in Chapters 6 and 7, respectively. Chapters 8 and 9 demonstrate that filamentation may be used also to improve remote detection of such optical signals. In Chapter 8, the transient structure left in air in the wake of a single-filament plasma driven by a near-Gaussian shape ultrashort laser pulse is used to suppress continuous and time-varying optical signals, including the characteristic emission from a solid-target LPP. This long-lasting filament anti-guide forms because the thermal properties of the gas perturb its refractive index on the ms-timescale. The anti-guide is used to suppress atomic emission signatures from an LPP. This method can improve the analytical performance of LIBS/FIBS and LIF; for example, the signal-to-background ratio of the Al I 396.15 nm line is improved nearly fourfold in this work. The anti-guide is proposed as a physics-based gating method that may be used as an alternative to electronically-gated detectors.

In Chapter 9, a split lens is used to seed and arrange three filament cores in order to shape an annular region with a depressed index, forming the equivalent of a waveguide clad. Similar to Chapter 8, the thermal properties of the gas in the wake

of filament plasma form this long-lasting peripheral clad region. Two such filament-driven thermal waveguides are generated and concatenated on the same axis to form a longer guiding structure. The concatenated waveguide is significantly longer than either of the individual waveguides and provides a notable increase in total signal enhancement with both a continuous-wave probe and the emission of an LPP from a copper metal target. The concatenated waveguide not only improves the total signal but also enhances the signal-to-background ratio of Cu I atomic lines in comparison to the individual waveguide segments. These results imply that this method may be used to improve the analytical performance of the standoff or remote LIBS/FIBS and LIF techniques used throughout this dissertation. Finally, the segments of the concatenated filament-driven thermal waveguide are arranged to redirect optical signal. The signal is steered to avoid an obstruction, implying that this method may be used to overcome obstacles in the line of sight or deliver signal to a desired location. Moreover, successful concatenation of two such structures suggests that filament-driven thermal waveguides may be elongated even farther by concatenation of a longer series of filaments, if a convenient method to scale the concatenation to a larger number of segments can be found. These results have implications for improving delivery of the excitation source and collection of distant optical signals in remote detection/sensing applications.

In conclusion, the work presented in this dissertation contributes to the development of laser-based optical spectroscopy methods including LIBS/FIBS, LA-LAS, and LIF for detection of nuclear materials, namely uranium and its compounds. These analytical spectroscopy methods are augmented with filamentation in order to enable remote detection. Filamentation is used to both extend the delivery of the laser excitation source as well as improve collection of distant optical signals with the filament-driven anti-guiding and waveguiding methods described herein.

10.2 Future work

Chapter 3 presents a comprehensive experimental investigation of the uranium-containing LPP. In Sec. 3.2.1, OES is used to determine the time- and space-dependent plasma temperature, free electron density, and species distributions, as well as assess local equilibrium conditions in the LPP formed in a low-pressure ambient environment. Later sections in Chapter 3 explore the formation and evolution of uranium oxides in higher-pressure environments. In the higher ambient pressure in which uranium oxides were studied, the plasma temperatures and species distributions are expected to differ vastly from those which were measured at lower pressures. In these higher pressures, macroscopic effects including plume confinement, which leads to an increased rate of collisional interactions, cause interesting plume morphology as shown in Sec. 3.3. To date, few works have investigated time- and space-resolved plasma temperatures in such environments [99, 124]. Non-invasive experimental diagnostics, like those proposed here which are derived from the OES technique, may be used to ascertain the time- and space-resolved temperatures in the uranium-LPP formed in higher pressure ambient environments which contain oxygen to support the modeling work in Refs. [68] and [69]. However, previous work demonstrates that even line-of-sight spatial averaging yields distinct temperatures from those measured locally due to segregation of neutral and ionized species using analyses like the Boltzmann plot and Saha-Eggert equation [2]. Therefore, special care should be taken in future studies to assess the local equilibrium conditions, especially using analyses like the Boltzmann plot or Saha-Eggert equation, which rely on the (P)LTE assumption. Complementary imaging (or similar space-resolved) measurements which can track the local distribution of species, using methods like Abel inversion to account for line-of-sight averaging [2], should be done in order to properly assess the existence of local equilibrium. These studies would yield better understanding of the conditions in the plasma which lead to formation of various uranium oxides. Knowledge of the

temperatures and species distributions which lead to formation of specific oxides may be used to guide the creation of a surrogate environment, which can be used to better study the conditions in the nuclear fireball and subsequent formation of debris on a laboratory scale. These results would have notable implications for forensics of nuclear detonations.

In Sec. 3.5, a broad emission feature centered at 355 nm is studied and identified as possibly originating from heavier gas-phase uranium oxide species like UO_2, UO_3, and U_3O_8 in the uranium-LPP. However, further work is necessary in order to confirm the assignment of this band. This assignment can be validated experimentally by varying uranium- and oxygen-isotope concentrations in the target and ambient, respectively. As discussed in Sec. 2.2 and described by Eq. (2.37), varied isotope abundance causes spectral broadening and shifting. These changes to the spectrum may be notable especially for varying oxygen-isotope abundance, because the ratio of reduced masses $\rho = \sqrt{\mu/\mu*}$ between varying oxygen-isotopes is significantly greater than that for varying uranium-isotopes. The reduced mass is determined by $\mu = m_1 m_2/(m_1 + m_2)$ for the isotopologue composed of two isotopes with respective masses m_1 and m_2 [98]. For example, $1 - \rho \approx 0.05$ comparing the most abundant isotopologue $U^{238}O^{16}$ to that containing the next most abundant isotope of oxygen, $U^{238}O^{18}$, whereas $1 - \rho \approx 4 \times 10^{-4}$ when comparing similarly uranium-isotopes, $U^{238}O^{16}$ to $U^{235}O^{16}$. Recent work [245] implies that future high resolution spectroscopy which can be used to identify the fine and hyperfine rovibrational lines would greatly benefit understanding and assignment of the various uranium oxide bands. Finally, the methods used in this dissertation to study uranium-containing LPPs and gas-phase uranium oxides may be applied for characterization of plutonium, relevant to both the nuclear fuel cycle and nonproliferation. To date, only Ref. [100] explores gas-phase plutonium and possible plutonium oxides in the LPP environment.

In Chapter 2, the fundamental differences between ns- and fs-pulsed LA mech-

anisms are emphasized; for example, phase explosion and laser-plasma interactions are expected to cause comparably greater temperatures in the LPP formed following ns-LA than those from fs-LA. Chapter 5 Sec. 5.2.1 shows a peculiar morphological behavior of the LPP formed during filament ablation, which includes the formation of internal shocks, that could be explained by simultaneous contributions from fast and slow mechanisms unique to filament ablation. Other works [97, 208] demonstrate that internal shocks may influence chemistry in the LPP, so further work should investigate the formation and evolution of molecular species during filament ablation, especially considering the measurements in Chapter 6, which track the signatures from U I and UO species following filament ablation. The non-invasive methods used in this dissertation, like time- and space-resolved OES and OTOFS could be used in combination with imaging methods like the selective species imaging using narrowband filters and shadowgraphy to study and compare the evolution of species to the macroscopic plume morphology. Two major remaining questions about filament ablation of uranium-containing targets that could be answered using these diagnostics include: (1) how strongly do the remnants of the filament air plasma contribute to preferential expansion of the LPP formed from the target in the normal direction, and (2) does the oxide species in the LPP formed from filament ablation of metals, like the depleted uranium target used in this dissertation, originate primarily from the target or from reactions in the plasma. Better understanding of the physical processes which occur in the LPP formed during filament ablation is important for understanding signal formation in FIBS.

Chapter 5 discusses several experiments studying the formation, propagation, and ablation of solid targets in the multiple filament regime. Multiple filaments are sporadically seeded by modulation instability, nonuniform intensity profile, and similar sources for high incident laser peak powers. In Sec. 5.2.1, a split lens is used to controllably seed and arrange two filament cores, overcoming shot-to-shot variations

in the location of the detonation site during ablation of a metal target. However, it remains uncertain if this stimulated multiple filament regime is truly representative of naturally-occuring, sporadic multiple filamentation in which the core positions and intensities could vary between shots. A shadowgraphic imaging method which uses multiple probe pulses to study subsequent delays with a single ablation laser shot may be suitable for studying the random nature of multiple filamentation instead. This investigation would provide better understanding of multiple filamentation and its effects on filament-target interactions, and similarly provide insights which would improve understanding of signal formation during multiple filament ablation for FIBS.

Chapters 6–9 demonstrate practical standoff detection of various materials using analytical spectroscopy methods like LIBS/FIBS and LIF augmented by filamentation. In Chapter 6, Sec. 6.3, the input second-order dispersion of the filament-driver is varied as a means to optimize the location of the filament along the propagation axis in a free-propagating filament configuration. Dispersion control proves a straightforward and pragmatic method to delay the onset of filamentation, and can be achieved by a programmable device. Programmable devices like the acousto-optic modulator used here and others like deformable optics may be used to improve the other FIBS and LIF methods described in Chapters 6 and 7, as well as the anti-guiding and waveguiding techniques proposed in Chapters 8 and 9. For example, in future work, a deformable mirror should be used to seed and arrange multiple filament cores in order to form the waveguide clad, and dispersion control may be used in conjunction to align several waveguide structures on axis. An optimization algorithm, like the one applied in Refs. [63] and [70], could be used for more precise control of the arrangement of a series of filament-driven thermal waveguides to further improve guided signal enhancement and elongate the concatenated waveguides. The machine-based approach would better address questions about the scalability of these waveguides considering the meticulous nature and sensitivity of the alignment. Along these lines,

it would be interesting to investigate the ability to redirect signal using a series of filament-driven thermal waveguides.

10.3 Outlook

Ultimately, the work presented in this dissertation builds an infrastructure for augmenting laser-based analytical spectroscopy methods with filamentation to enable remote detection or sensing of nuclear materials. The OES-based methods presented in Chapter 3 developed the understanding of the chemical processes which lead to the formation of uranium oxides. These and derivative techniques may be applied for direct measurements of uranium-containing samples, enabling rapid, *in-situ* discrimination of uranium isotopes with high fidelity using their molecular signatures. Such techniques may be applied for online monitoring of uranium enrichment processes, for example. Moreover, filamentation facilitates improved standoff and remote detection capabilities for nuclear materials, namely uranium and its compounds like UO_2F_2, as demonstrated by the work in Chapters 6 and 7 of this dissertation. These chapters demonstrate efficient excitation and detection from standoff distances, which can be adapted for field applications. Finally, Chapters 8 and 9 present means to improve the analytical performance of the LIBS/FIBS and LIF techniques by enhancing signal collection and background rejection using filamentation. These methods may be used to survey clandestine enrichment activities, audit known sites, or guide remediation efforts in the event of a leak or spill, marked by traces of UO_2F_2. Although the concepts and methods presented here were directed towards applications relevant to nuclear safeguards, security, and nonproliferation, they may also have broader implications relevant to laser-material processing and comprehending the relevant, underlying physics, analytical methods based on optical spectroscopy and their wide range of applications, remote and atmospheric sensing, as well as telecommunications and distant data transmission.

APPENDICES

APPENDIX A

Selected U I Lines for Boltzmann Plot Analysis

Selected atomic (U I) and singly-ionized (U II) uranium transitions for the Boltzmann plot and Saha-Eggert equation analyses in Chapter 3, Section 3.2.1, are listed along with relevant transition information in this appendix. The spectral line information is retrieved from Ref. [179]. The Boltzmann plot analysis, and these lines, are presented in more detail in Ref. [28].

Table A.1: Atomic parameters [179] of U I spectral lines considered for determination of excitation temperature using the Boltzmann plot method.

λ (nm)	E_u (eV)	J_u	E_l (eV)	J_l	g_f	λ (nm)	E_u (eV)	J_u	E_l (eV)	J_l	g_f
405.81	3.52	7	0.47	7	1.29E-09	506.38	2.92	7	0.47	7	1.58E-09
410.31	3.93	8	0.91	7	8.40E-10	516.41	3.41	8	1.01	7	1.53E-09
416.24	3.45	8	0.47	7	1.48E-09	530.85	2.81	7	0.47	7	3.61E-09
416.37	3.51	7	0.53	6	9.67E-10	549.64	2.76	6	0.53	6	1.95E-09
418.70	3.49	7	0.53	6	1.24E-09	556.42	2.70	7	0.47	7	6.68E-09
420.11	3.90	9	0.95	8	7.57E-10	561.09	2.98	7	0.77	6	2.88E-09
421.16	3.72	6	0.77	6	1.03E-09	562.15	2.68	6	0.47	7	2.23E-09
422.24	3.41	8	0.47	7	2.62E-09	578.06	2.92	7	0.77	6	4.04E-09
423.17	3.88	9	0.95	8	1.01E-09	597.63	2.55	8	0.47	7	1.02E-08
426.79	3.68	6	0.77	6	7.72E-10	598.61	2.55	4	0.48	3	4.71E-09
428.88	3.66	6	0.77	6	1.61E-09	599.73	2.84	7	0.77	6	3.87E-09
431.31	3.34	8	0.47	7	2.11E-09	602.81	2.54	2	0.48	3	1.98E-09
436.28	3.31	8	0.47	7	9.14E-10	606.23	2.57	7	0.53	6	2.11E-09
437.18	3.84	8	1.01	7	1.09E-09	617.19	2.96	9	0.95	8	4.13E-09
444.83	3.26	7	0.47	7	7.92E-10	617.54	2.54	7	0.53	6	4.27E-09
474.35	3.39	7	0.77	6	1.27E-09	621.54	2.46	7	0.47	7	2.76E-09
481.09	3.05	8	0.47	7	1.97E-09	629.85	2.50	5	0.53	6	2.96E-09
481.57	3.04	7	0.47	7	1.08E-09	637.25	2.42	8	0.47	7	9.95E-09
491.04	3.30	7	0.77	6	2.13E-09	638.98	2.68	5	0.74	4	3.87E-09
492.84	3.04	7	0.53	6	3.02E-09	646.50	2.82	8	0.91	7	7.05E-09
495.58	3.45	8	0.95	8	1.33E-09	650.36	2.44	7	0.53	6	3.88E-09
496.73	2.97	8	0.47	7	2.53E-09	651.89	2.68	6	0.77	6	3.02E-09
-	-	-	-	-	-	655.50	2.37	2	0.48	3	4.34E-09

Table A.2: Atomic parameters [179] of U I and U II spectral lines used for determination of electron temperture via Saha-Eggert equation.

Species	λ (nm)	E_u (eV)	J_u	E_l (eV)	J_l
U I	530.85	2.81	7	0.47	7
U I	578.06	2.92	7	0.77	6
U I	597.63	2.55	8	0.47	7
U II	417.16	3.19	6.5	0.12	6.5
U II	434.17	2.89	4.5	0.07	5.5
U II	447.23	2.81	4.5	0.06	5.5
U II	500.82	2.69	6.5	0.02	6.5

APPENDIX B

Relevant U-O Thermochemical Reactions

The relevant thermochemical reaction pathways for uranium and oxygen species are presented in this appendix. A more comprehensive list can be found in Ref. [69].

Table B.1: Relevant thermochemical reaction pathways for uranium-oxygen interactions. T represents the gas temperature in units of K. The units for rate coefficients are $cm^3.s^{-1}$ for Reactions 1–4, and s^{-1} for Reactions 5–12, respectively. A more extensive summary of the most probable reactions can be found in Ref. [69]. Table from Ref. [220].

No.	Reaction	$\Delta_r H_{298.15\ \mathrm{K}}$ (kJ mol^{-1})	Rate coefficient	Reference
1	$U + O_2 \rightleftharpoons UO + O$	-259.890	$3.36 \times 10^{-12} T^{0.5} \exp(-5161.7/T)$	[1,47,48]
2	$U + O_2 \rightleftharpoons UO_2$	-1011.363	$3.36 \times 10^{-12} T^{0.5} \exp(-12910/T)$	[1,47,48]
3	$UO + O2 \rightleftharpoons UO_2 + O$	-253.127	$3.8 \times 10^{-11} T^{0.17}$	[1]
4	$UO_2 + O_2 \rightleftharpoons UO_3 + O$	-74.129	$1.17 \times 10^{-11} T^{0.5} \exp(-8915.7/T)$	[1]
5	$U_2O_3 \rightleftharpoons U_2O_2 + O$	628.981	$3 \times 10^{15} \exp(-68148.6/T)$	[1]
6	$U_2O_3 \rightleftharpoons UO_2 + UO$	404.546	$3 \times 10^{15} \exp(-46023.3/T)$	[1]
7	$U_2O_3 \rightleftharpoons UO_3 + U$	592.696	$3 \times 10^{15} \exp(-64746/T)$	[1]
8	$U_2O_2 \rightleftharpoons 2UO$	527.038	$1 \times 10^{15} \exp(-60010.1/T)$	[1]
9	$U_2O_2 \rightleftharpoons U + UO_2$	533.801	$1 \times 10^{15} \exp(-61175.1/T)$	[1]
10	$UO_3 \rightleftharpoons UO + O_2$	823.213	$1 \times 10^{15} \exp(-90465.3/T)$	[1]
11	$UO_3 \rightleftharpoons UO_2 + O$	570.083	$1 \times 10^{15} \exp(-73300.3/T)$	[1]
12	$UO_2 \rightleftharpoons UO + O$	751.473	$1 \times 10^{15} \exp(-93229.8/T)$	[1]

APPENDIX C

Diagnostics of the Air Plasma Formed During Multiple Filamentation

This appendix provides examples of temperature and electron density diagnostics from emission spectroscopy of the multiple filament plasma. The results are summarized and discussed in detail in Chapter 5, Section 5.1.2.

Air plasma temperatures are determined using SPECAIR [1] to fit experimental spectra observing various N_2 and N_2^+ transitions. The individual rotational T_r, vibrational T_v, and electronic T_e temperatures are iterated to approximate a PLTE condition in the plasma, and a *best fit* is determined by minimizing the residuals between simulated and experimental spectra. An example fit is shown in Fig. C.1 for N_2 (1,3) and (0,2) bands. The measured temperatures are summarized in Chapter 5, Section 5.1.2.2.

Free electron densities of the air plasma are determined by deconvolving the Stark contribution to broadening of the O I 777.19 nm line [Eq. (2.23)]. Instrumental resolution and Doppler broadening are considered [72]. A Stark broadening parameter of 16.6 pm is used in the analysis [18]. A cumulative Voigt profile is used to fit experimental spectra, as shown in Fig. C.2.

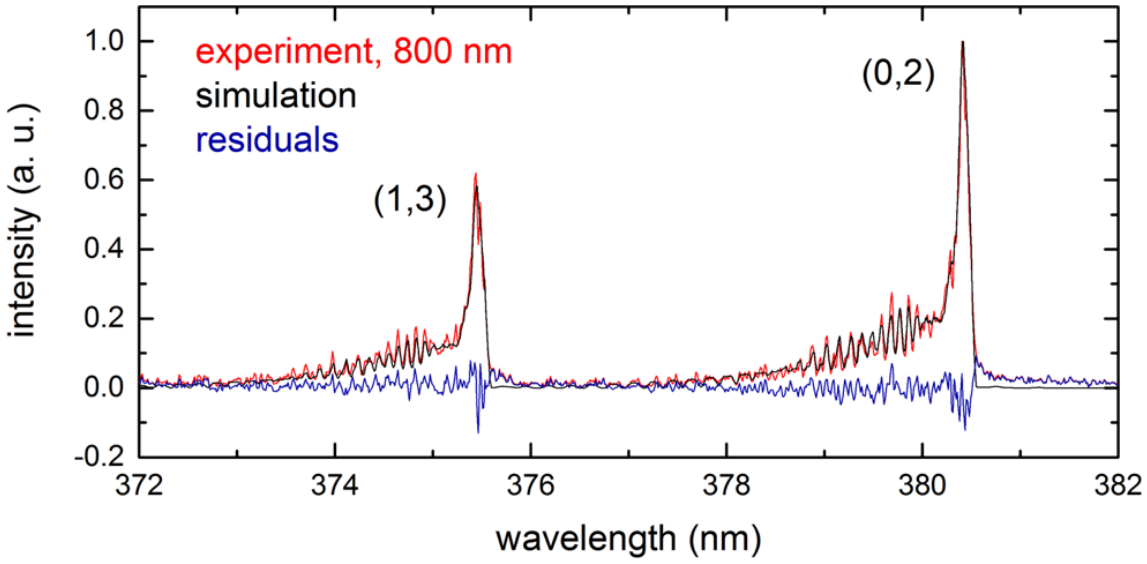

Figure C.1: Example experimental spectrum of the N_2 (1,3) and (0,2) emission bands fit using SPECAIR to determine temperatures of the air plasma formed during multiple filamentation of 3-mJ, 800-nm pulses [72].

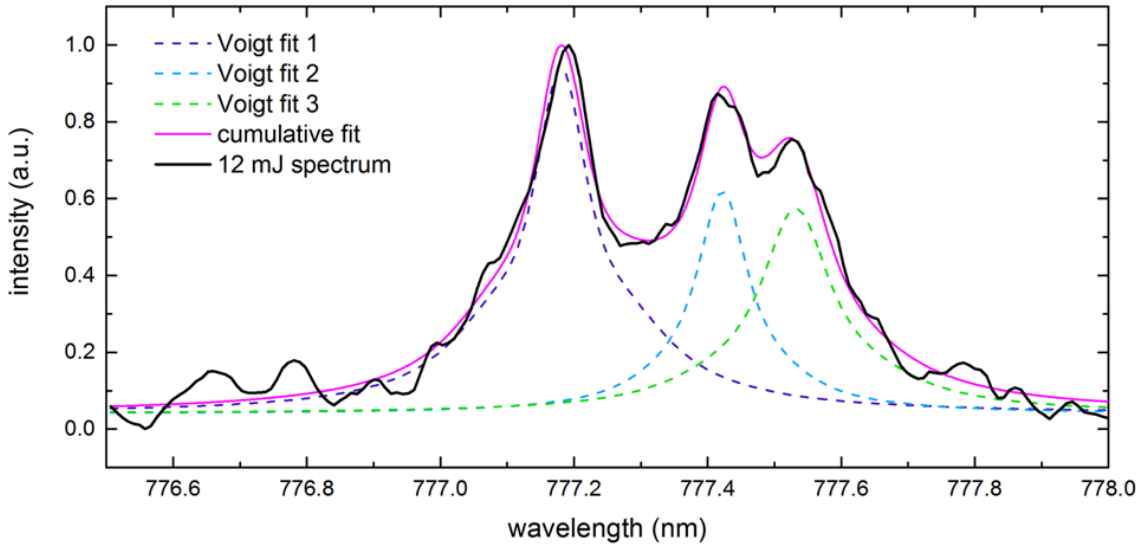

Figure C.2: A cumulative Voigt profile is used to fit the O I 777.19-, 777.42-, and 777.54-nm lines. The broadening contributions to the measured line widths are considered in order to determine the free electron densities in the air plasma formed during multiple filamentation. The spectrum is recorded for a laser wavelength of 800 nm and pulse energy of 12 mJ [72].

APPENDIX D

Diagnostics of the Target Plasma Formed Following Filament Ablation of Copper

Raw images of the plasma emission and pump-probe measurements of the shock following filament ablation of copper are presented in this appendix. The data are taken from Ref. [218] and discussed in detail in Chapter 5, Sec. 5.2.1. Additionally, Fig. D.2 shows example fits to the expanding shock dimension according to the spherical Sedov blast model given by Eq. (2.14).

Selected atomic copper (Cu I) transitions for the Boltzmann plot analyses in Chapter 5, Section 5.2.2, are also listed along with relevant transition information in this appendix, given in Table D.1. The spectral line information is retrieved from Ref. [173]. The Boltzmann plot analysis, and these lines, are presented in more detail in Ref. [29].

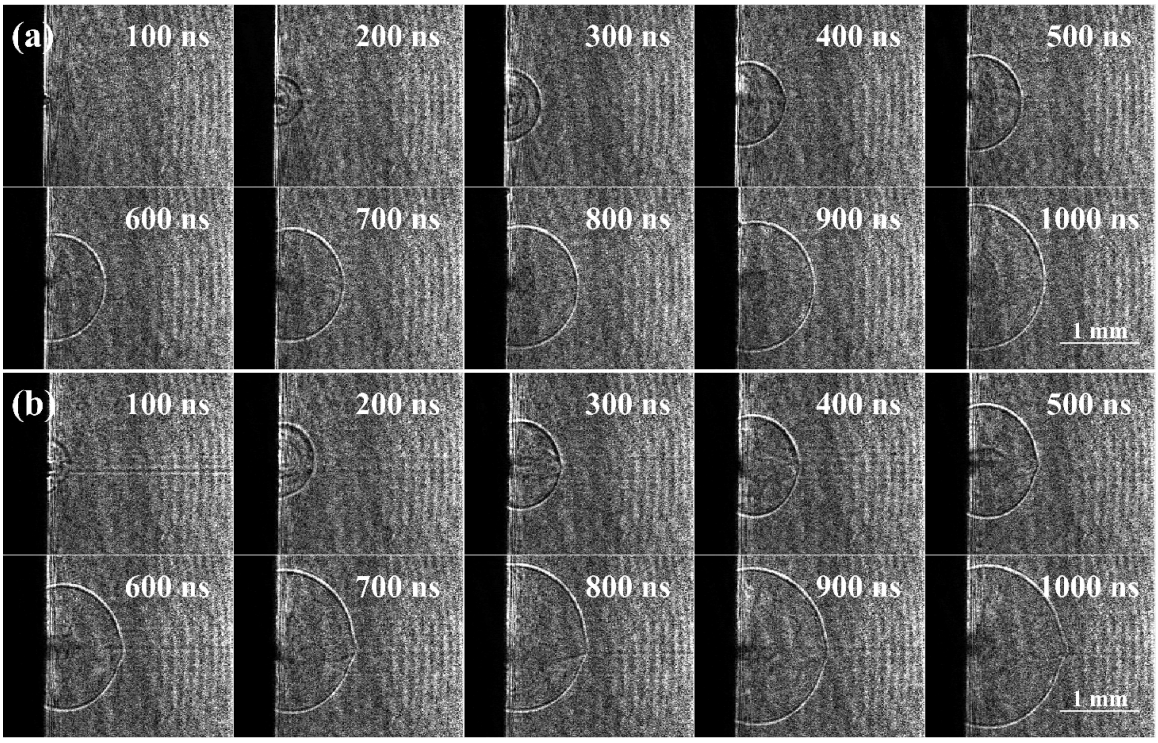

Figure D.1: Example shadowgraphs showing the evolution of the shockwave following filament ablation of a copper target with (a) 1.9 mJ and (b) 3.8 mJ pulse energies. For the 3.8 mJ energy which was found to exhibit multiple filamentation [see inset of Fig. 5.3(a)], frames were selected to avoid those which featured clear evidence of multiple detonation sites. These frames in which multiple detonation sites were observed constituted the majority (∼90%) of the measured data, motivating the split lens approach to seed reproducible multiple filamentation [218].

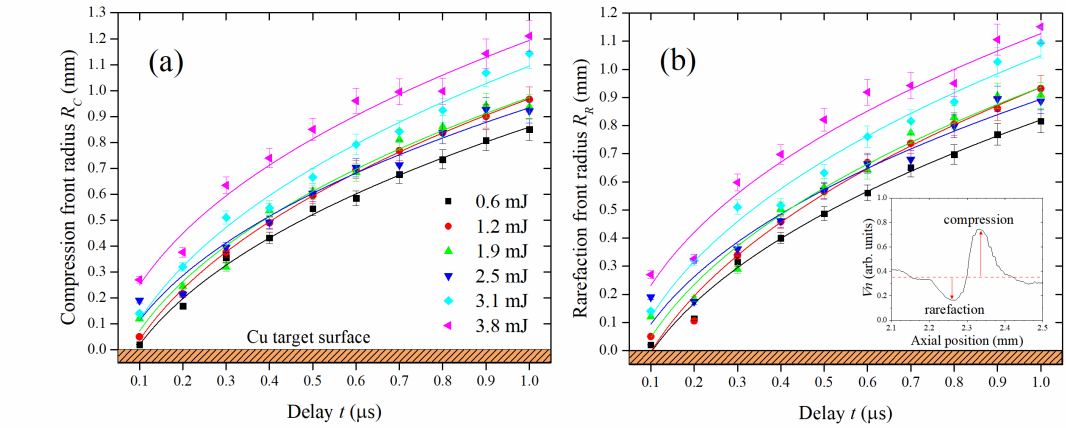

Figure D.2: (a) Compression and (b) rarefaction front radii were measured from the shadowgraphic images of the shocks. For laser energies >1.9 mJ, the expansion of the shock is not well represented by the blast model despite choosing frames to avoid those which featured clear evidence of multiple filamentation (Fig. D.1), motivating the split lens approach to seed reproducible multiple filamentation. The inset shows a lineout of the shadowgraphy image showing compression and rarefaction zones recorded for a laser energy of 0.6 mJ and delay of 300 ns [218].

Table D.1: The spectral line information is used in Boltzmann plot analysis in Sec. 5.2.2.2. The spectral line parameters include [173]: wavelength, λ_{ul}, transition probability, A_{ul}, statistical weight of upper level, g_u, and the lower and upper level energies, E_l and E_u, respectively [29].

λ_{ul} (nm)	A_{ul} (10^8 s^{-1})	g_u	E_l (eV)	E_u (eV)
406.26	0.210	6	3.82	6.87
424.89	0.195	2	5.08	7.99
427.51	0.345	8	4.84	7.74
448.03	0.030	2	3.79	6.55
450.93	0.275	2	5.24	7.99
453.08	0.084	2	3.82	6.55
453.97	0.212	4	5.15	7.88
458.69	0.320	6	5.10	7.80
465.11	0.380	8	5.07	7.74
470.45	0.055	8	5.10	7.74
510.55	0.020	4	1.39	3.82
515.32	0.600	4	3.79	6.19
521.82	0.750	6	3.82	6.19
570.02	0.002	4	1.64	3.82
578.21	0.017	2	1.64	3.79

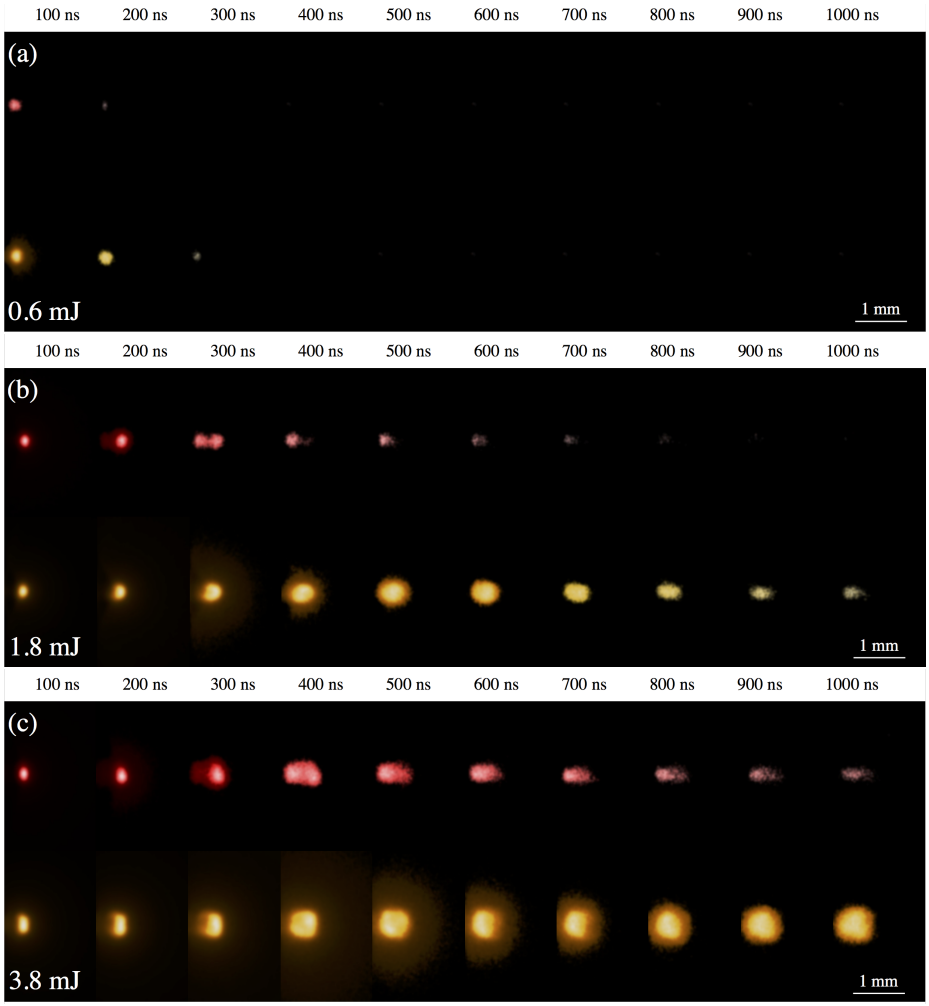

Figure D.3: Emission from (top, red) Cu II (490.97 nm) target species and (bottom, orange) Cu I (521.82 nm) target species for laser energies: (a) 0.6 mJ, (b) 1.9 mJ, and (c) 3.8 mJ [218].

APPENDIX E

Measured Parameters From UO_2F_2 Luminescence Spectrum

This appendix provides additional results from the experiments investigating filament-induced fluorescence spectroscopy of UO_2F_2 discussed in Chapter 7 [216].

Table E.1: Luminescence peak centroids and widths determined from a cumulative Voigt fit of data averaged for five measurements, shown in Fig. 7.4 [216].

Peak label	Centroid (nm)	Width (FWHM, nm)
1	500.25±0.11	13.21±0.59
2	521.56±0.21	13.45±0.66
3	546.16±0.39	16.29±0.70
4	572.65±0.22	17.31±0.94
5	599.74±0.69	20.64±3.68

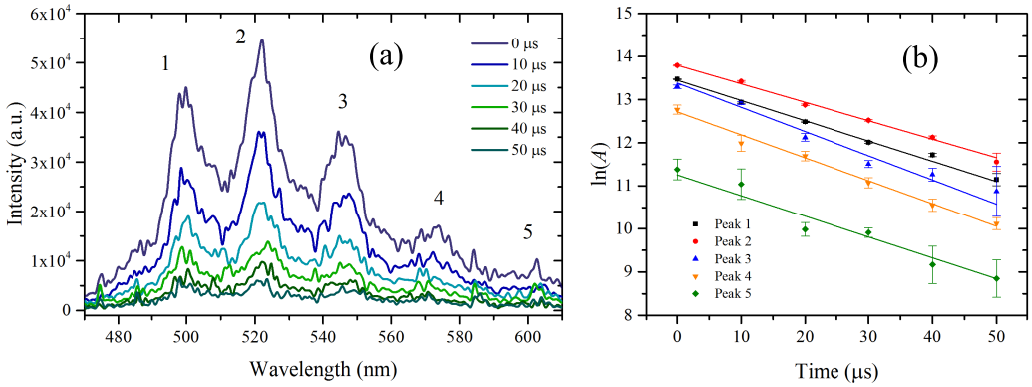

Figure E.1: (a) The time-dependent luminescence of aqueous UO_2F_2, excited by an ultrashort pulse which does not undergo filamentation with 1-mJ energy, is accumulated for 200 laser shots for each ICCD delay. (b) The logarithm of the individual peak areas A is fit with a linear model to determine the decay constants γ [216].

BIBLIOGRAPHY

BIBLIOGRAPHY

[1] SPECAIR (Version 3.0) Spectral Fitting Software, 2012.

[2] J. A.Aguilera and C. Aragón. Characterization of a laser-induced plasma by spatially resolved spectroscopy of neutral atom and ion emissions: Comparison of local and spatially integrated measurements. *Spectrochimica Acta Part B: Atomic Spectroscopy*, 59(12):1861–1876, 2004.

[3] I. Adamovich, S. D. Baalrud, A. Bogaerts, P. J. Bruggeman, M. Cappelli, V. Colombo, U. Czarnetzki, U. Ebert, J. G. Eden, P. Favia, D. B. Graves, S. Hamaguchi, G. Hieftje, M. Hori, I. D. Kaganovich, U. Kortshagen, M. J. Kushner, N. J. Mason, S. Mazouffre, S. Mededovic Thagard, H.-R. Metelmann, A. Mizuno, E. Moreau, A. B. Murphy, B. A. Niemira, G. S. Oehrlein, Z. Lj. Petrovic, L. C. Pitchford, Y.-K. Pu, S. Rauf, O. Sakai, S Samukawa, S. Starikovskaia, J. Tennyson, K. Terashima, M. M. Turner, M. C. M. van de Sanden, and A. Vardelle. The 2017 plasma roadmap: Low temperature plasma science and technology. *Journal of Physics D: Applied Physics*, 50(32):323001, 2017.

[4] R. S. Addleman and C. M. Wai. On-line time-resolved laser-induced fluorescence of $UO_2(NO_3)_2{\cdot}2TBP$ in supercritical fluid CO_2. *Analytical Chemistry*, 72(9):2109–2116, 2000.

[5] U.S. Energy Information Administration. International Energy Overview, url: https://www.eia.gov/international/data/world, 2020.

[6] U.S. Energy Information Administration. U.S. Nuclear Energy Overview, url: https://www.eia.gov/nuclear/data.php, 2021.

[7] J. A. Aguilera, C. Aragón, and J. Bengoechea. Spatial characterization of laser-induced plasmas by deconvolution of spatially resolved spectra. *Applied Optics*, 42(30):5938–5946, 2003.

[8] M. Alshershby, Z. Hao, A. Camino, and J. Lin. Modeling a femtosecond filament array waveguide for guiding pulsed infrared laser radiation. *Optics Communications*, 296:87–94, 2013.

[9] S. Amayri, T. Arnold, T. Reich, H. Foerstendorf, G. Geipel, G. Bernhard, and A. Massanek. Spectroscopic characterization of the uranium carbonate

andersonite $Na_2Ca[UO_2(CO_3)_3].6H_2O$. *Environmental Science & Technology*, 38(22):6032–6036, 2004.

[10] L. Arantchouk, G. Point, Y. Brelet, B. Prade, J. Carbonnel, Y.-B. André, A. Mysyrowicz, and A. Houard. Large scale tesla coil guided discharges initiated by femtosecond laser filamentation in air. *Journal of Applied Physics*, 116(1):013303–1–7, 2014.

[11] D. U. B. Aussems, D. Nishijima, C. Brandt, R. P. Doerner, and N. J. L. Cardozo. Spectroscopic characterization and imaging of laser- and unipolar arc-induced plasmas. *Journal of Applied Physics*, 116(6):063301, 2014.

[12] J. E. Barefield, E. J. Judge, K. R. Campbell, J. P. Colgan, D. P. Kilcrease, H. M. Johns, R. C. Wiens, R. E. McInroy, R. K. Martinez, and S. M. Clegg. Analysis of geological materials containing uranium using laser-induced breakdown spectroscopy. *Spectrochimica Acta Part B: Atomic Spectroscopy*, 120:1–8, 2016.

[13] M. Baudelet, C. C. C. Willis, L. Shah, and M. Richardson. Laser-induced breakdown spectroscopy of copper with a 2 µm thulium fiber laser. *Optics Express*, 18(8):7905, 2010.

[14] N. Baumann, T. Arnold, G. Geipel, E.R. Trueman, S. Black, and D. Read. Detection of U(VI) on the surface of altered depleted uranium by time-resolved laser-induced fluorescence spectroscopy (TRLFS). *Science of the Total Environment*, 366(2):905–909, 2006.

[15] J. V. Beitz and C. W. Williams. Uranyl fluoride luminescence in acidic aqueous solutions. *Alloys & Compounds*, 250(1):375–379, 1997.

[16] L. Bérge. Boosted propagation of femtosecond filaments in air by double-pulse combination. *Physical Review E: Statistical, Nonlinear, & Soft Matter Physics*, 69(6):1–65601, 2004.

[17] L. Bergé, S. Skupin, F. Lederer, G. Méjean, J. Yu, J. Kasparian, E. Salmon, J. P. Wolf, M. Rodriguez, L. Wöste, R. Bourayou, and R. Sauerbrey. Multiple filamentation of terawatt laser pulses in air. *Physical Review Letters*, 92:225002, 2004.

[18] J. Bernhardt, W. Liu, F. Théberge, H. L. Xu, J. F. Daigle, M. Châteauneuf, J. Dubois, and S. L. Chin. Spectroscopic analysis of femtosecond laser plasma filament in air. *Optics Communications*, 281(5):1268–1274, 2008.

[19] B. D. Boyer, N. Anheier, P. Cable-Dunlop, and L. Sexton. Incorporation of new, automated environmental sampling systems into safeguards approaches. Technical Report la-ur-13-28412, Los Alamos National Laboratory, 2013.

[20] A. Braun, G. Korn, X. Liu, D. Du, J. Squier, and G. Mourou. Self-channeling of high-peak-power femtosecond laser pulses in air. *Optics Letters*, 20(1):73–75, 1995.

[21] Y. Brelet, A. Houard, G. Point, B. Prade, L. Arantchouk, J. Carbonnel, Y.-B. André, M. Pellet, and A. Mysyrowicz. Radiofrequency plasma antenna generated by femtosecond laser filaments in air. *Applied Physics Letters*, 101(26):264106, 2012.

[22] S. G. Buckley. Laser-induced breakdown spectroscopy for toxic metal emission measurements: Experimental considerations and oxygen quenching. *Environmental Engineering Science*, 22(2):195–204, 2005.

[23] G. Budylin, E. Shirshin, V. Fadeev, V. Petrov, and S. Kalmykov. Laser-induced fluorescence of uranyl complexes in aqueous solutions: The role of diffusion-controlled excited states annihilation. *Optics Express*, 21(18):20517–20528, 2013.

[24] M. Burger, L. A. Finney, L. Garrett, S. S. Harilal, K. C. Hartig, J. Nees, P. J. Skrodzki, X. Xiao, and I. Jovanovic. Laser ablation spectrometry for studies of uranium plasmas, reactor monitoring, and spent fuel safety. *Spectrochimica Acta Part B: Atomic Spectroscopy*, 179:106095, 2021.

[25] M. Burger, P. Polynkin, and I. Jovanovic. Filament-induced breakdown spectroscopy with structured beams. *Optics Express*, 28(24):36812–36821, 2020.

[26] M. Burger, P. J. Skrodzki, L. A. Finney, J. Hermann, J. Nees, and I. Jovanovic. Isotopic analysis of deuterated water via single- and double-pulse laser-induced breakdown spectroscopy. *Physics of Plasmas*, 25(8):83115, 2018.

[27] M. Burger, P. J. Skrodzki, L. A. Finney, J. Nees, and I. Jovanovic. Remote detection of uranium using self-focusing intense femtosecond laser pulses. *Remote Sensing*, 12(8):1281, 2020.

[28] M. Burger, P. J. Skrodzki, I. Jovanovic, M. C. Phillips, and S. S. Harilal. Laser-produced uranium plasma characterization and stark broadening measurements. *Physics of Plasmas*, 26(9):93103, 2019.

[29] M. Burger, P. J. Skrodzki, J. Lin, J. Nees, K. Krushelnick, and I. Jovanovic. Intense laser filament-solid interactions from near-ultraviolet to mid-infrared. *Optics Express*, 26(13):16456–16465, 2018.

[30] M. Burger, P. J. Skrodzki, J. Nees, and I. Jovanovic. Electrical conductance of near-infrared femtosecond air filaments in the multi-filament regime. *Optics Letters*, 43(22):5520–5523, 2018.

[31] M. C. Chakravorti, M. Chowdhury, P. G. Eller, and R. J. Kissane. *Difluorodioxouranium(VI)*, pages 144–146. John Wiley & Sons, Hoboken, NJ, USA, 1989.

[32] G. C.-Y. Chan, I. Choi, X. Mao, V. Zorba, O. P. Lam, D. K. Shuh, and R. E. Russo. Isotopic determination of uranium in soil by laser induced breakdown spectroscopy. *Spectrochimica Acta Part B: Atomic Spectroscopy*, 122:31–39, 2016.

[33] H.-S. Chang, G. V. Korshin, Z. Wang, and J. M. Zachara. Adsorption of uranyl on Gibbsite: A time-resolved laser-induced fluorescence spectroscopy study. *Environmental Science & Technology*, 40(4):1244–1249, 2006.

[34] M. Châteauneuf, S. Payeur, J. Dubois, and J.-C. Kieffer. Microwave guiding in air by a cylindrical filament array waveguide. *Applied Physics Letters*, 92(9):091104, 2008.

[35] Y.-H. Cheng, S. Varma, T. M. Antonsen, and H. M. Milchberg. Direct measurement of the electron density of extended femtosecond laser pulse-induced filaments. *Physical Review Letters*, 105(21):215005, 2010.

[36] Y.-H. Cheng, J. K. Wahlstrand, N. Jhajj, and H. M. Milchberg. The effect of long timescale gas dynamics on femtosecond filamentation. *Optics Express*, 21(4):4740–4751, 2013.

[37] B. N. Chichkov, C. Momma, S. Nolte, F. Von Alvensleben, and A. Tunnermann. Femtosecond, picosecond and nanosecond laser ablation of solids. *Applied Physics A: Materials Science & Processing*, 63(2):109–115, 1996.

[38] S. L. Chin. *Femtosecond Laser Filamentation*, volume 55. Springer, New York City, NY, USA, 2009.

[39] R. C. Chinni, D. A. Cremers, L. J. Radziemski, M. Bostian, and C. Navarro-Northrup. Detection of uranium using laser-induced breakdown spectroscopy. *Applied Spectroscopy*, 63(11):1238–1250, 2009.

[40] I. Choi, G. C.-Y. Chan, X. Mao, D. L. Perry, and R. E. Russo. Line selection and parameter optimization for trace analysis of uranium in glass matrices by laser-induced breakdown spectroscopy (LIBS). *Applied Spectroscopy*, 67(11):1275–1284, 2013.

[41] J. Colgan, K. C. Hartig, D. P. Kilcrease, J. E. Barefield II, and I. Jovanovic. Laser-induced breakdown spectroscopy using mid-infrared femtosecond pulses. *Journal of Applied Physics*, 118(4):43107, 2015.

[42] A. Couairon, G. Méchain, S. Tzortzakis, M. Franco, B. Lamouroux, B. Prade, and A. Mysyrowicz. Propagation of twin laser pulses in air and concatenation of plasma strings produced by femtosecond infrared filaments. *Optics Communications*, 225(1):177–192, 2003.

[43] A. Couairon and A. Mysyrowicz. Femtosecond filamentation in transparent media. *Physics Reports*, 441(2):47–189, 2007.

[44] A. Couairon and S. Tzortzakis. A waveguide made of hot air. *Physics (College Park, MD)*, 7:1, 2014.

[45] F. Courvoisier, V. Boutou, J. Kasparian, E. Salmon, G. Mejean, J. Yu, and J. P. Wolf. Ultraintense light filaments transmitted through clouds. *Applied Physics Letters*, 83(2):213–215, 2003.

[46] L. Couston, D. Pouyat, C. Moulin, and P. Decambox. Speciation of uranyl species in nitric acid medium by time-resolved laser-induced fluorescence. *Applied Spectroscopy*, 49(3):349–353, 1995.

[47] J.-F Daigle, A Jaroń-Becker, S Hosseini, T.-J Wang, Y Kamali, G Roy, A Becker, and S. L Chin. Intensity clamping measurement of laser filaments in air at 400 and 800 nm. *Physical Review A: Atomic, Molecular, & Optical Physics*, 82(2), 2010.

[48] J.-F. Daigle, Y. Kamali, M. Châteauneuf, G. Tremblay, F. Théberge, J. Dubois, G. Roy, and S. L. Chin. Remote sensing with intense filaments enhanced by adaptive optics. *Applied Physics B: Lasers & Optics*, 97(3):701–713, 2009.

[49] J.-F. Daigle, G. Méjean, W. Liu, F. Théberge, H. L. Xu, Y. Kamali, J. Bernhardt, A. Azarm, Q. Sun, P. Mathieu, G. Roy, J.-R. Simard, and S. L. Chin. Long range trace detection in aqueous aerosol using remote filament-induced breakdown spectroscopy. *Applied Physics B: Lasers & Optics*, 87:749–754, 2007.

[50] J.-F. Daigle, F. Théberge, P. Lassonde, J.-C. Kieffer, T. Fujii, J. Fortin, M. Châteauneuf, and J. Dubois. Dynamics of laser-guided alternating current high voltage discharges. *Applied Physics Letters*, 103(18):184101–1–4, 2013.

[51] J. T. Davies and J. M. Vaughan. A new tabulation of the Voigt profile. *Astrophysical Journal*, 137:1302–1305, 1963.

[52] J. Davis, J. Browne, P. Lewis, C. Pura, A. Sessoms, T. Shea, F. Slakey, B. Tannenbaum, J. Tape, J. Taylor, and P. D. Zimmerman. Technical steps to support nuclear arsenal downsizing. Technical report, American Physical Society, 2010.

[53] G. de Izarra and C. de Izarra. Quantitative shadowgraphy made easy. *European Journal of Physics*, 33(6):1821–1842, 2012.

[54] J. P. deNeufville, A. Kasdan, and R. J. L. Chimenti. Selective detection of uranium by laser-induced fluorescence: a potential remote-sensing technique. 1: Optical characteristics of uranyl geologic targets. *Applied Optics*, 20(8):1279–1296, 1981.

[55] H. Deniau, P. Decambox, P. Mauchien, and C. Moulin. Time-resolved laser-induced spectrofluorometry of UO_2^{2+} in nitric acid solutions. Preliminary results for on-line uranium monitoring applications. *Radiochimica Acta*, 61(1):23–28, 1993.

[56] I. Dicaire, V. Jukna, C. Praz, C. Milián, L. Summerer, and A. Couairon. Space-borne laser filamentation for atmospheric remote sensing. *Laser & Photonics Reviews*, 10(3):481–493, 2016.

[57] P. K. Diwakar, S. S. Harilal, A. Hassanein, and M. C. Phillips. Expansion dynamics of ultrafast laser produced plasmas in the presence of ambient argon. *Journal of Applied Physics*, 116(13):133301, 2014.

[58] F. R. Doucet, G. Lithgow, R. Kosierb, P. Bouchard, and M. Sabsabi. Determination of isotope ratios using laser-induced breakdown spectroscopy in ambient air at atmospheric pressure for nuclear forensics. *Journal of Analytical Atomic Spectrometry*, 26:536–541, 2011.

[59] M. Durand, A. Houard, B. Prade, A. Mysyrowicz, A. Durécu, B. Moreau, D. Fleury, O. Vasseur, H. Borchert, and K. Diener. Kilometer range filamentation. *Optics Express*, 21(22):26836–26845, 2013.

[60] V. Eliet, G. Bidoglio, N. Omenetto, L. Parma, and I. Grenthe. Characterisation of hydroxide complexes of uranium(VI) by time-resolved fluorescence spectroscopy. *Journal of the Chemical Society, Faraday Transactions*, 91:2275–2285, 1995.

[61] V. Eliet, I. Grenthe, and G. Bidoglio. Time-resolved laser-induced fluorescence of uranium(VI) hydroxo-complexes at different temperatures. *Applied Spectroscopy*, 54(1):99–105, 2000.

[62] L. A. Emmert, R. C. Chinni, D. A. Cremers, C. R. Jones, and W. Rudolph. Comparative study of femtosecond and nanosecond laser-induced breakdown spectroscopy of depleted uranium. *Applied Optics*, (3):313–317, 2011.

[63] A. C. Englesbe, Z. He, J. A. Nees, A. G. R. Thomas, A. Schmitt-Sody, and K. Krushelnick. Control of the configuration of multiple femtosecond filaments in air by adaptive wavefront manipulation. *Optics Express*, 24(6):6071–6082, 2016.

[64] D. Faccio, A. Lotti, A. Matijosius, F. Bragheri, V. Degiorgio, A. Couairon, and P. Di Trapani. Experimental energy-density flux characterization of ultrashort laser pulse filaments. *Optics Express*, 17(10):8193–8200, 2009.

[65] A. J. Fahey, C. J. Zeissler, D. E. Newbury, J. Davis, and R. M. Lindstrom. Post-detonation nuclear debris for attribution. *Proceedings of the National Academy of Sciences*, 107(47):20207–20212, 2010.

[66] Z. Farooq, D. A. Chestakov, B. Yan, G. C. Groenenboom, W. J. van der Zande, and D. H. Parker. Photodissociation of singlet oxygen in the UV region. *Physical Chemistry Chemical Physics*, 16(7):3305–3316, 2014.

[67] Z.F Feng, W Li, C.X Yu, X Liu, J Liu, and L.B Fu. Extended laser filamentation in air generated by femtosecond annular gaussian beams. *Physical Review A: Atomic, Molecular, & Optical Physics*, 91(3), 2015.

[68] M. S. Finko and D. Curreli. Simulation of uranium plasma plume dynamics in atmospheric oxygen produced via femtosecond laser ablation. *Physics of Plasmas*, 25(8):083112, 2018.

[69] M. S. Finko, D. Curreli, D. G. Weisz, J. C. Crowhurst, T. P. Rose, B. Koroglu, H. B. Radousky, and M. R. Armstrong. A model of early formation of uranium molecular oxides in laser-ablated plasmas. *Journal of Physics D: Applied Physics*, 50(48):485201, 2017.

[70] L. A. Finney, J. Lin, P. J. Skrodzki, M. Burger, J. Nees, K. Krushelnick, and I. Jovanovic. Filament-induced breakdown spectroscopy signal enhancement using optical wavefront control. *Optics Communications*, 490:126902, 2021.

[71] L. A. Finney, P. J. Skrodzki, M. Burger, J. Nees, S. S. Harilal, and I. Jovanovic. Single-shot, multi-signature remote detection of uranium by filament-induced breakdown spectroscopy. *Optics Letters*, 44(11):2783–2786, 2019.

[72] L. A. Finney, P. J. Skrodzki, M. Burger, X. Xiao, J. Nees, and I. Jovanovic. Optical emission from ultrafast laser filament-produced air plasmas in the multiple filament regime. *Optics Express*, 26(22):29110–29122, 2018.

[73] B. La Fontaine, F. Vidal, D. Comtois, C.-Y. Chien, A. Desparois, T. W. Johnston, J. Kieffer, H. P. Mercure, H. Pepin, and F. A. M. Rizk. The influence of electron density on the formation of streamers in electrical discharges triggered with ultrashort laser pulses. *IEEE Transactions on Plasma Science*, 27(3):688–700, 1999.

[74] C. G. Found. Ionization potentials of argon, nitrogen, carbon monoxide, helium, hydrogen and mercury and iodine vapors. *Physics Reviews*, 16:41–53, 1920.

[75] Y. Fu, M. Hou, H. Zang, H. Li, S. L. Chin, and H. Xu. Remote discrimination of willow, pine and poplar trees and their growing environments by femtosecond filament-induced breakdown spectroscopy. *Spectrochimica acta. Part B: Atomic spectroscopy*, 155:107–114, 2019.

[76] Y. Fu, H. Xiong, H. Xu, J. Yao, B. Zeng, W. Chu, Y. Cheng, Z. Xu, W. Liu, and S. L. Chin. Generation of extended filaments of femtosecond pulses in air by use of a single-step phase plate. *Optics Letters*, 34(23):3752–3754, 2009.

[77] U. Gabriel, L. Charlet, C. W. Schlöpfer, J. C. Vial, A. Brachmann, and G. Geipel. Uranyl surface speciation on silica particles studied by time-resolved laser-induced fluorescence spectroscopy. *Colloid & Interface Science*, 239(2):358–368, 2001.

[78] A. L. Gaeta. Catastrophic collapse of ultrashort pulses. *Physical Review Letters*, 84(16):3582–3585, 2000.

[79] L. Gagliardi, M. C. Heaven, J. W. Krogh, and B. O. Roos. The electronic spectrum of the UO_2 molecule. *Journal of the American Chemical Society*, 127(1):86–91, 2005.

[80] Y. E. Geints, A. M. Kabanov, A. A. Zemlyanov, E. E. Bykova, O. A. Bukin, and S. S. Golik. Kerr-driven nonlinear refractive index of air at 800 and 400 nm measured through femtosecond laser pulse filamentation. *Applied Physics Letters*, 99(18):181114, 2011.

[81] G. Geipel. Some aspects of actinide speciation by laser-induced spectroscopy. *Coordination Chemistry Reviews*, 250(7):844–854, 2006.

[82] G. Geipel, G. Bernhard, M. Rutsch, V. Brendler, and H. Nitsche. Spectroscopic properties of uranium(VI) minerals studied by time-resolved laser-induced fluorescence spectroscopy (TRLFS). *Radiochimica Acta*, 88(9-11):757–762, 1999.

[83] G. Geipel, A. Brachmann, V. Brendler, G. Bernhard, and H. Nitsche. Uranium(VI) sulfate complexation studied by time-resolved laser-induced fluorescence spectroscopy (TRLFS). *Radiochimica Acta*, 75(4):199–204, 1996.

[84] I. Ghebregziabher, K. C. Hartig, and I. Jovanovic. Propagation distance-resolved characteristics of filament-induced copper plasma. *Optics Express*, 24(5):5263–5276, 2016.

[85] A. Glaser. About the enrichment limit for research reactor conversion: Why 20%? *International Meeting on Reduced Enrichment for Research and Test Reactors (RERTR)*, 37(INIS-XA-C–121), 2005.

[86] S. Glasstone and P. J. Dolan. *The Effects of Nuclear Weapons*. U.S. Atomic Energy Commission, Washington D.C., USA, 3rd edition, 1977.

[87] R. L. Gleason and D. W. Hahn. The effects of oxygen on the detection of mercury using laser-induced breakdown spectroscopy. *Spectrochimica Acta Part B: Atomic Spectroscopy*, 56(4):419–430, 2001.

[88] I. E. Gordon, L. S. Rothman, C. Hill, R. V. Kochanov, Y. Tan, P. F. Bernath, M. Birk, V. Boudon, A. Campargue, K. V. Chance, B. J. Drouin, J.-M. Flaud, R. R. Gamache, J. T. Hodges, D. Jacquemart, V. I. Perevalov, A. Perrin, K. P. Shine, M.-A. H. Smith, J. Tennyson, G. C. Toon, H. Tran, V. G. Tyuterev, A. Barbe, A. G. Csaszar, V. M. Devi, T. Furtenbacher, J. J. Harrison, J.-M. Hartmann, A. Jolly, T. J. Johnson, T. Karman, I. Kleiner, A. A. Kyuberis, J. Loos, O. M. Lyulin, S. T. Massie, S. N. Mikhailenko, N. Moazzen-Ahmadi, H. S. P. Muller, O. V. Naumenko, A. V. Nikitin, O. L. Polyansky, M. Rey, M. Rotger, S. W. Sharpe, K. Sung, E. Starikova, S. A. Tashkun, J. Vander

Auwera, G. Wagner, J. Wilzewski, P. Wcislo, S. Yu, and E. J. Zak. The HITRAN2016 Molecular Spectroscopic Database. *Journal of Quantitative Spectroscopy and Radiative Transfer*, 2017.

[89] H. R. Griem. *Plasma Spectroscopy*. Academic Press, New York City, NY, USA, 1964.

[90] H. R. Griem. *Spectral Line Broadening by Plasmas*. Academic Press, New York City, NY, USA, 1974.

[91] G. Y. Grigor'ev, S. S. Nabiev, S. L. Malyugin, M. A. Sukhanova, A. I. Nadezhdinskii, and Y. Y. Ponurovskii. Laser-spectroscopic techniques for monitoring releases from nuclear fuel cycle objects. *Atomic Energy*, 105(4):280, 2009.

[92] J. K. Gruetzner, R. J. Law, T. R. Nelson, N. L. Bruner, and I. T. Kohl. Filamentation in air at 1550 nm. In *Lasers and Electro-Optics/Quantum Electronics and Laser Science Conference: 2010 Laser Science to Photonic Applications, CLEO/QELS 2010*, 2010.

[93] D. W. Hahn and N. Omenetto. Laser-Induced Breakdown Spectroscopy (LIBS), Part I: Review of basic diagnostics and plasma-particle interactions: Still-challenging issues within the analytical plasma community. *Applied Spectroscopy*, 64(12):335A–336A, 2010.

[94] J. Han, V. Goncharov, L. A. Kaledin, A. V. Komissarov, and M. C. Heaven. Electronic spectroscopy and ionization potential of UO_2 in the gas phase. *Journal of Chemical Physics*, 120(11):5155–5163, 2004.

[95] S. S. Harilal, C. V. Bindhu, M. S. Tillack, F. Najmabadi, and A. C. Gaeris. Plume splitting and sharpening in laser-produced aluminium plasma. *Journal of Physics D: Applied Physics*, 35(22):2935, 2002.

[96] S. S. Harilal, C. V. Bindhu, M. S. Tillack, F. Najmabadi, and A. C. Gaeris. Internal structure and expansion dynamics of laser ablation plumes into ambient gases. *Journal of Applied Physics*, 93(5):2380–2388, 2003.

[97] S. S. Harilal, B. E. Brumfield, B. D. Cannon, and M. C. Phillips. Shock wave mediated plume chemistry for molecular formation in laser ablation plasmas. *Analytical Chemistry*, 88(4):2296–2302, 2016.

[98] S. S. Harilal, B. E. Brumfield, N. L. LaHaye, K. C. Hartig, and M. C. Phillips. Optical spectroscopy of laser-produced plasmas for standoff isotopic analysis. *Applied Physics Reviews*, 5:021301, 2018.

[99] S. S. Harilal, E. J. Kautz, B. E. Bernacki, M. C. Phillips, P. J. Skrodzki, M. Burger, and I. Jovanovic. Physical conditions for UO formation in laser-produced uranium plumes. *Physical Chemistry Chemical Physics*, 21(29):16161–16169, 2019.

[100] S. S. Harilal, C. M. Murzyn, E. J. Kautz, M. K. Edwards, S. I. Sinkov, S. E. Bisson, S. S. Mitra, and J. B. Martin. Spectral dynamics and gas-phase oxidation of laser-produced plutonium plasmas. *Journal of Analytical Atomic Spectrometry*, 36(1):150–156, 2021.

[101] S. S. Harilal, C. M. Murzyn, M. C. Phillips, and J. B. Martin. Hyperfine structures and isotopic shifts of uranium transitions using tunable laser spectroscopy of laser ablation plumes. *Spectrochimica Acta Part B: Atomic Spectroscopy*, 169:105828, 2020.

[102] S. S. Harilal, J. Yeak, B. E. Brumfield, and M. C. Phillips. Consequences of femtosecond laser filament generation conditions in standoff laser induced breakdown spectroscopy. *Optics Express*, 24(16):17941–17949, 2016.

[103] S. S. Harilal, J. Yeak, and M. C. Phillips. Plasma temperature clamping in filamentation laser induced breakdown spectroscopy. *Optics Express*, 23(21):27113–27122, 2015.

[104] K. C. Hartig, I. Ghebregziabher, and I. Jovanovic. Standoff detection of uranium and its isotopes by femtosecond filament laser ablation molecular isotopic spectrometry. *Scientific Reports*, 7(1):43852, 2017.

[105] K. C. Hartig, S. S. Harilal, M. C. Phillips, B. E. Brumfield, and I. Jovanovic. Evolution of uranium monoxide in femtosecond laser-induced uranium plasmas. *Optics Express*, 25(10):11477–11490, 2017.

[106] M. Hashida, A. F. Semerok, O. Gobert, G. Petite, and J.-F. Wagner. Ablation thresholds of metals with femtosecond laser pulses. In *Proceedings of SPIE*, volume 4423, pages 178–185, 2001.

[107] S. Henin, Y. Petit, J. Kasparian, J.-P. Wolf, A. Jochmann, S. D. Kraft, S. Bock, U. Schramm, R. Sauerbrey, and W. M. Nakaema. Saturation of the filament density of ultrashort intense laser pulses in air. *Applied Physics B: Lasers & Optics*, 100(1):77–84, 2010.

[108] J. Hermann, D. Grojo, E. Axente, C. Gerhard, M. Burger, and V. Craciun. Ideal radiation source for plasma spectroscopy generated by laser ablation. *Physical Review E: Statistical, Nonlinear, Biological, & Soft Matter Physics*, 96:053210, 2017.

[109] Z. Hong, Q. Zhang, S. A. Rezvani, P. Lan, and P. Lu. Extending plasma channel of filamentation with a multi-focal-length beam. *Optics Express*, 24(4):4029–4041, 2016.

[110] H. Hou, B. Yang, X. Mao, V. Zorba, P. Ran, and R. E. Russo. Characteristics of plasma plume in ultrafast laser ablation with a weakly ionized air channel. *Optics Express*, 26(10):13425–13435, 2018.

[111] I. H. Hutchinson. *Principles of Plasma Diagnostics*. Cambridge University Press, Cambridge, UK, 2002.

[112] J. D. Jackson. *Classical Electrodynamics*. John Wiley & Sons, New York City, NY, USA, 3rd edition, 1999.

[113] C. Jeon, D. Harper, K. Lim, M. Durand, M. Chini, M. Baudelet, and M. Richardson. Interaction of a single laser filament with a single water droplet. *Journal of Optics*, 17(055502):1–5, 2015.

[114] N. Jhajj. *Hydrodynamic and Electrodynamic Implications of Optical Femtosecond Filamentation*. PhD thesis, University of Maryland, 2017.

[115] N. Jhajj, Y.-H. Cheng, J. K. Wahlstrand, and H. M. Milchberg. Optical beam dynamics in a gas repetitively heated by femtosecond filaments. *Optics express*, 21(23):28980–28986, 2013.

[116] N. Jhajj, I. Larkin, E. W. Rosenthal, S. Zahedpour, J. K. Wahlstrand, and H. M. Milchberg. Spatiotemporal optical vortices. *Physical Review X*, 6(3):031037, 2016.

[117] N. Jhajj, E. W. Rosenthal, R. Birnbaum, J. K. Wahlstrand, and H. M. Milchberg. Demonstration of long-lived high-power optical waveguides in air. *Physical Review X*, 4:011027, 2014.

[118] N. Jhajj, J. K. Wahlstrand, and H. M. Milchberg. Optical mode structure of the air waveguide. *Optics Letters*, 39(21):6312–6315, 2014.

[119] E. J. Judge, G. Heck, E. B. Cerkez, and R. J. Levis. Discrimination of composite graphite samples using remote filament-induced breakdown spectroscopy. *Analytical Chemistry*, 81(7):2658–2663, 2009.

[120] L. A. Kaledin and M. C. Heaven. Electronic spectroscopy of UO. *Journal of Molecular Spectroscopy*, 185(1):1–7, 1997.

[121] A. Kasdan, R. J. L. Chimenti, and J. P. deNeufville. Selective detection of uranium by laser-induced fluorescence: A potential remote-sensing technique. 2: Experimental assessment of the remote sensing of uranyl geologic targets. *Applied Optics*, 20(8):1297–1307, 1981.

[122] J. Kasparian, R. Ackermann, Y.-B. André, G. Méchain, G. Méjean, B. Prade, P. Rohwetter, E. Salmon, K. Stelmaszczyk, J. Yu, A. Mysyrowicz, R. Sauerbrey, L. Wöste, and J.-P. Wolf. Electric events synchronized with laser filaments in thunderclouds. *Optics Express*, 16(8):5757–5763, 2008.

[123] J. Kasparian, M. Rodriguez, G. Méjean, J. Yu, E. Salmon, H. Wille, R. Bourayou, S. Frey, Y.-B. André, and A. Mysyrowicz. White-light filaments for atmospheric analysis. *Science (American Association for the Advancement of Science)*, 301(5629):61–64, 2003.

[124] E. J. Kautz, M. C. Phillips, and S. S. Harilal. Unraveling spatio-temporal chemistry evolution in laser ablation plumes and its relation to initial plasma conditions. *Analytical Chemistry*, 92(20):13839–13846, 2020.

[125] E. J. Kautz, P. J. Skrodzki, M. Burger, B. E. Bernacki, I. Jovanovic, M. C. Phillips, and S. S. Harilal. Time-resolved imaging of atoms and molecules in laser-produced uranium plasmas. *Journal of Analytical Atomic Spectrometry*, 34(11):2236–2243, 2019.

[126] E. J. Kautz, J. Yeak, B. E. Bernacki, M. C. Phillips, and S. S. Harilal. The role of ambient gas confinement, plasma chemistry, and focusing conditions on emission features of femtosecond laser-produced plasmas. *Journal of Analytical Atomic Spectrometry*, 35(8):1574–1586, 2020.

[127] H.-Y. D. Ke and G. D. Rayson. Luminescence linewidth broadening and non-radiative energy transfer studies of solid UO_2^{+2}-Datura. *Applied Spectroscopy*, 46(9):1376–1381, 1992.

[128] R. S. Kemp. Initial analysis of the detectability of UO_2F_2 aerosols produced by UF_6 released from uranium conversion plants. *Science & Global Security*, 16(3):115–125, 2008.

[129] K. Y. Kim, V. Kumarappan, and H. M. Milchberg. Measurement of the average size and density of clusters in a gas jet. *Applied Physics Letters*, 83(15):3210–3212, 2003.

[130] P. P. Kiran, S. Bagchi, C. L. Arnold, S. R. Krishnan, G. R. Kumar, and A. Couairon. Filamentation without intensity clamping. *Optics Express*, 18(20):21504–21510, 2010.

[131] S. E. Kirkwood, Y. Y. Tsui, R. Fedosejevs, A. V. Brantov, and V. Y. Bychenkov. Experimental and theoretical study of absorption of femtosecond laser pulses in interaction with solid copper targets. *Physical Review B: Condensed Matter & Materials Physics*, 79(14), 2009.

[132] G. F. Knoll. *Radiation Detection and Measurement*. John Wiley & Sons, New York City, NY, USA, 3rd edition, 2000.

[133] P. Ko, J. R. Scott, and I. Jovanovic. Analysis of high-resolution spectra from a hybrid interferometric/dispersive spectrometer. *Optics Communications*, 357:95–99, 2015.

[134] N. Konjević and W. L. Wiese. Experimental Stark widths and shifts for spectral lines of neutral and ionized atoms. *Journal of Physical & Chemical Reference Data*, 19(6):1307–1385, 1990.

[135] A. D. Koulouklidis, C. Lanara, C. Daskalaki, V. Y. Fedorov, and S. Tzortzakis. Impact of gas dynamics on laser filamentation THz sources at high repetition rates. *Optics Letters*, 45(24):6835–6838, 2020.

[136] D. LaGraffe. *Nuclear Security Science*, pages 1–34. Springer, New York City, NY, USA, 2018.

[137] O. Lahav, L. Levi, I. Orr, R. A. Nemirovsky, J. Nemirovsky, I. Kaminer, M. Segev, and O. Cohen. Long-lived waveguides and sound-wave generation by laser filamentation. *Physical Review A: Atomic, Molecular, & Optical Physics*, 90:021801, 2014.

[138] N. L. LaHaye, S. S. Harilal, P. K. Diwakar, and A. Hassanein. Persistence of uranium emission in laser-produced plasmas. *Journal of Applied Physics*, 115(16):163301, 2014.

[139] J. R. Lakowicz. *Principles of Fluorescence Spectroscopy*. Springer, New York City, NY, USA, 3rd edition, 2006.

[140] J. J. Laserna, R. Fernández Reyes, R. González, L. Tobaria, and P. Lucena. Study on the effect of beam propagation through atmospheric turbulence on standoff nanosecond laser induced breakdown spectroscopy measurements. *Optics Express*, 17(12):10265–10276, 2009.

[141] L. Lavisse, M. Girault, P. Berger, J.-M. Jouvard, J.-L. Le Garrec, E. Carvou, F.-X. Ouf, F. Calvo, J. Yu, G.-D. Förster, V. Potin, S. Bourgeois, M. C. Marco de Lucas, and J. B. A. Mitchell. Evolution of the composition of nanoparticles formed by the nanosecond Nd:YAG laser irradiation of an aluminium target in N2–O2 gas mixtures. *Applied Physics A: Materials Science & Processing*, 123(11):692, 2017.

[142] K. Lechner. *Classical Electrodynamics: A Modern Perspective*. Springer, New York City, NY, USA, 2018.

[143] N. Lemos, L. Cardoso, J. Geada, F. Albert G. Figueira, and J. M. Dias. Guiding of laser pulses in plasma waveguides created by linearly-polarized femtosecond laser pulses. *Scientific Reports*, 8(3165):1–9, 2018.

[144] H. Li, W. Chu, H. Zang, H. Xu, Y. Cheng, and S. L. Chin. Critical power and clamping intensity inside a filament in a flame. *Optics Express*, 24(4):3424–3431, 2016.

[145] H. Li, H. Zang, H. Xu, H.-B. Sun, A. Baltu, and P. Polynkin. Robust remote sensing of trace-level heavy-metal contaminants in water using laser filaments. *Global Challenges*, 3(1):1800070, 2019.

[146] W. Liu, J.-F. Gravel, F. Théberge, A. Becker, and S. L. Chin. Background reservoir: Its crucial role for long-distance propagation of femtosecond laser pulses in air. *Applied Physics B: Lasers & Optics*, 80(7):857–860, 2005.

[147] W. Liu, F. Théberge, E. Arevalo, J.-F. Gravel, A. Becker, and S. L. Chin. Experiment and simulations on the energy reservoir effect in femtosecond light filaments. *Optics Letters*, 30(19):2602–2604, 2005.

[148] W. Liu, H. L. Xu, G. Méjean, Y. Kamali, J.-F. Daigle, A. Azarm, P. T. Simard, P. Mathieu, G. Roy, and S. L. Chin. Efficient non-gated remote filament-induced breakdown spectroscopy of metallic sample. *Spectrochimica Acta Part B: Atomic Spectroscopy*, 62(1):76–81, 2007.

[149] X.-L. Liu, W. Cheng, M. Petrarca, and P. Polynkin. Measurements of fluence profiles in femtosecond laser filaments in air. *Optics Letters*, 41(20):4751–4754, 2016.

[150] G. Lu, A. J. Haes, and T. Z. Forbes. Detection and identification of solids, surfaces, and solutions of uranium using vibrational spectroscopy. *Coordination Chemistry Reviews*, 374:314–344, 2018.

[151] J.-Q. Lü, P.-P. Li, D. A. N. Wang, C. Tu, Y. Li, and H.-T. Wang. Extending optical filaments with phase-nested laser beams. *Photonics Research*, 6(12):1130–1136, 2018.

[152] C. J. Lue, Jin, M. J. Ortiz, J. C. Rienstra-Kiracofe, and M. C. Heaven. Electronic Spectroscopy of UO_2 Isolated in a solid Ar matrix. *Journal of the American Chemical Society*, 126(6):1812–1815, 2004.

[153] Q. Luo, W. Liu, and S. L. Chin. Lasing action in air induced by ultra-fast laser filamentation. *Applied Physics B: Lasers & Optics*, 76(3):337–340, 2003.

[154] P. Maioli, R. Salamé, N. Lascoux, E. Salmon, P. Béjot, J. Kasparian, and J.-P. Wolf. Ultraviolet-visible conical emission by multiple laser filaments. *Optics Express*, 17(6):4726–4731, 2009.

[155] X. Mao, G. C.-Y. Chan, I. Choi, V. Zorba, and R. E. Russo. Combination of atomic lines and molecular bands for uranium optical isotopic analysis in laser induced plasma spectrometry. *Radioanalytical & Nuclear Chemistry*, 312(1):121–131, 2017.

[156] D. J. Matthew and M. D. Morse. Resonant two-photon ionization spectroscopy of jet-cooled UN: Determination of the ground state. *Journal of Chemical Physics*, 138(18):184303, 2013.

[157] R. W. P. McWhirter. *Plasma Diagnostic Techniques*. Academic Press, New York City, NY, USA, 1965.

[158] G. Méchain, C. D'Amico, Y.-B. André, S. Tzortzakis, M. Franco, B. Prade, A. Mysyrowicz, A. Couairon, E. Salmon, and R. Sauerbrey. Range of plasma filaments created in air by a multi-terawatt femtosecond laser. *Optics Communications*, 247(1-3):171–180, 2005.

[159] G. Meinrath. Uranium(VI) speciation by spectroscopy. *Radioanalytical & Nuclear Chemistry*, 224(1):119–126, 1997.

[160] G. Méjean, R. Ackermann, J. Kasparian, E. Salmon, J. Yu, J.-P. Wolf, K. Rethmeier, W. Kalkner, P. Rohwetter, K. Stelmaszczyk, and L. Wöste. Improved laser triggering and guiding of meqavolt discharges with dual fs-ns pulses. *Applied Physics Letters*, 88(2):021101, 2006.

[161] S. Mihai, A. Marcu, and N. N. Puscas. *Pulsed Laser Ablation of Solids: Basics, Theory, and Applications*, volume 53. Springer, New York City, NY, USA, 2013.

[162] A. V. Mitrofanov, A. A. Voronin, D. A. Sidorov-Biryukov, A. Pug, E. A. Stepanov, G. Andriukaitis, T. Flöry, S. Ali, A. B. Fedotov, and A. Baltu. Mid-infrared laser filaments in the atmosphere. *Scientific Reports*, 5(1):8368, 2015.

[163] S. I. Mitryukovskiy, Y. Liu, A. Houard, and A. Mysyrowicz. Re-evaluation of the peak intensity inside a femtosecond laser filament in air. *Journal of Physics B: Atomic, Molecular, & Optical Physics*, 48(9):94003, 2015.

[164] M. Miyabe, M. Oba, H. Iimura, K. Akaoka, Y. Maruyama, H. Ohba, M. Tampo, and I. Wakaida. Absorption spectroscopy of uranium plasma for remote isotope analysis of next-generation nuclear fuel. *Applied Physics A: Materials Science & Processing*, 112(1):87–92, 2013.

[165] D. Mongin, V. Shumakova, S. Ali, E. Schubert, A. Pug, J. Kasparian, J. P. Wolf, and A. Baltu. Conductivity and discharge guiding properties of mid-IR laser filaments. *Applied Physics B: Lasers & Optics*, 122(10):267, 2016.

[166] C. Moulin, N. Charron, G. Plancque, and H. Virelizier. Speciation of uranium by electrospray ionization mass spectrometry: Comparison with time-resolved laser-induced fluorescence. *Applied Spectroscopy*, 54(6):843–848, 2000.

[167] C. Moulin, P. Decambox, and P. Mauchien. State of the art in time-resolved laser-induced fluorescence for actinides analysis: Applications and trends. *Radioanalytical & Nuclear Chemistry*, 226(1):135–138, 1997.

[168] C. Moulin, P. Decambox, P. Mauchien, D. Pouyat, and L. Couston. Direct uranium(VI) and nitrate determinations in nuclear reprocessing by time-resolved laser-induced fluorescence. *Analytical Chemistry*, 68(18):3204–3209, 1996.

[169] C. Moulin, P. Decambox, V. Moulin, and J. G. Decaillon. Uranium speciation in solution by time-resolved laser-induced fluorescence. *Analytical Chemistry*, 67(2):348–353, 1995.

[170] C. Moulin, I. Laszak, V. Moulin, and C. Tondre. Time-resolved laser-induced fluorescence as a unique tool for low-level uranium speciation. *Applied Spectroscopy*, 52(4):528–535, 1998.

[171] C. Moulin, S. Rougeault, D. Hamon, and P. Mauchien. Uranium determination by remote time-resolved laser-induced fluorescence. *Applied Spectroscopy*, 47(12):2007–2012, 1993.

[172] A. Naghilou, O. Armbruster, and W. Kautek. Femto- and nanosecond pulse laser ablation dependence on irradiation area: The role of defects in metals and semiconductors. *Applied Surface Science*, 418:487–490, 2017.

[173] National Institute of Standards and Technology (NIST). Atomic Spectra Database, url: http://physics.nist.gov/asd, 2018.

[174] M. R. New-Tolley, M. N. Shneider, and R. B. Miles. Hydrodynamic confirmation of quasi-similarity theory and its application to weak blast wave motion generated by ultrashort pulse laser breakdown in quiescent air. *Journal of Computational Physics*, 408:109306, 2020.

[175] M. B. D. Nikitin, A. Andrews, and M. Holt. *Managing the Nuclear Fuel Cycle: Policy Implications of Expanding Global Access to Nuclear Power*. Library of Congress: Congressional Research Service. Diane Publishing [for the Congressional Research Service], Washington D.C., USA, 2010.

[176] S. P. O'Connor, C. B. Marble, D. T. Nodurft, G. D. Noojin, A. R. Boretsky, A. W. Wharmby, M. O. Scully, and V. V. Yakovlev. Filamentation in atmospheric air with tunable 1100-2400 nm near-infrared femtosecond laser source. *Scientific Reports*, 9(1):12049–7, 2019.

[177] K. Orsel, R. Groenen, B. Bastiaens, G. Koster, G. Rijnders, and K.-J. Boller. Influence of the oxidation state of SrTiO3 plasmas for stoichiometric growth of pulsed laser deposition films identified by laser induced fluorescence. *APL Materials*, 3(10):106103, 2015.

[178] J. C. Owens. Optical refractive index of air: Dependence on pressure, temperature and composition. *Applied Optics*, 6(1):51–59, 1967.

[179] B. A. Palmer, R. A. Keller, and R. Engleman. Report No. LA 8251-MS: An atlas of uranium emission intensities in a hollow cathode discharge. Technical report, Los Alamos National Laboratory, 1980.

[180] D. G. Papazoglou and S. Tzortzakis. In-line holography for the characterization of ultrafast laser filamentation in transparent media. *Applied Physics Letters*, 93(4):41120, 2008.

[181] J. Papeer, R. Bruch, E. Dekel, O. Pollak, M. Botton, Z. Henis, and A. Zigler. Generation of concatenated long high-density plasma channels in air by a single femtosecond laser pulse. *Applied Physics Letters*, 107(12):124102, 2015.

[182] H. Pépin, D. Comtois, F. Vidal, C. Y. Chien, A. Desparois, T. W. Johnston, J. C. Kieffer, B. La Fontaine, F. Martin, F. A. M. Rizk, C. Potvin, P. Couture, H. P. Mercure, A. Bondiou-Clergerie, P. Lalande, and I. Gallimberti. Triggering and guiding high-voltage large-scale leader discharges with sub-joule ultrashort laser pulses. *Physics of Plasmas*, 8(5):2532–2539, 2001.

[183] M. C. Phillips, B. E. Brumfield, N. LaHaye, S. S. Harilal, K. C. Hartig, and I. Jovanovic. Two-dimensional fluorescence spectroscopy of uranium isotopes in femtosecond laser ablation plumes. *Scientific Reports*, 7(3784):3784–1–12, 2017.

[184] M. C. Phillips, S. S. Harilal, and J. Yeak. Tunable laser absorption spectroscopy of uranium in femtosecond laser ablation plasmas. In *2016 Conference on Lasers and Electro-Optics (CLEO)*, pages 1–2, 2016.

[185] W. Pietsch, A. Petit, and A. Briand. Isotope ratio determination of uranium by optical emission spectroscopy on a laser-produced plasma - basic investigations and analytical results. *Spectrochimica Acta Part B: Atomic Spectroscopy*, 53(5):751–761, 1998.

[186] G. Point, L. Arantchouk, J. Carbonnel, A. Mysyrowicz, and A. Houard. Plasma dynamics of a laser filamentation-guided spark. *Physics of Plasmas*, 23(9):093505–1–4, 2016.

[187] G. Point, E. Thouin, A. Mysyrowicz, and A. Houard. Energy deposition from focused terawatt laser pulses in air undergoing multifilamentation. *Optics Express*, 24(6):6271–6282, 2016.

[188] P. Polynkin and Y. Cheng. *Air Lasing*. Springer, New York City, NY, USA, 2017.

[189] P. Polynkin, M. Kolesik, A. Roberts, D. Faccio, P. D Trapani, and J. Moloney. Generation of extended plasma channels in air using femtosecond bessel beams. *Optics Express*, 16(20):15733–15740, 2008.

[190] V. S. Popov. Tunnel and multiphoton ionization of atoms and ions in a strong laser field (Keldysh theory). *Physics Uspekhi*, 47(9):855–885, 2004.

[191] D. F. Price, R. M. More, R. S. Walling, G. Guethlein, R. L. Shepherd, R. E. Stewart, and W. E. White. Absorption of ultrashort laser pulses by solid targets heated rapidly to temperatures 1-1000 ev. *Physical Review Letters*, 75(2):252–255, 1995.

[192] J. Ready. *Effects of High-Power Laser Radiation*. Elsevier Science & Technology, Saint Louis, MO, USA, 1971.

[193] G. I. Reeves. *Radiological Disperal Devices: Detection, Response, and Remediation*, pages 1–25. Springer, New York City, NY, USA, 2018.

[194] M. Rodriguez, R. Bourayou, G. Méjean, J. Kasparian, J. Yu, E. Salmon, A. Scholz, B. Stecklum, J. Eislöffel, U. Laux, A. P. Hatzes, R. Sauerbrey, L. Wöste, and J.-P. Wolf. Kilometer-range nonlinear propagation of femtosecond laser pulses. *Physical Review E: Statistical, Nonlinear, Biological, & Soft Matter Physics*, 69:036607, 2004.

[195] M. Rodriguez, R. Sauerbrey, H. Wille, L. Wöste, T. Fujii, Y.-B. André, A. Mysyrowicz, L. Klingbeil, K. Rethmeier, W. Kalkner, J. Kasparian, E. Salmon, J. Yu, and J.-P. Wolf. Triggering and guiding megavolt discharges by use of laser-induced ionized filaments. *Optics Letters*, 27(9):772–774, 2002.

[196] P. Rohwetter, K. Stelmaszczyk, L. Wöste, R. Ackermann, G. Méjean, E. Salmon, J. Kasparian, J. Yu, and J.-P. Wolf. Filament-induced remote surface ablation for long range laser-induced breakdown spectroscopy operation. *Spectrochimica Acta Part B: Atomic Spectroscopy*, 60(7):1025–1033, 2005.

[197] E. W. Rosenthal, N. Jhajj, J. K. Wahlstrand, and H. M. Milchberg. Collection of remote optical signals by air waveguides. *Optica*, 1(1):5–9, 2014.

[198] E. W. Rosenthal, J. P. Palastro, N. Jhajj, S. Zahedpour, J. K. Wahlstrand, and H. M. Milchberg. Sensitivity of propagation and energy deposition in femtosecond filamentation to the nonlinear refractive index. *Journal of Physics B: Atomic, Molecular, & Optical Physics*, 48(9):94011, 2015.

[199] M. Rutsch, G. Geipel, V. Brendler, G. Bernhard, and H. Nitsche. Interaction of uranium(VI) with arsenate(V) in aqueous solution studied by time-resolved laser-induced fluorescence spectroscopy (TRLFS). *Radiochimica Acta*, 86(3-4):135–142, 1999.

[200] B. Sallé, P. Mauchien, and S. Maurice. Laser-induced breakdown spectroscopy in open-path configuration for the analysis of distant objects. *Spectrochimica Acta Part B: Atomic Spectroscopy*, 62(8):739–768, 2007.

[201] J. A. R. Samson and J. L. Gardner. On the ionization potential of molecular oxygen. *Canadian Journal of Physics*, 53(19):1948–1952, 1975.

[202] A. Sarkar, D. Alamelu, and S. K. Aggarwal. Laser-induced breakdown spectroscopy for determination of uranium in thorium–uranium mixed oxide fuel materials. *Talanta*, 78(3):800–804, 2009.

[203] M. Scheller, M. S. Mills, M.-A. Miri, W. Cheng, J. V. Moloney, M. Kolesik, P. Polynkin, and D. N. Christodoulides. Externally refuelled optical filaments. *Nature Photonics*, 8:297, 2014.

[204] R. W. Schoenlein, W. Z. Lin, J. G. Fujimoto, and G. L. Eesley. Femtosecond studies of nonequilibrium electronic processes in metals. *Physical Review Letters*, 58:1680–1683, 1987.

[205] E. Schubert, D. Mongin, J. Kasparian, and J.-P. Wolf. Remote electrical arc suppression by laser filamentation. *Optics Express*, 23(22):28640–28648, 2015.

[206] J. Schwarz, P. Rambo, J.-C. Diels, M. Kolesik, E. M. Wright, and J. V. Moloney. Ultraviolet filamentation in air. *Optics Communications*, 180(4):383–390, 2000.

[207] L. I. Sedov. *Similarity and Dimensional Methods in Mechanics*. Academic Press, New York City, NY, USA, 1959.

[208] S. V. Shabanov and I. B. Gornushkin. Modeling chemical reactions in laser-induced plasmas. *Applied Physics A: Materials Science & Processing*, 121(3):1087–1107, 2015.

[209] A. K. Shaik, N. R. Epuru, H. Syed, C. Byram, and V. R. Soma. Femtosecond laser induced breakdown spectroscopy based standoff detection of explosives and discrimination using principal component analysis. *Optics Express*, 26(7):8069–8083, 2018.

[210] A. K. Shaik and V. R. Soma. Standoff discrimination and trace detection of explosive molecules using femtosecond filament induced breakdown spectroscopy combined with silver nanoparticles. *OSA Continuum*, 2(3):554–562, 2019.

[211] M. B. Shattan, D. J. Miller, M. T. Cook, A. C. Stowe, J. D. Auxier, C. Parigger, and H. L. Hall. Detection of uranyl fluoride and sand surface contamination on metal substrates by hand-held laser-induced breakdown spectroscopy. *Applied Optics*, 56(36):9868–9875, 2017.

[212] G. Shayeganrad. On the remote monitoring of gaseous uranium hexafluoride in the lower atmosphere using lidar. *Optics & Lasers in Engineering*, 51(10):1192–1198, 2013.

[213] M. Singh and A.Sarkar. Time-resolved evaluation of uranium plasma in different atmospheres by laser-induced breakdown spectroscopy. *Plasma Science & Technology*, 20(12):125501, 2018.

[214] M. Singh, V. Karki, R. K. Mishra, A. Kumar, C. P. Kaushik, X. Mao, R. E. Russo, and A. Sarkar. Analytical spectral dependent partial least squares regression: A study of nuclear waste glass from thorium based fuel using libs. *Journal of Analytical Atomic Spectrometry*, 30:2507–2515, 2015.

[215] P. J. Skrodzki, J. R. Becker, P. K. Diwakar, S. S. Harilal, and A. Hassanein. A comparative study of single-pulse and double-pulse laser-induced breakdown spectroscopy with uranium-containing samples. *Applied Spectroscopy*, 70(3):467–473, 2016.

[216] P. J. Skrodzki, M. Burger, L. A. Finney, F. Poineau, S. M. Balasekaran, J. Nees, K. R. Czerwinski, and I. Jovanovic. Ultrafast laser filament-induced fluorescence spectroscopy of uranyl fluoride. *Scientific Reports*, 8(1):11629–9, 2018.

[217] P. J. Skrodzki, M. Burger, L. A. Finney, F. Poineau, S. M. Balasekaran, J. Nees, K. R. Czerwinski, and I. Jovanovic. Standoff detection of uranyl fluoride using ultrafast laser filamentation-induced fluorescence. In *2019 Conference on Lasers and Electro-Optics (CLEO)*, pages 1–2, 2019.

[218] P. J. Skrodzki, M. Burger, and I. Jovanovic. Transition of femtosecond-filament-solid interactions from single to multiple filament regime. *Scientific Reports*, 7(1):12740–8, 2017.

[219] P. J. Skrodzki, M. Burger, I. Jovanovic, M. C. Phillips, B. E. Brumfield, and S. S. Harilal. Tracking of oxide formation in laser-produced uranium plasmas. *Optics Letters*, 43(20):5118–5121, 2018.

[220] P. J. Skrodzki, M. Burger, I. Jovanovic, M. C. Phillips, J. Yeak, B. E. Brumfield, and S. S. Harilal. Plume dynamics and gas-phase molecular formation in transient laser-produced uranium plasmas. *Physics of Plasmas*, 26(8):83508, 2019.

[221] P. J. Skrodzki, L. A. Finney, M. Burger, J. Nees, and I. Jovanovic. Millisecond suppression of counter-propagating optical signal using ultrafast laser filaments. In *2020 Conference on Lasers and Electro-Optics (CLEO)*, pages 1–2, 2020.

[222] P. J. Skrodzki, N. P. Shah, N. Taylor, K. C. Hartig, N. L. LaHaye, B. E. Brumfield, I. Jovanovic, M. C. Phillips, and S. S. Harilal. Significance of ambient conditions in uranium absorption and emission features of laser ablation plasmas. *Spectrochimica Acta Part B: Atomic Spectroscopy*, 125:112–119, 2016.

[223] A. V. Smith. How to use SNLO nonlinear optics software to select nonlinear crystals and model their performance. In *Proceedings of SPIE*, volume 4972, pages 50–57. SPIE, 2003.

[224] J. Song, G. C.-Y. Chan, X. Mao, J. D. Woodward, R. W. Smithwick, T. G. Schaaff, A. C. Stowe, C. D. Harris, R. Zheng, V. Zorba, and R. E. Russo. Multivariate nonlinear spectral fitting for uranium isotopic analysis with laser-induced breakdown spectroscopy. *Spectrochimica Acta Part B: Atomic Spectroscopy*, 150:67–76, 2018.

[225] K. Stelmaszczyk, P. Rohwetter, G. Méjean, J. Yu, E. Salmon, J. Kasparian, R. Ackermann, J.-P. Wolf, and L. Wöste. Long-distance remote laser-induced breakdown spectroscopy using filamentation in air. *Applied Physics Letters*, 85(18):3977–3979, 2004.

[226] G. Stibenz, N. Zhavoronkov, and G. Steinmeyer. Self-compression of millijoule pulses to 7.8 fs duration in a white-light filament. *Optics Letters*, 31(2):274–276, 2006.

[227] X. Sun, S. Xu, J. Zhao, W. Liu, Y. Cheng, Z. Xu, S. L. Chin, and G. Mu. Impressive laser intensity increase at the trailing stage of femtosecond laser filamentation in air. *Optics Express*, 20(4):4790–4795, 2012.

[228] R. L. Sutherland. *Handbook of Nonlinear Optics*, volume 82. CRC Press, New York City, NY, USA, 2003.

[229] A. Talebpour, S. Larochelle, and S. L. Chin. Suppressed tunnelling ionization of the molecule in an intense Ti:sapphire laser pulse. *Journal of Physics B: Atomic, Molecular, & Optical Physics*, 31(2):L49–L58, 1998.

[230] N. Taylor and M. C. Phillips. Differential laser absorption spectroscopy of uranium in an atmospheric pressure laser-induced plasma. *Optics Letters*, 39:594–597, 2014.

[231] G. Tempea and T. Brabec. Theory of self-focusing in a hollow waveguide. *Optics Letters*, 23(10):762–764, 1998.

[232] F. Théberge, W. Liu, P. T. Simard, A. Becker, and S. L. Chin. Plasma density inside a femtosecond laser filament in air: Strong dependence on external focusing. *Physical Review E: Statistical, Nonlinear, Biological, & Soft Matter Physics*, 74:036406, 2006.

[233] S. Tzortzakis, D. Anglos, and D. Gray. Ultraviolet laser filaments for remote laser-induced breakdown spectroscopy (LIBS) analysis: applications in cultural heritage monitoring. *Optics Letters*, 31(8):1139–1141, 2006.

[234] S. Tzortzakis, M. A. Franco, Y.-B. André, A. Chiron, B. Lamouroux, B. S. Prade, and A. Mysyrowicz. Formation of a conducting channel in air by self-guided femtosecond laser pulses. *Physical Review E: Statistical, Nonlinear, Biological, & Soft Matter Physics*, 60:R3505–R3507, 1999.

[235] S. Tzortzakis, B. Lamouroux, A. Chiron, M. Franco, B. Prade, A. Mysyrowicz, and S. D. Moustaizis. Nonlinear propagation of subpicosecond ultraviolet laser pulses in air. *Optics Letters*, 25(17):1270–1272, 2000.

[236] S. Tzortzakis, G. Méchain, G. Patalano, M. Franco, B. Prade, and A. Mysyrowicz. Concatenation of plasma filaments created in air by femtosecond infrared laser pulses. *Applied Physics B: Lasers & Optics*, 76(5):609–612, 2003.

[237] A. Valenzuela, C. Munson, A. Porwitzky, M. Weidman, and M. Richardson. Comparison between geometrically focused pulses versus filaments in femtosecond laser ablation of steel and titanium alloys. *Applied Physics B: Lasers & Optics*, 116(2):485–491, 2014.

[238] T. Valmari, M. Tarvainen, and J. Lehtinen. Aerosol sampling methods for wide area environmental sampling (WAES) Finnish support to IAEA (STUK-YTO-TR–183). Technical report, Radiation and Nuclear Safety Authority (STUK), 2002.

[239] G. V. Vogman and U. Shumlak. Deconvolution of Stark broadened spectra for multi-point density measurements in a flow Z-pinch. *Review of Scientific Instruments*, 82(10):103504–103504–7, 2011.

[240] J. K. Wahlstrand, Y.-H. Cheng, Y.-H. Chen, and H. M. Milchberg. Optical nonlinearity in ar and n_2 near the ionization threshold. *Physical Review Letters*, 107(10):103901, 2011.

[241] J. K. Wahlstrand, J. H. Odhner, E. T. McCole, Y.-H. Cheng, J. P. Palastro, R. J. Levis, and H. M. Milchberg. Effect of two-beam coupling in strong-field optical pump-probe experiments. *Physical Review A: Atomic, Molecular,& Optical Physics*, 87(5), 2013.

[242] G. Wang, Y. Su, and D. L. Monts. Parametric investigation of laser-induced fluorescence of solid-state uranyl compounds. *Journal of Physical Chemistry A*, 112(42):10502–10508, 2008.

[243] Q. Wang and R. M. Pitzer. Structure and spectra of UO_2F_2 and its hydrated species. *Journal of Physical Chemistry A*, 105(36):8370–8375, 2001.

[244] Z. Wang, J. M. Zachara, P. L. Gassman, C. Liu, O. Qafoku, W. Yantasee, and J. G. Catalano. Fluorescence spectroscopy of U(VI)-silicates and U(VI)-contaminated Hanford sediment. *Geochimica et Cosmochimica Acta*, 69(6):1391–1403, 2005.

[245] E. N. Weerakkody and N. G. Glumac. Quantitative absorption spectroscopy of laser-produced plasmas. *Journal of Physics D: Applied Physics*, 54(12), 2021.

[246] E. N. Weerakkody, D. G. Weisz, J. Crowhurst, B. Koroglu, T. Rose, H. Radousky, R. L. Stillwell, J. R. Jeffries, and N. G. Glumac. Time-resolved formation of uranium and silicon oxides subsequent to the laser ablation of U_3Si_2. *Spectrochimica Acta Part B: Atomic Spectroscopy*, 170:105925, 2020.

[247] M. Weidman, K. Lim, M. Ramme, M. Durand, M. Baudelet, and M. Richardson. Stand-off filament-induced ablation of gallium arsenide. *Applied Physics Letters*, 101(3):34101, 2012.

[248] D. G. Weisz, J. C. Crowhurst, W. J. Siekhaus, T. P. Rose, B. Koroglu, H. B. Radousky, J. M. Zaug, M. R. Armstrong, B. H. Isselhardt, M. R. Savina, M. Azer, M. S. Finko, and D. Curreli. Formation of $^{238}U^{16}O$ and $^{238}U^{18}O$ observed by time-resolved emission spectroscopy subsequent to laser ablation. *Applied Physics Letters*, 111(3):034101, 2017.

[249] S.-B. Wen, C.-F. Chen, X. Mao, and R. E. Russo. Guiding and focusing of a nanosecond infrared laser within transient hollow plasma femtosecond filament channels. *Journal of Physics D: Applied Physics*, 45(35):355203.

[250] P. R. Willmott and J. R. Huber. Pulsed laser vaporization and deposition. *Reviews of Modern Physics*, 72(1):315–328, 2000.

[251] J.-P. Wolf. Short-pulse lasers for weather control. *Reports on Progress in Physics*, 81(2):026001, 2017.

[252] J.-P. Wolf, K. Stelmaszczyk, M. Queiber, E. Salmon, L. Wöste, P. Rohwetter, S. Henin, R. Salamé, J. Kasparian, and N. Lascoux. Laser-induced water condensation in air. *Nature Photonics*, 4(7):451–456, 2010.

[253] J. Wu, Y. Qiu, X. Li, H. Yu, Z. Zhang, and A. Qiu. Progress of laser-induced breakdown spectroscopy in nuclear industry applications. *Journal of Physics D: Applied Physics*, 53(2):023001, 2019.

[254] G. Xu, S. F. Wandel, and I. Jovanovic. Nondegenerate parametric generation of 2.2-mj, few-cycle 2.05-µm pulses using a mixed phase matching scheme. *Review of Scientific Instruments*, 85(2):023102, 2014.

[255] H. L. Xu, A. Azarm, J. Bernhardt, Y. Kamali, and S. L. Chin. The mechanism of nitrogen fluorescence inside a femtosecond laser filament in air. *Chemical Physics*, 360(1-3):171–175, 2009.

[256] H. L. Xu, G. Méjean, W. Liu, Y. Kamali, J.-F. Daigle, A. Azarm, P. T. Simard, P. Mathieu, G. Roy, J.-R. Simard, and S. L. Chin. Remote detection of similar biological materials using femtosecond filament-induced breakdown spectroscopy. *Applied Physics B: Lasers & Optics*, 87(1):151–156, 2007.

[257] H. L. Xu, P. T. Simard, Y. Kamali, J.-F. Daigle, C. Marceau, J. Bernhardt, J. Dubois, M. Châteauneuf, F. Théberge, and G. Roy. Filament-induced breakdown remote spectroscopy in a polar environment. *Laser Physics*, 22(12):1767–1770, 2012.

[258] Y. Yu, X. Li, S. Zhao, X. An, X. Yu, D. Chen, and R. Sun. Repetitive laser-induced plasma ignition and assisted combustion of premixed methane/air flame. *Combustion Science and Technology*, 189(10):1681–1697, 2017.

[259] S. Yuan, S. L. Chin, and H.-P. Zeng. Femtosecond filamentation induced fluorescence technique for atmospheric sensing. *Chinese Physics B*, 24(1):43–51, 2015.

[260] V. E. Zakharov and A. B. Shabat. Exact theory of two-dimensional self-focusing and one-dimensional self-modulation of waves in nonlinear media. *JETP*, 34(1):62–69, 1971.

[261] Y. B. Zeldovich and Y. P. Raizer. *Physics of Shock Waves and High-Temperature Hydrodynamic Phenomena*. Academic Press, New York City, NY, USA, 1966.

[262] B. Zeng, T.-J. Wang, S. Hosseini, Y. Cheng, Z. Xu, W. Liu, and S. L. Chin. Enhanced remote filament-induced breakdown spectroscopy with spatiotemporally chirped pulses. *Journal of the Optical Society of America B*, 29(12):3226–3230, 2012.

[263] T. Zeng, S. Zhu, S. Zhou, and Y. He. Spatial evolution of laser filaments in turbulent air. *Optics Communications*, 412:161–165, 2018.

[264] X. M. Zhao, J.-C. Diels, C. Y. Wang, and J. M. Elizondo. Femtosecond ultraviolet laser pulse induced lightning discharges in gases. *IEEE Journal of Quantum Electronics*, 31(3):599–612, 1995.

[265] A. M. Zheltikov. Keldysh parameter, photoionization adiabaticity, and the tunneling time. *Physical Review A: Atomic, Molecular, & Optical Physics*, 94(4), 2016.